

Nonlinear Ultrasonic Diagnosis and Prognosis of ASR Damage in Dry Cask Storage

Fuel Cycle

Jianmin Qu

Northwestern University

In collaboration with:

Georgia Institute of Technology
Electric Power Research Institute

JC de la Garza, Federal POC
TJ Ulrich, Technical POC

FINAL REPORT

Project Title: Nonlinear Ultrasonic Diagnosis and Prognosis of ASR Damage in Dry Cask Storage

Covering Period: January 20, 2013 – October 20, 2015

Date of Report: November 30, 2015

Recipient: Northwestern University
633 Clark Street
Evanston, IL 60208

Award Number: DE-AC07-05ID14517

PI: Jianmin Qu

Co-PI: Zdenek Bazant, Northwestern University (NU)
Laurence J. Jacobs, Georgia Institute of Technology (GT)
Maria Guimaraes, Electrical Power Research Institute (EPRI)

Project Objective: Alkali-silica reaction (ASR) is a deleterious chemical process that may occur in cement-based materials such as mortars and concretes, where the hydroxyl ions in the highly alkaline pore solution attack the siloxane groups in the siliceous minerals in the aggregates. The reaction produces a cross-linked alkali-silica gel. The ASR gel swells in the presence of water. Expansion of the gel results in cracking when the swelling-induced stress exceeds the fracture toughness of the concrete. As the ASR continues, cracks may grow and eventually coalesce, which results in reduced service life and a decrease safety of concrete structures.

Since concrete is widely used as a critical structural component in dry cask storage of used nuclear fuels, ASR damage poses a significant threat to the sustainability of long term dry cask storage systems. Therefore, techniques for effectively detecting, managing and mitigating ASR damage are needed. Currently, there are no nondestructive methods to accurately detect ASR damage in existing concrete structures. The only current way of accurately assessing ASR damage is to drill a core from an existing structure, and conduct microscopy on this drilled cylindrical core. Clearly, such a practice is not applicable to dry cask storage systems. To meet these needs, this research is aimed at developing (1) a suite of nonlinear ultrasonic quantitative nondestructive evaluation (QNDE) techniques to characterize ASR damage, and (2) a physics-based model for ASR damage evolution using the QNDE data. Outcomes of this research will provide a nondestructive diagnostic tool to evaluate the extent of the ASR damage, and a prognostic tool to estimate the future reliability and safety of the concrete structures in dry cask storage systems.

Contents

I.SUMMARY OF ACCOMPLISHMENTS OF THE PROJECT.....	3
II.PUBLICATIONS DURING THE PAST THREE YEARS.....	6
III.APPENDIX.....	7
III.1 Report of the 1st year.....	7
III.1.1 Nonlinear Wave Mixing Technique to Measure the ANLP in Concrete Samples Nondestructively in a Laboratory Environment	7
III.1.2 Physics-Based Models for ASR Damage Evolution	14
III.1.3 Physics-Based Models for ASR Damage Evolution Collinear Mixing of Two Transient Pulses in Nonlinear Elastic Solids	22
III.1.4 Physics-Based Models for ASR Damage Evolution	40
III.1.5 Nonlinear wave mixing technique to measure the ANLP in concrete samples nondestructively in a laboratory environment	44
III.1.6 Physics-Based Models that Correlate the ANLP to ASR Damage.....	50
III.1.7 Physics-Based Models for ASR Damage Evolution	58
III.1.8 Nonlinear Wave Mixing Technique to Measure the ANLP in Concrete Samples Nondestructively in a Laboratory Environment	62
III.1.9 Physics-based Models that Correlate the ANLP to ASR Damage	68
III.1.10 Physics-Based Models for ASR Damage Evolution	85
III.2 Report of the 2nd year	94
III.2.1 Calculation of ASR Activation Energy	94
III.2.2 Physics-based Models that Correlate the ANLP to ASR Damage	97
III.2.3 Rate of Moisture Diffusion in Cement Pastes and Alkaline-Silica Reaction	102
III.2.4 ASR Damage Evolution and Acoustic Nonlinearity Parameter.....	109
III.2.5 Modeling ASR Gel Diffusion in Cement Pastes.....	112
III.2.6 ASR Activation Energy and Rate of Reaction	116
III.2.7 Constitutive Model for Continuum Analysis for ASR Damage in Concrete with Diffusion of Compressible Gel into Pores	129
III.2.8 Effects of Moisture on Ultrasound Propagation in Cement Mortar	138
III.2.9 Constitutive Model for Continuum Analysis for ASR Damage in Concrete with Diffusion of Compressible Gel into Pores	144
III.3 Report of the 3rd year.....	152
III.3.1 Effects of Moisture on Ultrasound Propagation in Cement Mortar	152
III.3.2 A Micromechanics Model for the Acoustic Nonlinearity Parameter in Solids with Distributed Microcracks.....	158
III.3.3 Mixing of Two Co-Directional Rayleigh Surface Waves in a Nonlinear Elastic Material.....	161
III.3.4 Constitutive Model for Continuum Analysis for ASR Damage	163
III.3.5 Ultrasound Propagation in ASR Damaged Specimens	170
III.3.6 The constitutive model for continuum analysis of ASR induced damage.....	182
III.3.7 Linear and Nonlinear Ultrasonic Test in ASR Damaged Concrete Prisms	187
III.3.8 The constitutive model for continuum analysis of ASR induced damage.....	210
III.3.9 Nonlinear Ultrasonic Test in ASR Damaged Concrete prisms.....	217
III.3.10 Nonlinear Ultrasonic Test in ASR Damaged Concrete slabs	232
III.3.11 Diffusion-Controlled and Creep-Mitigated ASR Damage via Microplane Model: I. Mass Concrete.....	239

I. Summary of Accomplishments of the Project

1. Nonlinear wave mixing technique to measure the ANLP in concrete samples nondestructively in a laboratory environment – We have developed a collinear wave mixing technique to characterize ASR damage nondestructively. The technique has been successfully demonstrated in laboratory concrete samples subjected to accelerated ASR damage. The robustness and accuracy of this collinear wave mixing technique has been assessed by measuring the expansion and by the postmortem destructive optical microscopy of the concrete samples.
2. Physics-based models that correlate the ANLP to ASR damage – A preliminary model that correlates the acoustic nonlinearity parameter (ANLP) to ASR damage has been developed. The model is based on the microstructure changes in the concrete induced by ASR damage. Since the ANLP can be measured directly from the collinear wave mixing technique, this ANLP-ASR relationship enables the quantitative nondestructive evaluation of ASR damage by using the collinear wave mixing technique.
3. Physics-based models for ASR damage evolution – A chemo-mechanics model to describe the ASR-induced microstructural damage evolution has been developed and incorporated into a numerical simulation code based on the Lattice Discrete Particle Model (LDPM). The chemo-mechanics model accounts for all major aspects of chemical and mechanical processes including alkaline diffusion, ASR gel production, water imbibition, gel expansion, gel permeation into the porous cement, and cement fracture. The LDPM is a full 3D numerical algorithm that simulates the mechanical interaction of coarse aggregate pieces through a system of three-dimensional polyhedral particles, each resembling a spherical coarse aggregate piece with its surrounding mortar, connected through lattice struts. It is capable of simulating the effect of material heterogeneity of the fracture processes.
4. Validation of the ASR-ANLP relationship using laboratory data
5. Collinear mixing of two pulses was investigated analytically. We derived a set of necessary and sufficient conditions for generating resonant waves by two propagating time-harmonic plane waves. It was shown that in collinear mixing, a resonant wave can be generated either by a pair of longitudinal waves, in which case the resonant mixing wave is also a longitudinal wave, or by a pair of longitudinal and transverse waves, in which case the resonant wave is a transverse wave. In addition, we obtained closed-form analytical solutions to the resonant waves generated by two collinearly propagating sinusoidal pulses. The results show that amplitude of the resonant pulse is proportional to the mixing zone size, which is determined by the spatial lengths of the input pulses. Finally, numerical simulations based on the finite element method and experimental measurements using one-way mixing were conducted. It is shown that both numerical and experimental results agree well with the analytical solutions.
6. The correlation between the moisture content in cement mortar and ultrasonic wave propagation is experimentally determined. Specifically, effects of moisture on the ultrasonic phase velocity and attenuation are examined. It is found that, for the cement mortar samples considered in this study, moisture has negligible effect on the ultrasonic phase velocity.

7. The response of large specimens 4" X 4" X 10" was simulated. It was found that the linear assumption of Alkali diffusion is very crude and results in an excessive expansion in large specimens if the same diffusion coefficient was used. So, an improved 3D nonlinear diffusion model was implemented and adopted. After calibration, ASR expansion and ANLP simulations were performed on both, small and large specimens. The details are listed here. Physics-based models for ASR damage evolution is introduced.
8. Conducted experimental measurements of the rate of ASR reaction under different temperatures and alkaline concentrations. The experimental data were then used to estimate the ASR reaction activation energy. These results are necessary input to building a predictive model for ASR damage evolution.
9. Conducted experimental measurement of alkaline solution diffusion in hydrated cement paste and microscopy has been implemented to see if ASR occurred around a glass ball.
10. Developed a model to simulate the transport of ASR gel in concrete. The model combines the widely used Biot's two-phase medium theory and Terzaghi's effective stress theory. The equality of macroscopic smeared-out deformation of both the solid and fluid phases is the same as in Biot's theory, but a major difference from Biot's theory is that the growth of fluid mass precludes applying the condition of equal strain in both phases. The model presented here should be applicable to any constitutive model for tensile softening damage.
11. Investigated alkalinity-dependent moisture diffusivity in cement mortar.
12. Developed a micromechanics-based model to simulate the effects of ASR induced microcracks on ultrasonic propagation.
13. Developed a model and a measurement technique for mixing of two co-directional Rayleigh surface waves in a nonlinear elastic material.
14. Simulated creep deformation and its effects on ASR damage.
15. Conducted ultrasonic measurements on concrete samples with various degrees of ASR damage. The samples were provided by EPRI. Preliminary ultrasonic measurements show that, when compared with the control samples, there is about 15% ~ 20% drop in ultrasonic phase velocity in samples with ASR damage. This is consistent with our modeling predictions.
16. Simulated ASR reaction and ASR induced damage using the microplane model combined with creep. Creep is modeled by using the B3 model. Also, various experimental data were used to verify the validity of the microplane model.
17. Microcracks are typically observed during ASR damage. To characterize such ASR induced microcracks, we developed micromechanics models to estimate the frequency-dependent tensile and compressive elastic moduli of elastic solids containing randomly distributed two-dimensional microcracks. The crack faces are open under tension and closed under compression. When the crack faces are closed, they may slide against one another following the Coulomb's law of dry friction. The micromechanics models provide analytical expressions of the tensile and compressive moduli for both static and

dynamic cases. It is found that the tensile and compressive moduli are different. Further, under dynamic loading, the compressive and tensile moduli are both frequency dependent. As a by-product, the micromechanics models also predict wave attenuation in the dynamic case. Numerical simulations using the finite element method are conducted to validate the micromechanics models.

18. ASR Samples have been produced and volume expansion of each sample has been measured. Nonlinear acoustic parameter for attenuated media has been introduced and wave velocity, attenuation and material nonlinearity measurements with ASR prisms have been conducted. To quantify amount of ASR gel, microscopy and image analysis were implemented. Compressive strengths of damaged samples were measured.
19. ASR reaction considered in more general and real conditions, means structures that they exposed to drying environment and structure would go under combination of different phenomena. These different phenomena can be listed as, a) Expansion due to ASR, b) Diffusion of moisture due to lower humidity of environment, c) Decreasing of humidity due to drying and self-desiccation, d) Shrinkage of structure due to decreasing humidity and e) Deceleration of ASR reaction due to decreasing of humidity. All of these different effects were considered combined together in order to find real and comprehensive model for predicting ASR induced damage and expansion. This model would be able to analyze structures in real conditions. Therefore, this model would be much more practical and it can be used for nuclear structures that they are exposed to environment without any sealing.
20. We conducted a systematic study using a series of ultrasonic techniques to nondestructively evaluate (NDE) the damage induced by alkali-silica reaction (ASR) in concrete. The study was conducted on concrete prism samples that contained reactive aggregates and were subjected to different ASR conditioning. The ultrasonic NDE techniques used in the study included measuring wave speed, attenuation and the acoustic nonlinearity parameter. Results of the study show that ASR damage reduces wave speed and increases wave attenuation in concrete. However, neither wave speed nor attenuation is sensitive enough to ASR damage to be considered a good measure for quantitative NDE of ASR damage in concrete. The acoustic nonlinearity parameter, on the other hand, shows greater sensitivity to ASR damage, can thus be used to track ASR damage in concrete nondestructively. However, due to the significant attenuation caused by ASR induced microcracks and scattering by the aggregates, attenuation measurements need to be conducted in order to accurately measure the acoustic nonlinearity parameter. Finally, destructive tests were also conducted in this work to measure the compressive strength of the concrete prisms subjected to different ASR conditioning. It is found that the measured acoustic nonlinearity parameter is well-correlated with the reduction of compressive strength induced by ASR damage.
21. We also investigated the feasibility of using nonlinear Rayleigh surface waves to evaluate the full-scale concrete slab for ASR damage. Our results show that the nonlinear surface wave technique is capable of detecting ASR damage with far greater sensitivity than that of any conventional linear ultrasonic techniques used for evaluation of ASR damage. More importantly, the nonlinear surface wave technique enables large area inspection with only one-side access. This makes it a field-deployable technique.

22. A diffusion- and creep-based chemo-mechanical model for calculating the evolution of damage caused in concrete and concrete structures by the alkali-silica reaction (ASR) is developed. First the model of Bazant and Steffens for the diffusion controlled kinetics of ASR is outlined, to be used for calculating the rate of production of the ASR gel within the aggregate. The next step is the formulation of a nonlinear diffusion model for the penetration of gel into the micro- and nanopores in mineral aggregate grain, into the interface transition zone (ITZ) and into the microcracks created in the cement paste of mortar. The gel that penetrates the pores and cracks in cement paste is considered to calcify and stop expanding. A novel point, crucial for unconditional numerical stability of time step algorithm, is that the diffusion analysis is converted to calculating the pressure relaxation at constant gel mass during the step. The gel expansion in the aggregate and the ITZ causes fracturing damage in the concrete, which is analyzed by microplane model M7, into which the aging creep of broad retardation spectrum is incorporated. The gel and the damaged concrete are macroscopically treated as a two-phase (solid-fluid) medium, which is non-standard because of load-bearing but mobile water in nanopores. The condition of equilibrium between the phases is what mathematically introduces the fracture producing load into the concrete. Depending on the stress tensor in the solid phase, the cracking damage is oriented and the expansion is directional. The creep is found to have a major mitigating effect on multi-decade evolution of ASR damage, and is important even for interpreting laboratory experiments. A stable explicit algorithm of time integration of the ASR problem is formulated. Finally, to validate the model, successful fits of various test data from the literature are demonstrated.

II. Publications during the Past Three Years

1. Ju, Taeho, Shuaili Li, Jan Achenbach, and Jianmin Qu, 2015, "Effects of moisture on ultrasound propagation in cement mortar." In 41ST Annual Review Of Progress In Quantitative Nondestructive Evaluation: Volume 34, vol. 1650, pp. 1409-1414. AIP Publishing.
2. Bazant, Z.P., Donmez, A., Masoero, E., Rahimi Aghdam, S. (2015). "Interaction of concrete creep, shrinkage and Swelling with Water, Hydration and Damage: Nano-Macro-Chemo." Proc., CONCREEP-10 (10th Int. Conf. on Mechanics and Physics of Creep, Shrinkage and Durability of Concrete and Concrete Structures, held in Vienna, Austria, Sept.), publ. by ASCE, Washington, D.C., pp. 1--10 (plenary lecture).
3. Zhao, Y., Qiu, Y., Jacobs, L.J. and Qu, J., 2015, "Frequency-Dependent Tensile and Compressive Effective Moduli of Elastic Solids with Distributed Penny-Shaped Microcracks," *Acta Mechanica*, accepted for publication.
4. Zhao, Y., Qiu, Y., Jacobs, L.J. and Qu, J., 2015, "Frequency-Dependent Tensile and Compressive Effective Moduli of Elastic Solids with Randomly Distributed Two-Dimensional Microcracks," *J. Appl. Mech.*, accepted for publication.

III. APPENDIX

III.1 Report of the 1st year

III.1.1 Nonlinear Wave Mixing Technique to Measure the ANLP in Concrete Samples Nondestructively in a Laboratory Environment

Nonlinear Mixing Wave Theory

One-dimensional longitudinal wave motion in a nonlinear solid is governed by the equation below

$$\frac{1}{c^2} \frac{\partial^2 u}{\partial t^2} - \frac{\partial^2 u}{\partial x^2} = \frac{\partial}{\partial x} \left(\frac{\beta}{2} \left(\frac{\partial u}{\partial x} \right)^2 \right) , \quad (1)$$

where c is the longitudinal wave velocity, u is the displacement, and β is the acoustic nonlinearity parameter. Since the nonlinearity parameter β is related to the material damage, it should change with the ASR damage in cement-based materials. To measure the β change, we use the co-linear mixing wave method.

Suppose an ultrasonic wave consists of two frequencies ω_1 and ω_2 as,

$$u_1 = U \cos \left[\omega_1 \left(t - \frac{x}{c} \right) \right] + V \cos \left[\omega_2 \left(t - \frac{x}{c} \right) \right] , \quad (2)$$

where U and V are, respectively, the displacement amplitude of these two frequency components. As the wave propagates through the test sample, ASR damage in the sample causes these two frequency components to interact, resulting in a mixed wave field whose amplitude is proportional to β ,

$$u_2 = -\frac{UV\beta\omega_1\omega_2}{4c^2} x \cos \left[(\omega_1 - \omega_2) \left(t - \frac{x}{c} \right) \right] + \frac{UV\beta\omega_1\omega_2}{4c^2} x \cos \left[(\omega_1 + \omega_2) \left(t - \frac{x}{c} \right) \right] \\ + \frac{U^2\beta\omega_1^2}{8c^2} x \cos \left[(2\omega_1) \left(t - \frac{x}{c} \right) \right] + \frac{V^2\beta\omega_2^2}{8c^2} x \cos \left[(2\omega_2) \left(t - \frac{x}{c} \right) \right] \quad (3)$$

In this work, we will focus on the first term in the high-hand side of (3), i.e.,

$$u_{2d} = -\frac{UV\beta\omega_1\omega_2}{4c^2} x \cos \left[(\omega_1 - \omega_2) \left(t - \frac{x}{c} \right) \right] . \quad (4)$$

By measuring the amplitude $\|u_{2d}\|$, one can obtain the acoustic nonlinearity parameter

$$\beta \propto \frac{\|u_{2d}\|}{UV} . \quad (5)$$

This way of measuring the acoustic nonlinear parameter β is called the nonlinear wave mixing (NWM) method.

Experimental Methods

Sample preparation:

Mortar bar samples were prepared using the procedure described by AASHTO T 303 [1]. The fine aggregates used are the Placitas 67 Blend from Lafarge Company. The cement used is the type I cement (potential Bogue composition 46.11% C_3S , 22.93% C_2S , 8.52% C_3A and 9.59% C_4AF and 0.83% Na_2O_{eq}).

Three thicker $285 \times 100 \times 100$ mm ($11\frac{1}{4} \times 4 \times 4$ in), and six thinner $285 \times 25 \times 25$ mm ($11\frac{1}{4} \times 1 \times 1$ in) mortar bars were casted. These samples are named, respectively, L1, L2 and L3 for the thicker ones, and S1 – S6 for the thinner ones. To cure the samples, molds with the concrete mix in them were placed in a chamber with 100% relative humidity at 23 °C (73.4 °F) for 24 hours. After demolding, the samples were immersed in tap water and placed in an oven at 80 °C (176 °F) for another 24 hours. The first set of expansion and nonlinear ultrasonic measurement were then taken on these as cured samples to obtain the initial values. These values were used as the baseline to normalize the subsequent measurements. To induce ASR damage, the thinner samples S1, S2 and S3 and the thicker samples L1 and L3 were immersed in a 1N NaOH solution at 80°C (176 °F), per the procedures described in AASTHO T 303 [1]. These samples were taken out of the solution at regular intervals for expansion and nonlinear ultrasonic measurements. The rest of the samples were left in an ambient room environment with 50%RH and 23°C.

Measurements:

A schematic of the collinear beam-mixing measurement setup is shown in Fig. 1. Two incident waves of different frequencies are generated simultaneously by the function generator. One has a frequency of ω_1 (0.75MHz) with 18 cycles and the other has frequency of ω_2 (1.25MHz) with 30 cycles, so both waves have the same duration. After amplification, these signals are sent into a high pass filter with a cut off frequency of 0.7 MHz to remove low (< 0.7 MHz) frequency components in the incident waves, which might be generated by the amplifier. An example of the frequency spectrum of the electrical signal sent to the transmitter is given in Fig. 2. Clearly, the signal has negligible frequency component below 0.6MHz.

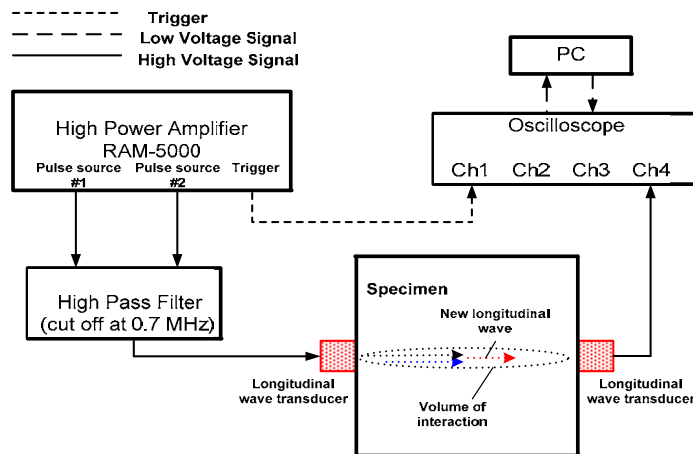


FIGURE 1. Experimental setup

The filtered signals are then sent to the broadband PZT transducer with the central frequency of 1MHz attached to one side of the sample. The two incident waves propagate

through the material and a new longitudinal wave at their difference frequency ($\omega_1 - \omega_2 = 0.5$ MHz) is generated along the wave propagation distance. Since the two incident waves propagate in a ‘phase matching’ fashion, the newly generated wave is a resonance wave, i.e., its amplitude increases with propagation distance. This resonance wave is received by another longitudinal wave receiver attached to the other end of the bar. The receiver has a center frequency of 0.5MHz and is recorded by a Tektronix TDS 5034B oscilloscope. After that, the digitized time-domain signal is sent to a PC for post signal processing. During the ultrasonic measurement, a high-vacuum grease was used as a couplant between the transducer and the sample. A force sensor is used to ensure that the transducers were clamped to the sample with the same pressure for all tests. After each measurement, the sample was cleaned with soap and tap water to remove any residual couplant. Ultrasonic measurements are taken on three different locations in the thicker samples L1, L2 and L3 as shown in Fig. 3.

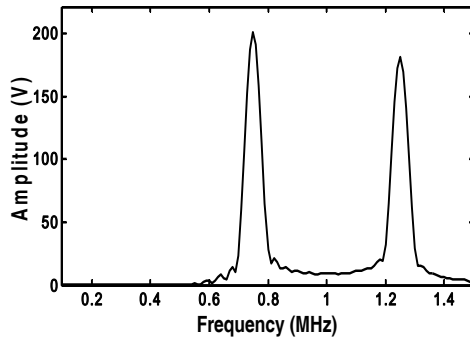


FIGURE 2. FFT of filtered signal

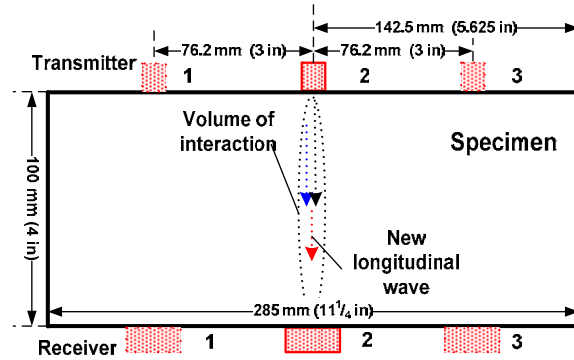


FIGURE 3. Locations of ultrasonic measurement on L1-L3

The PZT transducer converts the electrical signal into a propagating ultrasonic wave field in the mortar bar. This wave field consists of two frequency components as indicated in Eq. (2) and shown in Fig. 2. As the waves propagate, they interact with the ASR damage in the sample. This interaction generates the mixed wave fields that consists of several different frequency components. One of these frequency components is $(\omega_1 - \omega_2)$ at 0.5MHz. The amplitude of this frequency component $\|u_{2d}\|$ can be obtained by performing a Fourier transform of the received signal. Once $\|u_{2d}\|$ is measured, the ultrasonic nonlinear parameter β can be calculated from Eq.(5), since U and V are known input.

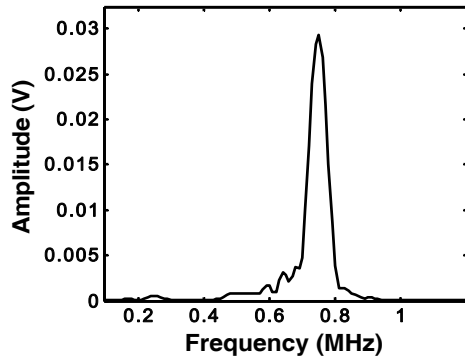


FIGURE 4a. FFT of received signal on day 0

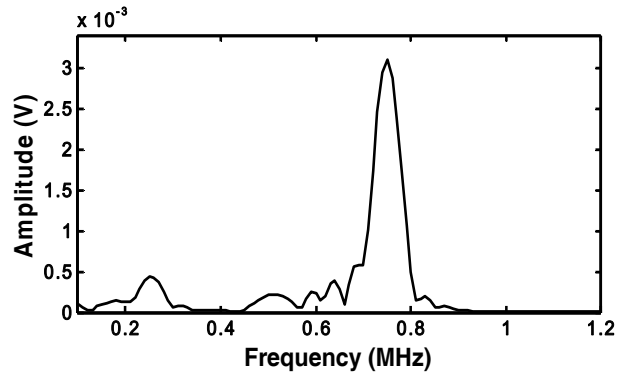


FIGURE 4b. FFT of received signal on day 10

Subsequent ultrasonic measurements were conducted at about the same time each day during the immersion. As an example, the frequency spectra of the received signals for day 0 and day 10 in L1 sample are shown in Figs. 4a and 4b, respectively. It is seen that (i) the amplitude ratio of resonance wave at 0.5 MHz over one of the principal beam at 0.75 MHz increases over time, a sign of increased acoustic nonlinearity parameter β ; and (ii) the amplitude corresponding to 0.75 MHz decreases over time, a sign of increased attenuation. Such increase in attenuation is frequency dependent, and can be accounted for by measuring the decay in the fundamental waves over time.

Results and Discussion

Expansion Measurement and Results

The immersed samples were taken out each day for the expansion measurements per the procedures described in AASHTO T 303 [1]. Results of the expansion per unit length for all samples are plotted in Figs. 5a and 5b as functions of the number of days under the exposure of alkali solution.

It is seen that samples immersed in the alkali solution all expanded. According to ASTM1260, if the expansion of thinner samples is more than 0.2% after 14 days immersed in alkali solution, it is considered potentially deleterious expansion[2]. Based on this criterion, our expansion measurement data show that the aggregate used in our test, the Placitas 67 Blend from the Lafarge Co. in New Mexico, is considered fairly alkali-silica reactive. It is also seen that the samples kept in the room environment did not expand at all. If any, there seems to be some shrinkage, possibly due to the experimental errors.

Comparison between Figs. 5a and 5b shows that the thinner samples have much large expansion than the thicker samples under the same exposure time. A plausible explanation of this difference is that the ASR damage across the bar's thickness is nonuniform. The damage is more severe near the sample surface and gradually decreases toward the center of the samples. Such non-uniformity is controlled by the rate of diffusion of water into the concrete. The diffusion rate-controlled process means that the center region of the thicker samples may not have been damaged yet during 14 days of exposure. In other words, after 14 days of exposure, the thicker samples may still contain a core of un-damaged concrete, which limits the axial expansion of the bar.

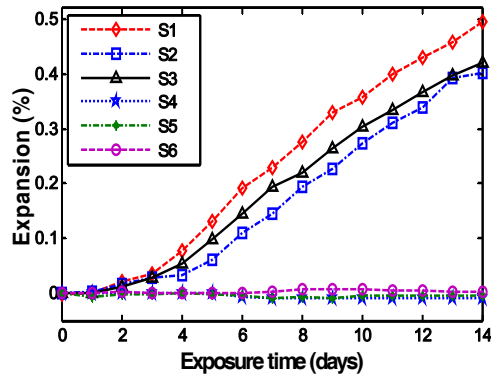


FIGURE 5a. Expansion of thinner samples

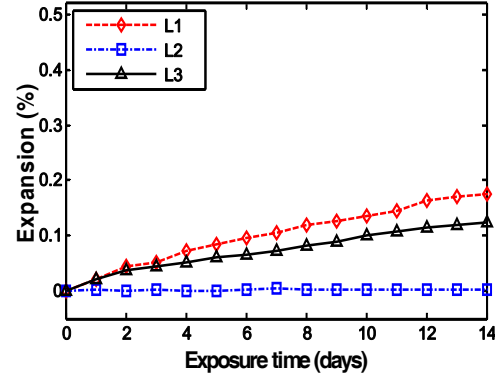


FIGURE 5b. Expansion of thicker samples

Ultrasonic Measurement Results

After each expansion measurement, ultrasonic tests were also conducted on each sample using the NWM method. As indicated in Fig. 3, the ultrasonic tests were conducted at three locations on each sample. It follows from Eq.(5) that the normalized acoustic nonlinearity is given by

$$\bar{\beta} = \frac{\beta}{\beta_0} = \frac{\|u_{2d}\|}{\|u_{2d}\|_0}, \quad (6)$$

where the quantities with subscript 0 are those measured before the samples were immersed in the alkaline solution (day 0). After accounting for the attenuation, the measured acoustic nonlinearity parameter $\bar{\beta}$ normalized by the day 0 value as defined in Eq.(6) is plotted in Fig. 6a for all three thicker samples. We note again that these values are the averages of measurements from all three locations on each sample. To show the scattering of the data, Fig.7 is plotted with error bars. Since ultrasonic measurements were conducted by taking the transducers off at one location, and putting them back on at a different location, these error bars can also be considered the upper limit of the uncertainties associated with the measurements.

It is seen clearly from these plots that (1) the NWM method yields consistent and repeatable results, (2) the acoustic nonlinearity parameter increases with exposure time, and (3) the acoustic nonlinearity parameter is much more sensitive to ASR damage than the volumetric expansion.

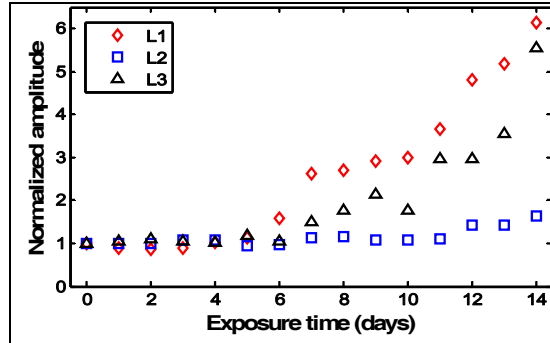


FIGURE 6a. $\bar{\beta}$ averaged over 3 locations in thicker samples

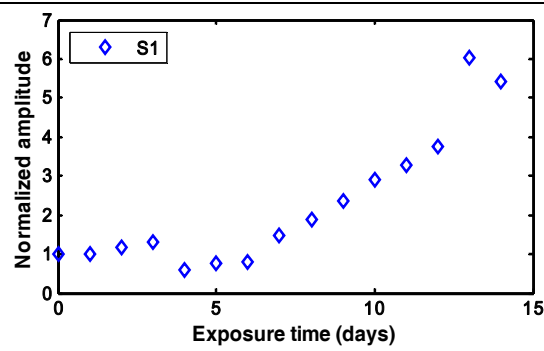


FIGURE 6b. $\bar{\beta}$ in thinner sample S1

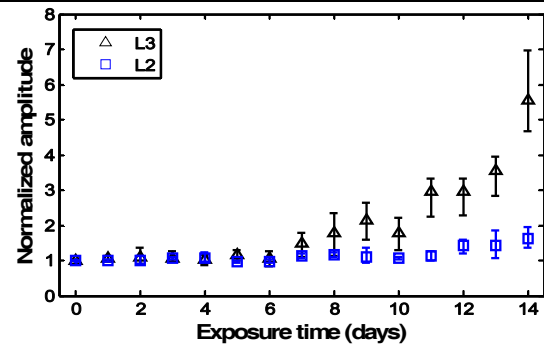
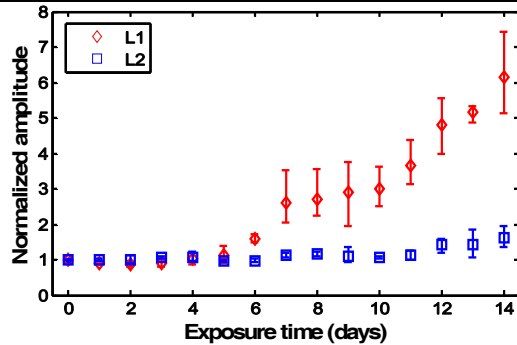


FIGURE 7. Error bars showing the variation of $\bar{\beta}$ for samples L1 and L2, L2 and L3.

We note that results from both the ultrasonic and the expansion measurements seem to indicate that sample L1 has more ASR damage than sample L3, although both samples were made of the same materials, and were subjected to the same exposure condition. However, since these two samples were from two different batches of concrete mix, we speculate that the amount of aggregate in these two samples may not be exactly the same.

Recall that the expansion results show that the thinner samples have much larger expansion than the thicker ones. The reason for such difference was explained on the basis of non-uniform ASR damage across the thickness of the sample. It was argued that ASR damage is controlled by the moisture diffusion so that even after 14 days of exposure, the moisture still has not progressed all the way through the thickness of the thicker samples yet, i.e., there is still a core of undamaged concrete in the thicker samples. This argument is further corroborated by the ultrasonic measurement results. Shown in Fig. 6b is the measured acoustic nonlinearity parameter β of the thinner sample S1. Comparison of Figs. 6a and 6b shows that, although the expansion is very different between the thinner and thicker samples, the measured acoustic nonlinear parameter β is almost the same. The reason for this is clear if we assume that in the thicker sample, there is a core of concrete that has not been reached by the moisture, therefore, has no ASR damage, and the thickness of the ASR damaged outer shell is about one half of the total thickness of the thinner sample. Since the increase of normalized β ($\bar{\beta}$) is only related to the region where ASR damage occurs, the measured acoustic nonlinearity parameter β has similar amount of increase in thicker samples and thinner sample after 14 days exposure to alkali solution.

Conclusions

The results clearly demonstrated the feasibility of using nonlinear ultrasonic techniques to track the progress of ASR damage in cement-based materials. This is significant in that nonlinear ultrasonic techniques have a number of unique advantages over the existing methods of characterizing ASR damage.

First of all, compared to the linear relationship between the expansion and exposure time, the acoustic nonlinearity parameter shows a stepped relationship with respect to exposure time as shown in Fig. 6a. Although more research is needed to understand the significance of these “steps”, it is plausible that such “steps” might be related to the different ASR damage modes. Secondly, as discussed before, the expansion of the concrete bar depends on the thickness of the sample. This means that the expansion-based methods, such as AMBT, the CPT, and ACPT, are not measuring the intrinsic characteristics of the ASR damage. On the other hand, nonlinear ultrasonic methods, such as the NWM method used here, measure the acoustic nonlinearity parameter which is a signature intrinsic to the state of ASR damage. Therefore, measurements from the NWM method are independent of the sample size as shown by our results. Last but not the least, unlike other existing nonlinear ultrasonic methods, the NWM method could detect the ASR damage at arbitrary locations. This could lead to ASR damage scan in the future.

The abilities of the nonlinear ultrasonic methods to provide the spatial variation, identify the different stages of ASR damage and to track the intrinsic characteristics of the ASR damage make such methods potentially useful tools for rapid screening of aggregates for ASR reactivity in the lab, and for field assessments of ASR damage in existing concrete structures.

III.1.2 Physics-Based Models for ASR Damage Evolution

Physicochemical Modeling

Configuration of the microstructure:

The reactive aggregate and the representative volume element (RVE) of concrete surrounding the reactive aggregate are assumed to be spherical [3]. The basic element of the microstructure in Fig. 1 is then a composite sphere composed of two different phases in which the ratio of radii R_a/R_{REV}^a is a constant. Thus the basic element is independent of the absolute size of the spheres.

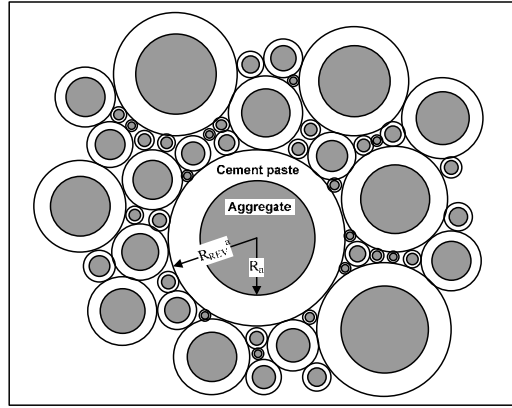


FIGURE 1. Definition of the Relative Elementary Volume for different reactive aggregate sizes

Mathematical model for diffusion of alkali ions:

To compare with our former experiment [4], two kinds of mortar samples with the dimension of $25 \times 25 \times 285 \text{ mm}$ ($1 \times 1 \times 11\frac{1}{4} \text{ in}$) and $100 \times 100 \times 285 \text{ mm}$ ($4 \times 4 \times 11\frac{1}{4} \text{ in}$) respectively are considered in our numerical simulations. Alkali ions penetrating from the specimen boundary into the concrete is considered as macro-diffusion process. Symmetry of mortar bars leads to two-dimensional diffusion problem governed by the 2D Fickian Equation [5],

$$\left(\frac{\partial C}{\partial t}\right)_{x,y,t} = D_{xy} \cdot (\partial^2 C / \partial x^2 + \partial^2 C / \partial y^2) \quad (7)$$

where C is the alkali ion concentration, and D_{xy} is the diffusivity of alkali ions at 80°C [2].

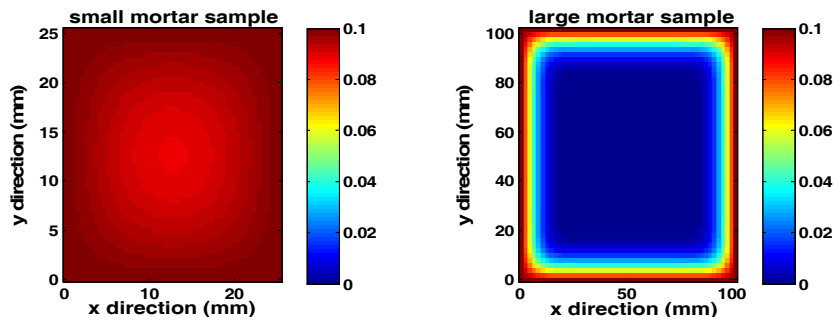


FIGURE 2. Ion diffusion in small and large mortar samples after 14 days

Suppose the alkali ions penetrate with moisture, then D_{xy} can be determined by experimental measurements as described by Shen [5]. From Eq.(1), one can obtain the ion concentration $C(x, y, t)$. As a result, after 14 days, the alkali ions has penetrated thoroughly in small mortar sample, while there is still a very large core in large mortar sample that the ion has not penetrated in as shown in Fig. 2. Note that the alkali ion concentration at the boundary of mortar sample is $C_0=0.1$ mol/liter of solution [6].

In our samples, the size of aggregates varies from 0.225mm to 3.56mm [2]. To compute the ion concentration near each aggregate, each mortar bar is divided into several layers with layer thickness of 5.34mm. As a result, there are three layers in small samples and nine layers in large samples. For simplicity, the ion concentration within each layer is assumed uniform and equal to the value at the middle point of each layer.

The micro-diffusion is the diffusion of alkali ions into the aggregate. This process can be described by Fick's law in spherical coordinate as,

$$B_{ion} \frac{\partial C_{ion}}{\partial t} = \nabla \cdot (D_{ion} \nabla C_{ion}) \quad (8)$$

where C_{ion} is the free ion concentration of the pore solution inside the aggregate. B_{ion} and D_{ion} are the binding capacity and ion diffusivity of the aggregate, respectively. The initial condition is $C_{ion} = 0$ for $t = 0$ in the aggregate. The boundary condition is $C_b = C(t)$ at the surface of aggregate, and $\partial C_{ion} / \partial r = 0$ at the center of the aggregate particle. Eq.(2) can be solved numerically using the finite difference method.

The ASR process takes place within the surface layer of each aggregate particle, where C_{ion} reaches a certain concentration level C_{crt} . One can inversely determine the thickness of the ASR layer, r , from the numerical solution of Eq.(2). The volume of the reacted portion of the aggregate particle of radius R_a can then be calculated,

$$V_a^{Ra} = \left[\frac{R_a^3 - (R_a - r)^3}{R_a^3} \right] \left(\frac{4}{3} \pi R_a^3 \right) \quad (9)$$

This volume is converted into the volume of ASR gel, V_{gel}^{Ra} ,

$$V_{gel}^{Ra} = \eta V_a^{Ra} \quad (10)$$

where η is the coefficient volumetric expansion from aggregate to ASR gel.

Mathematical model for permeation of ASR gel into the surrounding cement:

Because of the volumetric expansion when the aggregate is converted into ASR gel, the gel causes internal pressure near the interface zone between the aggregate and the surround cement. This pressure pushes the gel into the pores around this interface zone. As more pores nearby are filled up with the gel, the pressure increases. which deformed the concrete. The mount of gel that is capable of generating the internal pressure is given by

$$V_{gel,eff}^{Ra} = \langle V_{gel}^{Ra} - V_{pore}^{Ra} \rangle_+ \quad (11)$$

where V_{pore}^{Ra} is the total volume of pores in the surrounding interface zone that can be calculated using,

$$V_{pore}^{Ra} = V_{unit} A_{agg}^{Ra} \quad (12)$$

where V_{unit} is a material constant (a length scale) representing the capacity of the porous zone to absorb ASR gel per unit area, and A_{agg}^{Ra} is the surface area of an aggregate particle of size R_a . When the effective gel volume $V_{gel,eff}^{Ra}$ is larger than zero, the ASR gel begins to permeate. This process can be characterized by Darcy's law for viscous flow as,

$$\frac{\partial C_{gel}}{\partial t} = \nabla \left(\frac{\kappa_{gel}}{\eta_{gel}} \nabla P_{gel} \right) \quad (13)$$

in which C_{gel} and η_{gel} are the concentration and viscosity of the gel, respectively, κ_{gel} is the gel permeability of the porous cement paste, and P_{gel} is the pressure distribution of the gel, which depends on the degree of saturation of the pores. At the boundary, the interface pressure, P_{int} , is applied. However, as P_{int} is an unknown and a function of time, it needs to be calculated simultaneously from the equilibrium of the composite system (see micro-mechanical modeling), the diffusion of ions, and the permeation of the gel. So this is a coupled chemo-mechanical problem.

In order to solve the coupled equations, a state equation must be introduced, which relates the concentration of ASR gel in the pores, C_{gel} , the gel pressure P_{gel} ,

$$C_{gel} = \beta P_{gel} \quad (14)$$

where β is the state function for cement paste [6]. The initial condition is $C_{gel}(r, 0) = 0$. The boundary condition at the interface is $C_{gel}(R_a, t) = \beta P_{int}(t)$, and at the far field is $C_{gel}(R_{REV}^a, t) = 0$. Eq.(13) can then be solved numerically using a finite difference method for the gel concentration as a function of radius and time, $C_{gel}(r, t)$. The gel volume in the porous cement paste can then be evaluated by integrating the gel concentration over the surrounding cement paste,

$$V_{pg}^{Ra} = \int_{R_a}^{R_{REV}^a} 4\pi r^2 C_{gel} dr \quad (15)$$

The coefficient of expansion for the aggregate with radius R_a due to ASR is thus,

$$\alpha_1 = \frac{\Delta V_{gel}^{Ra}}{V_a^{Ra}} = \frac{V_{gel,eff}^{Ra} - V_{pg}^{Ra}}{V_a^{Ra}} = \frac{V_{gel}^{Ra} - V_{pore}^{Ra} - V_{pg}^{Ra}}{V_a^{Ra}} \quad (16)$$

Micro-Mechanical Modeling

Three-phase expansion model:

By a standard homogenization argument, the micro-structural configuration shown in Fig. 1 can be considered equivalent to that shown in Fig. 3, where phase 3 is the effective homogeneous medium equivalent to the heterogeneous medium in Fig. 1. Following the three-phase expansion model developed by Jin et al [7], one can obtain the effective expansion coefficient for the two-phase composite as well as the interface pressure between the aggregate and cement paste. For brevity, we only list the results here, and details can be found in [6]. The effective expansion and interface pressure can be written as,

$$\alpha_{eff} = \frac{K_a V_1 (3K_{SC} + 4G_{SC})}{K_{SC} (3K_a + 4G_{SC}) - 4V_1 G_{SC} (K_{SC} - K_a)} \alpha_1 \quad (17)$$

$$P_{int} = \frac{12K_a G_{SC} K_{SC} (1 - V_1)}{4V_1 G_{SC} (K_a - K_{SC}) + K_{SC} (3K_a + 4G_{SC})} \alpha_1 \quad (18)$$

where K_a , K_{SC} are the bulk modulus of aggregate and cement paste matrix, respectively, G_{SC} is the shear modulus of the cement paste, and $V_1 = R_a^3 / (R_{REV}^a)^3$ is the volume fraction of aggregate.

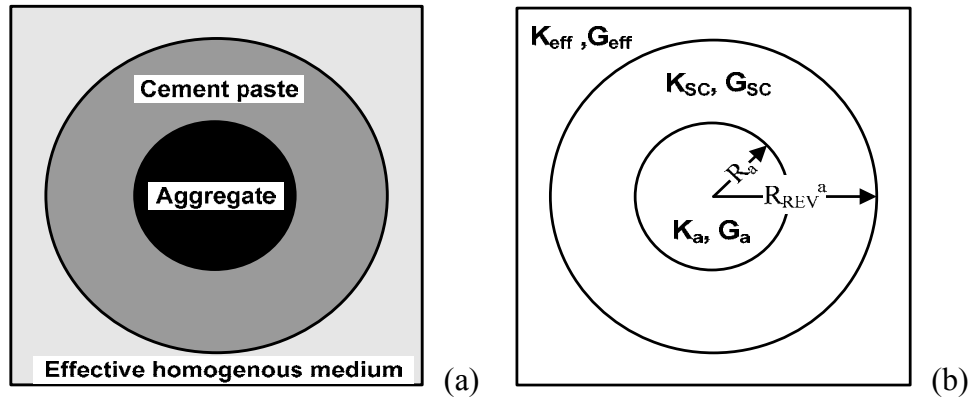


FIGURE 3. (a) Three phase expansion model and (b) its mechanical properties

The unknown parameter in Eq. (17) and (18) is the expansion coefficient of aggregate due to ASR, α_1 , which can be evaluated by Eq.(16). As one can see, both α_1 and P_{int} involve the ASR gel formation due to alkali ion diffusion and the ASR gel permeation driven by interface pressure P_{int} .

Damaged RVE:

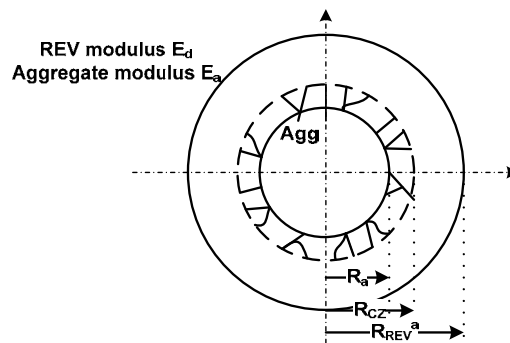


FIGURE 4. Mechanical property of damaged REV

Since the Young's modulus in cement paste matrix is much lower than in aggregate, crack will initiate at the boundary and propagate into the cement paste matrix. According to the Griffith criterion, the critical pressure for crack initiation can be obtained,

$$P_{cr} = \sqrt{\frac{E_{SC} G_{IC}}{\pi(R_a + c_r)}} \quad (19)$$

where E_{SC} is the Young's modulus of cement paste, G_{IC} is the fracture energy of concrete, c_r is the initial crack length in the cement paste. Once the interface pressure P_{int} exceeds the critical pressure P_{cr} , crack starts to propagate which causes a decrease in the modulus. This can be described by a damage parameter [3], which is defined by,

$$d = \frac{R_{CZ} - R_a}{R_{REV}^a - R_a} \quad (20)$$

where R_{CZ} represents the crack front as shown in Fig. 4. The modulus of the equivalent medium E_d can then be determined,

$$E_d = (1 - d)E_{SC} \quad (21)$$

The newly generated cracks also increase the volume of the RVE. The amount of volume expansion induced by crack growth is given by,

$$\alpha_C = \frac{\Delta V}{V_{REV}^a} = \frac{c_{pnew} - c_p}{1 - c_{pnew}} \cdot (1 - V_l) \quad (22)$$

where $V_{REV}^a = \frac{4}{3}\pi(R_{REV}^a)^3$ is the volume of the RVE, c_p and c_{pnew} are the porosity of cement paste matrix before and after crack opening respectively. The total expansion is the linear superposition of α_{eff} and α_C , i.e., $\alpha_{total}^{Ra} = \alpha_{eff}^{Ra} + \alpha_C^{Ra}$. Since the ASR induced expansion of aggregate is size dependent [6], the overall ASR expansion of concrete must be determined as the volumetric average of ASR expansion of the RVE with different sizes. For each aggregate, the final expansion should also include the volumetric average of each layer as described in macro-diffusion process. Thus the overall expansion is,

$$\alpha_{total} = \sum \phi_a \sum \phi_i^a \alpha_{total,i}^{Ra} \quad (23)$$

where ϕ_a is the volume fraction of aggregate with size R_a , ϕ_i^a is the volume fraction of each layer for a fixed aggregate size R_a , and $\alpha_{total,i}^{Ra}$ is the ASR expansion of the concrete located at the i^{th} layer with the aggregate size R_a .

Equations (1)-(23) form a complete model for ASR expansion. It is unlikely to solve the problem analytically because the diffusion and the permeation of gel are coupled with the interface pressure. Instead, a piecewise numerical procedure is adopted. More details can be found in [6].

Compare Numerical Results with Experiments

Since the only unknown parameter in our numerical calculation is the crack opening speed, a set of ASR expansion measurements in small mortar samples are used to fit this model and determine this parameter. It is then used to predict the expansion of other samples. As shown in Fig. 5, the expansion calculated by the model based on Eq. (23) (red solid line) has the same trend as in experiment measurements.

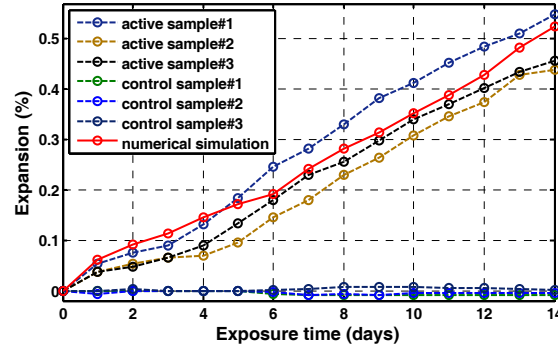


FIGURE 5. Expansion in small mortar samples with comparison to numerical calculation

Following Cantrell's theory [8], the acoustic nonlinearity parameter in materials with dilute distribution of microcracks can be written as,

$$\beta = \beta_0 + \frac{24}{5} \frac{\Omega \Lambda_{mp} L_0^4 R^3 \overline{A_{11}^2}}{\mu^3 b^2} |\sigma_1| + (\beta' N_0^{crk} / 7) \quad (24)$$

where β_0 is the original material nonlinearity before cracking, σ_1 is the initial stress, N_0^{crk} is the crack density, and other parameters are all material constants. To avoid the complexity of determining these material constants, we assume that,

$$\overline{\beta} = \frac{\beta}{\beta_0} - 1 = \alpha |\overline{\sigma_1}| + (1 - \alpha) \overline{N_0^{crk}} \quad (25)$$

where $\overline{\beta}$ is the normalized acoustic nonlinearity parameter reflecting the nonlinearity change, $|\overline{\sigma_1}|$ is the initial stress (comparable to interface pressure) normalized by its maximum value, $0 < |\overline{\sigma_1}| < 1$, and $\overline{N_0^{crk}}$ is the crack density (comparable to damage variable d) normalized by its maximum value, $0 < \overline{N_0^{crk}} < 1$. For a reasonable approximation, the weight parameter α is taken in the range: $0 < \alpha < 0.5$.

Following an equation similar to Eq.(23), one can obtain the volumetric averaged interface pressure and damage variable d up to 14 days exposure time as shown in Fig. 6(a) and (b). As one can see, in both samples, the damage becomes obvious around day 6, and afterwards, in small sample, it shows a linear increase; while in large sample, the damage shows a faster increase after 12 days. This is because in large sample, alkali ions have only penetrated into the outer layers after 14 days as shown in Fig. 2. As more and more ions get into the large sample, the cracks accumulate, and as a result, the damage shows a faster increase after 12 days.

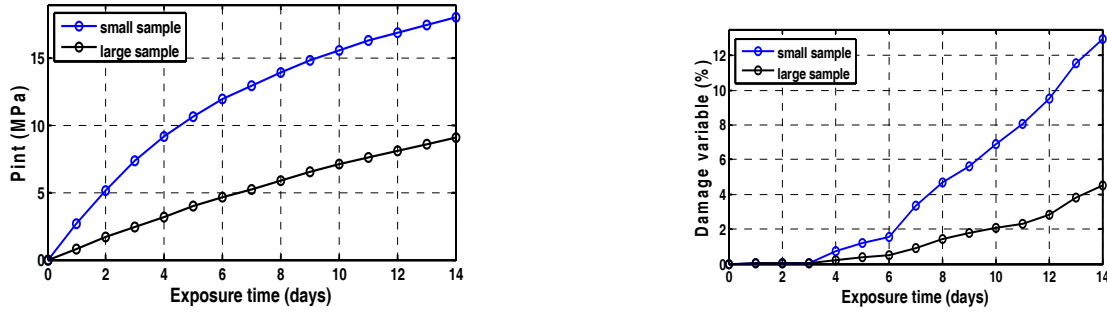


FIGURE 6. Volumetric averaged (a) interface pressure and (b) damage variable d in both mortar samples

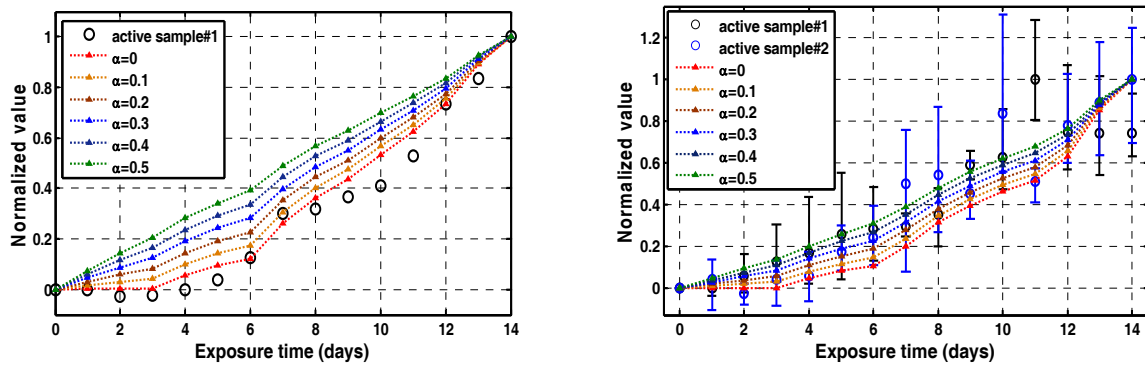


FIGURE 7. Predicted and measured variation of $\bar{\beta}$ in (a) small and (b) large mortar samples

The predicted variation of $\bar{\beta}$ in both small and large mortar samples can be obtained from Eq. (25) as shown in Fig. 7(a) and (b) respectively. By comparing with experimental measurements, we observe in small mortar sample, when $\alpha=0$, the predicted curve compares well with experimental measurements. This is because the small sample has damage everywhere after 14 days, the nonlinearity change is microcrack dominated. While in large sample, this is not the case. As shown in Fig 7(b), when $\alpha=0.2$ or 0.3 , the predicted curve matches better with experimental measurements. One possible explanation is that in large samples, since alkali ions have not penetrated thoroughly after 14 days, the interface pressure also contributes to the nonlinearity change. However, the results in both samples show that this numerical model can effectively predict the nonlinearity parameter jump at both day 7 and day 12. These jumps may indicate different damage stages during ASR process. Before day 6, since the ASR damage is only limited to the interface pressure built up, $\bar{\beta}$ increase is very slow. After day 6, due to the rise of crack density, $\bar{\beta}$ increase is accelerated. Finally after day 11, more cracks are formed which further reduces the Young's modulus. Consequently, there is another jump of $\bar{\beta}$. So in all, our numerical model seems to be capable of predicting the acoustic nonlinearity change.

Conclusions

This paper presents a new model to predict acoustic nonlinearity change during ASR damage. This new model includes a chemo-mechanical model, a micromechanical model and a fracture model. These models are tightly coupled. In the fracture model, a damage variable is introduced to simulate crack opening. The interface pressure and damage variable are then used to calculate the acoustic nonlinearity change. The results of numerical prediction and experimental measurements are in good agreement. Although more experiments on aggregates with different activities are needed to further validate this model, the present work has shown that the proposed method has a good potential to quantitatively predict the acoustic nonlinearity variation during ASR damage and can be used to guide experimental measurements in the future.

REFERENCES

1. AASHT, *Standard method of test for accelerated detection of potentially deleterious expansion of mortar bars due to alkali-silica reaction*, in *Standard specifications for transportation materials and methods of sampling and testing Part 2B: Tests*. 2006, American Association of State Highway and Transportation: Washington D.C.
2. Officials, A.C., *Standard Test Method for Potential Alkali Reactivity of Aggregates (Mortar-Bar Method)*. 2007, ASTM International, West Conshohocken, PA.
3. Multon, S., A. Sellier, and M. Cyr, *Cement and Concrete Research*, 2009. **39**(6): p. 490-500.
4. Liu, M., G. Tang, L.J. Jacobs, and J. Qu, *Review of Progress in Quantitative Nondestructive Evaluation*, 2012. **1430**(1524-1531).
5. Shen, C.H. and G.S. Springer, *Journal of Composite Materials*, 1976. **10**(Jan): p. 2-20.
6. Suwito, A., W. Jin, Y. Xi, and C. Meyer, *Concrete Science and Engineering*, 2002. **4**: p. 23-34.
7. Jin, W., *Alkali-silica reaction in concrete with glass aggregate - A chemo-physico-mechanical approach*. 1998, Columbia University: New York.
8. Cantrell, J.H., *Proceedings of the Royal Society of London Series a-Mathematical Physical and Engineering Sciences*, 2004. **460**(2043): p. 757-780.

III.1.3 Physics-Based Models for ASR Damage Evolution Collinear Mixing of Two Transient Pulses in Nonlinear Elastic Solids

INTRODUCTION

When two elastic waves propagate and meet in a linear medium, the equations of motion are linear and the two elastic waves do not interact, i.e., there will be no scattering of wave by wave and the total wave field is simply the superposition of these two wave fields. On the other hand, if we consider the quadratic or higher order terms of displacement in the stress-strain relationship, the equations of motion become nonlinear (Jones and Korbett, 1963) and scattering of elastic wave by wave happens (Rollins *et al.*, 1964; Taylor and Rollins, 1964).

Generally, the interaction of two elastic waves produces both “sum” and “difference” frequency waves. Under the phase matching condition (Jones and Korbett, 1963), the second order waves will be resonant (synchronous interaction). This phenomena was observed experimentally (Rollins *et al.*, 1964; Johnson *et al.*, 1987; Johnson and Shankland, 1989; Croxford *et al.*, 2009) and approved theoretically by both steady state Green’s function approach (Jones and Korbett, 1963) and quantum-mechanical analysis (Childress and Hambrick, 1964), in which the interaction of two elastic waves is called, by analogy with Raman scattering of light, Raman scattering of sound by sound (Zarembo and Krasilnikov, 1971).

Most of the existing work investigates the steady state interaction of two monochromatic waves, i.e., the two primary waves are all of single frequency in frequency domain and infinite length in time domain. On the other hand, as we know that, many experiments in solid-state physics use transient pulses as excitations which usually have a finite time length as well as a finite bandwidth of frequency. As a result, solutions that include the transient analysis are needed.

In this paper, we will investigate the interaction of two transient elastic waves. Without loss of generality, a special case, in which a longitudinal wave and a shear wave are mixed in a collinear (opposite) direction is considered. The potential of this collinear mixing technique in detecting the spatial distribution of nonlinearity by timing the transducers is also discussed.

PROBLEM STATEMENT

Assume that a shear transducer located at $y = 0$ generates a shear pulse u_1 with amplitude U and central frequency ω_T in the positive y -direction and a longitudinal transducer located at $y = L$ generates a longitudinal pulse v_1 of amplitude V and central frequency ω_L in the negative y -direction, see Figure 1. The expressions of u_1 and v_1 can be written as

$$u_1 = U \left[H \left((t - \delta_T) - \frac{y}{c_T} \right) - H \left((t - \delta_T) - \frac{y}{c_T} - \tau_T \right) \right] \sin \left(\omega_T \left((t - \delta_T) - \frac{y}{c_T} \right) \right), \quad (26)$$

$$v_1 = V \left[H \left((t - \delta_L) + \frac{y-L}{c_L} \right) - H \left((t - \delta_L) + \frac{y-L}{c_L} - \tau_L \right) \right] \sin \left(\omega_L \left((t - \delta_L) + \frac{y-L}{c_L} \right) \right), \quad (27)$$

where H is the Heaviside step function, L is the thickness of the sample, c_T is the shear wave velocity, c_L is the longitudinal wave velocity, δ_T , τ_T and δ_L , τ_L are the delay time and duration of the shear pulse and the longitudinal pulse, respectively.

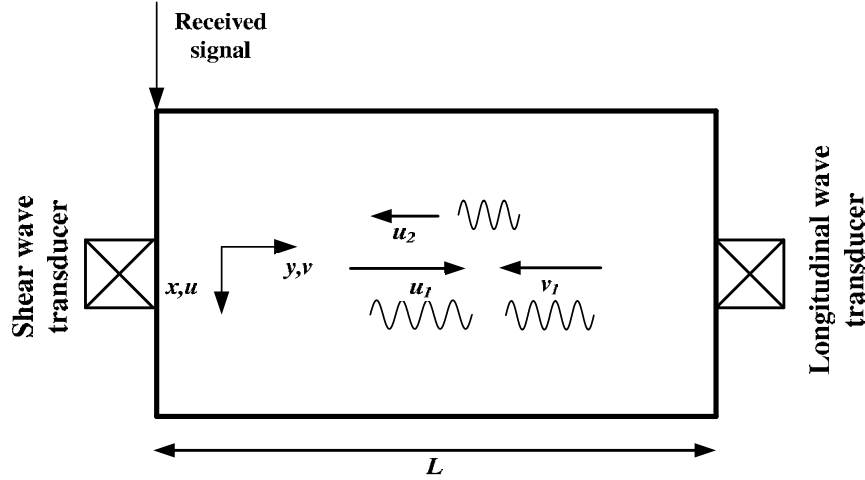


Figure 1 Collinear mixing (opposite direction) of two elastic waves

For simplicity, we neglect the absorption and the equation of motion can be written as (Liu *et al.*, 2012)

$$\frac{\partial^2 u}{\partial t^2} - c_T^2 \frac{\partial^2 u}{\partial y^2} = \beta_T c_T^2 \frac{\partial}{\partial y} \left(\frac{\partial u}{\partial y} \frac{\partial v}{\partial y} \right), \quad (28)$$

$$\frac{\partial^2 v}{\partial t^2} - c_L^2 \frac{\partial^2 v}{\partial y^2} = \beta_L c_L^2 \frac{\partial v}{\partial y} \frac{\partial^2 v}{\partial y^2} + \beta_T c_T^2 \frac{\partial u}{\partial y} \frac{\partial^2 u}{\partial y^2}. \quad (29)$$

The second order wave u_2 can be found by direct substitution of (26) and (27) into the right hand side of (28) and (29). In this paper, we will focus on the generation of the second order shear wave with difference frequency, thus the corresponding equation can be derived by plugging (26) and (27) into right side of (28). The direct substitution yields

$$\frac{\partial^2 u_2^-}{\partial t^2} - c_T^2 \frac{\partial^2 u_2^-}{\partial y^2} = f(y, t), \quad (30)$$

where

$$f = F \cdot \left[H \left((t - \delta_T) - \frac{y}{c_T} \right) - H \left((t - \delta_T) - \frac{y}{c_T} - \tau_T \right) \right] \left[H \left((t - \delta_L) + \frac{y-L}{c_L} \right) - H \left((t - \delta_L) + \frac{y-L}{c_L} - \tau_L \right) \right] \quad (31)$$

$$F = \frac{\beta_T UV \omega_L \omega_T (\omega_L c_T + \omega_T c_L)}{2c_L^2} \sin \left[(\omega_L - \omega_T)t + \left(\frac{\omega_L}{c_L} + \frac{\omega_T}{c_T} \right)y - (\omega_L \delta_L - \omega_T \delta_T) - \frac{\omega_L L}{c_L} \right]. \quad (32)$$

In (30), we only keep part of the driving force with difference frequency $\omega_L - \omega_T$. This is because we are only interested in the generation of second order shear wave of difference

frequency. The corresponding displacement on the left side of (30) is thus represented by u_2^- .

SECOND ORDER SHEAR WAVE UNDER RESONANT CONDITION

It can be proved that the resonance condition for u_2^- in this special case as shown in Fig. 1 is (Jones and Korbett, 1963)

$$\frac{\omega_L}{\omega_T} = \frac{2c_L}{c_L - c_T} = \frac{2\kappa}{\kappa - 1}. \quad (33)$$

Under the resonance condition (33), u_2^- will propagate along negative y direction and received by the shear transducer. Substitution of (33) into (31) - (32) yields

$$\hat{f} = \hat{F} \cdot \left[H\left(t - \delta_T - \frac{y}{c_T}\right) - H\left(t - \delta_T - \frac{y}{c_T} - \tau_T\right) \right] \left[H\left(t - \delta_L + \frac{y-L}{c_L}\right) - H\left(t - \delta_L + \frac{y-L}{c_L} - \tau_L\right) \right] \quad (34)$$

$$\hat{F} = \frac{\beta_T UV \omega_T^3 (c_L + c_T)}{(c_L - c_T)^2} \sin\left[\left(\frac{c_L + c_T}{c_L - c_T}\right) \omega_T \cdot \left(t + \frac{y}{c_T}\right) - \omega_T \frac{2c_L \delta_L - (c_L - c_T) \delta_T - 2\omega_T L}{c_L - c_T}\right]. \quad (35)$$

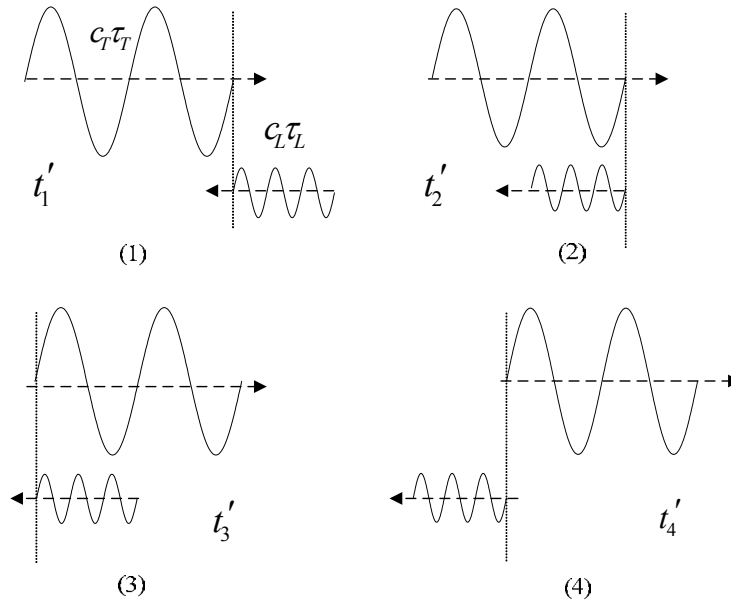


Figure 2 Different stages of two wave mixing ($c_L \tau_L < c_T \tau_T$)

The corresponding u_2^- generated by (34) can be solved by

$$u_2^-(y, t) = \int_{-\infty}^{\infty} \int_{-\infty}^{\infty} \frac{\hat{f}(y_s, t_s)}{c_T^2} g(y - y_s, t - t_s) dy_s dt_s, \quad (36)$$

where $g(y - y_s, t - t_s) = \frac{c_T}{2} H\left(t - t_s - \frac{|y - y_s|}{c_T}\right)$ is the 1D transient Green's function of equation

(30).

In the following, we will show how to simplify (36). Without loss of generality, we assume $c_L \tau_L < c_T \tau_T$. It is shown in Figure 2 that the interaction length y_s of mixing in (36) is different at different time t_s . The time when the two waves start mixing is (see (1) in Figure 2)

$$t_1' = t_1 + \frac{c_T \delta_T + c_L \delta_L}{c_L + c_T}, \quad (37)$$

where $t_1 = \frac{L}{c_L + c_T}$ is the time when the two waves start mixing without any delay time, i.e.,

$\delta_T = \delta_L = 0$. After t_1' , the interaction length increases and eventually gets to the length of the longitudinal wave $c_L \tau_L$ (see (2) in Figure 2). The time when the interaction length is equal to the length of the longitudinal wave is

$$t_2' = t_2 + \frac{c_T \delta_T + c_L \delta_L}{c_L + c_T}, \quad (38)$$

where $t_2 = (L + c_L \tau_L) / (c_L + c_T)$. When $t_1' < t_s < t_2'$, $L - c_L(t_s - \delta_L) < y_s < c_T(t_s - \delta_T)$. After t_2' , the interaction length keeps as a constant until t_3' when the front of the longitudinal pulse reaches the end of the shear pulse and the two pulses start separating (see (3) in Figure 2). We have

$$t_3' = t_3 + \frac{c_T \delta_T + c_L \delta_L}{c_L + c_T}, \quad (39)$$

where $t_3 = \frac{L + c_L \tau_L}{c_L + c_T}$. When $t_2' < t_s < t_3'$, $L - c_L(t_s - \delta_L) < y_s < L - c_L(t_s - \delta_L) + c_L \tau_L$. After t_3' ,

the interaction length diminishes and eventually gets back to zero at t_4' when the two pulses totally separate (see (4) in Figure 2). We have

$$t_4' = t_4 + \frac{c_T \delta_T + c_L \delta_L}{c_L + c_T}, \quad (40)$$

where $t_4 = \frac{L + c_L \tau_L + c_T \tau_T}{c_L + c_T}$. When $t_3' < t_s < t_4'$, $c_T(t_s - \delta_T) - c_T \tau_T < y_s < L - c_L(t_s - \delta_L) + c_L \tau_L$.

It can be shown that, only when $t_1' < t_s < t_4'$, the product of the two rectangular windows in $\hat{f}(y_s, t_s)$ is nonzero and the equation (36) can be simplified as

$$u_2^-(y, t) = \frac{1}{2c_T} \left[\int_{t_1'}^{t_2'} \int_{L-c_L(t_s-\delta_L)}^{c_T(t_s-\delta_T)} \hat{F}(y_s, t_s) H\left(t-t_s - \frac{|y-y_s|}{c_T}\right) dy_s dt_s \right. \\ \left. + \int_{t_2'}^{t_3'} \int_{L-c_L(t_s-\delta_L)}^{L-c_L(t_s-\delta_L)+c_L\tau_L} \hat{F}(y_s, t_s) H\left(t-t_s - \frac{|y-y_s|}{c_T}\right) dy_s dt_s \right. \\ \left. + \int_{t_3'}^{t_4'} \int_{c_T(t_s-\delta_T)-c_T\tau_T}^{L-c_L(t_s-\delta_L)+c_L\tau_L} \hat{F}(y_s, t_s) H\left(t-t_s - \frac{|y-y_s|}{c_T}\right) dy_s dt_s \right]. \quad (41)$$

Once the condition (33) is satisfied, u_2^- will propagate along negative y direction. As a result, we record it at the left end of the sample ($y=0$) in a real experiment. The theoretical expression of u_2^- at $y=0$ can be obtained by substituting $y=0$ into (41) and written as

$$u_2^-(0, t) = \frac{1}{2c_T} \left[\int_{t_1'}^{t_2'} \int_{L-c_L(t_s-\delta_L)}^{c_T(t_s-\delta_T)} \hat{F}(y_s, t_s) H\left(t-t_s - \frac{y_s}{c_T}\right) dy_s dt_s \right. \\ \left. + \int_{t_2'}^{t_3'} \int_{L-c_L(t_s-\delta_L)}^{L-c_L(t_s-\delta_L)+c_L\tau_L} \hat{F}(y_s, t_s) H\left(t-t_s - \frac{y_s}{c_T}\right) dy_s dt_s \right. \\ \left. + \int_{t_3'}^{t_4'} \int_{c_T(t_s-\delta_T)-c_T\tau_T}^{L-c_L(t_s-\delta_L)+c_L\tau_L} \hat{F}(y_s, t_s) H\left(t-t_s - \frac{y_s}{c_T}\right) dy_s dt_s \right]. \quad (42)$$

Assume the first term in (42) is

$$I_1 = \frac{1}{2c_T} \int_{t_1'}^{t_2'} \int_{L-c_L(t_s-\delta_L)}^{c_T(t_s-\delta_T)} \hat{F}(y_s, t_s) H\left(t-t_s - \frac{y_s}{c_T}\right) dy_s dt_s. \quad (43)$$

Clearly, (43) is a 2D integral over the triangular area ABD shown in Figure 3. The AD line is described by $y_s = c_T(t_s - \delta_T)$, and the line AB is described by $y_s = L - c_L(t_s - \delta_L)$. The dash line is described by $y_s = c_T(t - t_s)$, or $t = \frac{y_s}{c_T} + t_s$. Clearly, for $y_s > c_T(t - t_s)$, we have

$H\left(t - t_s - \frac{y_s}{c_T}\right) = 0$. Therefore, for any $y_s > c_T(t - t_s)$, the integration in (43) vanishes. t_{min1} , t_0

and t_{max1} represent three critical values of t , at which $y_s = c_T(t - t_s)$ cross B , A and D , respectively. A simple geometric analysis gives

$$t_{min1} = \frac{2Lc_T - c_L\tau_L(c_L - c_T)}{(c_L + c_T)c_T} + \frac{2c_L\delta_L - (c_L - c_T)\delta_T}{c_L + c_T}, \quad (44)$$

$$t_0 = \frac{2L}{c_L + c_T} + \frac{2c_L\delta_L - (c_L - c_T)\delta_T}{c_L + c_T}, \quad (45)$$



For $t_{\min 1} < t < t_0$, we have

where s_1 can be found by solving $L - c_l(s_1 - \delta_l) = c_T(t - s_1)$

The integration (47) can be carried out as

where $\omega_R = (\frac{c_L + c_T}{c_L - c_T})\omega_T$ and $\varphi_0 = \omega_T \frac{2c_L\delta_L - (c_L - c_T)\delta_T}{c_L - c_T} + \frac{2\omega_T L}{c_L - c_T}$.

For $t_0 < t < t_{\max 1}$, we have

$$I_1 = I_{12} = \frac{1}{2c_T} \left(\int_{t_1'}^{s_2} \int_{L-c_L(t_s-\delta_L)}^{c_T(t_s-\delta_T)} \hat{F}(y_s, t_s) dy_s dt_s + \int_{s_2}^{t_2'} \int_{L-c_L(t_s-\delta_L)}^{c_T(t-t_s)} \hat{F}(y_s, t_s) dy_s dt_s \right), \quad (50)$$

where s_2 can be found by solving $c_T(s_2 - \delta_T) = c_T(t - s_2)$

$$s_2 = \frac{t + \delta_T}{2}. \quad (51)$$

The integration (50) can be carried out as

$$I_{12} = \frac{UV\omega_T^3\beta_T}{4\omega_R^2(c_L - c_T)^3} \left[\begin{aligned} & -\omega_R(c_L - c_T)(2L + 2c_L\tau_L - (c_L + c_T)(t - \frac{2c_L\delta_L - (c_L - c_T)\delta_T}{c_L + c_T})) \cos(\omega_R t - \varphi_0) \\ & -(c_L - c_T)(c_L + c_T) \sin(\omega_R t - \varphi_0) \\ & + (c_L + c_T)^2 \sin(\frac{2\omega_R L + \omega_R(2c_L\delta_L - (c_L - c_T)\delta_T)}{c_L + c_T} - \varphi_0) \\ & - 2c_T(c_L + c_T) \sin(\frac{\omega_R(2c_T L - c_L\tau_L(c_L - c_T)) + c_T\omega_R(2c_L\delta_L - (c_L - c_T)\delta_T)}{c_T(c_L + c_T)} - \varphi_0) \end{aligned} \right]. \quad (52)$$

For $t > t_{\max 1}$, we have

$$I_1 = I_{13} = \frac{1}{2c_T} \int_{t_1'}^{t_2'} \int_{L-c_L(t_s-\delta_L)}^{c_T(t_s-\delta_T)} \hat{F}(y_s, t_s) dy_s dt_s \quad (53)$$

and (53) can be carried out as

$$I_{13} = \frac{UV\omega_T^3\beta_T}{4\omega_R^2(c_L - c_T)^3} \left[\begin{aligned} & (c_L + c_T)^2 \sin(\frac{2\omega_R L - (c_L + c_T)\varphi_0 + \omega_R(2c_L\delta_L - (c_L - c_T)\delta_T)}{c_L + c_T}) \\ & -(c_L - c_T)(c_L + c_T) \sin(\frac{2\omega_R(L + c_L\tau_L) + \omega_R(2c_L\delta_L - (c_L - c_T)\delta_T)}{c_L + c_T} - \varphi_0) \\ & - 2c_T(c_L + c_T) \sin(\frac{\omega_R(2c_T L - c_L\tau_L(c_L - c_T)) + c_T\omega_R(2c_L\delta_L - (c_L - c_T)\delta_T)}{c_T(c_L + c_T)} - \varphi_0) \end{aligned} \right]. \quad (54)$$

For $t < t_{\min 1}$, we have $H\left(t - t_s - \frac{y_s}{c_T}\right) = 0$. Thus $I_1 = 0$.

Summarize the above, we have

$$I_1 = I_{11}H(t - t_{\min 1})H(t_0 - t) + I_{12}H(t - t_0)H(t_{\max 1} - t) + I_{13}H(t - t_{\max 1}). \quad (55)$$

The other integrals in Eq. (42) can be carried out explicitly in a similar manner. If we use I_2 to represent the second term in (42), it can be shown that

$$\begin{aligned} I_2 = & I_{21}H(t - t_{\min 2})H(t_{c1} - t) + I_{22}H(t - t_{c1})H(t_{c2} - t) \\ & + I_{23}H(t - t_{c2})H(t_{\max 2} - t) + I_{24}H(t - t_{\max 2}) \end{aligned} \quad (56)$$

where

$$I_{21} = \frac{\omega_T^3 UV \beta_T c_T}{2\omega_R^2 (c_L - c_T)^3} \left[\begin{aligned} &\omega_R (2L - (c_L + c_T)(t - \frac{2c_L \delta_L - (c_L - c_T)\delta_T}{c_L + c_T}) - (c_L - c_T)\tau_T) \cos(\omega_R t - \varphi_0) \\ &-(c_L + c_T) \sin(\frac{\omega_R (2L - (c_L - c_T)\tau_T) + \omega_R (2c_L \delta_L - (c_L - c_T)\delta_T)}{c_L + c_T} - \varphi_0) \\ &+(c_L + c_T) \sin(\omega_R t - \varphi_0) \end{aligned} \right], \quad (57)$$

$$I_{22} = \frac{\omega_T^3 UV \beta_T}{2\omega_R^2 (c_L - c_T)^3} \left[\begin{aligned} &\omega_R (c_L - c_T)(c_L \tau_L - c_T \tau_T) \cos(\omega_R t - \varphi_0) \\ &-c_T (c_L + c_T) \sin(\frac{\omega_R (2L - (c_L - c_T)\tau_T) + \omega_R (2c_L \delta_L - (c_L - c_T)\delta_T)}{c_L + c_T} - \varphi_0) \\ &+c_T (c_L + c_T) \sin(\frac{\omega_R (2c_T L - c_L \tau_L (c_L - c_T)) + c_T \omega_R (2c_L \delta_L - (c_L - c_T)\delta_T)}{c_T (c_L + c_T)} - \varphi_0) \end{aligned} \right], \quad (58)$$

$$I_{23} = \frac{\omega_T^3 UV \beta_T c_T}{2\omega_R^2 (c_L - c_T)^3} \left[\begin{aligned} &-\omega_R (2L + 2c_L \tau_L - (c_L + c_T)(t - \frac{2c_L \delta_L - (c_L - c_T)\delta_T}{c_L + c_T})) \cos(\omega_R t - \varphi_0) \\ &-(c_L + c_T) \sin(\frac{-2\omega_R c_L \tau_L + \omega_R c_T t}{c_T} - \varphi_0) \\ &-(c_L + c_T) \sin(\frac{\omega_R (2L - (c_L - c_T)\tau_T) + \omega_R (2c_L \delta_L - (c_L - c_T)\delta_T)}{c_L + c_T} - \varphi_0) \\ &+(c_L + c_T) \sin(\frac{\omega_R (2c_T L - c_L \tau_L (c_L - c_T)) + c_T \omega_R (2c_L \delta_L - (c_L - c_T)\delta_T)}{c_T (c_L + c_T)} - \varphi_0) \\ &+(c_L + c_T) \sin(\frac{\omega_R (2c_T L - c_T \tau_T (c_L - c_T) - c_L \tau_L (c_L + c_T)) + c_T \omega_R (2c_L \delta_L - (c_L - c_T)\delta_T)}{c_T (c_L + c_T)} - \varphi_0) \end{aligned} \right], \quad (59)$$

$$I_{24} = \frac{\omega_T^3 UV \beta_T c_T}{2\omega_R^2 (c_L - c_T)^3} \left[\begin{aligned} &-(c_L + c_T) \sin(\frac{2\omega_R (L + c_L \tau_L) + \omega_R (2c_L \delta_L - (c_L - c_T)\delta_T)}{c_L + c_T} - \varphi_0) \\ &-(c_L + c_T) \sin(\frac{\omega_R (2L - (c_L - c_T)\tau_T) + \omega_R (2c_L \delta_L - (c_L - c_T)\delta_T)}{c_L + c_T} - \varphi_0) \\ &+(c_L + c_T) \sin(\frac{\omega_R (2c_T L - (c_L - c_T)c_L \tau_L) + c_T \omega_R (2c_L \delta_L - (c_L - c_T)\delta_T)}{c_T (c_L + c_T)} - \varphi_0) \\ &+(c_L + c_T) \sin(\frac{\omega_R (2c_T L - (c_L - c_T)c_T \tau_T + (c_L + c_T)c_L \tau_L) + c_T \omega_R (2c_L \delta_L - (c_L - c_T)\delta_T)}{c_T (c_L + c_T)} - \varphi_0) \end{aligned} \right], \quad (60)$$

$$t_{\min 2} = \frac{2L - (c_L - c_T)\tau_T + 2c_L \delta_L - (c_L - c_T)\delta_T}{c_L + c_T}, \quad (61)$$

$$t_{c1} = \frac{(2L + c_L \tau_L) c_T - c_L^2 \tau_L + (2c_L \delta_L - (c_L - c_T) \delta_T) c_T}{(c_L + c_T) c_T}, \quad (62)$$

$$t_{c2} = \frac{c_T^2 \tau_T + ((\tau_L - \tau_T) c_L + 2L) c_T + c_L^2 \tau_L + (2c_L \delta_L - (c_L - c_T) \delta_T) c_T}{(c_L + c_T) c_T}, \quad (63)$$

$$t_{\max 2} = \frac{2L + 2c_L \tau_L + 2c_L \delta_L - (c_L - c_T) \delta_T}{c_L + c_T}. \quad (64)$$

Similarly , if we use I_3 to represent the third term in (42), it can be shown that

$$I_3 = I_{31} H(t - t_{\min 3}) H(t_d - t) + I_{32} H(t - t_d) H(t_{\max 3} - t) + I_{33} H(t - t_{\max 3}), \quad (65)$$

where

$$I_{31} = \frac{\omega_T^3 UV \beta_T}{4\omega_R^2 (c_L - c_T)^2} \left[\begin{aligned} & \omega_R (2L - (c_L - c_T) \tau_T - (c_L + c_T) (t - \frac{2c_L \delta_L - (c_L - c_T) \delta_T}{c_L + c_T})) \cos(\omega_R t - \varphi_0) \\ & - (c_L + c_T) \sin(\frac{\omega_R (2L - (c_L - c_T) \tau_T) + \omega_R (2c_L \delta_L - (c_L - c_T) \delta_T)}{c_L + c_T} - \varphi_0) \\ & + (c_L + c_T) \sin(\omega_R t - \varphi_0) \end{aligned} \right], \quad (66)$$

$$I_{32} = \frac{\omega_T^3 UV \beta_T}{4\omega_R^2 (c_L - c_T)^3} \left[\begin{aligned} & -2\omega_R \left(\frac{2c_T L - (c_L - c_T) c_T \tau_T + (c_L + c_T) c_L \tau_L}{-c_T (c_L + c_T) (t - \frac{2c_L \delta_L - (c_L - c_T) \delta_T}{c_L + c_T})} \right) \cos(\omega_R t - \varphi_0) \\ & - (c_L - c_T) (c_L + c_T) \sin(\frac{\omega_R (2L - (c_L - c_T) \tau_T) + \omega_R (2c_L \delta_L - (c_L - c_T) \delta_T)}{c_L + c_T} - \varphi_0) \\ & + (c_L + c_T)^2 \sin(\frac{\omega_R (2L - (c_L - c_T) \tau_T + 2c_L \tau_L) + \omega_R (2c_L \delta_L - (c_L - c_T) \delta_T)}{c_L + c_T} - \varphi_0) \\ & - 2c_T (c_L + c_T) \sin(\omega_R t - \varphi_0) \end{aligned} \right], \quad (67)$$

$$I_{33} = \frac{\omega_T^3 UV \beta_T}{4\omega_R^2 (c_L - c_T)^3} \left[\begin{aligned} & - (c_L - c_T) (c_L + c_T) \sin(\frac{\omega_R (2L - (c_L - c_T) \tau_T) + \omega_R (2c_L \delta_L - (c_L - c_T) \delta_T)}{c_L + c_T} - \varphi_0) \\ & + (c_L + c_T)^2 \sin(\frac{\omega_R (2L - (c_L - c_T) \tau_T + 2c_L \tau_L) + \omega_R (2c_L \delta_L - (c_L - c_T) \delta_T)}{c_L + c_T} - \varphi_0) \\ & - 2c_T (c_L + c_T) \sin(\frac{\omega_R (2c_T L - (c_L - c_T) c_T \tau_T + (c_L + c_T) c_L \tau_L) + c_T \omega_R (2c_L \delta_L - (c_L - c_T) \delta_T)}{c_T (c_L + c_T)} - \varphi_0) \end{aligned} \right] \quad (68)$$

$$t_{\min 3} = \frac{2L - (c_L - c_T) \tau_T + 2c_L \delta_L - (c_L - c_T) \delta_T}{c_L + c_T}, \quad (69)$$

$$t_d = \frac{2L + (2\tau_L - \tau_T)c_L + c_T\tau_T + 2c_L\delta_L - (c_L - c_T)\delta_T}{c_L + c_T}, \quad (70)$$

$$t_{\max 3} = \frac{2Lc_T + (c_L + c_T)c_L\tau_L - (c_L - c_T)c_T\tau_T + c_T(2c_L\delta_L - (c_L - c_T)\delta_T)}{c_T(c_L + c_T)}. \quad (71)$$

From (55), (56) and (65), the integrand (42) can be written as

$$u_2^-(0, t) = I_1 + I_2 + I_3. \quad (72)$$

By substituting the definition of φ_0 back into (72), one can find that u_2^- can be written as $u_2^-(t - C, \tau_L, \tau_T)$, where $C = \frac{2c_L\delta_L - (c_L - c_T)\delta_T}{c_L + c_T}$. Physically, this means the two delay time δ_L and δ_T of the primary waves will give rise to a time delay of value C to the second order shear wave u_2^- . It is easy to show that the Fourier Transform of $u_2^-(t - C, \tau_L, \tau_T)$ is

$$\mathcal{F}[u_2^-(t - C, \tau_L, \tau_T)] = e^{-i\omega C} \mathcal{F}[u_2^-(t, \tau_L, \tau_T)]. \quad (73)$$

This means the time delays (δ_L and δ_T) of the two primary waves only affect the phase of the second order difference shear wave u_2^- . From the expression of each term in (72), one can see that u_2^- is proportional to β_T within the region of interaction. As a result, if we adjust the delay time and let the two primary waves mix at different locations, a relative spatial distribution of β_T can be obtained by measuring u_2^- generated at different locations.

ARRIVAL TIME ANALYSIS

In this part, we will begin from another point of view to analyze the physical meaning of delay C in (73). We already know that the resonant shear wave u_2^- having a difference frequency ω_R will propagate “backward” to the left and wave speed is shear wave speed c_T under the condition (33). Without loss of generality, we assume the two delay times $\delta_L = \delta_T = 0$ in the analysis below. The distance between the left end ($y=0$) and the location where the two primary waves meet is $d = c_T(\frac{L}{c_L + c_T})$ (See Figure 4, L is the sample length). Imagine that the shear wave contains many “points”. Each point of the shear wave will interact with the longitudinal wave (actually interact with each vibrating point of the longitudinal wave) and the interaction generates a difference shear wave with frequency ω_R and shear wave speed c_T . As shown in Figure 4, the lengths of the shear and longitudinal wave are L_1 ($L_1 = c_T\tau_T$) and L_2 ($L_2 = c_L\tau_L$), respectively. Again, without loss of generality, we assume $L_1 > L_2$.

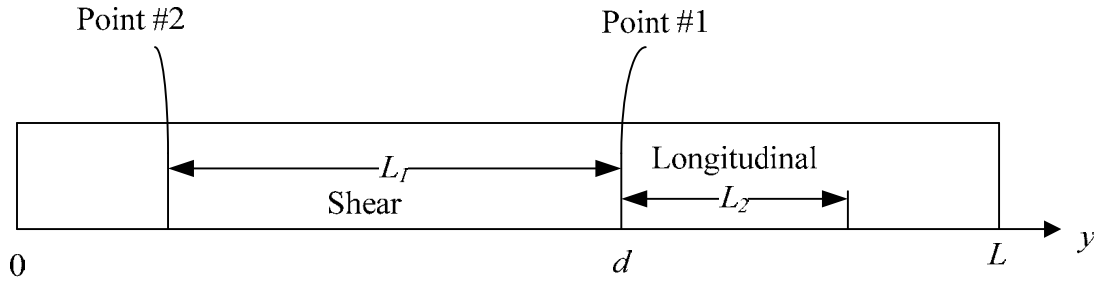


Figure 4 Start of interaction between point #1 and the longitudinal wave

Let's then consider the second order shear wave generated by the interaction between the first point (point #1) of the primary shear wave and the whole longitudinal wave. The time when it starts appearing is t_c , which should be equal to the time when the interaction begins, i.e.,

$$t_c = \frac{L}{c_L + c_T}. \quad (74)$$

Once this second order shear wave generates, it will propagate along negative y direction and be received by the shear transducer at $y=0$. The arrival time (to $y=0$) is

$$t_{1_arrive} = t_c + \frac{d}{c_T} = \frac{2L}{c_L + c_T}. \quad (75)$$

The question now is when this wave will be ending at $y=0$. If we use t_{1_end} to represent the time when this shear wave ends at $y=0$, we have

$$t_{1_end} = t_{1_arrive} + t_{1_duration}, \quad (76)$$

where $t_{1_duration}$ represents the duration of the second order shear wave generated by the interaction between point #1 and the whole longitudinal wave. Clearly, it takes $L_2/(c_L + c_T)$ for the front of the primary shear pulse (point #1) to reach the end of the longitudinal pulse. In other words, there is a $L_2/(c_L + c_T)$ time delay after t_c that the interaction between point #1 and the whole primary longitudinal wave ends. The location of point #1 now is at $y = d + c_T L_2/(c_L + c_T)$ (see Figure 5). Since the phase velocity of second order shear wave is c_T , it means that it takes

another $\left[c_T \left(\frac{L_2}{c_L + c_T} \right) \right] / c_T$ for the last generated shear wave (generated at $y = d + c_T L_2/(c_L + c_T)$) to arrive at the same location where the first generated shear wave (generated at $y=d$) arrives.

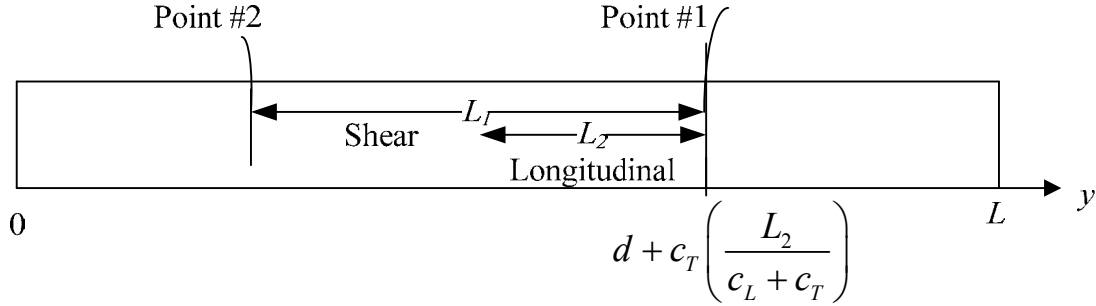


Figure 5 Ending of interaction between point #1 and the longitudinal wave

Based on the analysis above, we can conclude that

$$t_{1_duration} = \frac{L_2}{c_L + c_T} + \left[c_T \left(\frac{L_2}{c_L + c_T} \right) \right] / c_T = \frac{2L_2}{c_L + c_T}. \quad (77)$$

Substitution of (75) and (77) into (76) yields

$$t_{1_end} = \frac{2(L + L_2)}{c_L + c_T}. \quad (78)$$

Next, we consider the interaction between the last point (point #2) of the primary shear wave and the whole longitudinal wave. The difference wave generated by the interaction between point #2 and the longitudinal wave starts at $L_1/(c_L + c_T)$ after t_c , and the location where it starts generating is at $y = d - c_L L_1/(c_L + c_T)$. Similarly, we have

$$t_{2_arrive} = \frac{2L}{c_L + c_T} - \frac{c_L - c_T}{c_T} \left(\frac{L_1}{c_L + c_T} \right), \quad (79)$$

$$t_{2_duration} = t_{1_duration} = \frac{2L_2}{c_L + c_T}, \quad (80)$$

$$t_{2_end} = t_{2_arrive} + t_{2_duration} = \frac{2(L + L_2)}{c_L + c_T} - \frac{c_L - c_T}{c_T} \left(\frac{L_1}{c_L + c_T} \right). \quad (81)$$

Compare (79) to (75), one can find that $t_{2_arrive} < t_{1_arrive}$, which means the second order shear wave generated last (by point #2) will arrive at the left end ($y=0$) early than that generated first (by point #1) and thus be observed early. Actually, the total second order shear wave is the superposition of all the shear waves generated by the interaction between each point of L_1 and the whole longitudinal wave. The total second order shear wave arrives at $y=0$ at t_{2_arrive} and ends at $y=0$ at t_{1_end} . The mechanism of superposition will be discussed later.

In most of metallic materials, we have $c_L/c_T \approx 2$ so that the expressions (75), (78), (79) and (81) can be simplified as

$$t_{1_arrive} = \frac{2L}{c_L + c_T}, \quad (82)$$

$$t_{1_end} = \frac{2(L + L_2)}{c_L + c_T}, \quad (83)$$

$$t_{2_arrive} = \frac{2L}{c_L + c_T} - \left(\frac{L_1}{c_L + c_T} \right), \quad (84)$$

$$t_{2_end} = \frac{2L}{c_L + c_T} + \left(\frac{2L_2 - L_1}{c_L + c_T} \right). \quad (85)$$

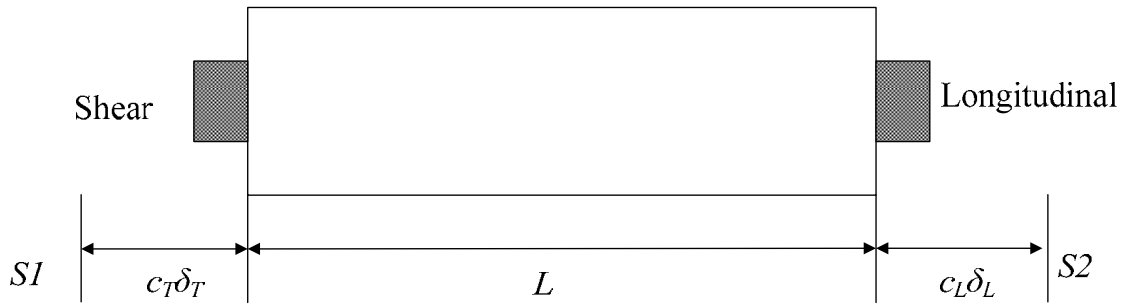


Figure 6 Mixing with delay time

Next, we will take the delay time of the primary waves into consideration. If the longitudinal wave has a delay time δ_L and shear wave has a delay time δ_T , it's like we put the shear and longitudinal transducer at S1 and S2 shown in the Figure 6. The arrival and ending time of the resonant shear wave can be obtain by replacing L in (84) and (83) by $L + c_L \delta_L + c_T \delta_T$. However, the results after substitution represents the time when the shear wave transducer is also put at S1. Since the shear wave transducer is still at its original location, the real arrival and ending time should be equal to the time of the substitution mentioned above subtracts $\frac{c_T \delta_T}{c_T} = \delta_T$.

. So the new arrival and ending time are

$$t'_{start} = \frac{2(L + c_L \delta_L + c_T \delta_T)}{c_L + c_T} - \left(\frac{L_1}{c_L + c_T} \right) - \delta_T, \quad (86)$$

$$t'_{end} = \frac{2(L + c_L \delta_L + c_T \delta_T + L_2)}{c_L + c_T} - \delta_T. \quad (87)$$

Simplification of (86) and (87) yields

$$t'_{start} = \frac{2L}{c_L + c_T} - \left(\frac{L_1}{c_L + c_T} \right) + \frac{2c_L \delta_L - (c_L - c_T) \delta_T}{c_L + c_T}, \quad (88)$$

$$t'_{end} = \frac{2(L + L_2)}{c_L + c_T} + \frac{2c_L \delta_L - (c_L - c_T) \delta_T}{c_L + c_T}. \quad (89)$$

It can be seen from (88)-(89) that delay time δ_L and δ_T give a delay

$$C = \frac{2c_L\delta_L - (c_L - c_T)\delta_T}{c_L + c_T} \quad (90)$$

to the second order shear wave. Definition of C in (90) is the same as the one in (73).

FORMATION OF SECOND ORDER SHEAR WAVE BY SUPERPOSITION

In previous section, we gave the analysis of second order wave generation by the interaction between each point of the primary shear wave and the whole longitudinal wave. The total second order shear wave is the superposition of all these second order waves. In this section, we will take the interaction in metallic materials ($c_L/c_T \approx 2$) as an example and investigate how the superposition affects the shape of the total signal.

Based on (82)-(85), if $L_1 > 2L_2$, we have $t_{2_end} < t_{1_arrive}$. The second order shear wave in this case can be represented by Figure 7. The x -coordinate in this figure represents the time-axis. Each solid line represents a second order shear wave generated by the interaction between one point of the primary shear wave and the whole longitudinal wave. The total resonant shear wave can be found by the superposition of all these second order waves. Once the resonant

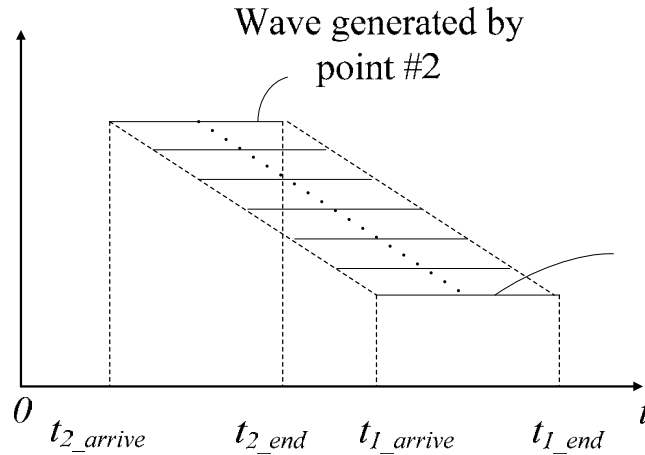


Figure 7 Superposition of second order shear wave ($L_1 > 2L_2$)

condition (33) is satisfied, it can be proved that all these second order waves are in phase, so the superposition gets to a maximum (constant) between t_{2_end} and t_{1_arrive} .

If $L_1 = 2L_2$, we have $t_{2_end} = t_{1_arrive}$ and the second order shear waves can be represented by Figure 8. The summation gets to its maximum at $t = t_{2_end} = t_{1_arrive}$. Since there is only one maximum value for this case, the total shear wave will have a diamond shape.

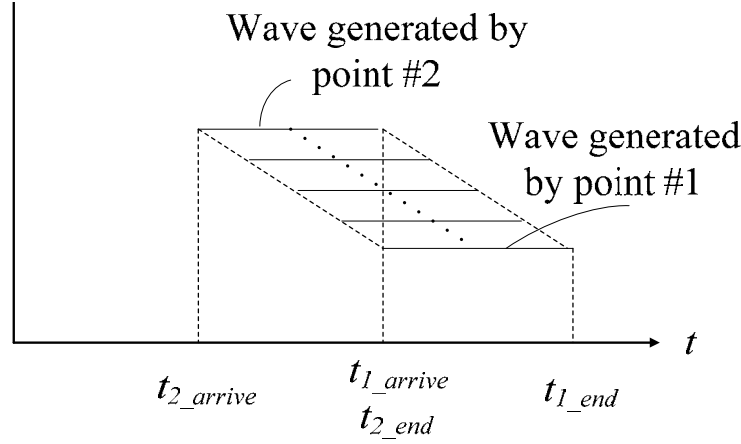


Figure 8 Superposition of second order shear wave ($L_1 = 2L_2$)

If $L_1 < 2L_2$, we have $t_{2_end} > t_{1_arrive}$ and the second order shear waves can be represented by Figure 9. The summation gets to its maximum between t_{1_arrive} and t_{2_end} .

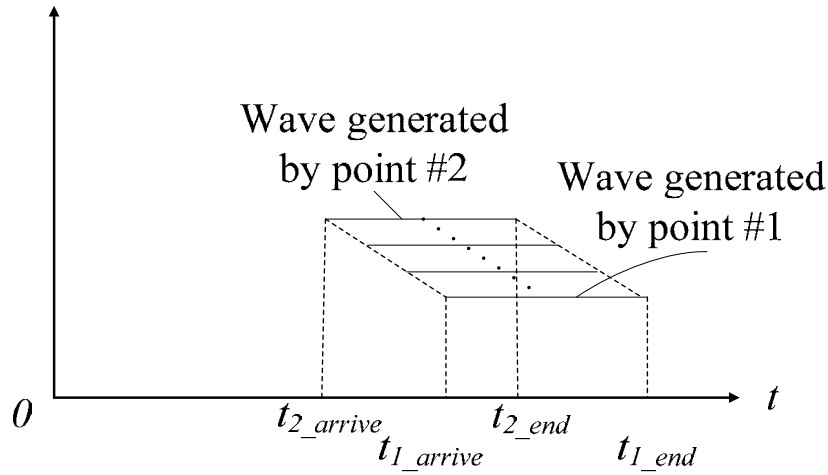


Figure 9 Superposition of second order shear wave ($L_1 < 2L_2$)

Figure 10 (a)-(c) shows the numerical calculation of (72) for the three special cases mentioned above. It's clear that the diamond shape signal only appears when $L_1 = 2L_2$. Actually, it can be shown that the maximum amplitude of the mixing wave does not change when we decrease the length L_1 from $L_1 > 2L_2$ to $L_1 = 2L_2$ while keeping the length of L_2 as a constant (see Fig.10 (a)-(b)). It is only the width of the maximum region that reduces with the decrease L_1 . This can be explained by the mechanism of superposition shown in Fig. 7-9. In this special case, the height of the region between t_{2_end} and t_{1_arrive} in Fig. 7 is equal to that in Fig. 8. If we keep decreasing the length of L_1 from $L_1 = 2L_2$ to $L_1 < 2L_2$, the maximum amplitude of the mixing wave starts decreasing with the decrease of L_1 (see Fig. 10(c)). This is because the height of the region between t_{1_arrive} and t_{2_end} in Fig. 9 is shorter than those in Fig. 7 and Fig. 8.

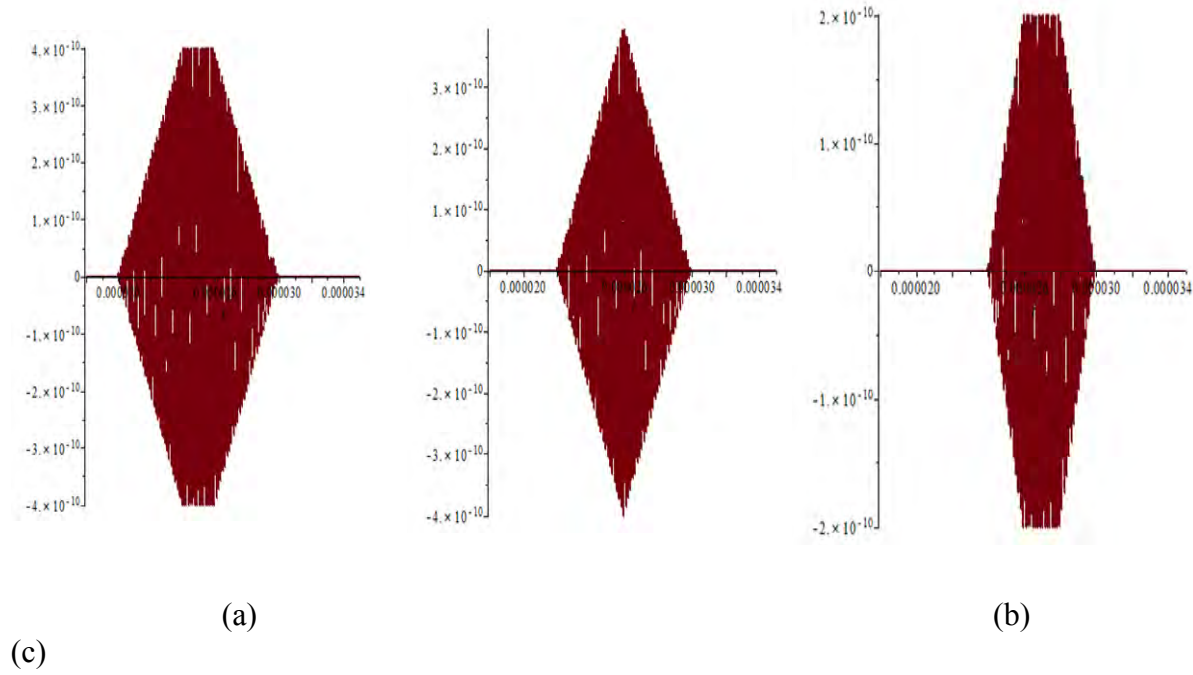


Figure 10 Numerical calculation of the total shear wave for (a) $L_1 > 2L_2$, (b) $L_1 = 2L_2$, and (c) $L_1 < 2L_2$

Figure 11 shows an comparison between the theoretical solution (72) and the experimental result in an aluminum sample ($c_L = 6300\text{m/s}$, $c_T = 3140\text{m/s}$) for $\delta_L = \delta_T = 0$, $L = 0.183\text{m}$. The primary shear wave is 2.5MHz with 5 cycles, and the corresponding duration time is $\tau_T = 2\mu\text{s}$. The primary longitudinal wave is 9.65MHz with 9 cycles, and the corresponding duration time is $\tau_L = 0.93\mu\text{s}$. The spatial lengths of the shear and the longitudinal waves are $L_1 = c_T \tau_T = 0.0063\text{m}$ and $L_2 = c_L \tau_L = 0.0059\text{m}$, respectively. It's clear that $L_1 < 2L_2$. Based on (82)-(85), we can calculate the four critical times in Figure 9 : $t_{2_arrive} = 38.1\mu\text{s}$, $t_{1_arrive} = 38.7\mu\text{s}$, $t_{2_end} = 39.3\mu\text{s}$ and $t_{1_end} = 40.0\mu\text{s}$. It is shown in Figure 11 that: (1) the superposition analysis gives the same arrival time, ending time and shape as that given by the theoretical solution, (2) the four transition points of time (shown by dashed lines) of the mixing wave show good agreement to the four critical times calculated by (82)-(85).

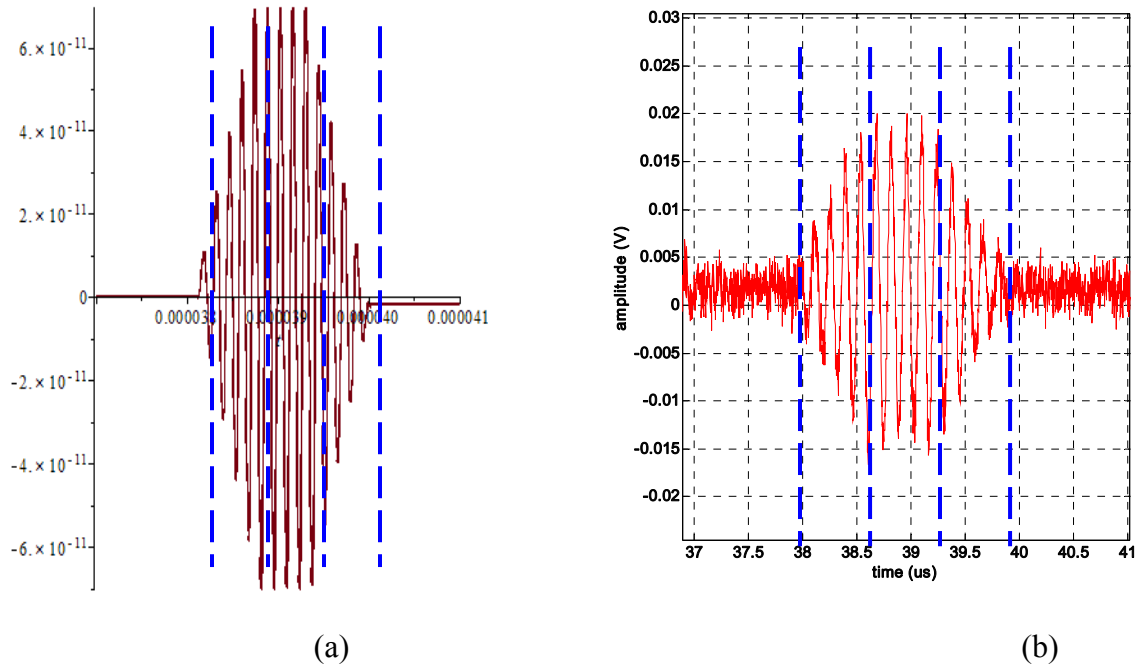


Figure 11 Collinear mixing wave in an aluminum sample (a) Theoretical results, (b) Experimental results

SUMMARY AND CONCLUSION

This paper investigates the nonlinear mixing of a pair of collinear transient longitudinal and shears waves. The solution for the second order shear wave with difference frequency is obtained under the phase matching condition by using the transient Green's function. The physical meaning of the delay time of the resonant wave is investigated and the mechanism of its formation is analyzed by a superposition analysis.

We found that the amplitude of the resonant wave is proportional to the acoustic nonlinearity β_T within the region where the two primary waves mix. It is thus possible to obtain a relative spatial distribution of β_T through the thickness direction of the sample by adjusting the delay times of the two primary waves.

REFERENCES

- Childress, J. D., and Hambrick, C. G. (1964). "Interactions between Elastic Waves in Isotropic Solid," *Physical Review a-General Physics* **136**, A411-A418.
- Croxford, A. J., Wilcox, P. D., Drinkwater, B. W., and Nagy, P. B. (2009). "The use of non-collinear mixing for nonlinear ultrasonic detection of plasticity and fatigue," *Journal of the Acoustical Society of America* **126**, E1117-E1122.
- Johnson, P. A., and Shankland, T. J. (1989). "Nonlinear Generation of Elastic-Waves in Granite and Sandstone - Continuous Wave and Travel Time Observations," *Journal of Geophysical Research-Solid Earth and Planets* **94**, 17729-17733.
- Johnson, P. A., Shankland, T. J., Oconnell, R. J., and Albright, J. N. (1987). "Nonlinear

- Generation of Elastic-Waves in Crystalline Rock," *Journal of Geophysical Research-Solid Earth and Planets* **92**, 3597-3602.
- Jones, G. L., and Korbett, D. R. (1963). "Interaction of Elastic Waves in an Isotropic Solid," *Journal of the Acoustical Society of America* **35**, 5-10.
- Liu, M. H., Tang, G. X., Jacobs, L. J., and Qu, J. M. (2012). "Measuring acoustic nonlinearity parameter using collinear wave mixing," *Journal of Applied Physics* **112**.
- Rollins, F. R., Todd, P. H., and Taylor, L. H. (1964). "Ultrasonic Study of 3-Phonon Interactions .2. Experimental Results," *Physical Review a-General Physics* **136**, A597-A601.
- Taylor, L. H., and Rollins, F. R. (1964). "Ultrasonic Study of 3-Phonon Interactions .I. Theory," *Physical Review a-General Physics* **136**, A591-A596.
- Zarembo, L. K., and Krasilnikov, V. A. (1971). "Nonlinear Phenomena in Propagation of Elastic Waves in Solids," *Soviet Physics Uspekhi-Ussr* **13**, 778-797.

III.1.4 Physics-Based Models for ASR Damage Evolution

A novel approach, entitled ASR-LDPM [1] was formulated to simulate the effect of ASR on concrete structures. ASR-LDPM implements, within the mesoscale framework of LDPM, a model describing ASR gel formation and expansion at the level of each individual aggregate particle. ASR-LDPM was calibrated and validated with reference to several sets of experimental data dealing with ASR effects on concrete under a variety of different loading and environmental conditions with the limitation to saturated conditions.

The main effect of ASR is a progressive deterioration of concrete stiffness and strength that results from the long term formation and expansion of ASR gel inducing expansive pressure on the internal structure of concrete. This pressure causes non-uniform deformations that eventually lead to cracking and damage. While the chemical description of the reaction was addressed intensively in the literature, the fracture mechanics associated with the progressive expansion has received little attention due to the lack of models describing concrete internal structure satisfactorily. The main objective of the ASR-LDPM model is to fill this knowledge gap.

Despite some success, the common disadvantage of the various models previously developed is the inability to simulate crack patterns and crack distribution due to ASR. This, in turn, limits the ability to predict the degradation effect of ASR and forces the assumption of phenomenological relationships between ASR gel expansion and concrete mechanical properties. In addition, it also limits the ability of such models to explain complex triaxial behavior of concrete under ASR and also forces the assumption of phenomenological relationships between ASR gel expansion and stress state. These limitations are inherently connected to modeling concrete as an isotropic and homogenous continuum.

ASR-LDPM overcomes these problems by modeling ASR effects within the Lattice Discrete Particle Model (LDPM) [2, 3]. LDPM, in a full 3D setting, simulates the mechanical interaction of coarse aggregate pieces through a system of three-dimensional polyhedral particles, each resembling a spherical coarse aggregate piece with its surrounding mortar, connected through lattice struts [2] and it has the ability of simulating the effect of material heterogeneity of the fracture processes [3]. ASR-LDPM introduced here is limited to fully saturated conditions as the consideration of water macro diffusion will be considered in the future work.

In the formulated model, the following assumptions were used.

- (1) Water needs to be available in the pores to act as transport medium for hydroxyl and alkali ions for ASR to occur.
- (2) The expansion of ASR gel is mostly due to water imbibition.
- (3) Continuous supply of water is needed for the swelling to continue over time.
- (4) The aggregate particles are assumed to have spherical shape.
- (5) The whole volume of each particle is assumed to be reactive.
- (6) Silica is smeared uniformly over each aggregate volume.
- (7) Under these approximations, the dissolution of silica may be assumed to progress roughly in a uniform manner in the radial direction inward from the surface towards the particle center.
- (8) Only saturation condition is considered so far. This case has practical relevance in situations

in which concrete is continuously exposed to water. The effect of relative humidity change is to be considered in the future work.

(9) Shrinkage and possible creep are compensated using relevant models in literature (B3 and CEB models) but not implicitly coupled with the formulation.

Based on the aforementioned assumptions, two main processes have been formulated and connected; (1) Basic gel formation, and (2) Water imbibition, then volume increase due to water imbibition is translated into inhomogeneous gel strain, and is imposed on the concrete meso-structure using the LDPM model. The highlights of each part are as follows.

(1) Basic Gel Formation.

The gel mass M_g generated from an aggregate particle with diameter D , is derived from solving the steady state mass balance of the radial diffusion process of alkali rich water into the aggregate particle. The solution is given by,

$$M_g = \kappa_a \frac{\pi D^3}{6} (1 - \zeta^3) c_s \frac{m_g}{m_s}$$

Where $m_g = 94.1$ g/mole, $m_s = 60.09$ g/mole are the gel and silica molar weights respectively, $\zeta = 2z/D$ is the non-dimensional reaction front position where z is the reaction front position measured from aggregate particle external surface, c_s is the silica content assumed here for lack of experimental data to be 440 kg/m^3 , and κ_a accounts for the fact that alkali content available in the cement paste surrounding each aggregate particle, is not always enough for the ASR reaction to occur. In other words, the discussed availability of water at reaction front is not a sufficient condition for ASR and such water needs to be alkali rich. In this study, in absence of more detailed information, a simple linear relationship between alkali content, c_a , and the produced gel mass is assumed: $\kappa_a = \min(\frac{c_a - c_{0a}}{c_{1a} - c_{0a}}, 1)$, where c_{0a} is the threshold alkali content at which, no or minimal expansion is observed, and c_{1a} is the saturation alkali content enough for complete silica reaction.

(2) Water imbibition

The water imbibition process was described by relating the rate of water mass \dot{M}_i imbibed by gel to the thermodynamic affinity and a characteristic imbibition time. This leads to the following expression,

$$\dot{M}_i = \frac{C_i^0}{\delta^2} \exp(-\eta M_i) \left[K_i^0 (1 - \zeta^3) D^3 \kappa_a \exp\left(\frac{E_{ai}}{RT_0} - \frac{E_{ai}}{RT}\right) - M_i \right]$$

Where R is the universal gas constant, T is the absolute temperature in Kelvins, T_0 is a reference absolute temperature where the imbibed water at thermodynamic equilibrium has been assumed to be proportional to the mass of formed gel and temperature-dependent through an Arrhenius-type equation governed by the activation energy of the imbibition process E_{ai} . δ is the average (or effective) distance of water transport process from the concrete around the aggregate into the ASR gel. The micro-diffusivity C_i for microdiffusion of water close to the aggregate was considered to be a decreasing function of M_i , because the imbibition of the layers of gel increases the diffusion time of the free water to reach the not imbibed gel. This phenomenon can be captured by setting $C_i = C_{i0} \exp(-\eta M_i)$, and $\eta(M_i)$ is an increasing function of M_i .

Analysis of experimental data carried out in this study suggests that, in absence of more precise information about the water imbibition process,

$$K_i^0 = \pi \kappa_i^0 c_s m_g / (6 m_s).$$

Where $\kappa_i^0 \approx 1$ for $T_0 = 23^\circ\text{C} = 296^\circ\text{K}$.

(3) Lattice Discrete Particle Modeling of ASR effect

To account for ASR in LDPM, first the radius variation of each aggregate particle of initial radius $r = D/2$ can be calculated from the volume variation of the ASR gel due to water imbibition:

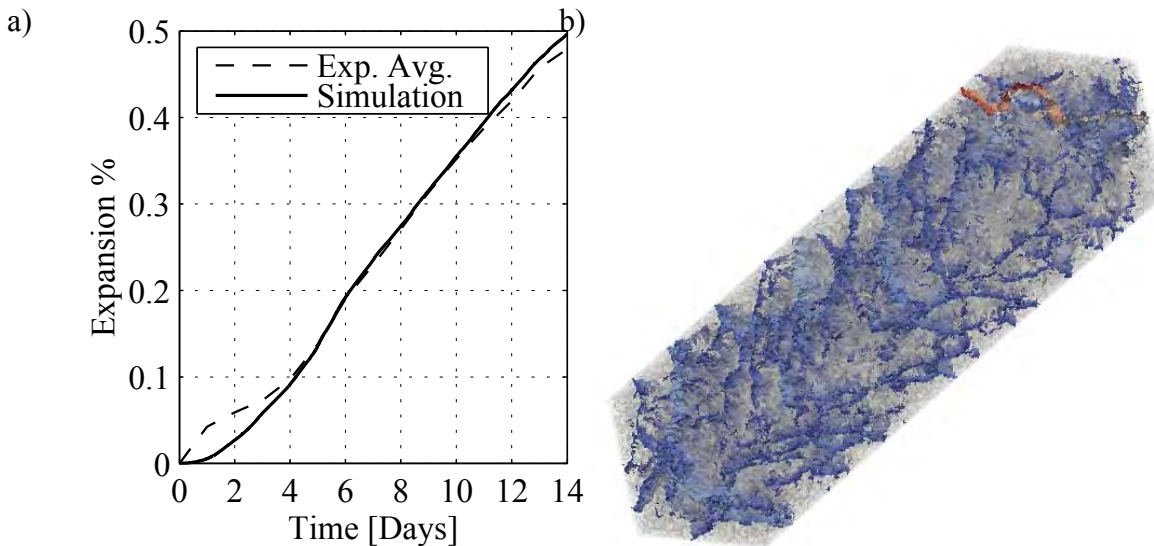
$$\Delta r = \left(\frac{3M_i}{4\pi\rho_w} + r^3 \right)^{1/3} - r$$

This result can be then used to calculate an incompatible ASR strain e_N^0 to be applied to the LDPM system assuming that strain additivity holds: where the total strain is given by where $e_N = e_N^t + e_N^0$; Δr_1 and Δr_2 are the radius changes of the two aggregate particles sharing a generic facet; l is the distance between these two aggregate particles; and is the normal strain that is calculated according to the LDPM constitutive equation.

$$e_N^0 = (\Delta r_1 + \Delta r_2 - \delta_c) / l$$

After calibrating the model it was able to capture (1) the general characteristics of ASR S-shaped expansion versus time curves; (2) the effect of stress states on observed expansion; (3) the effect of expansion on concrete strength; (4) the effect of alkali content; and (5) the effect of temperature.

The relevant results for small specimens carried out here were used to calibrate the model which was able to accurately capture the expansion curves with very high accuracy as shown in figure a).



In addition, the model was capable of reproducing the corresponding crack patterns found in the experiments as shown in figure b).

The simulation of large specimens requires the consideration of alkali ion macrodiffusion and thus, it was scheduled to be done within the next quarter work. It is to be mentioned also that the model can reproduce the current damage state of the specimens and as it is now calibrated on the given expansion history, it can predict the remaining expansion history and hence, the expected strength reduction.

References

- [1] M. Alnaggar, G. Cusatis, and G. Di Luzio, “Lattice Discrete Particle Modeling (LDPM) of Alkali Silica Reaction (ASR) Deterioration of Concrete Structures”, *Cement and Concrete Composites*, (Accepted).
- [2] G. Cusatis, D. Pelessone, and A. Mencarelli, Lattice Discrete Particle Model (LDPM) for Concrete failure Behavior of Concrete. I: Theory, *Cement and Concrete Composites*, 33(9):881–890, 2011.
- [3] G. Cusatis, A. Mencarelli, D. Pelessone, and J. Baylot, Lattice Discrete Particle Model (LDPM) for Failure Behavior of Concrete. II: Calibration and Validation, *Cement and Concrete Composites*, 33(9):891–905, 2011.

III.1.5 Nonlinear wave mixing technique to measure the ANLP in concrete samples nondestructively in a laboratory environment

One-Sided Collinear Wave Mixing

In many cases of practical interest, NDE can only be performed on one-side of the sample. To meet this need, we develop a one-sided collinear wave mixing technique. The basic idea of the technique is to send a shear wave pulse into the sample first, then send a longitudinal wave pulse from the same location and in the same direction later. Since the longitudinal pulse propagates faster, it will catch, overlap and eventually pass the shear pulse. During the overlap period, the two waves interact and may generate a resonant shear wave the frequencies of the two primary waves satisfy the resonant condition. The resonant shear wave propagates back towards the shear wave transducer, and the corresponding signals can then be recorded would contain the ANLP of the material at the region where the two primary wave mix. By adjusting the time delay between the longitudinal and shear pulses, one can control the location where the two wave mix. Thus, it is possible to scan the sample in the depth direction from only one side.

Theory

When the quadratic terms of displacement are considered in the stress-strain relationship, the nonlinear equations of motion for an isotropic solid in one dimension are

$$\frac{\partial^2 u}{\partial t^2} - C_L^2 \frac{\partial^2 u}{\partial x^2} = \beta_L C_L^2 \frac{\partial u}{\partial x} \frac{\partial^2 u}{\partial x^2} + \beta_T C_T^2 \frac{\partial v}{\partial x} \frac{\partial^2 v}{\partial x^2} \quad (1)$$

$$\frac{\partial^2 v}{\partial t^2} - C_T^2 \frac{\partial^2 v}{\partial x^2} = \beta_T C_T^2 \left(\frac{\partial u}{\partial x} \frac{\partial^2 v}{\partial x^2} + \frac{\partial v}{\partial x} \frac{\partial^2 u}{\partial x^2} \right) \quad (2)$$

where

$$C_T = \sqrt{\mu/\rho}, \quad C_L = \sqrt{(\lambda + 2\mu)/\rho} \quad \beta_L = 3 + 2 \frac{l + 2m}{\lambda + 2\mu}, \quad \beta_T = \frac{\lambda + 2\mu}{\mu} + \frac{m}{\mu}$$

and ρ is the density of the solid. λ is the compression modulus and μ is the shear modulus. l and m are third-order elastic constants.

If we set $u = u^0 + u^s$ and $v = v^0 + v^s$ where u^0 and v^0 are the solutions when the right side of (1) and (2) is 0, u^s and v^s can be treated as the correction arising from the right side.

Since we are interested in the mixing of a longitudinal wave and a shear wave propagating in the same direction (positive x -direction), the expressions of the primary monochromatic waves are taken as

$$u^0 = U \cos(\omega_L t - k_L x + \varphi_L) \quad (3)$$

$$v^0 = V \cos(\omega_T t - k_T x + \varphi_T) \quad (4)$$

where the wavenumbers are $k_L = \frac{\omega_L}{c_L}$, $k_T = \frac{\omega_T}{c_T}$.

If u^s and v^s are small enough compared to u^0 and v^0 , we can substitute $u = u^0 + u^s$, $v = v^0 + v^s$ into the left side of (1) and (2), and $u = u^0$, $v = v^0$ on the right side as an approximation. The substitution yields

$$\frac{\partial^2 u^s}{\partial t^2} - C_L^2 \frac{\partial^2 u^s}{\partial x^2} = \beta_L C_L^2 \frac{\partial u^0}{\partial x} \frac{\partial^2 u^0}{\partial x^2} + \beta_T C_T^2 \frac{\partial v^0}{\partial x} \frac{\partial^2 v^0}{\partial x^2} \quad (5)$$

$$\frac{\partial^2 v^s}{\partial t^2} - C_T^2 \frac{\partial^2 v^s}{\partial x^2} = \beta_T C_T^2 \left(\frac{\partial u^0}{\partial x} \frac{\partial^2 v^0}{\partial x^2} + \frac{\partial v^0}{\partial x} \frac{\partial^2 u^0}{\partial x^2} \right) \quad (6)$$

Since we are only interested in the terms representing interactions between the primary waves, terms represent self-interactions will be neglected. Thus, the mixing wave exists only in the form of a shear wave and the superscript “s” is omitted from this point on for brevity. Equation (6) is then written as

$$\frac{\partial^2 v}{\partial t^2} - C_T^2 \frac{\partial^2 v}{\partial x^2} = f(x, t) \quad (7)$$

where

$$\begin{aligned} f(x, t) = & A^+ \sin([\omega_L + \omega_T]t - [k_L + k_T]x + [\varphi_L + \varphi_T]) \\ & + A^- \sin([\omega_L - \omega_T]t - [k_L - k_T]x + [\varphi_L - \varphi_T]) \\ A^- = & \frac{UV\beta_T C_T^2 k_L k_T}{2} (k_L - k_T), \quad A^+ = \frac{UV\beta_T C_T^2 k_L k_T}{2} (k_L + k_T). \end{aligned}$$

The interaction term $f(x, t)$, which is proportional to the product of the primary beams

amplitudes, should be zero outside the region where the two wave mix.

The equation for the Fourier transform from (7) is

$$-\omega^2 v(x, \omega) - C_T^2 \frac{\partial^2 v(x, \omega)}{\partial x^2} = f(x, \omega) \quad (8)$$

where $v(x, \omega)$ and $s(x, \omega)$ are the Fourier transform from $v(x, t)$ and $f(x, t)$. If we assume that the resonant wave propagates from the point $x = x_0$, the boundary condition can be given as $v(x_0, \omega) = 0$. The solution for (8) is written as

$$v(x, \omega) = \frac{C_T}{\omega} \left[\left(\cos \frac{\omega}{C_T} x \right) \int_{x_0}^x f(a, \omega) \sin \frac{\omega}{C_T} a da - \left(\sin \frac{\omega}{C_T} x \right) \int_{x_0}^x f(a, \omega) \cos \frac{\omega}{C_T} a da \right] \quad (9)$$

Then from inverse Fourier transform, $v(x, t)$ can be obtained as

$$\begin{aligned} v(x, t) &= -\frac{C_T}{4\pi} \int_{x_0}^x \int_{\frac{(x-a)}{C_T}}^{\frac{(x-a)}{C_T}} f(a, t-\tau) d\tau da \\ &= -\frac{C_T}{4\pi} \int_{x_0}^x \left[\frac{A^-}{\omega_L - \omega_T} \cos \left(\left(\frac{[\omega_L - \omega_T]}{C_T} - [k_L - k_T] \right) a + [\omega_L - \omega_T] \left(t - \frac{x}{C_T} \right) + [\varphi_L - \varphi_T] \right) \right] da \\ &\quad + \frac{C_T}{4\pi} \int_{x_0}^x \left[\frac{A^-}{\omega_L - \omega_T} \cos \left(\left(-\frac{[\omega_L - \omega_T]}{C_T} - [k_L - k_T] \right) a + [\omega_L - \omega_T] \left(t + \frac{x}{C_T} \right) + [\varphi_L - \varphi_T] \right) \right] da \\ &\quad - \frac{C_T}{4\pi} \int_{x_0}^x \left[\frac{A^+}{\omega_L + \omega_T} \cos \left(\left(\frac{[\omega_L + \omega_T]}{C_T} - [k_L + k_T] \right) a + [\omega_L + \omega_T] \left(t - \frac{x}{C_T} \right) + [\varphi_L + \varphi_T] \right) \right] da \\ &\quad + \frac{C_T}{4\pi} \int_{x_0}^x \left[\frac{A^+}{\omega_L + \omega_T} \cos \left(\left(-\frac{[\omega_L + \omega_T]}{C_T} - [k_L + k_T] \right) a + [\omega_L + \omega_T] \left(t + \frac{x}{C_T} \right) + [\varphi_L + \varphi_T] \right) \right] da \end{aligned} \quad (10)$$

The first and second terms in (10) are shear wave with the difference frequency, while the third and fourth terms are shear wave with the sum frequency. The terms of the cosine function in (10) have the similar form with the solution given by Gerald Lee Jones, so the resonance condition for an isotropic solid in one dimension can be given as

$$\begin{aligned}
\frac{[\omega_L - \omega_T]}{C_T} - [k_L - k_T] &= 0 \\
\frac{[\omega_L - \omega_T]}{C_T} + [k_L - k_T] &= 0 \\
\frac{[\omega_L + \omega_T]}{C_T} - [k_L + k_T] &= 0 \\
\frac{[\omega_L + \omega_T]}{C_T} + [k_L + k_T] &= 0
\end{aligned} \tag{11}$$

When the primary waves propagate in the same direction, if the first and second resonance conditions are satisfied, we can have

$$\frac{(\omega_L - \omega_T)^2}{C_T^2} = (k_L - k_T)^2 = \frac{\omega_L^2}{C_L^2} + \frac{\omega_T^2}{C_T^2} + 2 \frac{\omega_L \omega_T}{C_L C_T} \tag{12}$$

The resonance conditions can be simplified to a relationship between the frequency ratio and the velocity ratio.

$$\omega = \frac{1+c}{2} \tag{13}$$

where $\omega = \frac{\omega_T}{\omega_L} > 0$, $c = \frac{C_T}{C_L}$. In other words, a resonant wave with the difference frequency

can be generated when the primary waves propagate in the same direction if (13) is met. The expression of the resonant wave can be expressed as

$$v(x, t) = -\frac{UV \beta_T C_T^3 k_L k_T |k_L - k_T| (x - x_0)}{8\pi (\omega_L - \omega_T)} \cos \left([\omega_L - \omega_T] \left(t - \frac{x}{C_T} \right) + [\varphi_L - \varphi_T] \right) \tag{14}$$

As a result, the amplitude of the scattered wave is proportional to the length of the intersection region of the two primary waves.

Waveform of the Resonant Wave under the Resonance Conditions

When transient pulses are used as excitations in the nonlinearity measurement experiments, the amplitude of the resonant wave received by the transducer at a given time t_r can be treated as part of the continuous solution which is infinite in the time domain. Without loss of generality, a special case, in which a longitudinal wave and a shear wave are mixed in the same direction, is

considered.

Assume that a shear wave transducer located at $x = 0$ generates a shear pulse of N_s cycles at t_{s_0} , and a longitudinal wave transducer located at $x = 0$ generates a longitudinal pulse of N_L cycles t_{L_0} . Both of the transient pulses propagate in the positive x -direction, and they are under the resonance conditions with the frequency f_s and f_L . The velocity of the shear wave and longitudinal wave are C_s and C_L , respectively.

The resonant wave can be generated between the time when the two pulses meet and the time when the two pulses separate completely. When one of the transient pulses reaches the point x_0 and another is passing through it, the resonant wave starts its propagation at the point x_0 towards the negative x -direction. Before the resonant wave meets one of the pulse ends at the point x , the propagation of the resonant wave can be described by the continuous solution $v(x, t)$ in the infinite time domain because all the region it passed through is the interaction region. After that, the resonant wave propagates without amplitude change.

Without loss of generality, the case that the resonant wave generated at the point x_0 reaches the transducer with the amplitude A is considered. If the front of the longitudinal wave passes the end of the shear wave and reaches the point x_0 , the resonant wave starts its propagation at the time t . The time at which the resonant wave reaches the transducer is $t_r = t + \frac{x_0}{C_s}$. It is easy to obtain the duration that the resonant wave propagates in the interaction region

$$t_{mix} = \min \left(\frac{N_L \lambda_L}{C_L + C_s}, \frac{(C_L - C_s)(t - t_{meet})}{2C_s} \right) \quad (15)$$

The length of the interaction region is $d_{mix} = C_s \cdot t_{mix}$. Thus, the amplitude of the scattered wave should be

$$A = \frac{UV \beta_T C_T^3 k_L k_T |k_L - k_T|}{8\pi(\omega_L - \omega_T)} \cdot d_{mix} \quad (16)$$

Similarly, if the front of the longitudinal wave passes the front of the shear wave and the

front of the shear wave reaches the point x_0 , the resonant wave starts its propagation at the time t . We can obtain the duration that the resonant wave propagates in the interaction region

$$t_{mix} = \min \left(\frac{N_s \lambda_s}{2C_s}, \frac{N_L \lambda_L - (C_L - C_s) \left(t - t_{meet} - \frac{N_s \lambda_s}{C_L - C_s} \right)}{C_L + C_s} \right) \quad (17)$$

The amplitude of the resonant wave can also be expressed by (16).

Eliminate x_0 and t , we can finally obtain the expression of the amplitude as a function of t_r , which can be used to predict the waveform displayed on the oscilloscope. As a result, when the delay between the two transient pulses are adjusted, the primary waves can mix at different locations so that a distribution of β_T is then obtained. Especially, if $N_s = N_L$ under the resonance conditions, the shape of the scattered waveform will be a standard diamond.

III.1.6 Physics-Based Models that Correlate the ANLP to ASR Damage

Change of Acoustic Nonlinearity due to ASR Damage

The original acoustic nonlinearity parameter β only relates to material properties, and is usually defined as [1]:

$$\beta = -\left(3 + \frac{4m + 2l}{\lambda + 2\mu}\right) \quad (1.1)$$

in which λ and μ are the Lamé constants, and l and m are the third order elastic constants (the Murnaghan coefficients). However, when material is under residual stresses, or experiences plastic deformations, the nonlinearity parameter β changes correspondingly as has been shown in extensive experimental results [2-8]. Our previous work has demonstrated the feasibility of using nonlinear ultrasonic techniques to track the progress of ASR damage in cement-based materials [9]. Here we want to predict the β change using our previous model validated by expansion measurements of small mortar samples. An example of acoustic nonlinearity parameter β change in metallic materials due to dislocation and microcracks can be found in ref. [10]. Basically β change is a linear superposition of two terms, one is proportional to the initial stress and the other is proportional to the crack density. In our problem here, since the gel layer is also nonlinear, at least three factors can contribute to β change during ASR damage process: the nonlinearity from gel layer β_{gel} as a function of gel thickness δ_{gel} , the nonlinearity due to internal stress β_{stress} as a function of interface pressure P_{int} , and the nonlinearity caused by microcracks β_{crk} as a function of crack density N_0^{crk} . Suppose the β change from these three factors is not substantial, as the first order approximation, β can be expressed as the linear superposition from these three terms as,

$$\beta = \beta_0 + \beta_{gel}(\delta_{gel}) + \beta_{stress}(P_{int}) + \beta_{crk}(N_0^{crk}) \quad (1.2)$$

where β_0 is the original material nonlinearity before cracking. The expressions of β_{gel} , β_{stress} and β_{crk} will be given next.

Nonlinearity β from the gel layer

Consider gel layer as a distinct layer, due to its aqueous behavior, there is no shear stress

generated inside this layer. However, since the gel layer is nonlinear, it can cause nonlinearity to the whole three phase unit, whose structure is shown in Fig. 6.12. Suppose this three phase unit is subjected to a tensile stress σ_0 at the outer boundary as shown in Fig. 6.12, by calculating the tensile strain generated by the tensile stress at the outer boundary, one can get the expression of β_{gel} .

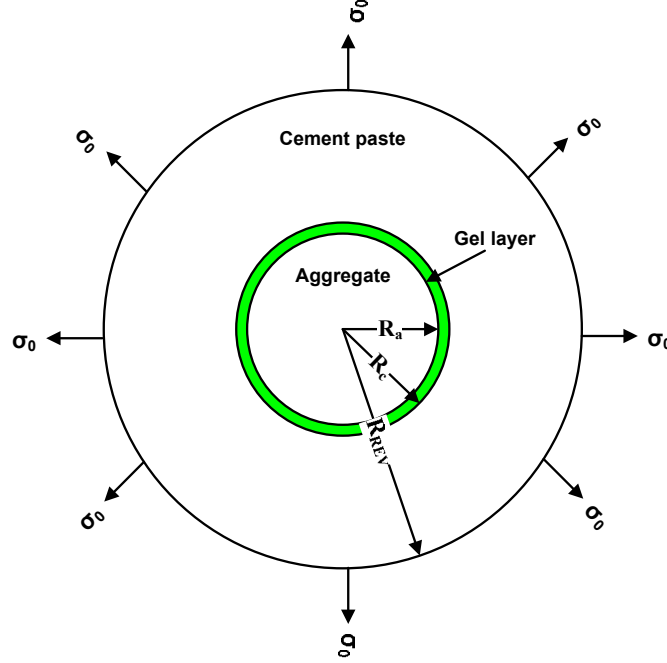


Fig. 6.12 Three-layer unit subjected to tensile loading at outer boundary

1). Following the similar procedure described in Section 6.4.1, one can firstly get the displacement and stress expression within each layer from the equilibrium equation $\sigma_{ij,j} = 0$ as,

In aggregate,

$$u_r^a = A_a \cdot r \quad \sigma_r^a = 3K_a A_a \quad (1.3)$$

In cement paste,

$$u_r^c = A_c \cdot r + B_c / r^2 \quad \sigma_r^c = 3K_c A_c - 4B_c G_c / r^3 \quad (1.4)$$

In gel,

$$u_r^g = f(r) \quad \sigma_r^g = P = a_1 e_g + a_2 e_g^2 \quad (1.5)$$

in which K_a is the bulk modulus in aggregate, while K_c , G_c are the bulk, shear modulus in cement paste respectively. P is the pressure in gel layer and e_g is the strain in gel layer. Since the gel layer is nonlinear, the stress and strain has nonlinear term in gel layer. The constant a_2 corresponds to the third order elastic constant of gel layer. The displacement in gel layer u_r^g is a function of radius r , thus the strain in gel layer is

$$e_g = e_{rr} + e_{\theta\theta} + e_{\varphi\varphi} = f'(r) + \frac{2}{r} f(r), \quad (1.6)$$

and the stress in gel layer should be

$$\sigma_{rr}^g = \sigma_{\theta\theta}^g = \sigma_{\varphi\varphi}^g = a_1 e_g + a_2 e_g^2 = a_1 \left(f' + \frac{2}{r} f \right) + a_2 \left(f' + \frac{2}{r} f \right)^2. \quad (1.7)$$

From the equilibrium equation one can get,

$$\frac{\partial \sigma_{rr}}{\partial r} + \frac{2\sigma_{rr} - \sigma_{\theta\theta} - \sigma_{\varphi\varphi}}{r} = 0 \quad (1.8)$$

Plugging Eq. (1.7) into Eq. (1.8), one can further get

$$\begin{aligned} a(f'' + 2(\frac{f'}{r})') + a_2 \cdot 2(f' + \frac{2}{r}f) \cdot (f'' + 2(\frac{f'}{r})') &= 0 \\ \Rightarrow (a + 2a_2 f' + \frac{4a_2}{r}f)(f'' + 2\frac{f'}{r} - 2\frac{f}{r^2}) &= 0 \end{aligned} \quad (1.9)$$

The solution of Eq. (1.9) yields $u_r^g = A_g \cdot r + B_g / r^2$. Then the strain in gel layer is

$e_g = \frac{\partial u_r^g}{\partial r} + 2\frac{u_r^g}{r} = 3A_g$. Plugging the strain in gel layer into Eq. (1.5), one can further get the pressure in gel layer,

$$P = 3a_1(A_g + 3\frac{a_2}{a_1}A_g^2) \quad (1.10)$$

2). The boundary conditions are listed as follows:

The stresses continuity at the boundary of aggregate $r = R_a$ and at the boundary of gel $r = R_c$,

$$\sigma_r^a(R_a) = \sigma_r^c(R_c) = P \quad (1.11)$$

The stress at the outer boundary R_{REV} equals to the loading stress,

$$\sigma_0 = \sigma_r^c(R_{REV}) \quad (1.12)$$

The displacements at R_a and R_c are equal,

$$u_r^a(R_a) = u_r^g(R_a) \quad u_r^g(R_c) = u_r^c(R_c) \quad (1.13)$$

Plugging Eqs. (1.3)-(1.5) and (1.10) into Eqs. (1.11)-(1.13), one can get a group of equations

$$\begin{cases} 3K_a A_a = 3K_c A_c - 4B_c G_c / R_c^3 = 3a A_g + 9ab A_g^2 \\ 3K_c A_c - 4B_c G_c / R_{REV}^3 = \sigma_0 \\ A_a \cdot R_a = A_g \cdot R_a + B_g / R_a^2 \\ A_g \cdot R_c + B_g / R_c^2 = A_c \cdot R_c + B_c / R_c^2 \end{cases} \quad (1.14)$$

From Eq. (1.14), one can eliminate A_g, B_g, A_c, B_c in function of A_a as

$$A_c = -\frac{K_a R_c^3}{(-R_c^3 + R_{REV}^3)K_c} A_a + \frac{1}{3} \frac{\sigma_0 R_{REV}^3}{(-R_c^3 + R_{REV}^3)K_c}, \quad (1.15)$$

$$B_c = -\frac{3}{4} \frac{K_a R_c^3 R_{REV}^3}{G_c (-R_c^3 + R_{REV}^3)} A_a + \frac{1}{4} \frac{R_c^3 \sigma_0 R_{REV}^3}{G_c (-R_c^3 + R_{REV}^3)}, \quad (1.16)$$

$$\begin{aligned} A_g = & \frac{1}{12} \frac{-12R_c^3 R_a^3 K_c G_c + 12R_c^6 G_c K_a + 9R_c^3 K_c R_{REV}^3 K_a + 12K_c G_c R_a^3 R_{REV}^3}{K_c G_c (R_c^6 - R_c^3 R_{REV}^3 - R_c^3 R_a^3 + R_a^3 R_{REV}^3)} A_a \\ & + \frac{1}{12} \frac{-3R_c^3 K_c R_{REV}^3 \sigma_0 - 4R_c^3 \sigma_0 G_c R_{REV}^3}{K_c G_c (R_c^6 - R_c^3 R_{REV}^3 - R_c^3 R_a^3 + R_a^3 R_{REV}^3)}, \end{aligned} \quad (1.17)$$

$$\begin{aligned} B_g = & -\frac{1}{12} \frac{R_c^3 R_a^3 (12R_c^3 K_c G_c - 12R_c^3 G_c K_a - 9K_c R_{REV}^3 K_a - 12K_c G_c R_{REV}^3)}{K_c G_c (R_c^6 - R_c^3 R_{REV}^3 - R_c^3 R_a^3 + R_a^3 R_{REV}^3)} A_a \\ & - \frac{1}{12} \frac{R_c^3 R_a^3 (3K_c R_{REV}^3 \sigma_0 + 4\sigma_0 G_c R_{REV}^3)}{K_c G_c (R_c^6 - R_c^3 R_{REV}^3 - R_c^3 R_a^3 + R_a^3 R_{REV}^3)}, \end{aligned} \quad (1.18)$$

Note that A_a is dimensionless. We can further simplify this problem by two assumptions,

a) $R_a = R_c - d$ with d to be the thickness of gel layer. One can further get $R_a = R_c - R_c \cdot \delta_{gel}$

with the gel thickness ratio $\delta_{gel} = d / R_c \ll 1$.

b) $P = a_1(e_g + be_g^2)$ with $a_2 = a_1b$ the third order elastic constant. b is the ratio of third order over the second order elastic constant of gel.

Note that δ_{gel} and b are both dimensionless.

3). The solution of A_a :

Based on the simplifications, one can obtain a quadratic equation regarding to A_a from Eq. (1.14),

$$W_1 A_a^2 + (W_2 + W_3 \sigma_0) A_a + (W_4 \sigma_0 + W_5 \sigma_0^2) = 0 \quad (1.19)$$

In which W_1 to W_5 are all the combination of modulus and radius in aggregate, cement paste and gel. Eq. (1.19) has the solution

$$\begin{aligned} A_a &= \frac{-W_2 - W_3 \sigma_0 \pm \sqrt{(W_2 + W_3 \sigma_0)^2 - 4W_1(W_4 \sigma_0 + W_5 \sigma_0^2)}}{2W_1} \\ &= -\frac{W_2}{2W_1} - \frac{W_3 \sigma_0}{2W_1} \pm \frac{1}{2W_1} \sqrt{(W_3^2 - 4W_1 W_5) \sigma_0^2 + (2W_2 W_3 - 4W_1 W_4) \sigma_0 + W_2^2} \end{aligned} \quad (1.20)$$

This solution can be simplified by assuming $Y_1 = W_2^2$, $Y_2 = 2W_2 W_3 - 4W_1 W_4$ and $Y_3 = W_3^2 - 4W_1 W_5$. Since the applied load σ_0 is due to ultrasonic wave vibration, it is very small. One can then expand the square root of σ_0 and get

$$\begin{aligned} &\sqrt{Y_3 \sigma_0^2 + Y_2 \sigma_0 + Y_1} \\ &\approx \sqrt{Y_1} + \frac{1}{2} \frac{Y_2}{\sqrt{Y_1}} \sigma_0 + \sqrt{Y_1} \left(\frac{1}{2} \frac{Y_3}{Y_1} - \frac{1}{8} \frac{Y_2^2}{Y_1^2} \right) \sigma_0^2 + \sqrt{Y_1} \left(-\frac{1}{4} \frac{Y_2 Y_3}{Y_1^2} + \frac{1}{16} \frac{Y_2^3}{Y_1^3} \right) \sigma_0^3 \end{aligned} \quad (1.21)$$

Substitute Eq. (1.21) into Eq.(1.20),

$$\begin{aligned} A_a &= -\frac{W_2}{2W_1} - \frac{W_3 \sigma_0}{2W_1} \\ &\pm \frac{1}{2W_1} \left[W_2 + \frac{1}{2} \frac{2W_2 W_3 - 4W_1 W_4}{W_2} \sigma_0 + \sqrt{Y_1} \left(\frac{1}{2} \frac{Y_3}{Y_1} - \frac{1}{8} \frac{Y_2^2}{Y_1^2} \right) \sigma_0^2 + \sqrt{Y_1} \left(-\frac{1}{4} \frac{Y_2 Y_3}{Y_1^2} + \frac{1}{16} \frac{Y_2^3}{Y_1^3} \right) \sigma_0^3 \right] \end{aligned} \quad (1.22)$$

To make the solution simpler, choose '+' in Eq. (1.22) and one can get

$$A_a = \frac{-W_4}{W_2} \sigma_0 + \frac{1}{2W_1} \left[\sqrt{Y_1} \left(\frac{1}{2} \frac{Y_3}{Y_1} - \frac{1}{8} \frac{Y_2^2}{Y_1^2} \right) \sigma_0^2 + \sqrt{Y_1} \left(-\frac{1}{4} \frac{Y_2 Y_3}{Y_1^2} + \frac{1}{16} \frac{Y_2^3}{Y_1^3} \right) \sigma_0^3 \right] \quad (1.23)$$

4). Calculate β :

From Eq.(1.4), one can get the strain on the outer boundary as

$$\begin{aligned} \varepsilon(R_{REV}) &= \frac{\partial u_r^c}{\partial r} = A_c - 2 \frac{B_c}{R_{REV}^3} \\ &= \frac{1}{R_{REV}^3 - R_c^3} \left[\left(\frac{3K_a}{2G_c} - \frac{K_a}{K_c} \right) R_c^3 A_a + \frac{R_{REV}^3 \sigma_0}{3K_c} - \frac{R_c^3 \sigma_0}{2G_c} \right] \end{aligned} \quad (1.24)$$

Substitute Eq. (1.23) into Eq. (1.24), one can get

$$\begin{aligned} \varepsilon(R_{REV}) &= \frac{1}{R_{REV}^3 - R_c^3} \left\{ \left[\frac{-W_4}{W_2} \left(\frac{3K_a}{2G_c} - \frac{K_a}{K_c} \right) R_c^3 + \frac{R_{REV}^3}{3K_c} - \frac{R_c^3}{2G_c} \right] \sigma_0 \right. \\ &\quad \left. + \frac{\sqrt{Y_1}}{2W_1} \left(\frac{1}{2} \frac{Y_3}{Y_1} - \frac{1}{8} \frac{Y_2^2}{Y_1^2} \right) \left(\frac{3K_a}{2G_c} - \frac{K_a}{K_c} \right) R_c^3 \sigma_0^2 + \frac{\sqrt{Y_1}}{2W_1} \left(-\frac{1}{4} \frac{Y_2 Y_3}{Y_1^2} + \frac{1}{16} \frac{Y_2^3}{Y_1^3} \right) \left(\frac{3K_a}{2G_c} - \frac{K_a}{K_c} \right) R_c^3 \sigma_0^3 \right\} \end{aligned} \quad (1.25)$$

According to Cantrell's derivation[11],

$$\begin{aligned} \sigma &= \sigma_1 + \left(\frac{\partial \sigma}{\partial \bar{\varepsilon}} \right)_x (\bar{\varepsilon} - \bar{\varepsilon}_1) + \frac{1}{2} \left(\frac{\partial^2 \sigma}{\partial \bar{\varepsilon}^2} \right)_x (\bar{\varepsilon} - \bar{\varepsilon}_1)^2 + \dots \\ &= \sigma_1 + \left(\frac{\partial \bar{\varepsilon}}{\partial \sigma} \right)_x^{-1} (\bar{\varepsilon} - \bar{\varepsilon}_1) - \frac{1}{2} \left[\left(\frac{\partial^2 \bar{\varepsilon}}{\partial \sigma^2} \right)_x \left(\frac{\partial \bar{\varepsilon}}{\partial \sigma} \right)_x^{-3} \right] (\bar{\varepsilon} - \bar{\varepsilon}_1)^2 + \dots \\ &= \sigma_1 + P(\bar{\varepsilon} - \bar{\varepsilon}_1) + \frac{1}{2} Q(\bar{\varepsilon} - \bar{\varepsilon}_1)^2 + \dots \end{aligned} \quad (1.26)$$

with σ_1 the initial stress that gives rise to an initial strain $\bar{\varepsilon}_1$. The nonlinearity parameter can

be obtained from Eq. (1.26) as $\beta = -\frac{Q}{P}$. Compared to Eq. (1.26), one can obtain β from Eq.

(1.25) as

$$\begin{aligned} \beta_{gel} &= \frac{R_{REV}^3 - R_c^3}{R_c^3} \frac{2G_c K_c}{K_a (3K_c - 2G_c)} \left[\frac{W_2}{W_1} \left(\frac{1}{2} \frac{Y_3}{Y_1} - \frac{1}{8} \frac{Y_2^2}{Y_1^2} \right) + \frac{3W_2}{W_1} \left(-\frac{1}{4} \frac{Y_2 Y_3}{Y_1^2} + \frac{1}{16} \frac{Y_2^3}{Y_1^3} \right) \sigma_0 \right] \\ &\quad \left[\frac{-W_4}{W_2} + \frac{2G_c R_{REV}^3 / R_c^3 - 3K_c}{3K_a (3K_c - 2G_c)} \right]^{-2} \end{aligned} \quad (1.27)$$

Sine the ratio of gel thickness over the radius of aggregates δ_{gel} is very small, one can further expand β with δ_{gel} at $\delta_{gel} = 0$ and keep the first order of δ_{gel} . One can finally get,

$$\beta_{gel} \approx -S_1 + S_2 \cdot |\sigma_0| \quad (1.28)$$

$$\text{with } S_1 = \frac{36\delta_g b(-3K_c + 2G_c)V_1(4G_c + 3K_c)^2 K_a^3}{a_1^2[4K_a G_c V_1 + 3K_a K_c + 4K_c G_c(1 - V_1)](3K_a - 6K_c V_1 + 4G_c + 6K_a V_1)^2} \quad (1.29)$$

$$\text{and } S_2 = \frac{-216\delta_g b^2(-3K_c + 2G_c)V_1(4G_c + 3K_c)^3 K_a^4}{a_1^3[4K_a G_c V_1 + 3K_a K_c + 4K_c G_c(1 - V_1)]^2(3K_a - 6K_c V_1 + 4G_c + 6K_a V_1)^2} \quad (1.30)$$

in which $V_1 = \frac{R_c^3}{R_{REV}^3}$ is the volume ratio of aggregate. From Eq. (1.29) and (1.30) one can tell

that the only parameter that varies with exposure time is the gel thickness ratio, δ_g , and other parameters are all constants. Unfortunately due to lack of the information in gel modulus, one cannot decide a_1 and b in these equations. If we choose a_1 equals to water's modulus 2.25 GPa, and nonlinearity ratio in gel layer $b=5$, one can get an estimated nonlinearity $\beta_{gel} \approx 2.67 \times 10^2 \delta_{gel} - 4.2 \times 10^{-6} \delta_{gel} |\sigma_0|$. So if the gel thickness ratio is 10%, the absolute nonlinearity change is around 26.7 considering σ_0 is very small and S_2 is negligible.

REFERENCES

1. Tang, G., L.J. Jacobs, and J. Qu, *Scattering of time-harmonic elastic waves by an elastic inclusion with quadratic nonlinearity*. Journal of the Acoustical Society of America, 2012. **131**(4): p. 2570-2578.
2. Nagy, P.B., *Fatigue damage assessment by nonlinear ultrasonic materials characterization*. Ultrasonics, 1998. **36**(1-5): p. 375-381.
3. Cantrell, J.H. and W.T. Yost, *Nonlinear ultrasonic characterization of fatigue microstructures*. International Journal of Fatigue, 2001. **23**: p. S487-S490.
4. Pruell, C., et al., *Evaluation of plasticity driven material damage using Lamb waves*. Applied Physics Letters, 2007. **91**: p. 231911.
5. Bermes, C., et al., *Nonlinear Lamb waves for the detection of material nonlinearity*. Mechanical Systems and Signal Processing, 2008. **22**(3): p. 638-646.
6. Muller, M.F., et al., *Characteristics of second harmonic generation of Lamb waves in nonlinear elastic plates*. Journal of the Acoustical Society of America, 2010. **127**(4): p. 2141-2152.

7. Liu, M., et al., *Experimental study of nonlinear Rayleigh wave propagation in shot-peened aluminum plates-Feasibility of measuring residual stress*. Ndt & E International, 2011. **44**(1): p. 67-74.
8. Matlack, K.H., et al., *Experimental characterization of efficient second harmonic generation of Lamb wave modes in a nonlinear elastic isotropic plate*. Journal of Applied Physics, 2011. **109**(1).
9. Liu, M., et al., *A nonlinear wave mixing method for detecting Alkali-Silica reactivity of aggregates*. Review of Progress in Quantitative Nondestructive Evaluation, 2012. **1430**(1524-1531).
10. Cantrell, J.H., *Substructural organization, dislocation plasticity and harmonic generation in cyclically stressed wavy slip metals*. Proceedings of the Royal Society of London Series a-Mathematical Physical and Engineering Sciences, 2004. **460**(2043): p. 757-780.
11. Cantrell, J.H., *Fundamentals and Applications of Nonlinear Ultrasonic Nondestructive Evaluation*, in *ULTRASONIC NONDESTRUCTIVE EVALUATION - Engineering and Biological Material Characterization*, T. Kundu, Editor. 2004, CRC Press LLC.

III.1.7 Physics-Based Models for ASR Damage Evolution

The LDPM model was improved by adding the alkali ion diffusion to it. In this regard, two important modifications were formulated as follows,

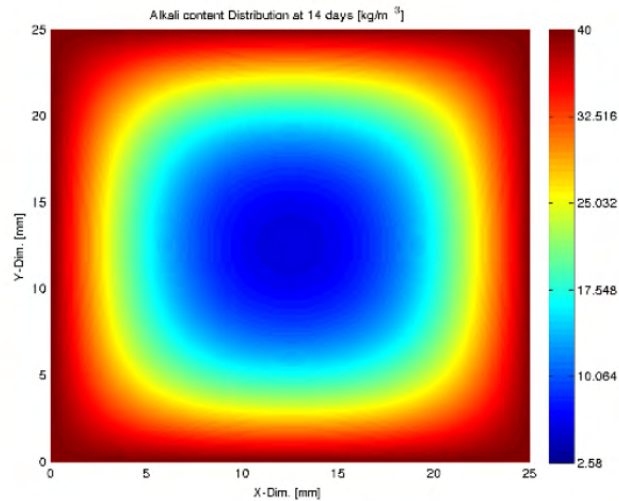
Solution of diffusion problem

Here, two assumptions were made: 1) The diffusion process can be assumed as a 2D diffusion as sample cross section dimensions are much smaller than its length, 2) Constant diffusion coefficient is used as the self dissication of concrete effect on internal relative humidity was neglected, this is because specimens already have high water to cement ratio (0.5) and they are immersed in water for the whole curing and test period. Based on that, an implicit integration method (The alternating Directions implicit) with Crank Nicolson scheme was implemented to solve the 2D diffusion problem. This method discretizes the solution as follows

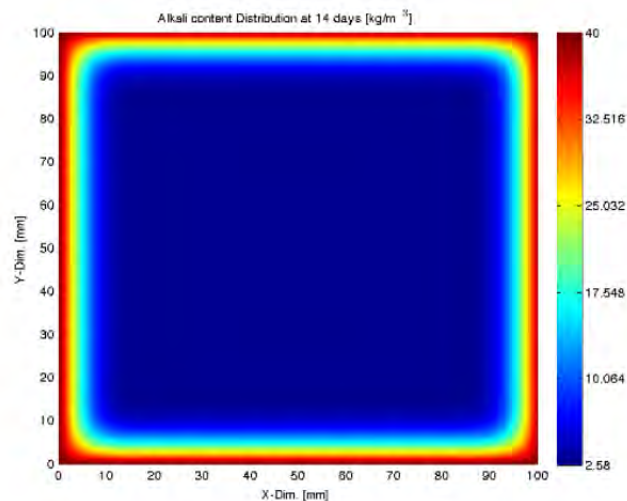
$$D^+U_t = \frac{C}{2} (D_0U_{xx}^{n+1} + D_0U_{xx}^n + D_0U_{yy}^{n+1} + D_0U_{yy}^n)$$

where U_t , U_{xx} and U_{yy} are the first time derivative, second spatial derivative in x and second spatial derivative in y, respectively. D^+ is the forward Euler operator and D_0 is the central difference operator, C is the constant diffusivity parameter.

In addition, the ASR-LDPM model deals with the concentration of ions as an overall alkali content in kg/m^3 of concrete, while the diffusion process is in terms of moles/Litre. So, after solving for the concentration, it is converted into alkali content. The final alkali content distributions for small and large samples of 1”X1” and 4”X4” after 14 days have the following profiles



Small Sample



Large Sample

Consideration of variable alkali content on ASR-LDPM formulation

The ASR-LDPM model was formulated for fully saturated conditions with uniform alkali content over the concrete volume. This is the condition of mostly all real structures in which, the source of alkali is the initial alkali content of the concrete mix and water just helps transferring it into the aggregates, so the alkali ions only undergo micro diffusion. This is also the same case for long term concrete prisms and cylinders experiments, as the alkali content is increased by adding alkali to the mixing water, then after curing, the specimens are either sealed or kept in

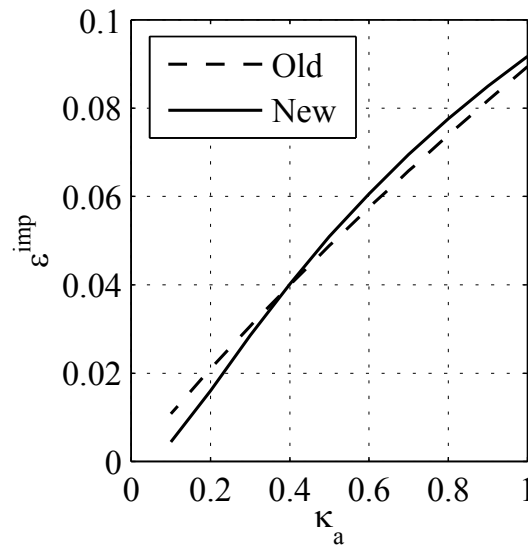
various humidity conditions. For the special case of accelerated mortar bar test, the source of alkali becomes the water in which the bar is immersed after curing. In this case, alkali undergoes both macro and micro diffusion to reach the aggregate. For this case, the reaction front evolution with time is delayed due to the alkali macro diffusion process. In ASR-LDPM, the alkali content effect is introduced through κ_a as a reduction factor of the formulated gel mass. To extend its effect to the reaction front evolution, the cubic root of κ_a is moved to the reaction front rate. The initial ASR-LDPM gel mass equation is modified as,

$$\begin{aligned}
 M_g &= K_i^0 \left(1 - \left(\frac{2z}{D} \right)^3 \right) D^3 \kappa_a \exp \left(\frac{E_{ai}}{RT_0} - \frac{E_{ai}}{RT} \right) \\
 &= K_i^0 \left(\kappa_a - \left(\frac{2z \sqrt[3]{\kappa_a}}{D} \right)^3 \right) D^3 \exp \left(\frac{E_{ai}}{RT_0} - \frac{E_{ai}}{RT} \right) \\
 &= K_i^0 \left(\kappa_a - \left(\frac{2z \kappa}{D} \right)^3 \right) D^3 \exp \left(\frac{E_{ai}}{RT_0} - \frac{E_{ai}}{RT} \right)
 \end{aligned}$$

Where the reaction front speed can be approximately given by,

$$\dot{z}_\kappa = - \frac{a_s(T) w_s}{r_w C_s z_\kappa \left(1 - \frac{2z_\kappa}{D} \right)} \sqrt[3]{\kappa_a}$$

For a wide range of different constant alkali contents both old and new formulations give very close results as shown below.



References

- [1] M. Alnaggar, G. Cusatis, and G. Di Luzio, “Lattice Discrete Particle Modeling (LDPM) of Alkali Silica Reaction (ASR) Deterioration of Concrete Structures”, *Cement and Concrete Composites*, (Accepted).
- [2] G. Cusatis, D. Pelessone, and A. Mencarelli, Lattice Discrete Particle Model (LDPM) for Concrete failure Behavior of Concrete. I: Theory, *Cement and Concrete Composites*, 33(9):881–890, 2011.
- [3] G. Cusatis, A. Mencarelli, D. Pelessone, and J. Baylot, Lattice Discrete Particle Model (LDPM) for Failure Behavior of Concrete. II: Calibration and Validation, *Cement and Concrete Composites*, 33(9):891–905, 2011.

III.1.8 Nonlinear Wave Mixing Technique to Measure the ANLP in Concrete Samples Nondestructively in a Laboratory Environment

Nonlinear Mixing Wave Theory

One-dimensional longitudinal wave motion in a nonlinear solid is governed by the equation below

$$\frac{1}{c^2} \frac{\partial^2 u}{\partial t^2} - \frac{\partial^2 u}{\partial x^2} = \frac{\partial}{\partial x} \left(\frac{\beta}{2} \left(\frac{\partial u}{\partial x} \right)^2 \right) , \quad (1.31)$$

where c is the longitudinal wave velocity, u is the displacement, and β is the acoustic nonlinearity parameter. Since the nonlinearity parameter β is related to material damage, it should change with the ASR damage in cement-based materials. To measure the β change, we use the co-linear mixing wave method.

Suppose an ultrasonic wave consists of two frequencies ω_1 and ω_2 as,

$$u_1 = U \cos \left[\omega_1 \left(t - \frac{x}{c} \right) \right] + V \cos \left[\omega_2 \left(t - \frac{x}{c} \right) \right] , \quad (1.32)$$

where U and V are, respectively, the displacement amplitude of these two frequency components. As the wave propagates through the test sample, ASR damage in the sample causes these two frequency components to interact, resulting in a mixed wave field whose amplitude is proportional to β ,

$$\begin{aligned} u_2 = & -\frac{UV\beta\omega_1\omega_2}{4c^2} x \cos \left[(\omega_1 - \omega_2) \left(t - \frac{x}{c} \right) \right] + \frac{UV\beta\omega_1\omega_2}{4c^2} x \cos \left[(\omega_1 + \omega_2) \left(t - \frac{x}{c} \right) \right] \\ & + \frac{U^2\beta\omega_1^2}{8c^2} x \cos \left[(2\omega_1) \left(t - \frac{x}{c} \right) \right] + \frac{V^2\beta\omega_2^2}{8c^2} x \cos \left[(2\omega_2) \left(t - \frac{x}{c} \right) \right] \end{aligned} \quad (1.33)$$

In this work, we will focus on the first term in the high-hand side of (3), i.e.,

$$u_{2d} = -\frac{UV\beta\omega_1\omega_2}{4c^2} x \cos \left[(\omega_1 - \omega_2) \left(t - \frac{x}{c} \right) \right] . \quad (1.34)$$

By measuring the amplitude $\|u_{2d}\|$, one can obtain the acoustic nonlinearity parameter

$$\beta \propto \frac{\|u_{2d}\|}{UV} . \quad (1.35)$$

This way of measuring the acoustic nonlinear parameter β is called the nonlinear wave mixing (NWM) method.

Experimental Methods

Sample preparation:

Mortar bar samples were prepared using the procedure described by AASHTO T 303 [1].

The fine aggregates used are the Placitas 67 Blend from Lafarge Company. The cement used is the type I cement (potential Bogue composition 46.11% C_3S , 22.93% C_2S , 8.52% C_3A and 9.59% C_4AF and 0.83% Na_2O_{eq}).

Three thicker $285 \times 100 \times 100$ mm ($11\frac{1}{4} \times 4 \times 4$ in), and six thinner $285 \times 25 \times 25$ mm ($11\frac{1}{4} \times 1 \times 1$ in) mortar bars were casted. These samples are named, respectively, L1, L2 and L3 for the thicker ones, and S1 – S6 for the thinner ones. To cure the samples, molds with the concrete mix in them were placed in a chamber with 100% relative humidity at 23 °C (73.4 °F) for 24 hours. After demolding, the samples were immersed in tap water and placed in an oven at 80 °C (176 °F) for another 24 hours. The first set of expansion and nonlinear ultrasonic measurement were then taken on these as cured samples to obtain the initial values. These values were used as the baseline to normalize the subsequent measurements. To induce ASR damage, the thinner samples S1, S2 and S3 and the thicker samples L1 and L3 were immersed in a 1N NaOH solution at 80°C (176 °F), per the procedures described in AASTHO T 303 [1]. These samples were taken out of the solution at regular intervals for expansion and nonlinear ultrasonic measurements. The rest of the samples were left in an ambient room environment with 50%RH and 23°C.

Measurements

A schematic of the collinear beam-mixing measurement setup is shown in Fig. 1.1. Two incident waves of different frequencies are generated simultaneously by the function generator. One has a frequency of ω_1 (0.75MHz) with 18 cycles and the other has frequency of ω_2 (1.25MHz) with 30 cycles, so both waves have the same duration. After amplification, these signals are sent into a high pass filter with a cut off frequency of 0.7 MHz to remove low (< 0.7 MHz) frequency components in the incident waves, which might be generated by the amplifier.. An example of the frequency spectrum of the electrical signal sent to the transmitter is given in Fig. 2. Clearly, the signal has negligible frequency component below 0.6MHz.

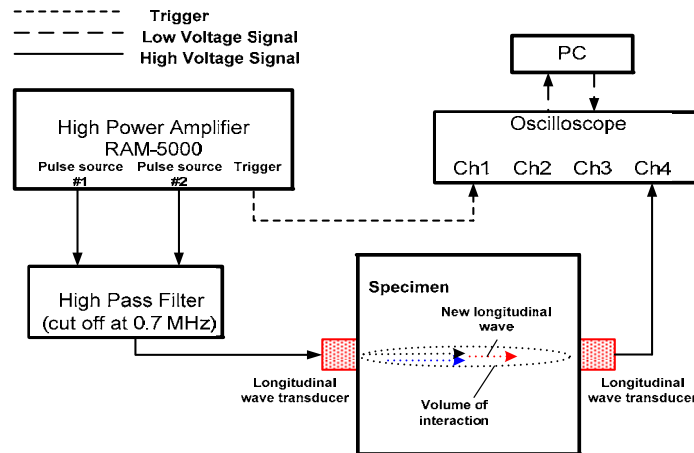


Fig. 1.1 Experimental setup

The filtered signals are then sent to the broadband PZT transducer with the central frequency of 1MHz attached to one side of the sample. The two incident waves propagate through the material and a new longitudinal wave at their difference frequency ($\omega_1 - \omega_2 = 0.5$ MHz) is

generated along the wave propagation distance. Since the two incident waves propagate in a ‘phase matching’ fashion, the newly generated wave is a resonance wave, i.e., its amplitude increases with propagation distance. This resonance wave is received by another longitudinal wave receiver attached to the other end of the bar. The receiver has a center frequency of 0.5MHz and is recorded by a Tektronix TDS 5034B oscilloscope. After that, the digitized time-domain signal is sent to a PC for post signal processing. During the ultrasonic measurement, a high-vacuum grease was used as a couplant between the transducer and the sample. A force sensor is used to ensure that the transducers were clamped to the sample with the same pressure for all tests. After each measurement, the sample was cleaned with soap and tap water to remove any residual couplant. Ultrasonic measurements are taken on three different locations in the thicker samples L1, L2 and L3 as shown in Fig. 1.3.

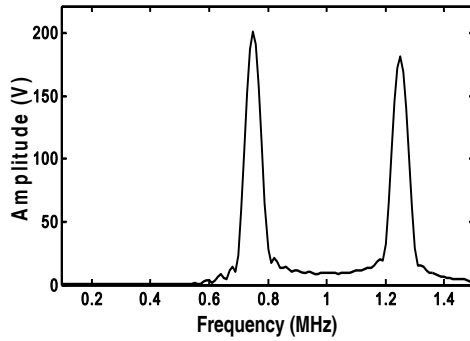


Fig. 1.2. FFT of filtered signal

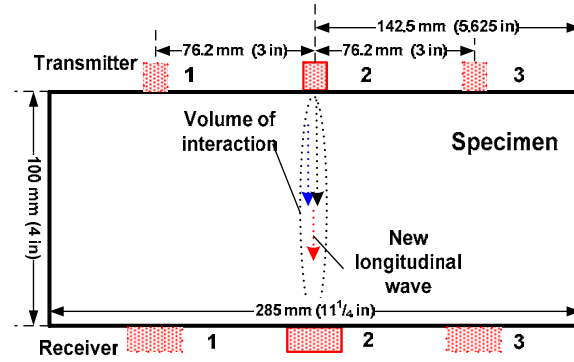


Fig. 1.3. Locations of ultrasonic measurement on L1-L3

The PZT transducer converts the electrical signal into a propagating ultrasonic wave field in the mortar bar. This wave field consists of two frequency components as indicated in Eq. (2) and shown in Fig. 1.2. As the waves propagate, they interact with the ASR damage in the sample. This interaction generates the mixed wave fields that consists of several different frequency components. One of these frequency components is $(\omega_1 - \omega_2)$ at 0.5MHz. The amplitude of this frequency component $\|u_{2d}\|$ can be obtained by performing a Fourier transform of the received signal. Once $\|u_{2d}\|$ is measured, the ultrasonic nonlinear parameter β can be calculated from Eq.(5), since U and V are known input.

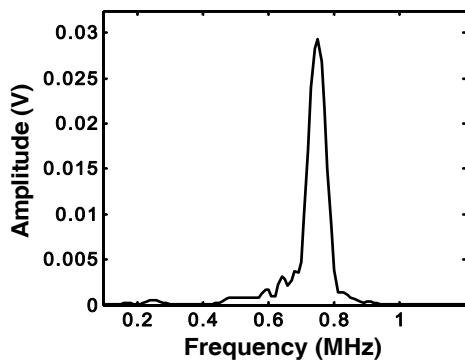


Fig. 1.4a. FFT of received signal on day 0

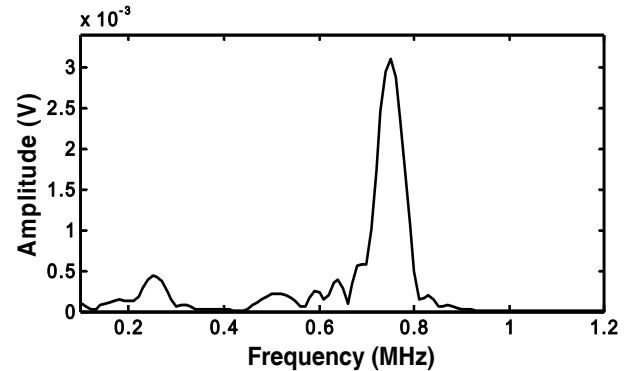


Fig. 1.4b. FFT of received signal on day 10

Subsequent ultrasonic measurements were conducted at about the same time each day during the

immersion. As an example, the frequency spectra of the received signals for day 0 and day 10 in L1 sample are shown in Figs. 1.4a and 1.4b, respectively. It is seen that (i) the amplitude ratio of resonance wave at 0.5MHz over one of the principal beam at 0.75MHz increases over time, a sign of increased acoustic nonlinearity parameter β ; and (ii) the amplitude corresponding to 0.75MHz decreases over time, a sign of increased attenuation. Such increase in attenuation is frequency dependent, and can be accounted for by measuring the decay in the fundamental waves over time.

Results and Discussion

Expansion Measurement and Results

The immersed samples were taken out each day for the expansion measurements per the procedures described in AASHTO T 303 [1]. Results of the expansion per unit length for all samples are plotted in Figs. 1.5a and 1.5b as functions of the number of days under the exposure of alkali solution.

It is seen that samples immersed in the alkali solution all expanded. According to ASTM1260, if the expansion of thinner samples is more than 0.2% after 14 days immersed in alkali solution, it is considered potentially deleterious expansion [2]. Based on this criterion, our expansion measurement data show that the aggregate used in our test, the Placitas 67 Blend from the Lafarge Co. in New Mexico, is considered fairly alkali-silica reactive. It is also seen that the samples kept in the room environment did not expand at all. If any, there seems to be some shrinkage, possibly due to the experimental errors.

Comparison between Figs. 1.5a and 1.5b shows that the thinner samples have much large expansion than the thicker samples under the same exposure time. A plausible explanation of this difference is that the ASR damage across the bar's thickness is nonuniform. The damage is more severe near the sample surface and gradually decreases toward the center of the samples. Such non-uniformity is controlled by the rate of diffusion of water into the concrete. The diffusion rate-controlled process means that the center region of the thicker samples may not have been damaged yet during 14 days of exposure. In other words, after 14 days of exposure, the thicker samples may still contain a core of un-damaged concrete, which limits the axial expansion of the bar.

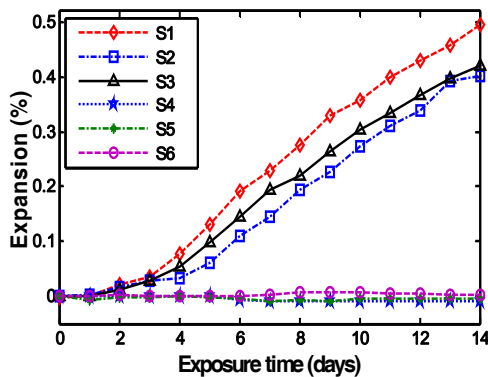


Fig. 1.5a. Expansion of thinner samples

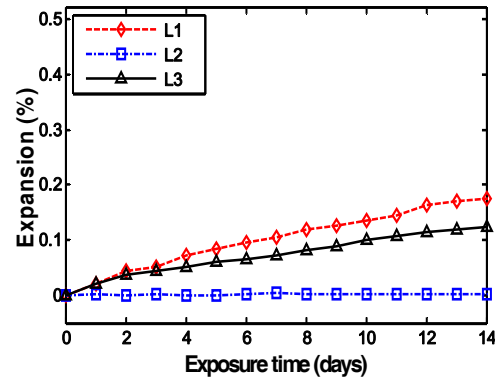


Fig. 1.5b. Expansion of thicker samples

Ultrasonic Measurement Results

After each expansion measurement, ultrasonic tests were also conducted on each sample using the NWM method. As indicated in Fig. 3, the ultrasonic tests were conducted at three locations on each sample. It follows from Eq.(5) that the normalized acoustic nonlinearity is given by

$$\bar{\beta} = \frac{\beta}{\beta_0} = \frac{\|u_{2d}\|}{\|u_{2d}\|_0}, \quad (1.36)$$

where the quantities with subscript 0 are those measured before the samples were immersed in the alkaline solution (day 0). After accounting for the attenuation, the measured acoustic nonlinearity parameter $\bar{\beta}$ normalized by the day 0 value as defined in Eq.(6) is plotted in Fig. 1.6a for all three thicker samples. We note again that these values are the averages of measurements from all three locations on each sample. To show the scattering of the data, Fig. 1.7 is plotted with error bars. Since ultrasonic measurements were conducted by taking the transducers off at one location, and putting them back on at a different location, these error bars can also be considered the upper limit of the uncertainties associated with the measurements.

It is seen clearly from these plots that (1) the NWM method yields consistent and repeatable results, (2) the acoustic nonlinearity parameter increases with exposure time, and (3) the acoustic nonlinearity parameter is much more sensitive to ASR damage than the volumetric expansion.

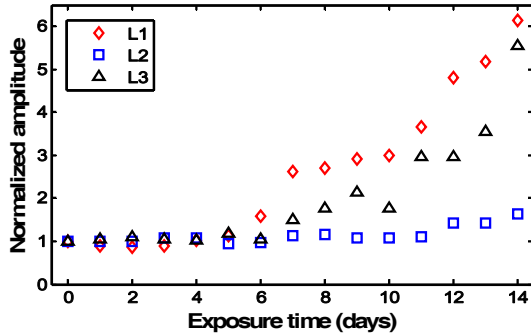


Fig. 1.6a. $\bar{\beta}$ averaged over 3 locations in thicker samples

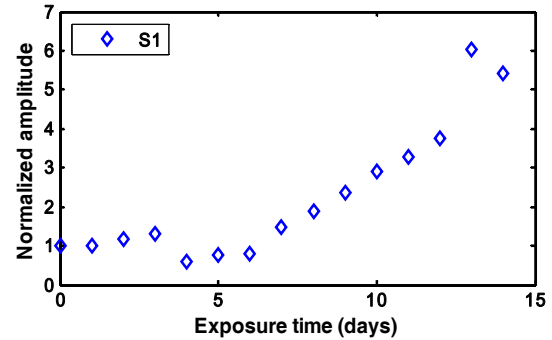


Fig. 1.6b. $\bar{\beta}$ in thinner sample S1

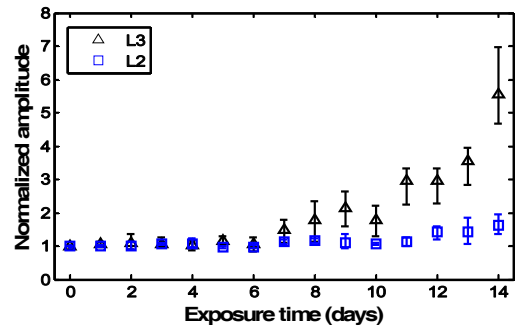
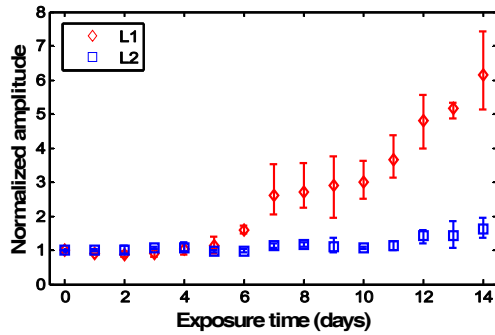


Fig. 1.7. Error bars showing the variation of $\bar{\beta}$ for samples L1 and L2, L2 and L3.

We note that results from both the ultrasonic and the expansion measurements seem to indicate that sample L1 has more ASR damage than sample L3, although both samples were made of the same materials, and were subjected to the same exposure condition. However, since these two samples were from two different batches of concrete mix, we speculate that the amount of aggregate in these two samples may not be exactly the same.

Recall that the expansion results show that the thinner samples have much larger expansion than the thicker ones. The reason for such difference was explained on the basis of non-uniform ASR damage across the thickness of the sample. It was argued that ASR damage is controlled by the moisture diffusion so that even after 14 days of exposure, the moisture still has not progressed all the way through the thickness of the thicker samples yet, i.e., there is still a core of undamaged concrete in the thicker samples. This argument is further corroborated by the ultrasonic measurement results. Shown in Fig. 1.6b is the measured acoustic nonlinearity parameter β of the thinner sample S1. Comparison of Figs. 1.6a and 1.6b shows that, although the expansion is very different between the thinner and thicker samples, the measured acoustic nonlinear parameter β is almost the same. The reason for this is clear if we assume that in the thicker sample, there is a core of concrete that has not been reached by the moisture, therefore, has no ASR damage, and the thickness of the ASR damaged outer shell is about one half of the total thickness of the thinner sample. Since the increase of normalized β ($\bar{\beta}$) is only related to the region where ASR damage occurs, the measured acoustic nonlinearity parameter β has similar amount of increase in thicker samples and thinner sample after 14 days exposure to alkali solution.

Conclusions

The results clearly demonstrated the feasibility of using nonlinear ultrasonic techniques to track the progress of ASR damage in cement-based materials. This is significant in that nonlinear ultrasonic techniques have a number of unique advantages over the existing methods of characterizing ASR damage.

First of all, compared to the linear relationship between the expansion and exposure time, the acoustic nonlinearity parameter shows a stepped relationship with respect to exposure time as shown in Fig. 6a. Although more research is needed to understand the significance of these “steps”, it is plausible that such “steps” might be related to the different ASR damage modes. Secondly, as discussed before, the expansion of the concrete bar depends on the thickness of the sample. This means that the expansion-based methods, such as AMBT, the CPT, and ACPT, are not measuring the intrinsic characteristics of the ASR damage. On the other hand, nonlinear ultrasonic methods, such as the NWM method used here, measure the acoustic nonlinearity parameter which is a signature intrinsic to the state of ASR damage. Therefore, measurements from the NWM method are independent of the sample size as shown by our results. Last but not the least, unlike other existing nonlinear ultrasonic methods, the NWM method could detect the ASR damage at arbitrary locations. This could lead to ASR damage scan in the future.

The abilities of the nonlinear ultrasonic methods to provide the spatial variation, identify the different stages of ASR damage and to track the intrinsic characteristics of the ASR damage make such methods potentially useful tools for rapid screening of aggregates for ASR reactivity in the lab, and for field assessments of ASR damage in existing concrete structures.

III.1.9 Physics-based Models that Correlate the ANLP to ASR Damage

Configuration of the Microstructure

The reactive aggregate and the representative volume element (RVE) of concrete surrounding the reactive aggregate are assumed to be spherical [3]. The basic element of the microstructure in Fig. 2.1 is then a composite sphere composed of two different phases in which the ratio of radii R_a/R_{REV}^a is a constant. Thus the basic element is independent of the absolute size of the spheres.

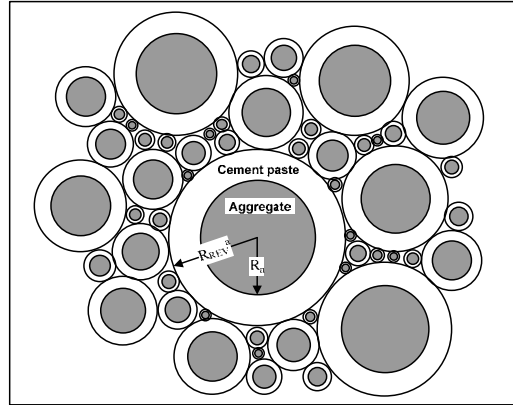


Fig. 2.1. Definition of the Relative Elementary Volume for different reactive aggregate sizes

Mathematical Model for Diffusion of Alkali Ions

To compare with our former experiment [4], two kinds of mortar samples with the dimension of $25 \times 25 \times 285 \text{ mm}$ ($1 \times 1 \times 11 \frac{1}{4} \text{ in}$) and $100 \times 100 \times 285 \text{ mm}$ ($4 \times 4 \times 11 \frac{1}{4} \text{ in}$) respectively are considered in our numerical simulations. Alkali ions penetrating from the specimen boundary into the concrete is considered as macro-diffusion process. Symmetry of mortar bars leads to two-dimensional diffusion problem governed by the 2D Fickian Equation [5],

$$\left(\frac{\partial C}{\partial t}\right)_{x,y,t} = D_{xy} \cdot (\partial^2 C / \partial x^2 + \partial^2 C / \partial y^2) \quad (1.37)$$

where C is the alkali ion concentration, and D_{xy} is the diffusivity of alkali ions at 80°C [2].

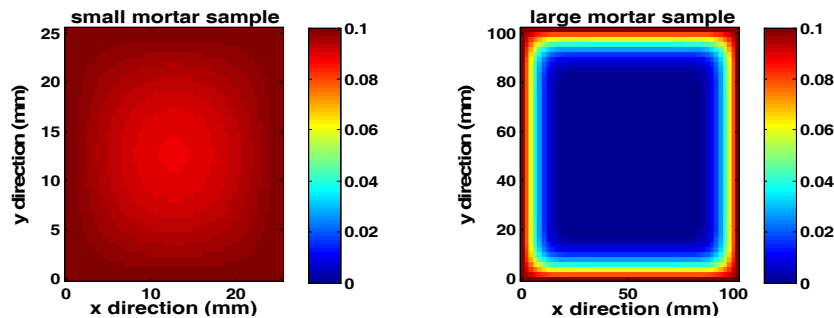


Fig. 2.2. Ion diffusion in small and large mortar samples after 14 days

Suppose the alkali ions penetrate with moisture, then D_{xy} can be determined by experimental measurements as described by Shen [5]. From Eq.(1), one can obtain the ion concentration $C(x, y, t)$. As a result, after 14 days, the alkali ions has penetrated thoroughly in small mortar

sample, while there is still a very large core in large mortar sample that the ion has not penetrated in as shown in Fig. 2.2. Note that the alkali ion concentration at the boundary of mortar sample is $C_0=0.1$ mol/liter of solution [6].

In our samples, the size of aggregates varies from 0.225mm to 3.56mm [2]. To compute the ion concentration near each aggregate, each mortar bar is divided into several layers with layer thickness of 5.34mm. As a result, there are three layers in small samples and nine layers in large samples. For simplicity, the ion concentration within each layer is assumed uniform and equal to the value at the middle point of each layer.

The micro-diffusion is the diffusion of alkali ions into the aggregate. This process can be described by Fick's law in spherical coordinate as,

$$B_{ion} \frac{\partial C_{ion}}{\partial t} = \nabla \cdot (D_{ion} \nabla C_{ion}) \quad , \quad (1.38)$$

where C_{ion} is the free ion concentration of the pore solution inside the aggregate. B_{ion} and D_{ion} are the binding capacity and ion diffusivity of the aggregate, respectively. The initial condition is $C_{ion} = 0$ for $t = 0$ in the aggregate. The boundary condition is $C_b = C(t)$ at the surface of aggregate, and $\partial C_{ion} / \partial r = 0$ at the center of the aggregate particle. Eq.(2) can be solved numerically using the finite difference method.

The ASR process takes place within the surface layer of each aggregate particle, where C_{ion} reaches a certain concentration level C_{crt} . One can inversely determine the thickness of the ASR layer, r , from the numerical solution of Eq.(2). The volume of the reacted portion of the aggregate particle of radius R_a can then be calculated,

$$V_a^{Ra} = \left[\frac{R_a^3 - (R_a - r)^3}{R_a^3} \right] \left(\frac{4}{3} \pi R_a^3 \right) \quad . \quad (1.39)$$

This volume is converted into the volume of ASR gel, V_{gel}^{Ra} ,

$$V_{gel}^{Ra} = \eta V_a^{Ra} \quad , \quad (1.40)$$

where η is the coefficient volumetric expansion from aggregate to ASR gel.

Mathematical model for permeation of ASR gel into the surrounding cement:

Because of the volumetric expansion when the aggregate is converted into ASR gel, the gel causes internal pressure near the interface zone between the aggregate and the surround cement. This pressure pushes the gel into the pores around this interface zone. As more pores nearby are filled up with the gel, the pressure increases. which deformed the concrete. The mount of gel that is capable of generating the internal pressure is given by

$$V_{gel,eff}^{Ra} = \langle V_{gel}^{Ra} - V_{pore}^{Ra} \rangle_+ \quad , \quad (1.41)$$

where V_{pore}^{Ra} is the total volume of pores in the surrounding interface zone that can be calculated using,

$$V_{pore}^{Ra} = V_{unit} A_{agg}^{Ra} \quad , \quad (1.42)$$

where V_{unit} is a material constant (a length scale) representing the capacity of the porous zone to absorb ASR gel per unit area, and A_{agg}^{Ra} is the surface area of an aggregate particle of size R_a .

When the effective gel volume $V_{gel,eff}^{Ra}$ is larger than zero, the ASR gel begins to permeate. This process can be characterized by Darcy's law for viscous flow as,

$$\frac{\partial C_{gel}}{\partial t} = \nabla \left(\frac{\kappa_{gel}}{\eta_{gel}} \nabla P_{gel} \right) \quad , \quad (1.43)$$

in which C_{gel} and η_{gel} are the concentration and viscosity of the gel, respectively, κ_{gel} is the gel permeability of the porous cement paste, and P_{gel} is the pressure distribution of the gel, which depends on the degree of saturation of the pores. At the boundary, the interface pressure, P_{int} , is applied. However, as P_{int} is an unknown and a function of time, it needs to be calculated simultaneously from the equilibrium of the composite system (see micro-mechanical modeling), the diffusion of ions, and the permeation of the gel. So this is a coupled chemo-mechanical problem.

In order to solve the coupled equations, a state equation must be introduced, which relates the concentration of ASR gel in the pores, C_{gel} , the gel pressure P_{gel} ,

$$C_{gel} = \beta P_{gel} \quad , \quad (1.44)$$

where β is the state function for cement paste [6]. The initial condition is $C_{gel}(r, 0) = 0$. The boundary condition at the interface is $C_{gel}(R_a, t) = \beta P_{int}(t)$, and at the far field is $C_{gel}(R_{REV}^a, t) = 0$. Eq.(13) can then be solved numerically using a finite difference method for the gel concentration as a function of radius and time, $C_{gel}(r, t)$. The gel volume in the porous cement paste can then be evaluated by integrating the gel concentration over the surrounding cement paste,

$$V_{pg}^{Ra} = \int_{R_a}^{R_{REV}^a} 4\pi r^2 C_{gel} dr \quad . \quad (1.45)$$

The coefficient of expansion for the aggregate with radius R_a due to ASR is thus,

$$\alpha_1 = \frac{\Delta V_{gel}^{Ra}}{V_a^{Ra}} = \frac{V_{gel,eff}^{Ra} - V_{pg}^{Ra}}{V_a^{Ra}} = \frac{V_{gel}^{Ra} - V_{pore}^{Ra} - V_{pg}^{Ra}}{V_a^{Ra}} \quad (1.46)$$

Micro-Mechanical Modeling

Three-phase expansion model

By a standard homogenization argument, the micro-structural configuration shown in Fig. 1 can be considered equivalent to that shown in Fig. 2.3, where phase 3 is the effective homogeneous medium equivalent to the heterogeneous medium in Fig. 1. Following the three-phase expansion model developed by Jin et al [7], one can obtain the effective expansion coefficient for the two-phase composite as well as the interface pressure between the aggregate and cement paste. For brevity, we only list the results here, and details can be found in [6]. The effective expansion and interface pressure can be written as,

$$\alpha_{eff} = \frac{K_a V_1 (3K_{SC} + 4G_{SC})}{K_{SC} (3K_a + 4G_{SC}) - 4V_1 G_{SC} (K_{SC} - K_a)} \alpha_1 \quad (1.47)$$

$$P_{int} = \frac{12K_a G_{SC} K_{SC} (1 - V_1)}{4V_1 G_{SC} (K_a - K_{SC}) + K_{SC} (3K_a + 4G_{SC})} \alpha_1 \quad (1.48)$$

where K_a , K_{SC} are the bulk modulus of aggregate and cement paste matrix, respectively, G_{SC} is the shear modulus of the cement paste, and $V_1 = R_a^3 / (R_{REV}^a)^3$ is the volume fraction of aggregate.

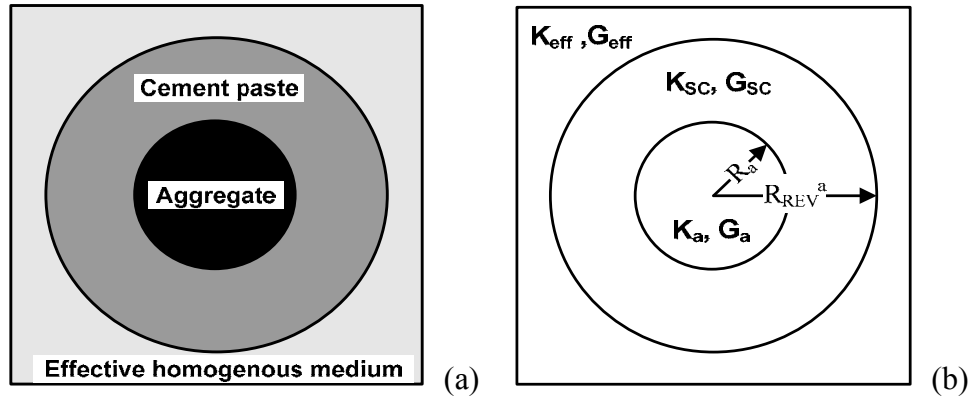


Fig. 2.3. (a) Three phase expansion model and (b) its mechanical properties

The unknown parameter in Eq. (17) and (18) is the expansion coefficient of aggregate due to ASR, α_1 , which can be evaluated by Eq. (16). As one can see, both α_1 and P_{int} involve the ASR gel formation due to alkali ion diffusion and the ASR gel permeation driven by interface pressure P_{int} .

Damaged RVE

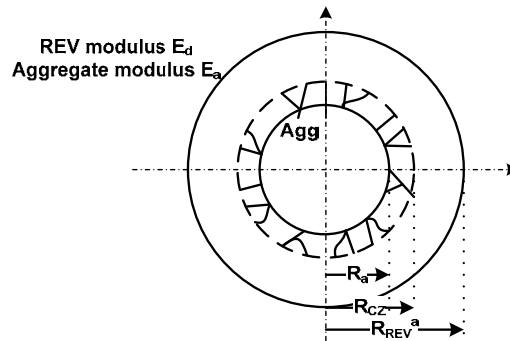


Fig. 2.4. Mechanical property of damaged REV

Since the Young's modulus in cement paste matrix is much lower than in aggregate, crack will initiate at the boundary and propagate into the cement paste matrix. According to the Griffith criterion, the critical pressure for crack initiation can be obtained,

$$P_{cr} = \sqrt{\frac{E_{SC} G_{IC}}{\pi(R_a + c_r)}} \quad , \quad (1.49)$$

where E_{SC} is the Young's modulus of cement paste, G_{IC} is the fracture energy of concrete, c_r is the initial crack length in the cement paste. Once the interface pressure P_{int} exceeds the critical pressure P_{cr} , crack starts to propagate which causes a decrease in the modulus. This can be

described by a damage parameter [3], which is defined by,

$$d = \frac{R_{CZ} - R_a}{R_{REV}^a - R_a} \quad , \quad (1.50)$$

where R_{CZ} represents the crack front as shown in Fig. 2.4. The modulus of the equivalent medium E_d can then be determined,

$$E_d = (1 - d)E_{SC} \quad . \quad (1.51)$$

The newly generated cracks also increase the volume of the RVE. The amount of volume expansion induced by crack growth is given by,

$$\alpha_C = \frac{\Delta V}{V_{R_{REV}}^a} = \frac{c_{pnew} - c_p}{1 - c_{pnew}} \cdot (1 - V_1) \quad , \quad (1.52)$$

where $V_{R_{REV}}^a = \frac{4}{3}\pi(R_{REV}^a)^3$ is the volume of the RVE, c_p and c_{pnew} are the porosity of cement paste matrix before and after crack opening respectively. The total expansion is the linear superposition of α_{eff} and α_C , i.e., $\alpha_{total}^{Ra} = \alpha_{eff}^{Ra} + \alpha_C^{Ra}$. Since the ASR induced expansion of aggregate is size dependent [6], the overall ASR expansion of concrete must be determined as the volumetric average of ASR expansion of the RVE with different sizes. For each aggregate, the final expansion should also include the volumetric average of each layer as described in macro-diffusion process. Thus the overall expansion is,

$$\alpha_{total} = \sum \phi_a \sum \phi_i^a \alpha_{total,i}^{Ra} \quad , \quad (1.53)$$

where ϕ_a is the volume fraction of aggregate with size R_a , ϕ_i^a is the volume fraction of each layer for a fixed aggregate size R_a , and $\alpha_{total,i}^{Ra}$ is the ASR expansion of the concrete located at the i^{th} layer with the aggregate size R_a .

Equations (1)-(23) form a complete model for ASR expansion. It is unlikely to solve the problem analytically because the diffusion and the permeation of gel are coupled with the interface pressure. Instead, a piecewise numerical procedure is adopted. More details can be found in [6].

Change of Acoustic Nonlinearity due to ASR Damage

The original acoustic nonlinearity parameter β only relates to material properties, and is usually defined as [8]

$$\beta = -\left(3 + \frac{4m + 2l}{\lambda + 2\mu}\right) \quad , \quad (1.54)$$

in which λ and μ are the Lamé constants, and l and m are the third order elastic constants (the Murnaghan coefficients). However, when material is under residual stresses, or experiences plastic deformations, the nonlinearity parameter β changes correspondingly as has been shown in extensive experimental results [9-15]. Our previous work has demonstrated the feasibility of using nonlinear ultrasonic techniques to track the progress of ASR damage in cement-based materials [4]. Here we want to predict the β change using our previous model validated by

expansion measurements of small mortar samples. An example of acoustic nonlinearity parameter β change in metallic materials due to dislocation and microcracks can be found in ref. [16]. Basically β change is a linear superposition of two terms, one is proportional to the initial stress and the other is proportional to the crack density. In our problem here, since the gel layer is also nonlinear, at least three factors can contribute to β change during ASR damage process: the nonlinearity from gel layer β_{gel} as a function of gel thickness δ_{gel} , the nonlinearity due to internal stress β_{stress} as a function of interface pressure P_{int} , and the nonlinearity caused by microcracks β_{crk} as a function of crack density N_0^{crk} . Suppose the β change from these three factors is not substantial, as the first order approximation, β can be expressed as the linear superposition from these three terms as,

$$\beta = \beta_0 + \beta_{gel}(\delta_{gel}) + \beta_{stress}(P_{int}) + \beta_{crk}(N_0^{crk}) \quad (1.55)$$

where β_0 is the original material nonlinearity before cracking. The expressions of β_{gel} , β_{stress} and β_{crk} will be given next.

Nonlinearity β from the Gel Layer

Consider gel layer as a distinct layer, due to its aqueous behavior, there is no shear stress generated inside this layer. However, since the gel layer is nonlinear, it can cause nonlinearity to the whole three phase unit, whose structure is shown in Fig. 6.12. Suppose this three phase unit is subjected to a tensile stress σ_0 at the outer boundary as shown in Fig. 6.12, by calculating the tensile strain generated by the tensile stress at the outer boundary, one can get the expression of β_{gel} .

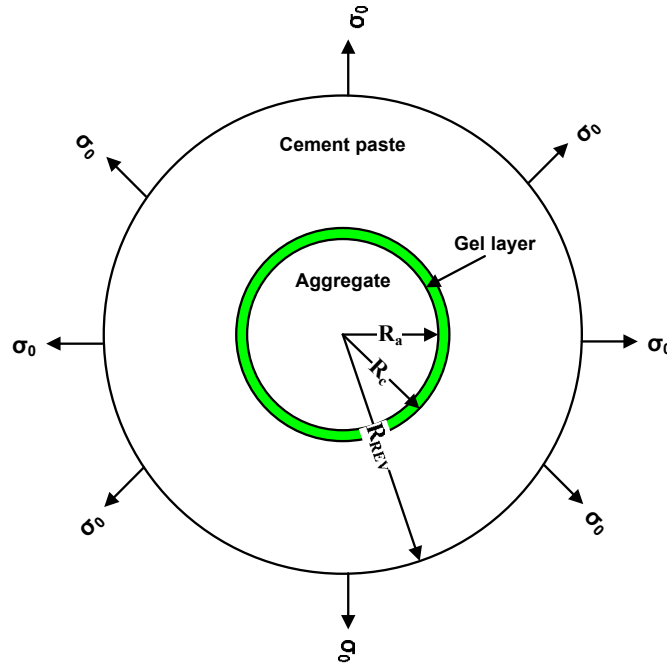


Fig. 2.5. Three-layer unit subjected to tensile loading at outer boundary

One can firstly get the displacement and stress expression within each layer from the equilibrium equation $\sigma_{ij,j} = 0$ as,

In the aggregate,

$$u_r^a = A_a \cdot r \quad \sigma_r^a = 3K_a A_a \quad . \quad (1.56)$$

In the cement paste,

$$u_r^c = A_c \cdot r + B_c / r^2 \quad \sigma_r^c = 3K_c A_c - 4B_c G_c / r^3 \quad (1.57)$$

In the gel,

$$u_r^g = f(r) \quad \sigma_r^g = P = a_1 e_g + a_2 e_g^2 \quad (1.58)$$

in which K_a is the bulk modulus in aggregate, while K_c , G_c are the bulk, shear modulus in cement paste respectively. P is the pressure in gel layer and e_g is the strain in gel layer. Since the gel layer is nonlinear, the stress and strain has nonlinear term in gel layer. The constant a_2 corresponds to the third order elastic constant of gel layer. The displacement in gel layer u_r^g is a function of radius r , thus the strain in gel layer is

$$e_g = e_{rr} + e_{\theta\theta} + e_{\varphi\varphi} = f'(r) + \frac{2}{r} f(r), \quad (1.59)$$

and the stress in gel layer should be

$$\sigma_{rr}^g = \sigma_{\theta\theta}^g = \sigma_{\varphi\varphi}^g = a_1 e_g + a_2 e_g^2 = a_1 \left(f' + \frac{2}{r} f \right) + a_2 \left(f' + \frac{2}{r} f \right)^2. \quad (1.60)$$

From the equilibrium equation one can get,

$$\frac{\partial \sigma_{rr}}{\partial r} + \frac{2\sigma_{rr} - \sigma_{\theta\theta} - \sigma_{\varphi\varphi}}{r} = 0 \quad . \quad (1.61)$$

Plugging Eq. (1.7) into Eq. (1.8), one can further get

$$\begin{aligned} a(f'' + 2(\frac{f}{r})') + a_2 \cdot 2(f' + \frac{2}{r}f) \cdot (f'' + 2(\frac{f}{r})') &= 0 \\ \Rightarrow (a + 2a_2 f' + \frac{4a_2}{r}f)(f'' + 2\frac{f'}{r} - 2\frac{f}{r^2}) &= 0 \end{aligned} \quad (1.62)$$

The solution of Eq. (1.9) yields $u_r^g = A_g \cdot r + B_g / r^2$. Then the strain in the gel layer is

$e_g = \frac{\partial u_r^g}{\partial r} + 2\frac{u_r^g}{r} = 3A_g$. Plugging the strain in gel layer into Eq. (1.5), one can further get the pressure in gel layer,

$$P = 3a_1(A_g + 3\frac{a_2}{a_1}A_g^2) \quad . \quad (1.63)$$

Next, the stresses continuity at the boundary of aggregate $r = R_a$ and at the boundary of gel

$r = R_c$ gives

$$\sigma_r^a(R_a) = \sigma_r^c(R_c) = P \quad . \quad (1.64)$$

The stress at the outer boundary R_{REV} equals to the loading stress,

$$\sigma_0 = \sigma_r^c(R_{REV}) \quad . \quad (1.65)$$

The displacements at R_a and R_c are equal,

$$u_r^a(R_a) = u_r^g(R_a) \quad u_r^g(R_c) = u_r^c(R_c) \quad . \quad (1.66)$$

Plugging Eqs. (1.3)-(1.5) and (1.10) into Eqs. (1.11)-(1.13), one can get a group of equations

$$\begin{cases} 3K_a A_a = 3K_c A_c - 4B_c G_c / R_c^3 = 3a A_g + 9ab A_g^2 \\ 3K_c A_c - 4B_c G_c / R_{REV}^3 = \sigma_0 \\ A_a \cdot R_a = A_g \cdot R_a + B_g / R_a^2 \\ A_g \cdot R_c + B_g / R_c^2 = A_c \cdot R_c + B_c / R_c^2 \end{cases} \quad . \quad (1.67)$$

From Eq. (1.14), one can eliminate A_g, B_g, A_c, B_c in function of A_a as

$$A_c = -\frac{K_a R_c^3}{(-R_c^3 + R_{REV}^3)K_c} A_a + \frac{1}{3} \frac{\sigma_0 R_{REV}^3}{(-R_c^3 + R_{REV}^3)K_c} \quad , \quad (1.68)$$

$$B_c = -\frac{3}{4} \frac{K_a R_c^3 R_{REV}^3}{G_c (-R_c^3 + R_{REV}^3)} A_a + \frac{1}{4} \frac{R_c^3 \sigma_0 R_{REV}^3}{G_c (-R_c^3 + R_{REV}^3)} \quad , \quad (1.69)$$

$$\begin{aligned} A_g = & \frac{1}{12} \frac{-12R_c^3 R_a^3 K_c G_c + 12R_c^6 G_c K_a + 9R_c^3 K_c R_{REV}^3 K_a + 12K_c G_c R_a^3 R_{REV}^3}{K_c G_c (R_c^6 - R_c^3 R_{REV}^3 - R_c^3 R_a^3 + R_a^3 R_{REV}^3)} A_a \\ & + \frac{1}{12} \frac{-3R_c^3 K_c R_{REV}^3 \sigma_0 - 4R_c^3 \sigma_0 G_c R_{REV}^3}{K_c G_c (R_c^6 - R_c^3 R_{REV}^3 - R_c^3 R_a^3 + R_a^3 R_{REV}^3)} \quad , \end{aligned} \quad (1.70)$$

$$\begin{aligned} B_g = & -\frac{1}{12} \frac{R_c^3 R_a^3 (12R_c^3 K_c G_c - 12R_c^3 G_c K_a - 9K_c R_{REV}^3 K_a - 12K_c G_c R_{REV}^3)}{K_c G_c (R_c^6 - R_c^3 R_{REV}^3 - R_c^3 R_a^3 + R_a^3 R_{REV}^3)} A_a \\ & - \frac{1}{12} \frac{R_c^3 R_a^3 (3K_c R_{REV}^3 \sigma_0 + 4\sigma_0 G_c R_{REV}^3)}{K_c G_c (R_c^6 - R_c^3 R_{REV}^3 - R_c^3 R_a^3 + R_a^3 R_{REV}^3)} \end{aligned} \quad (1.71)$$

Note that A_a is dimensionless. We can further simplify this problem by two assumptions,

a) $R_a = R_c - d$ with d to be the thickness of gel layer. One can further get $R_a = R_c - R_c \cdot \delta_{gel}$ with the gel thickness ratio $\delta_{gel} = d / R_c \ll 1$.

b) $P = a_1(e_g + be_g^2)$ with $a_2 = a_1 b$ the third order elastic constant. b is the ratio of third order over the second order elastic constant of gel.

Note that δ_{gel} and b are both dimensionless.

One can now consider A_a . Based on the simplifications, one can obtain a quadratic equation regarding to A_a from Eq. (1.14),

$$W_1 A_a^2 + (W_2 + W_3 \sigma_0) A_a + (W_4 \sigma_0 + W_5 \sigma_0^2) = 0 \quad (1.72)$$

In which W_1 to W_5 are all the combination of modulus and radius in aggregate, cement paste and gel. Eq. (1.19) has the solution

$$\begin{aligned} A_a &= \frac{-W_2 - W_3 \sigma_0 \pm \sqrt{(W_2 + W_3 \sigma_0)^2 - 4W_1(W_4 \sigma_0 + W_5 \sigma_0^2)}}{2W_1} \\ &= -\frac{W_2}{2W_1} - \frac{W_3 \sigma_0}{2W_1} \pm \frac{1}{2W_1} \sqrt{(W_3^2 - 4W_1 W_5) \sigma_0^2 + (2W_2 W_3 - 4W_1 W_4) \sigma_0 + W_2^2} \end{aligned} \quad (1.73)$$

This solution can be simplified by assuming $Y_1 = W_2^2$, $Y_2 = 2W_2 W_3 - 4W_1 W_4$ and $Y_3 = W_3^2 - 4W_1 W_5$. Since the applied load σ_0 is due to ultrasonic wave vibration, it is very small. One can then expand the square root of σ_0 and get

$$\begin{aligned} &\sqrt{Y_3 \sigma_0^2 + Y_2 \sigma_0 + Y_1} \\ &\approx \sqrt{Y_1} + \frac{1}{2} \frac{Y_2}{\sqrt{Y_1}} \sigma_0 + \sqrt{Y_1} \left(\frac{1}{2} \frac{Y_3}{Y_1} - \frac{1}{8} \frac{Y_2^2}{Y_1^2} \right) \sigma_0^2 + \sqrt{Y_1} \left(-\frac{1}{4} \frac{Y_2 Y_3}{Y_1^2} + \frac{1}{16} \frac{Y_2^3}{Y_1^3} \right) \sigma_0^3 \end{aligned} \quad (1.74)$$

Substitute Eq. (1.21) into Eq.(1.20),

$$\begin{aligned} A_a &= -\frac{W_2}{2W_1} - \frac{W_3 \sigma_0}{2W_1} \\ &\pm \frac{1}{2W_1} \left[W_2 + \frac{1}{2} \frac{2W_2 W_3 - 4W_1 W_4}{W_2} \sigma_0 + \sqrt{Y_1} \left(\frac{1}{2} \frac{Y_3}{Y_1} - \frac{1}{8} \frac{Y_2^2}{Y_1^2} \right) \sigma_0^2 + \sqrt{Y_1} \left(-\frac{1}{4} \frac{Y_2 Y_3}{Y_1^2} + \frac{1}{16} \frac{Y_2^3}{Y_1^3} \right) \sigma_0^3 \right] \end{aligned} \quad (1.75)$$

To make the solution simpler, choose '+' in Eq. (1.22) and one can get

$$A_a = \frac{-W_4}{W_2} \sigma_0 + \frac{1}{2W_1} \left[\sqrt{Y_1} \left(\frac{1}{2} \frac{Y_3}{Y_1} - \frac{1}{8} \frac{Y_2^2}{Y_1^2} \right) \sigma_0^2 + \sqrt{Y_1} \left(-\frac{1}{4} \frac{Y_2 Y_3}{Y_1^2} + \frac{1}{16} \frac{Y_2^3}{Y_1^3} \right) \sigma_0^3 \right] \quad (1.76)$$

Finally, we are ready to calculate β . From Eq.(1.4), one can get the strain on the outer boundary as

$$\begin{aligned} \varepsilon(R_{REV}) &= \frac{\partial u_r^c}{\partial r} = A_c - 2 \frac{B_c}{R_{REV}^3} \\ &= \frac{1}{R_{REV}^3 - R_c^3} \left[\left(\frac{3K_a}{2G_c} - \frac{K_a}{K_c} \right) R_c^3 A_a + \frac{R_{REV}^3 \sigma_0}{3K_c} - \frac{R_c^3 \sigma_0}{2G_c} \right] \end{aligned} \quad (1.77)$$

Substitute Eq. (1.23) into Eq. (1.24), one can get

$$\begin{aligned} \varepsilon(R_{REV}) = & \frac{1}{R_{REV}^3 - R_c^3} \left\{ \left[\frac{-W_4}{W_2} \left(\frac{3K_a}{2G_c} - \frac{K_a}{K_c} \right) R_c^3 + \frac{R_{REV}^3}{3K_c} - \frac{R_c^3}{2G_c} \right] \sigma_0 \right. \\ & \left. + \frac{\sqrt{Y_1}}{2W_1} \left(\frac{1}{2} \frac{Y_3}{Y_1} - \frac{1}{8} \frac{Y_2^2}{Y_1^2} \right) \left(\frac{3K_a}{2G_c} - \frac{K_a}{K_c} \right) R_c^3 \sigma_0^2 + \frac{\sqrt{Y_1}}{2W_1} \left(-\frac{1}{4} \frac{Y_2 Y_3}{Y_1^2} + \frac{1}{16} \frac{Y_2^3}{Y_1^3} \right) \left(\frac{3K_a}{2G_c} - \frac{K_a}{K_c} \right) R_c^3 \sigma_0^3 \right\} \end{aligned} \quad (1.78)$$

According to Cantrell's derivation [17],

$$\begin{aligned} \sigma &= \sigma_1 + \left(\frac{\partial \sigma}{\partial \bar{\varepsilon}} \right)_X (\bar{\varepsilon} - \bar{\varepsilon}_1) + \frac{1}{2} \left(\frac{\partial^2 \sigma}{\partial \bar{\varepsilon}^2} \right)_X (\bar{\varepsilon} - \bar{\varepsilon}_1)^2 + \dots \\ &= \sigma_1 + \left(\frac{\partial \bar{\varepsilon}}{\partial \sigma} \right)_X^{-1} (\bar{\varepsilon} - \bar{\varepsilon}_1) - \frac{1}{2} \left[\left(\frac{\partial^2 \bar{\varepsilon}}{\partial \sigma^2} \right)_X \left(\frac{\partial \bar{\varepsilon}}{\partial \sigma} \right)_X^{-3} \right] (\bar{\varepsilon} - \bar{\varepsilon}_1)^2 + \dots \\ &= \sigma_1 + P(\bar{\varepsilon} - \bar{\varepsilon}_1) + \frac{1}{2} Q(\bar{\varepsilon} - \bar{\varepsilon}_1)^2 + \dots \end{aligned} \quad (1.79)$$

with σ_1 the initial stress that gives rise to an initial strain $\bar{\varepsilon}_1$. The nonlinearity parameter can be obtained from Eq. (1.26) as $\beta = -\frac{Q}{P}$. Compared to Eq. (1.26), one can obtain β from Eq. (1.25) as

$$\begin{aligned} \beta_{gel} = & \frac{R_{REV}^3 - R_c^3}{R_c^3} \frac{2G_c K_c}{K_a (3K_c - 2G_c)} \left[\frac{W_2}{W_1} \left(\frac{1}{2} \frac{Y_3}{Y_1} - \frac{1}{8} \frac{Y_2^2}{Y_1^2} \right) + \frac{3W_2}{W_1} \left(-\frac{1}{4} \frac{Y_2 Y_3}{Y_1^2} + \frac{1}{16} \frac{Y_2^3}{Y_1^3} \right) \sigma_0 \right] \\ & \left[\frac{-W_4}{W_2} + \frac{2G_c R_{REV}^3 / R_c^3 - 3K_c}{3K_a (3K_c - 2G_c)} \right]^{-2} \end{aligned} \quad (1.80)$$

Sine the ratio of gel thickness over the radius of aggregates δ_{gel} is very small, one can further expand β with δ_{gel} at $\delta_{gel} = 0$ and keep the first order of δ_{gel} . One can finally get,

$$\beta_{gel} \approx -S_1 + S_2 \cdot |\sigma_0| \quad (1.81)$$

with

$$S_1 = \frac{36\delta_g b(-3K_c + 2G_c)V_1(4G_c + 3K_c)^2 K_a^3}{a_1^2[4K_a G_c V_1 + 3K_a K_c + 4K_c G_c(1 - V_1)](3K_a - 6K_c V_1 + 4G_c + 6K_a V_1)^2} \quad (1.82)$$

$$S_2 = \frac{-216\delta_g b^2(-3K_c + 2G_c)V_1(4G_c + 3K_c)^3 K_a^4}{a_1^3[4K_a G_c V_1 + 3K_a K_c + 4K_c G_c(1 - V_1)]^2(3K_a - 6K_c V_1 + 4G_c + 6K_a V_1)^2} \quad (1.83)$$

in which $V_1 = \frac{R_c^3}{R_{REV}^3}$ is the volume ratio of aggregate. From Eq. (1.29) and (1.30) one can tell

that the only parameter that varies with exposure time is the gel thickness ratio, δ_g , and other parameters are all constants. Unfortunately due to lack of the information in gel modulus, one cannot decide a_1 and b in these equations. If we choose a_1 equals to water's modulus 2.25 GPa, and nonlinearity ratio in gel layer $b=5$, one can get an estimated nonlinearity

$\beta_{gel} \approx 2.67 \times 10^2 \delta_{gel} - 4.2 \times 10^{-6} \delta_{gel} |\sigma_0|$. So if the gel thickness ratio is 10%, the absolute

nonlinearity change is around 26.7 considering σ_0 is very small and S_2 is negligible.

Nonlinearity β from the internal stress

To get β_{stress} , again we use the generalized self-consistent three-phase model in which the gel layer is not considered as a distinct layer. Instead, we only consider the precipitate strain on the interface generated by the gel expansion. According to Cantrell's theory [18], acoustic nonlinearity in polycrystalline solids with initial stress can be expressed by,

$$\beta - \beta_0 = (3 - \frac{\bar{c}_{111}}{\bar{c}_{11}} - \frac{\bar{c}_{1111}}{\bar{c}_{11}} + \frac{\bar{c}_{111}^2}{\bar{c}_{11}^2})\bar{u}_{11} + (3\frac{\bar{c}_{12}}{\bar{c}_{11}} - \frac{\bar{c}_{1112}}{\bar{c}_{11}} + \frac{\bar{c}_{12}\bar{c}_{111}}{\bar{c}_{11}^2} + \frac{\bar{c}_{112}\bar{c}_{111}}{\bar{c}_{11}^2})(\bar{u}_{22} + \bar{u}_{33}) \quad (1.84)$$

where $\beta_0 = -(\frac{3\bar{c}_{11} + \bar{c}_{111}}{\bar{c}_{11}})$ is the acoustic nonlinearity parameter referred to the zero stress state

\bar{X} , and \bar{u}_{11} , \bar{u}_{22} and \bar{u}_{33} are the averaged strain components. As the first approximation, we apply Eq. (1.84) to calculate the nonlinearity caused by internal stress. In this calculation, $\bar{c}_{11} = 3K_{eff}(1 - 2\nu)$, where $\nu=0.2$ is the Poisson's ratio of this unit and K_{eff} is the effective bulk modulus of the unit as shown in Fig. 6.6. One can get the effective bulk modulus,

$$K_{eff} = \frac{K_c(3K_a + 4G_c) - 4V_1G_c(K_c - K_a)}{(3K_a + 4G_c) + (3K_c - 3K_a)V_1} \quad (1.85)$$

and effective displacement of the whole unit,

$$u_{reff} = \frac{K_a V_1 (3K_c + 4G_c)}{K_c (3K_a + 4G_c) - 4V_1 G_c (K_c - K_a)} \cdot \varepsilon_{imp1} \cdot r \quad (1.86)$$

with $\varepsilon_{imp1} = \frac{4V_1 G_c (K_a - K_c) + K_c (3K_a + 4G_c)}{12K_a K_c G_c (1 - V_1)} P_{int}$ the expansion of aggregate. Since this unit is considered as effectively homogeneous, the averaged strain components can be obtained as

$$\begin{aligned} \bar{u}_{11} &= \varepsilon_{rr} = \frac{\partial u_{reff}}{\partial r} \\ \bar{u}_{22} &= \varepsilon_{\theta\theta} = \frac{u_{reff}}{r} \\ \bar{u}_{33} &= \varepsilon_{\phi\phi} = \frac{u_{reff}}{r} \end{aligned} \quad (1.87)$$

Substitute Eq. (1.86) into Eq.(1.87), one can get,

$$\bar{u}_{11} = \bar{u}_{22} = \bar{u}_{33} = \alpha_{eff} = \frac{K_a V_1 (3K_c + 4G_c)}{K_c (3K_a + 4G_c) - 4V_1 G_c (K_c - K_a)} \cdot \varepsilon_{imp1} \quad (1.88)$$

This leads to,

$$\bar{u}_{11} = \bar{u}_{22} = \bar{u}_{33} = \frac{V_1 (3K_c + 4G_c)}{12G_c K_c (1 - V_1)} \cdot P_{int} \quad (1.89)$$

Assume that the Hiki-Granato relationship holds for the elastic constants, thus $C_{11} = 2C_{12}$, $C_{111} = 2C_{112}$, and $C_{1111} = 2C_{1112}$. Applying them into Eq. (1.84), one can get,

$$\beta - \beta_0 = (6 - 2 \frac{C_{1111}}{C_{11}} + 2 \frac{C_{111}^2}{C_{11}^2}) \cdot u_{11} \quad (1.90)$$

$$\text{with } \beta_0 = -\frac{3(C_{11} + C_{111})}{C_{11}} = -(3 + \frac{C_{111}}{C_{11}}).$$

Substitute Eq. (1.89) into Eq.(1.90), one can finally get

$$\frac{\beta_{stress} - \beta_0}{\beta_0} \approx (\frac{\beta_0}{6} + 1) \frac{V_1(3K_c + 4G_c)}{K_c G_c (V_1 - 1)} \cdot P_{int} \quad (1.91)$$

The only variable in Eq. (1.91) is the interface pressure P_{int} and all the other parameters are constants. However, again we cannot get the absolute value of the initial nonlinearity parameter β_0 . If we assume $\beta_0 = 50$, and for the internal pressure $P_{int} = 20 \text{ MPa}$, one can get the variation of β : $\frac{\beta_{stress} - \beta_0}{\beta_0} = 40\%$.

Nonlinearity β from the microcracks

Assume for our cement-based materials, we can still use Cantrell's theory [17] based on metallic materials to calculate the nonlinearity change due to microcracks. So the nonlinearity change β_{crk} can be expressed as

$$\beta_{crk} = (\beta' N_0^{crk} / 7) [1 + (\alpha' N_0^{crk} / 5)]^{-2}, \quad (1.92)$$

where

$$\alpha' = \frac{16h_s R^3 (1 - \nu^2)}{3(d_s)_0} \left(1 + \frac{h_s}{(d_s)_0} \right)^{-1} \quad (1.93)$$

$$\beta' = \frac{256h_s R^4 (1 - \nu^2)^2}{9\pi(d_s)_0^2} \left(1 + \frac{h_s}{(d_s)_0} \right)^{-3} \quad (1.94)$$

can be represented by crack model parameters as follows: h_s is the initial crack length; R is the crack radius, ν is the Poisson's ratio of the whole unit which equals to 0.2, $(d_s)_0$ is the averaged crack length in each unit, N_0^{crk} is the crack density per unit volume which is also a parameter of time.

As we only have the effective damage variable in our calculation, we cannot obtain the specific crack information like crack length, crack radius from our model. However, if we choose h_s to be $0.00025 \times (R_{RVE}^a - R_a)$, R to be the radius of aggregate R_a , $(d_s)_0$ to be one tenth of the thickness of cracked area and N_0^{crk} to be inverse proportional to the volume change

caused by cracks ΔV . For a typical aggregate with radius 0.89 mm, one can get $\beta_{crk} \approx 245$ after 14 days exposure time.

Variation of δ_{gel} , P_{int} and N_0^{crk} during 14 days exposure time

In our numerical simulation, we can obtain the ratio of gel thickness (over the aggregate radius Ra) δ_{gel} , interface pressure P_{int} and damage variable d which is dimensionless and can represent the crack density N_0^{crk} . Since these are the only parameters that vary with time, they directly determine the variation of nonlinearity parameter β during 14 days exposure time. As all the variables δ_{gel} , P_{int} and damage variable d vary from sizes of aggregates and the location of each layer, to obtain a whole picture of δ_{gel} , P_{int} and d up to 14 days, one needs to calculate the volumetric average of each size of aggregate and within each layer. From the foregoing discussions, we can get the volumetric averaged δ_{gel} , interface pressure P_{int} and damage variable d up to 14 days exposure time in both small and large mortar samples as shown in Fig. 2.6 – 2.8 respectively.

Since the interface pressure is generated by gel, the averaged interface pressure P_{int} should be directly related to the averaged gel thickness ratio δ_{gel} . Therefore one can see from Figs 2.6 – 2.7 that both δ_{gel} and P_{int} show a very similar trend for both small and large mortar samples. First of all, as alkali ion diffused very fast into the small mortar sample, the interface pressure built up very quickly, therefore both δ_{gel} and P_{int} increases very fast during the first few days. Secondly, in small mortar sample, both δ_{gel} and P_{int} shows a slower rate of increase after about 6 days. Refer to Fig.2.8, one can find that in small sample, at around day 6, the cracks were generated and after day 6, they propagated very fast. Due to the generation of microcracks, excess gel flowed into the cracks and part of the interface pressure was released. Furthermore, due to the crack propagation, both the correspondingly increased porosity and decreased Young's modulus in cement paste matrix cause slower increase in δ_{gel} , P_{int} after around day 6 in small mortar sample. After 14 days, the gel thickness has reached around 16% of aggregate radius and interface pressure has come to around 17 MPa in small sample.

While in large mortar sample, both averaged gel thickness ratio and interface pressure shows almost a linear increase during 14 days exposure time. For the large sample, since alkali ion has only penetrated into the outer layers after 14 days, the correspondingly crack initiation is not that obvious, which is only 4% as shown in Fig. 2.8. Therefore both δ_{gel} and P_{int} shows almost a linear increase during 14 days exposure time. After 14 days, the gel thickness has only reached around 6% of aggregate radius and interface pressure has come to around 8 MPa in large sample.

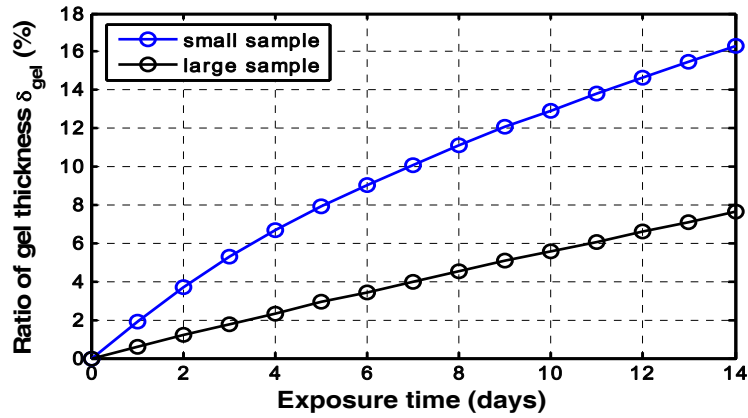


Fig. 2.6 The volumetric averaged gel thickness ratio (δ_{gel}) versus exposure time in small and large mortar samples

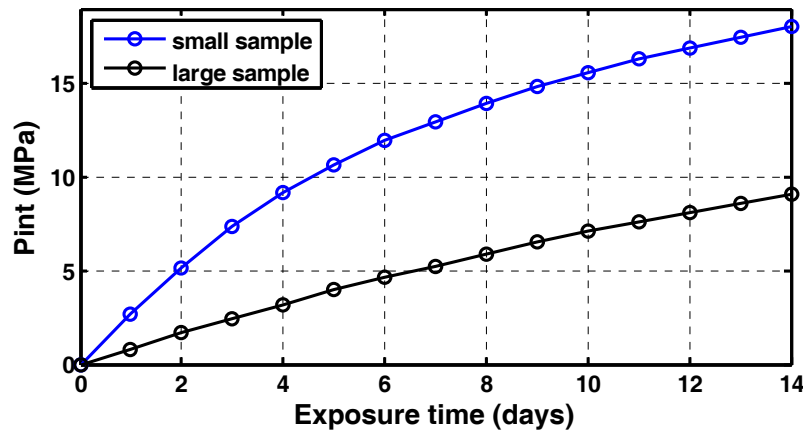


Fig. 2.7 The volumetric averaged interface pressure (P_{int}) versus exposure time in small and large mortar samples

While the damage variable d which can represent crack density shows a different trend of increase than δ_{gel} and P_{int} as shown in Fig. 2.8. As one can see, after 14 days, the crack density in small sample is around 3 times higher than that in large samples. In both samples, the damage becomes obvious at around day 6, and afterwards, in small sample, it shows a linear increase, while in large sample, the damage shows a faster increase after 12 days. This is because in large mortar sample, alkali ions have not penetrated thoroughly after 14 days. As more and more ions get into the large sample, the crack density keeps increase, and as a result, the damage shows a faster increase after 12 days.

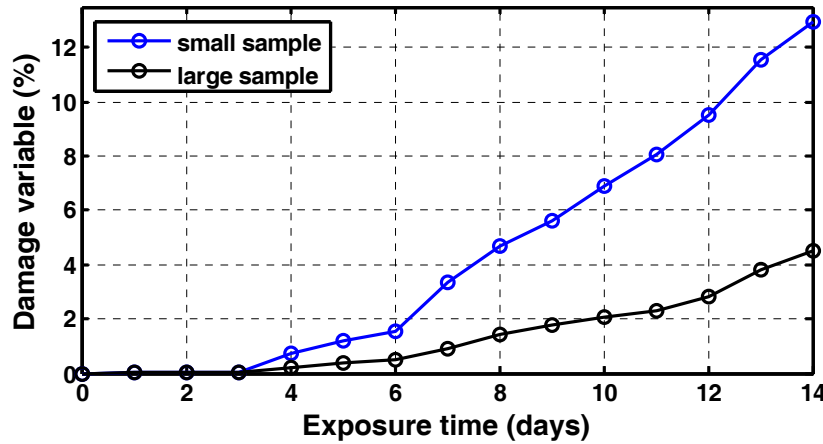


Fig. 2.8 The volumetric averaged damage variable (d) versus exposure time in small and large mortar samples

Predicting β variation during 14 days exposure time

Now we have obtained the expressions of β variation from three parts (gel layer, internal stress and crack density), we can then predict β change based on Eq. (1.2). However, due to lack of the information in gel layer, absolute original nonlinearity β_0 , specific cracks size and distribution, we cannot determine all the constants to calculate β . To avoid the complexity of determining these constants, we simply use a weight parameter α to estimate the β variation from three parts. Note that since both δ_{gel} and P_{int} have similar trend of increase, they are combined together as a single parameter P_{int} . Then we can get the normalized acoustic nonlinearity parameter $\bar{\beta}$ as,

$$\bar{\beta} = \frac{\beta}{\beta_0} - 1 = \alpha |\bar{P}_{int}| + (1 - \alpha) \bar{N}_0^{crk} \quad , \quad (1.95)$$

in which $|\bar{P}_{int}|$ is the internal stress normalized by its maximum value, $0 < |\bar{P}_{int}| < 1$, and \bar{N}_0^{crk} is the crack density normalized by its maximum value, $0 < \bar{N}_0^{crk} < 1$. Since the acoustic nonlinearity change caused by cracks is much larger than initial stresses in metallic materials[16], as a reasonable approximation, the weight parameter α is taken in the range of $0 < \alpha < 0.5$. Compare to our ASR effect, N_0^{crk} can be simulated by the damage variable d .

Follow Eq. (1.95) and let the weight parameter α vary from 0 to 0.5, one can get the normalized acoustic nonlinearity parameter $\bar{\beta}$ change up 14 days exposure time in alkali solution. Note that all the nonlinearity parameters from experiment measurements are normalized by their maximum value. The comparison between experiment measurements and numerical prediction is plotted in Figs. 2.9 – 2.10 for small and large mortar sample respectively. By comparing with experimental measurements, we observe in small mortar sample, when $\alpha = 0$, the predicted curve fits well with the experimental measurements. This is because the small

sample has damage everywhere after 14 days, the nonlinearity change is microcrack dominated. While in large sample, this is not the case. As shown in Fig. 2.7, when $\alpha = 0.2$, the predicted curve matches better with the experimental measurements. One possible explanation is that in large sample, since alkali ions have not penetrated thoroughly after 14 days, interface pressure also contributes to the nonlinearity change during 14 days exposure time. However, the results in both samples show that this numerical model can effectively capture the nonlinearity parameter jump at both day 7 and day 12. These jumps may indicate different stages of ASR process. Before day 6, since the ASR damage is only limited to the interface pressure built up, $\bar{\beta}$ increase is very slow. After day 6, due to the rise of crack density as shown in Fig. 2.8, $\bar{\beta}$ increase is accelerated. Finally after day 11, more cracks are formed which further reduces the Young's modulus and increased porosity in cement paste. Consequently, there is another jump of $\bar{\beta}$. So in all, our numerical model seems to be capable of predicting the acoustic nonlinearity change.

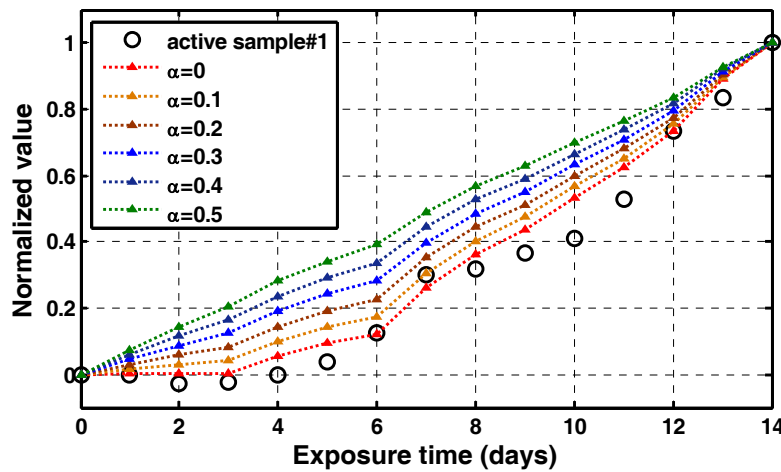


Fig. 2.9. Predicted and measured acoustic nonlinearity change versus exposure time in small mortar samples

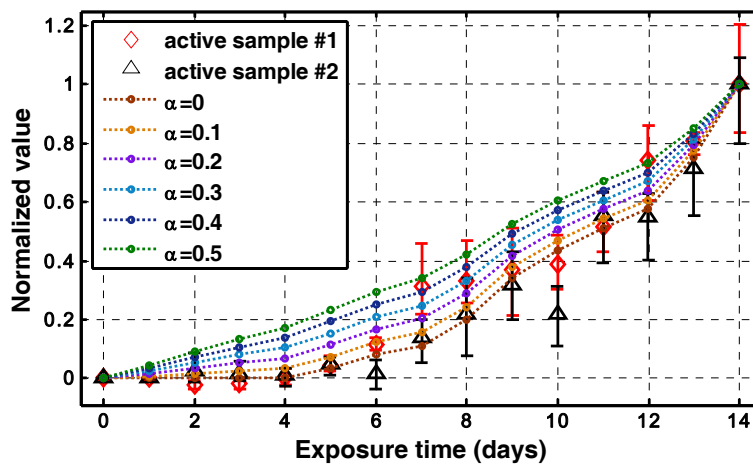


Fig. 2.10. Predicted and measured acoustic nonlinearity change versus exposure time in large mortar samples

Limitations and Improvements of the Model

The model presented here is mainly based on a previous model developed by Jin et al.[7]. Several improvements can be made.

First, to predict the total expansion of the whole mortar sample, the consideration of macro-diffusion process has been added to assess the localized alkali ion concentration of each aggregate before conducting micro-diffusion process. By adding the macro-diffusion process, the overall expansion makes more sense since the mortar sample has certain thickness and the alkali ion concentration should not be the same for each aggregate with different locations.

Second, due to the large interface pressure generated on the surface of certain aggregates, crack initiation has been added to get more accurate expansion. In this new model, damage variable is introduced. It is tightly related to the crack density, porosity, as well as Young's modulus change of cement paste matrix and finally contributes to the prediction of acoustic nonlinearity change, which is in very good agreement with experimental measurements.

Finally, the model was developed with several assumptions (about the diffusion, the composition of the ASR gel, the mechanical properties of cement paste matrix after crack initiation, etc.). To get more accurate prediction of acoustic nonlinearity change, the exact micro-scale material constants as shown in Eqs. (1.28), (1.91) and (1.94) needs to be determined. Supplementary investigations are also needed before it can be applied to real structures. In particular, the effect of temperature on all the chemo-mechanical and micromechanical mechanisms needs to be analyzed.

Conclusion

This Appendix presents a new model to predict acoustic nonlinearity change during ASR damage. This new model mainly includes three parts. The first part is the chemo-mechanical model which accounts for two opposing processes. One is the diffusion of alkali ions from surface of mortar sample to the surface of each aggregate (macro-diffusion process) and the diffusion of localized alkali ions in the pore solution into each aggregate. The other is the permeation of ASR gel from the aggregate surface into the surrounding porous cement matrix. The second part is the micromechanical model based on a modified version of the generalized self-consistent theory. The last part is the fracture model which simulates the crack initiation and growth. A damage variable is introduced in this part to get the crack density and total expansion. Finally, the acoustic nonlinearity parameter is determined as a function of exposure time based on gel thickness, interface pressure and the crack density caused by gel expansion. This numerical model is first validated by curve fitting of the crack opening speed based on the expansion measurement in small mortar samples during 14 days, then the validated model is used to predict the acoustic nonlinearity change up to 14 days exposure to alkali solution. The results of numerical prediction and experimental measurements of acoustic nonlinearity are in very good agreement. Although more experiments on aggregates with different activities are needed to further validate this model, the present work has shown that the proposed method has a good potential to quantitatively predict the acoustic nonlinearity variation during ASR damage and can be used to guide experimental measurements in the future.

III.1.10 Physics-Based Models for ASR Damage Evolution

Model Description

A novel approach, entitled ASR-LDPM [19] was formulated to simulate the effect of ASR on concrete structures. ASR-LDPM implements, within the mesoscale framework of LDPM, a model describing ASR gel formation and expansion at the level of each individual aggregate particle. ASR-LDPM was calibrated and validated with reference to several sets of experimental data dealing with ASR effects on concrete under a variety of different loading and environmental conditions with the limitation to saturated conditions.

The main effect of ASR is a progressive deterioration of concrete stiffness and strength that results from the long term formation and expansion of ASR gel inducing expansive pressure on the internal structure of concrete. This pressure causes non-uniform deformations that eventually lead to cracking and damage. While the chemical description of the reaction was addressed intensively in the literature, the fracture mechanics associated with the progressive expansion has received little attention due to the lack of models describing concrete internal structure satisfactorily. The main objective of the ASR-LDPM model is to fill this knowledge gap.

Despite some success, the common disadvantage of the various models previously developed is the inability to simulate crack patterns and crack distribution due to ASR. This, in turn, limits the ability to predict the degradation effect of ASR and forces the assumption of phenomenological relationships between ASR gel expansion and concrete mechanical properties. In addition, it also limits the ability of such models to explain complex triaxial behavior of concrete under ASR and also forces the assumption of phenomenological relationships between ASR gel expansion and stress state. These limitations are inherently connected to modeling concrete as an isotropic and homogenous continuum.

ASR-LDPM overcomes these problems by modeling ASR effects within the Lattice Discrete Particle Model (LDPM) [20, 21]. LDPM, in a full 3D setting, simulates the mechanical interaction of coarse aggregate pieces through a system of three-dimensional polyhedral particles, each resembling a spherical coarse aggregate piece with its surrounding mortar, connected through lattice struts [20, 21] and it has the ability of simulating the effect of material heterogeneity of the fracture processes. ASR-LDPM introduced here is limited to fully saturated conditions as the consideration of water macro diffusion will be considered in the future work.

Model Basic Assumptions

In the formulated model, the following assumptions were used.

- (1) Water needs to be available in the pores to act as transport medium for hydroxyl and alkali ions for ASR to occur.
- (2) The expansion of ASR gel is mostly due to water imbibition.
- (3) Continuous supply of water is needed for the swelling to continue over time.
- (4) The aggregate particles are assumed to have spherical shape.
- (5) The whole volume of each particle is assumed to be reactive.
- (6) Silica is smeared uniformly over each aggregate volume.

- (7) Under these approximations, the dissolution of silica may be assumed to progress roughly in a uniform manner in the radial direction inward from the surface towards the particle center.
- (8) Only saturation condition is considered so far. This case has practical relevance in situations in which concrete is continuously exposed to water. The effect of relative humidity change is to be considered in the future work.
- (9) Shrinkage and possible creep are compensated using relevant models in literature (B3 and CEB models) but not implicitly coupled with the formulation.

Model Formulation

Based on the aforementioned assumptions, two main processes have been formulated and connected; (1) Basic gel formation, and (2) Water imbibition, then volume increase due to water imbibition is translated into inhomogeneous gel strain, and is imposed on the concrete meso-structure using the LDPM model. The highlights of each part are as follows.

Gel Formation

The gel mass M_g generated from an aggregate particle with diameter D , is derived from solving the steady state mass balance of the radial diffusion process of alkali rich water into the aggregate particle. The solution is given by,

$$M_g = \kappa_a \frac{\pi D^3}{6} (1 - \zeta^3) c_s \frac{m_g}{m_s} \quad (3.1)$$

where $m_g = 94.1$ g/mole, $m_s = 60.09$ g/mole are the gel and silica molar weights respectively, $\zeta = 2z/D$ is the non-dimensional reaction front position where z is the reaction front position measured from aggregate particle external surface, c_s is the silica content assumed here for lack of experimental data to be 440 kg/m^3 , and κ_a accounts for the fact that alkali content available in the cement paste surrounding each aggregate particle, is not always enough for the ASR reaction to occur. In other words, the discussed availability of water at reaction front is not a sufficient condition for ASR and such water needs to be alkali rich. In this study, in absence of more detailed information, a simple linear relationship between alkali content, c_a , and the produced gel mass is assumed: $\kappa_a = \min((c_a - c_{0a}) / (c_{1a} - c_{0a}), 1)$, where c_{0a} is the threshold alkali content at which, no or minimal expansion is observed, and c_{1a} is the saturation alkali content enough for complete silica reaction.

Water Imbibition

The water imbibition process was described by relating the rate of water mass M_i imbibed by gel to the thermodynamic affinity and a characteristic imbibition time. This leads to the following expression,

$$\dot{M}_i = \frac{C_i^0}{\delta^2} \exp(-\eta M_i) \left[K_i^0 (1 - \zeta^3) D^3 \kappa_a \exp\left(\frac{E_{ai}}{RT_0} - \frac{E_{ai}}{RT}\right) - M_i \right] \quad (3.2)$$

where R is the universal gas constant, T is the absolute temperature in Kelvins, T_0 is a reference absolute temperature where the imbibed water at thermodynamic equilibrium has been assumed to be proportional to the mass of formed gel and temperature-dependent through an Arrhenius-

type equation governed by the activation energy of the imbibition process E_{ai} . δ is the average (or effective) distance of water transport process from the concrete around the aggregate into the ASR gel. The micro-diffusivity C_i for microdiffusion of water close to the aggregate was considered to be a decreasing function of M_i , because the imbibition of the layers of gel increases the diffusion time of the free water to reach the not imbibed gel. This phenomenon can be captured by setting $C_i = C_{i0} \exp(-\eta M_i)$, and $\eta(M_i)$ is an increasing function of M_i .

Analysis of experimental data carried out in this study suggests that, in absence of more precise information about the water imbibition process, $K_i^0 = \pi \kappa_i^0 c_s m_g / (6m_s)$. $\kappa_i^0 \approx 1$
Where for $T_0 = 23^\circ\text{C} = 296^\circ\text{K}$.

Lattice Discrete Particle Modeling of ASR Effect

To account for ASR in LDPM, first the radius variation of each aggregate particle of initial radius $r = D/2$ can be calculated from the volume variation of the ASR gel due to water imbibition:

$$\Delta r = \left(\frac{3M_i}{4\pi\rho_w} + r^3 \right)^{1/3} - r \quad (3.3)$$

This result can be then used to calculate an incompatible ASR strain to be applied to the LDPM system assuming that strain additivity holds: where the total strain on each LDPM facet is given by $e_N = e_N^t + e_N^0$ where $e_N^0 = (\Delta r_1 + \Delta r_2 - \Delta \delta_c)/l$; Δr_1 and Δr_2 are the radius changes of the two aggregate particles sharing a generic facet; l is the distance between these two aggregate particles; and e_N is the normal strain that is calculated according to the LDPM constitutive equation.

After calibration, the model is able to capture (1) the general characteristics of ASR S-shaped expansion versus time curves; (2) the effect of stress states on observed expansion; (3) the effect of expansion on concrete strength; (4) the effect of alkali content; and (5) the effect of temperature.

Application of the Model to the Experimental Results

The relevant results for small specimens carried out here were used to calibrate the model which was able to accurately capture the expansion curves with very high accuracy as shown in Fig. 3.1a.

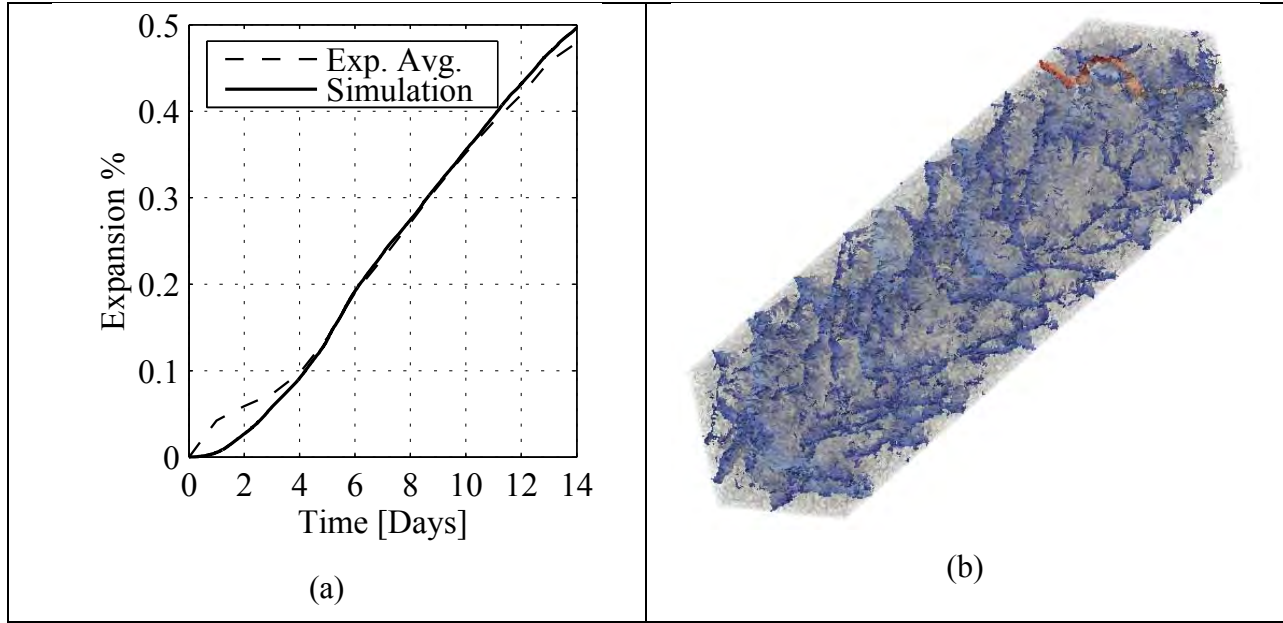


Figure 3.1: a) Experimental and numerical expansions, b) Simulated Crack patterns in the specimen after 14 days

In addition, the model is capable of reproducing the corresponding crack patterns found in the experiments as shown in Fig. 3.1b.

The model can reproduce the current damage state of the specimens and as it is now calibrated on the given expansion history, it can predict the remaining expansion history and hence, the expected strength reduction.

Refinement of the ASR-LDPM Model to Account for Alkaline Macrodiffusion

The current model was improved by adding the alkali ion diffusion to it. In this regard, two important modifications were formulated as follows,

Solution of Diffusion Problem

Here, two assumptions were made: 1) The diffusion process can be assumed as a 2D diffusion as sample cross section dimensions are much smaller than its length, 2) Constant diffusion coefficient is used as the self dissication of concrete effect on internal relative humidity was neglected, this is because specimens already have high water to cement ratio (0.5) and they are immersed in water for the whole curing and test period. Based on that, an implicit integration method (The alternating Directions implicit) with Crank Nicolson scheme was implemented to solve the 2D diffusion problem. This method discretizes the solution as follows

$$D^+U_t = \frac{C}{2} (D_0U_{xx}^{n+1} + D_0U_{xx}^n + D_0U_{yy}^{n+1} + D_0U_{yy}^n) \quad (3.4)$$

where U_t , U_{xx} and U_{yy} are the first time derivative, second spatial derivative in x and second spatial derivative in y, respectively. D^+ is the forward Euler operator and D_0 is the central difference operator, C is the constant diffusivity parameter.

In addition, the ASR-LDPM model deals with the concentration of ions as an overall alkali content in kg/m^3 of concrete, while the diffusion process is in terms of moles/Litre. So, after solving for the concentration, it is converted into alkali content. The final alkali content distributions for small and large samples of 1”X1” and 4”X4” after 14 days have the profiles shown in Fig. 3.2a and b respectively.

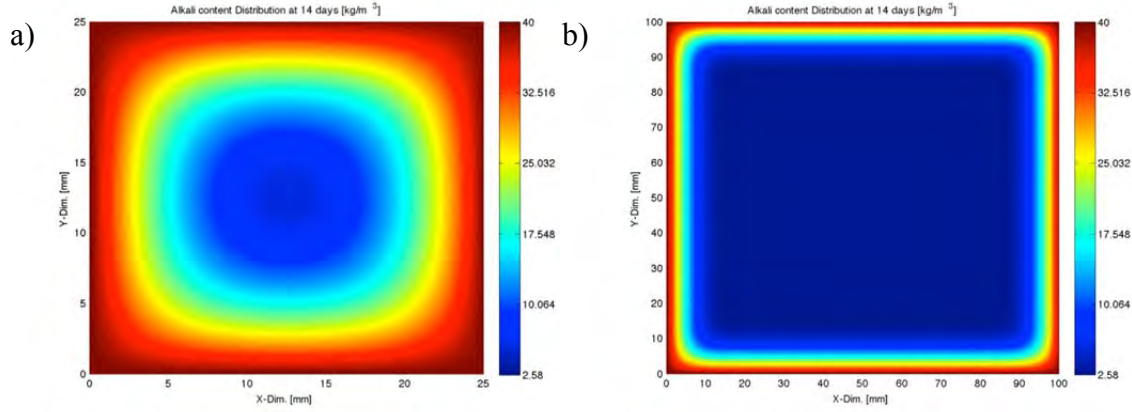


Figure 3.2: a) Small Sample, b) Large Sample

Consideration of Variable Alkali Content on ASR-LDPM Formulation

The ASR-LDPM model was formulated for fully saturated conditions with uniform alkali content over the concrete volume. This is the condition of mostly all real structures in which, the source of alkali is the initial alkali content of the concrete mix and water just helps transferring it into the aggregates, so the alkali ions only undergo micro diffusion. This is also the same case for long term concrete prisms and cylinders experiments, as the alkali content is increased by adding alkali to the mixing water, then after curing, the specimens are either sealed or kept in various humidity conditions. For the special case of accelerated mortar bar test, the source of alkali becomes the water in which the bar is immersed after curing. In this case, alkali undergoes both macro and micro diffusion to reach the aggregate. For this case, the reaction front evolution with time is delayed due to the alkali macro diffusion process. In ASR-LDPM, the alkali content effect is introduced through κ_a as a reduction factor of the formulated gel mass. To extend its effect to the reaction front evolution, the cubic root of κ_a is moved to the reaction front rate. The initial ASR-LDPM gel mass equation is modified as,

$$\begin{aligned}
 M_g &= K_i^0 \left(1 - \left(\frac{2z}{D} \right)^3 \right) D^3 \kappa_a \exp \left(\frac{E_{ai}}{RT_0} - \frac{E_{ai}}{RT} \right) \\
 &= K_i^0 \left(\kappa_a - \left(\frac{2z \sqrt[3]{\kappa_a}}{D} \right)^3 \right) D^3 \exp \left(\frac{E_{ai}}{RT_0} - \frac{E_{ai}}{RT} \right) \\
 &= K_i^0 \left(\kappa_a - \left(\frac{2z \kappa}{D} \right)^3 \right) D^3 \exp \left(\frac{E_{ai}}{RT_0} - \frac{E_{ai}}{RT} \right)
 \end{aligned} \tag{3.5}$$

where the reaction front speed can be approximately given by,

$$\dot{z}_\kappa = -\frac{a_s(T)w_s}{r_w c_s z_\kappa \left(1 - \frac{2z_\kappa}{D}\right)} \sqrt[3]{\kappa_a} \quad (3.6)$$

For a wide range of different constant alkali contents both old and new formulations give very close results as in Fig. 3.3.

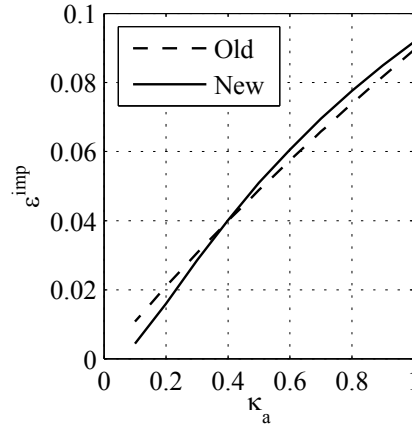


Figure 3.3: Comparison between old and new model considering variable alkali content.

Simulating Acoustic Nonlinearity Change in Small Specimens

At this stage, the model is mature enough to start simulation the acoustic nonlinearity change. So, to check the capability of the model to predict realistic acoustic response, the model was used to simulate the experimental measurements on the small samples 1" X 1" cross-section. The work was done on the following stages

Calibrating the Mechanical Model Parameters

This was done by simulating the mechanical tests done on similar specimens which were three point bending tests (Fig. 3.4a) and by matching the unconfined compressive strength reported in the same experiment which was 40.70 MPa [22].

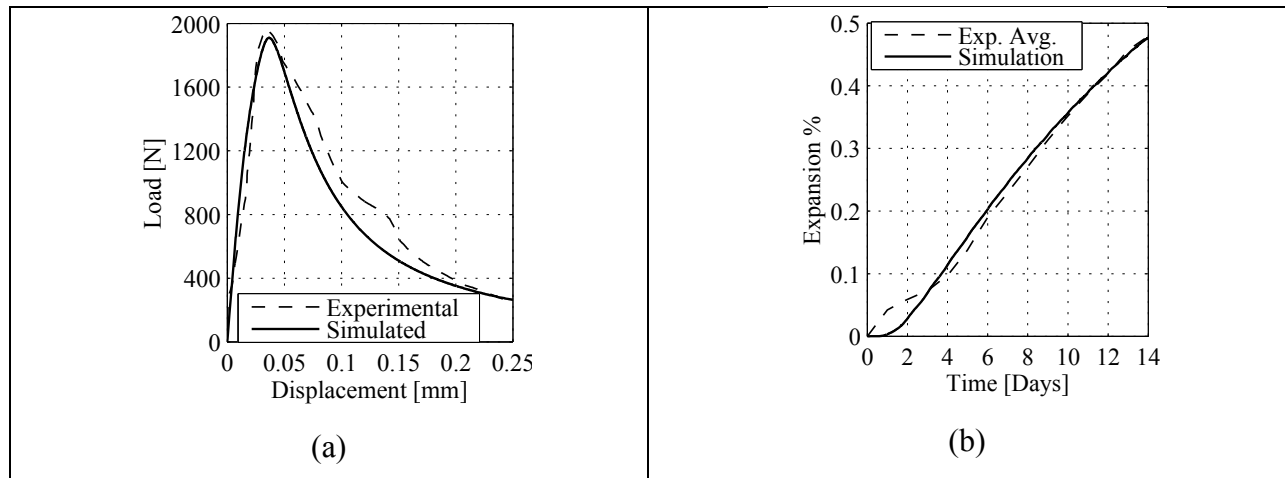


Figure 3.4: a) Calibration results for the Mechanical model parameters on 3 Point bending test b) Calibration results for the ASR model parameters on expansion of small specimens

Calibrating the ASR Model Parameters

This was done by simulating matching the average expansion of small specimens (Fig. 3.4b). In this simulation, the diffusivity of alkalines was assumed based on experimental values from literature [21].

Numerical Simulation of Ultrasonic Wave Experiment

A pressure wave was applied at different time intervals on one side of the simulated specimen by applying a sinusoidally varying pressure load with 0.25 MHz frequency. On the opposite side, the velocity of the nodes corresponding to the receiver area was gathered over time as shown schematically in Fig. 3.5.

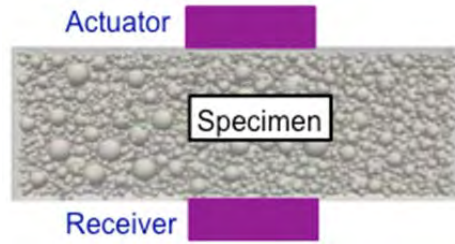


Figure 3.5: Schematic drawing of the experiment simulation

Both velocity histories are shown in Fig 3.6a. By doing FFT (Fast Fourier Transform) of the received signal, a clear second harmonic can be found, which shows the capability of the model to reproduce acoustic nonlinearity behavior (Fig. 3.6b). The change in acoustic nonlinearity over the test period is simulated by doing the same simulation at different time points (2, 4, 8 ..., 14) days, then a numerical β can be defined as $\beta = a_{\omega}/a_{2\omega}^2$ assuming that the initial numerical β_0 equals zero (corresponding to zero initial cracking in the model), the normalized β can be calculated as

$$\bar{\beta}_{num} = \frac{\beta}{\beta_{max}} \quad (3.7)$$

The model results show very good agreement with the numerical data, which suggests a large dependence of the acoustic nonlinearity on cracking. Fig. 3.6c shows the normalized numerical and experimental values.

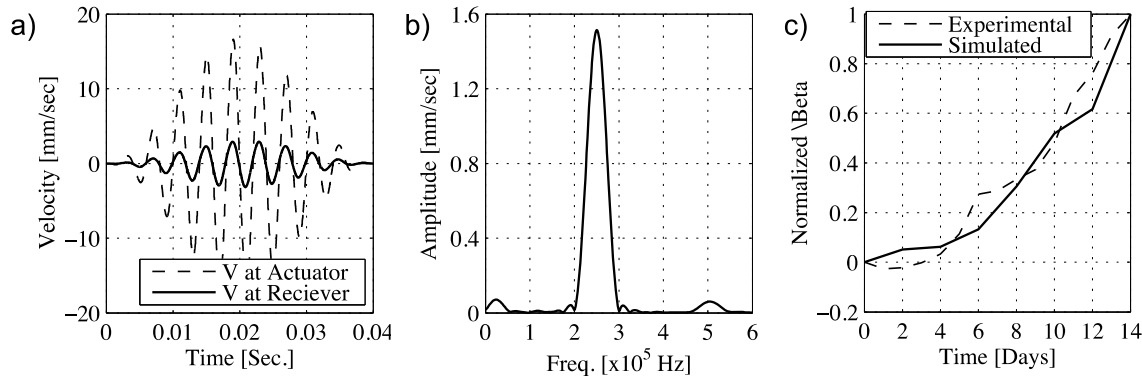


Figure 3.6: a) Sent and received velocities, b) Frequency content of received signal, and c) Experimental and numerical acoustic nonlinearity change.

REFERENCES

1. AASHT, *Standard method of test for accelerated detection of potentially deleterious expansion of mortar bars due to alkali-silica reaction*, in *Standard specifications for transportation materials and methods of sampling and testing Part 2B: Tests* 2006, American Association of State Highway and Transportation: Washington D.C.
2. Officials, A.C., *Standard Test Method for Potential Alkali Reactivity of Aggregates (Mortar-Bar Method)*, 2007, ASTM International, West Conshohocken, PA.
3. Multon, S., A. Sellier, and M. Cyr, *Chemo-mechanical modeling for prediction of alkali silica reaction (ASR) expansion*. Cement and Concrete Research, 2009. **39**(6): p. 490-500.
4. Liu, M., et al., *A nonlinear wave mixing method for detecting Alkali-Silica reactivity of aggregates*. Review of Progress in Quantitative Nondestructive Evaluation, 2012. **1430**(1524-1531).
5. Shen, C.H. and G.S. Springer, *Moisture Absorption and Desorption of Composite-Materials*. Journal of Composite Materials, 1976. **10**(Jan): p. 2-20.
6. Suwito, A., et al., *A mathematical model for the pessimum size effect of ASR in concrete*. Concrete Science and Engineering, 2002. **4**: p. 23-34.
7. Jin, W., *Alkali-silica reaction in concrete with glass aggregate - A chemo-physico-mechanical approach*, 1998, Columbia University: New York.
8. Tang, G., L.J. Jacobs, and J. Qu, *Scattering of time-harmonic elastic waves by an elastic inclusion with quadratic nonlinearity*. Journal of the Acoustical Society of America, 2012. **131**(4): p. 2570-2578.
9. Nagy, P.B., *Fatigue damage assessment by nonlinear ultrasonic materials characterization*. Ultrasonics, 1998. **36**(1-5): p. 375-381.
10. Cantrell, J.H. and W.T. Yost, *Nonlinear ultrasonic characterization of fatigue microstructures*. International Journal of Fatigue, 2001. **23**: p. S487-S490.
11. Pruell, C., et al., *Evaluation of plasticity driven material damage using Lamb waves*. Applied Physics Letters, 2007. **91**: p. 231911.
12. Bermes, C., et al., *Nonlinear Lamb waves for the detection of material nonlinearity*. Mechanical Systems and Signal Processing, 2008. **22**(3): p. 638-646.
13. Muller, M.F., et al., *Characteristics of second harmonic generation of Lamb waves in nonlinear elastic plates*. Journal of the Acoustical Society of America, 2010. **127**(4): p. 2141-2152.
14. Liu, M., et al., *Experimental study of nonlinear Rayleigh wave propagation in shot-peened aluminum plates-Feasibility of measuring residual stress*. Ndt & E International, 2011. **44**(1): p. 67-74.
15. Matlack, K.H., et al., *Experimental characterization of efficient second harmonic generation of Lamb wave modes in a nonlinear elastic isotropic plate*. Journal of Applied Physics, 2011. **109**(1).
16. Cantrell, J.H., *Substructural organization, dislocation plasticity and harmonic generation in cyclically stressed wavy slip metals*. Proceedings of the Royal Society of London Series a-Mathematical Physical and Engineering Sciences, 2004. **460**(2043): p. 757-780.
17. Cantrell, J.H., *Fundamentals and Applications of Nonlinear Ultrasonic Nondestructive Evaluation*, in *ULTRASONIC NONDESTRUCTIVE EVALUATION - Engineering and Biological Material Characterization*, T. Kundu, Editor. 2004, CRC Press LLC.

18. Cantrell, J.H. and W.T. Yost, *Effect of precipitate coherency strains on acoustic harmonic generation*. Journal of Applied Physics, 1997. **81**(7): p. 2957-2962.
19. Alnaggar, M., G. Cusatis, and G. Di Luzio, *Lattice Discrete Particle Modeling (LDPM) of Alkali Silica Reaction (ASR) deterioration of concrete structures*. Cement & Concrete Composites, 2013. **41**: p. 45-59.
20. Schaufert, E.A. and G. Cusatis, *Lattice Discrete Particle Model for Fiber-Reinforced Concrete. I: Theory*. Journal of Engineering Mechanics-Asce, 2012. **138**(7): p. 826-833.
21. Schaufert, E.A., et al., *Lattice Discrete Particle Model for Fiber-Reinforced Concrete. II: Tensile Fracture and Multiaxial Loading Behavior*. Journal of Engineering Mechanics-Asce, 2012. **138**(7): p. 834-841.
22. Yazıcı, H., *The effect of steel micro-fibers on ASR expansion and mechanical properties of mortars*. Construction and Building Materials, 2012. **30**: p. 607-615.

III.2 Report of the 2nd year

III.2.1 Calculation of ASR Activation Energy

Introduction of Activation Energy

Alkali-silica reaction (ASR) is a deleterious chemical reaction. To predict ASR damage in concrete, the study on reactivity of ASR is needed and it is closely related to the activation energy the ASR. Activation energy is considered as the height of the potential barrier for a chemical reaction and it can be obtained experimentally.

Weight Loss Measurement

As a fundamental approach to study characteristics of ASR, measurement of weight loss of reactive aggregates was carried out. This experiment is mainly for calculating the reaction rate of ASR from which activation energy can be gained. To this end, aggregates were placed in each container filled with 0.5N, 2N and 4N alkali solutions, respectively. Each container contains 10 aggregates. These containers are then placed in environmental chambers with the temperature set at 40 °C, 60 °C and 80 °C, respectively, see Fig. 1-1.

The aggregates were taken out from the containers each day at the same time. They were first rinsed in clean water carefully to wash off the gel grow on the surface. Then, they were placed on a high-accuracy scale one at a time to measure their individual weight loss after weight loss.

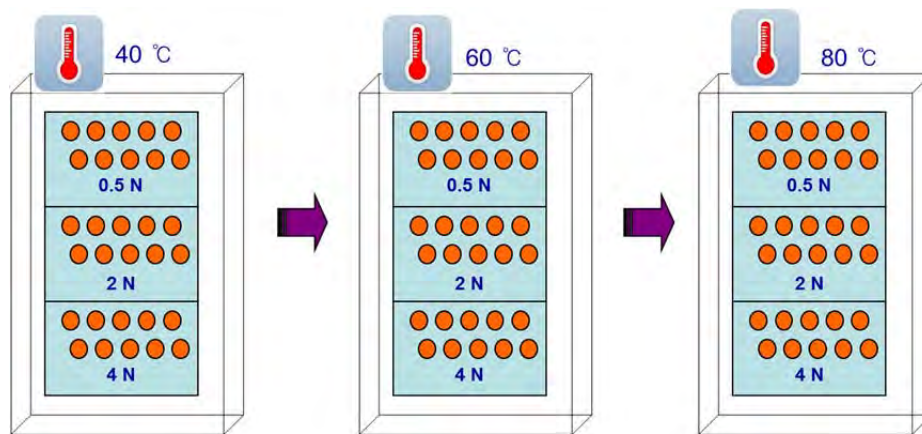


Fig.1-1 Experimental Setup

Activation Energy Calculation

As shown in Fig. 1-2, the weight loss represents the amount of aggregates being consumed by the ASR. Therefore, it is proportional to the ASR rate. Thus, the ASR rate constant k can be calculated by taking the derivative of the weight loss ΔW with respect to time.

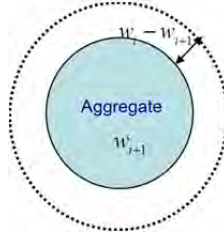


Fig. 1-2 weight loss of an aggregate

In other words, the rate of ASR is $r = \Delta W / \Delta t \propto k$. We note that all quantities are temperature dependent. On the other hand, rate of reaction should satisfy the Arrhenius' equation,

$k = A \exp(-\frac{E_a}{RT})$, where A is a constant, R is the standard gas constant, and T is the absolute

temperature. Thus, one may write $\Delta W / \Delta t = A \exp(-\frac{E_a}{RT})$. From this equation, the activation energy can be written as $E_a = RT \log A - RT \log(\Delta W / \Delta t)$.

Experiment Results

Fig. 1-3 shows that %weight loss of aggregates caused by ASR with respect to the exposure time of aggregates to alkali solution where % weight loss is defined as $(-\Delta W / W) \times 100$.

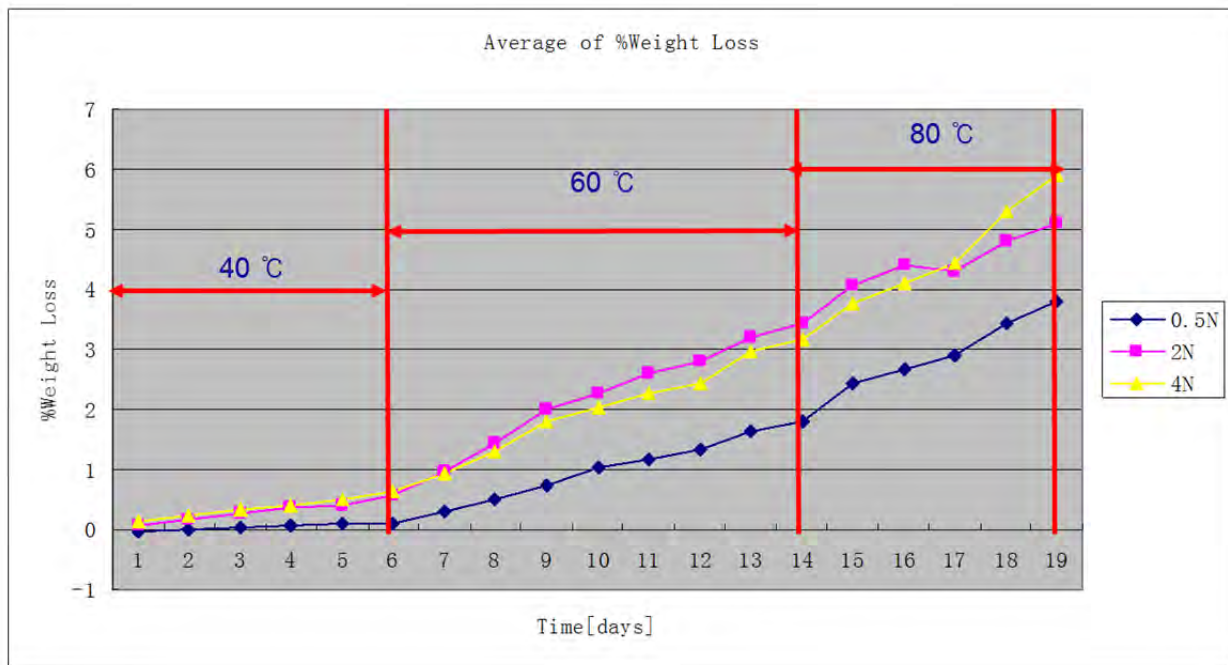


Fig. 1-3 %Weight Loss of Aggregates

Several observations can be made. (1) The $\Delta W/W$ vs. time curves are straight line for a given temperature; (2) the slope of the $\Delta W/W$ vs time curves increases with increasing temperature, thus the rate of reaction increases with increasing temperature; (3) $\Delta W/W$ increases with increasing alkali concentration, but the slope of the $\Delta W/W$ vs time curves do not seem to change much with the alkali concentration.

We note that the experimental data shown in Fig. 1-3 is the average of 10 aggregates under each condition. The raw data are rather scattered. Careful analysis seems to show that the scatter is primarily due to the variation among the individual aggregates, particularly their shape and size. Next quarter, we plan to use glass beads to repeat the measurements.

III.2.2 Physics-based Models that Correlate the ANLP to ASR Damage

Nonlinear Alkali Diffusion

Ion diffusion involves very complicated phenomena that usually require multi-physics formulations. For the special case of AMBT, the specimen is almost fully saturated and any loss of saturation due to self dissection can be quickly compensated as the thickness of bars is relatively small. Assuming no water macro diffusion allows for simplifying the alkali ion diffusion using a nonlinear diffusion problem. While there are many researches available in literature on ion diffusion through concrete, very limited amount is dealing with alkali diffusion modeling and most of the literature deals with chloride ingress into concrete as part of corrosion modeling of RC structures. Adding to that, the very limited experimental data, as the diffusion measurements are not required by code standards and also are not easy to measure, a reasonable general model for nonlinear ion diffusion was adopted based on [1]. The model assumes that the nonlinearity comes from two parts, ion binding to the solid C-S-H gel, and nonlinearity of the diffusion coefficient. A further simplification of this model can be obtained by considering the special case of sodium ion diffusion. For sodium, experimental data by [2] suggested a constant distribution ratio of sodium concentration in pore solution and C-S-H structure which means a linear relation between the binding capacity and concentration. So, one can eliminate the nonlinearity coming from the binding capacity and simply solve a nonlinear diffusion problem with nonlinear diffusion coefficient D_i .

$$\frac{dc_i}{dt} = \nabla \cdot (D_i(c_i) \nabla c_i)$$

The shape of the diffusion coefficient D_i dependence on alkali concentration c_i is assumed to be similar to the water diffusion coefficient in [3] as follows;

$$D_i(c_i) = D_{max} \left[1 + \left(\frac{D_{max}}{D_{min}} - 1 \right) \left\langle 1 - \frac{c_i}{c_i^{max}} \right\rangle^n \right]^{-1}$$

Where D_{max} is the maximum diffusion coefficient corresponding to a specific alkali concentration c_i^{max} , D_{min} is a minimum diffusion coefficient at zero alkali concentration and n is assumed to be a material parameter. Figure 1a shows the change of the diffusion coefficient as a function of the alkali concentration. The solution of the diffusion problem is carried out using explicit 3D forward Euler discretization. Space discretization is within the size of the minimum simulated aggregate size. The calculation of time step was done considering the maximum anticipated diffusion coefficient (which represents the PDE traveling speed). At each LDPM mesh node, space and time interpolation is performed to feed the ASR-LDPM model with the evolution of alkali content c_a over time. Note that the diffusion solution is in concentration units c_i (mole/liter) while the ASR model uses alkali content units c_a (kg/m³), so the values are converted using the molar weight of NaOH of 40 gm/mole which gives $c_a = 40 c_i$.

The next step was to calibrate the ASR and diffusion parameters. Due to lack of experimental data, only guidelines about diffusion parameters were available. Calibration was performed on two steps: first, using a simplified 2D linear diffusion model with the $D_{xy}=1.2\text{e-}6$ m²/s as reported in [4], the ASR parameters were calibrated to match the expansions of the small specimens, then, fine tuning of the ASR parameters and the 3D nonlinear diffusion model parameters was performed to match both expansions of the small and large specimens.

The analyzed experiments are relevant to (1) a very accelerated reaction, (2) all aggregate are reactive; and (3) very high temperature of 80 C. Under these conditions it is likely that all pores

surrounding each reactive aggregate surface were filled quickly with ASR products during curing. In this case, it is reasonable to assume δ_c . In addition, since the experimental data did not contain information on temperature effect, the reference temperature T_0 was assumed to be equal to the room temperature (80 C= 353 K) at which the experiments were carried out.

The remaining ASR parameters were calibrated with the diffusion parameters and gave the values ($a_{s0}=7.8125*10^{-11}$ m²/day, $C_0^i=5.51*10^{-13}$ m²/day, $\eta=10,000$ kg⁻¹, $c_a^0=0.50$ kg/m³, $c_a^l=25.0$ kg/m³, $D_{max}=2*10^{-5}$ m²/day, $D_{min}=2*10^{-6}$ m²/day, $n=3$, $c_i^{max}=1.00$ mole/liter. Figure 1b,c show the alkali concentration distribution over the cross section of the small and large specimens at their center after 14 days respectively. The large specimens show very limited extent of alkali, while the small one has been fully saturated with alkali after 14 days. The results of this difference can describe the lower expansions measured on large specimens and also it gives reasons for the cracking recorded both experimentally and numerically as will be discussed later. Finally, the simulated expansions of both small and large specimens are compared with the averages of experimental data as shown in fig. 1d. It should be noted that the measurement on experimental specimens were taken between the center points of the specimen ends, and for very small expansions, heterogeneity and initial errors can be large, and that is why the measurements in the beginning look unusually large.

Simulation Results

Here, the results of simulation are shown. Simulations were carried out on half-length specimens (125 mm out of the 250 mm length) to reduce computational cost by making use of symmetry. At the centerline, symmetry restraints were applied. The actuators and receivers were simulated by square areas of 15 mm edges aligned on opposite faces. The simulation of ultrasonic wave was done by applying a sinusoidal varying pressure at a frequency of 0.25 MHz on the actuator area. The pressure replicates the applied wave from the actuator. Arrangement of actuators and receivers is shown in fig. 1e. As the explicit algorithm used for solving the dynamic equation of motion is based on a mid point equation for the velocity, this means that the velocity has a second order accuracy while displacement is only first order, so, the measured quantity at both actuators and receivers was the velocity. A typical velocity time history at the actuator and the corresponding received one at the receiver is shown in fig. 1f. The frequency domain of the received velocity signal is obtained by using Fast Fourier Transformation (FFT). As, shown in fig. 1g, the amplitudes of first and second harmonics (amplitudes at the fundamental frequency of the incident wave and at twice that frequency) are extracted and β is calculated. The simulations for ultrasonic wave effect are very expensive computationally, because it requires a very small time step to be able to replicate the very high frequencies generated. In this simulation, a time step of $2.5*10^{-9}$ sec was used. This time step allows the sampling of one cycle at 0.25 MHz with 1600 points and at 0.50 MHz (second harmonic frequency) with 800 points. With this sampling, the accuracy of capturing high frequencies was achieved. Here, it should be mentioned that the natural time period of the smallest element in the model (which controls the maximum stable time step for the explicit algorithm) was $1.4*10^{-7}$ sec, so the used time step was about 1/56 times the smallest time period. Simulation of ultrasonic measurements was done at two days intervals, so for both small and large specimens, simulations were done at 2,4,6,8,10,12 and 14 days. For each time, the ASR expansion simulation is held still and the ultrasonic wave is introduced.

For the small specimens, 3 different geometries were generated. For each half specimen, the four actuators shown in fig. 1e were utilized. For each actuator the pressure wave is sent and the

velocity time history at the corresponding receiver is gathered. After applying FFT, β is calculated for each received wave. The sum of all four values at each time for one specimen, represents its β evolution over time. The values for each specimen are normalized by dividing all of them by the maximum value encountered for this specimen. Finally, the normalized β evolutions of the three specimens were averaged and plotted in fig. 1h versus the average values from experimental data corresponding to 3 specimens with 3 measurements for each. Recalling that the scatter in experimental data is quite big, the simulated values can be generally considered in excellent agreement with experimental ones. To give more insight of the physics involved, the cracking evolution was examined. Normalized average crack volume was obtained by summing the volume of cracks (crack opening of each facet multiplied by its area) at each time point then dividing by the maximum value over time. In addition, normalized maximum crack volume was calculated by recording the maximum crack volume at each time point then dividing by the maximum value over time. Both evolutions are presented in fig. 1h. While both evolutions correlate very well with both experimental and numerical evolutions for β , the maximum crack volume is closer to the experimental data and seems to be an average curve of the numerical simulations, while the average crack volume is matching the numerical β evolution exactly from 4 to 8 days, but it deviates a little more than the maximum crack volume curve later. Regardless of these very slight deviations, the correlation between acoustic nonlinearity and cracking volume is very evident and clear from fig. 1h.

Large specimens are extensively computationally demanding (its cost is 16 times the cost of small specimen) so, only one half specimen was used for ultrasonic simulation. It should also be mentioned here that, with larger specimens and distributed damage, difference in simulated response due to difference in samples is very small and can be safely neglected. The values of β were obtained from the first 3 receivers and the 4th was neglected because it was too close to the boundary zone here. The results obtained at each receiver were summed and normalized by their maximum value. Experimental values were obtained by averaging the evolutions of two large specimens and plotted along with numerical β evolution in fig. 1i. Even more accurate results were obtained here. Only very slight deviation at 8 and 14 days. But it should be noticed that the experimental data again showed a big amount of scatter. For the crack volume correlation, it is also clear from fig. 1h that both maximum and average crack volume evolutions are perfectly correlated with both experimental and numerical β evolutions. Here it is actually very hard to tell which crack volume evolution matches better as both are very close.

In summary, figs 1h and i show that the evolution of acoustic nonlinearity parameter in concrete is mostly a function of the amount of cracking.

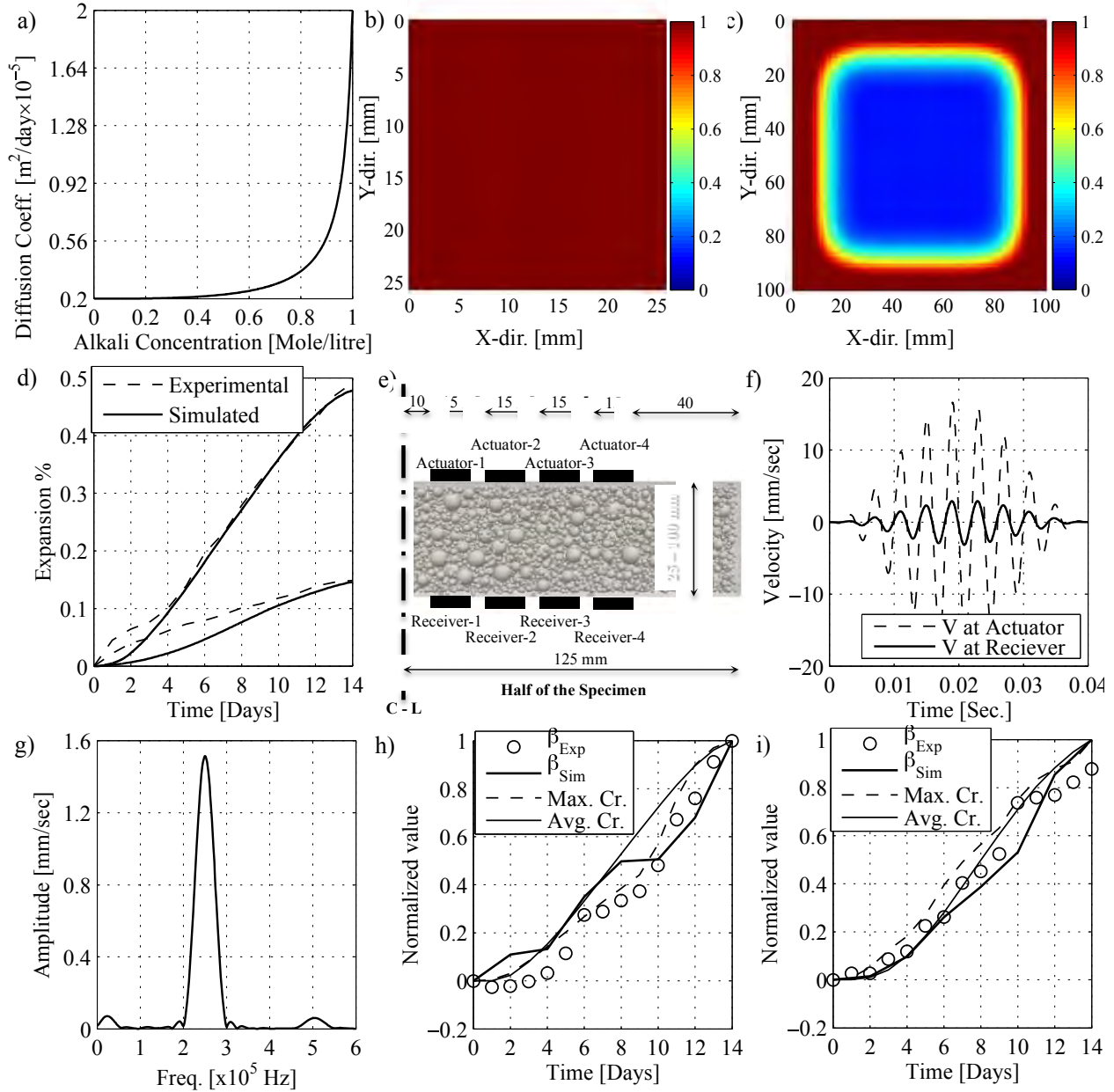


Figure 1: a) Nonlinear alkali diffusion coefficient change with alkali concentration. b) Alkali Concentration [mole/litre] distribution over mid section of small specimen at 14 days. c) Alkali Concentration [mole/litre] distribution over mid section of large specimen at 14 days. d) Axial expansion evolution for small and large specimens. e) Actuator and receiver positions on simulated half specimens. f) Typical velocity time histories at an actuator and the corresponding receiver. g) Typical frequency content of the velocity time history at the receiver. h) Experimental and numerical β evolution for small specimens with normalized maximum and average crack volume evolution. i) Experimental and numerical β evolution for large specimens with normalized maximum and average crack volume evolution.

REFERENCES

- [1] Y. Xi and Z. P. Bazant, "Modeling Chloride Penetration in Saturated Concrete", *Journal of Materials in Civil Engineering*, 11(1):58--65, 1999.
- [2] S.-Y. Hong and F. Glasser, "Alkali binding in cement pastes Part I. The C-S-H phase", *Cement and Concrete Research*, 29:1893--1903, 1999.

- [3] G. Di-Luzio and G. Cusatis, “Hygro-thermo-chemical modeling of high performance concrete. I: Theory”, *Cement and Concrete Composites*, 31(5):301--308, 2009.
- [4] S. M. Shafaatian, A. Akhavan, H. Maraghechi, and F. Rajabipour, “How does fly ash mitigate alkalisilica reaction (ASR) in accelerated mortar bar test (ASTM C1567)?”, *Cement and Concrete Composites*, 37:143--153, 2013

III.2.3 Rate of Moisture Diffusion in Cement Pastes and Alkaline-Silica Reaction

Introduction

In this task, we focus on experimental investigation of the diffusivity of moisture in cement pastes and the rate of ASR. To this end, 2" (5.08cm) cubic hydrated cement paste samples were prepared and their moisture absorbing behaviors were observed. It was found that higher concentration of alkali solution encourages the sample to absorb more amount of water from the solution. In addition to the weight gaining measurement, the microcopy was taken to see cross sectional area of each sample. A measurement with a glass bead was also carried out where reaction speed of silica with respect to different degree of alkalinity was found.

Sample preparation

2" (5.08cm) cubic hydrated cement paste samples were prepared. The type I cement (potential Bogue composition 46.11% C₃S, 22.93% C₂S, 8.52% C₃A and 9.59% C₄AF and 0.83% Na₂O_{eq}) is used. Aggregates which are usually mixed with cement to make a normal concrete are replaced by a single glass bead for this experiment to make the bead serve as an only agent providing siliceous ion. The photo of the glass beads are shown in Fig. 1 and its diameter is approximately 10mm. The composition of the glass bead is described in Table 1. While sand and gravel are added to cement mixture to make a usual concrete, only cement powder and a glass bead are mixed with water to make this sample. This measurement has been done twice with water to different water to cement ratio and different range of various concentrations.



Fig. 1 Soda-Lime Glass Bead

Table1. Chemical composition of glass bead

Properties	Chemical Composition wt%
SiO ₂	74
Na ₂ O	13
CaO	10.5
Al ₂ O ₃	1.3
K ₂ O, SO ₃ , MgO, Fe ₂ O ₃ and TiO ₂	0.45

A planetary mixer was used for the mixing and well mixed cement paste was poured into the

molds as shown in Fig. 2.



Fig. 2 Pouring cement paste into 2" cubic molds

4 batches of different concentration solution were prepared which vary from 0N to 4N where 1N indicates 40g of NaOH beads per a liter of pure water. Prepared 6 samples were put into the batches. 6 samples were divided by two categories; 3 samples have the glass bead in its body and the other 3 are pure cement block without the bead in side. Finally, total 24 samples were immersed in the solutions and their weight changes were monitored day by day. As an initial temperature, 50°C was chosen.

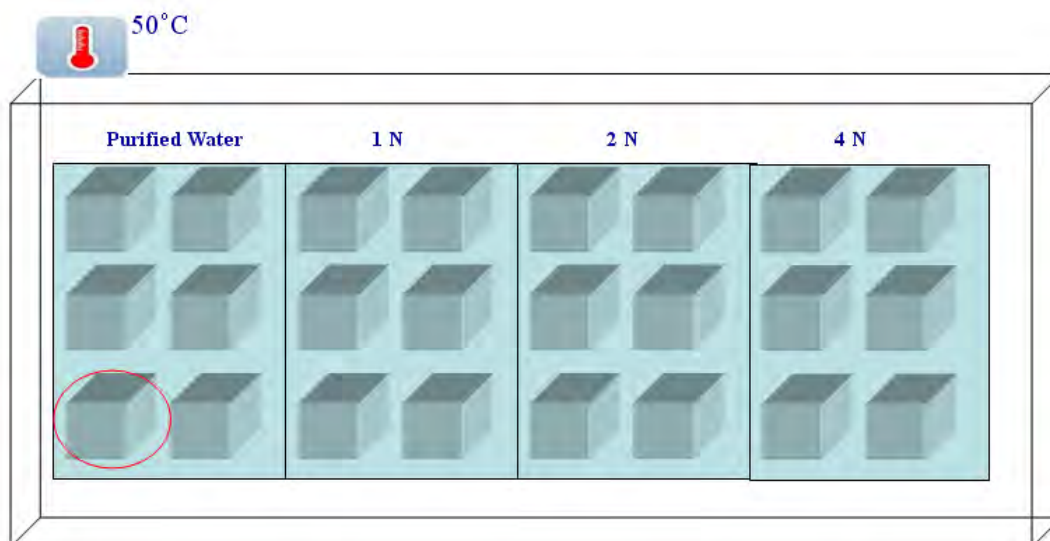


Fig. 3 Schematic diagram of hydrated cement paste sample weight change test

Result of Hydrated cement paste sample weight change with 0.33 w/c ratio

The immersed samples were taken out each day for the weight gaining measurement. Results of the % weight gaining of samples are plotted in Fig. 4 as function of the number of days under 50°C alkali solution exposure by using equation (1).

$$\frac{W_{n^{th} \text{ day}} - W_{\text{initial}}}{W_{\text{initial}}} \times 100(\%) \quad (1)$$

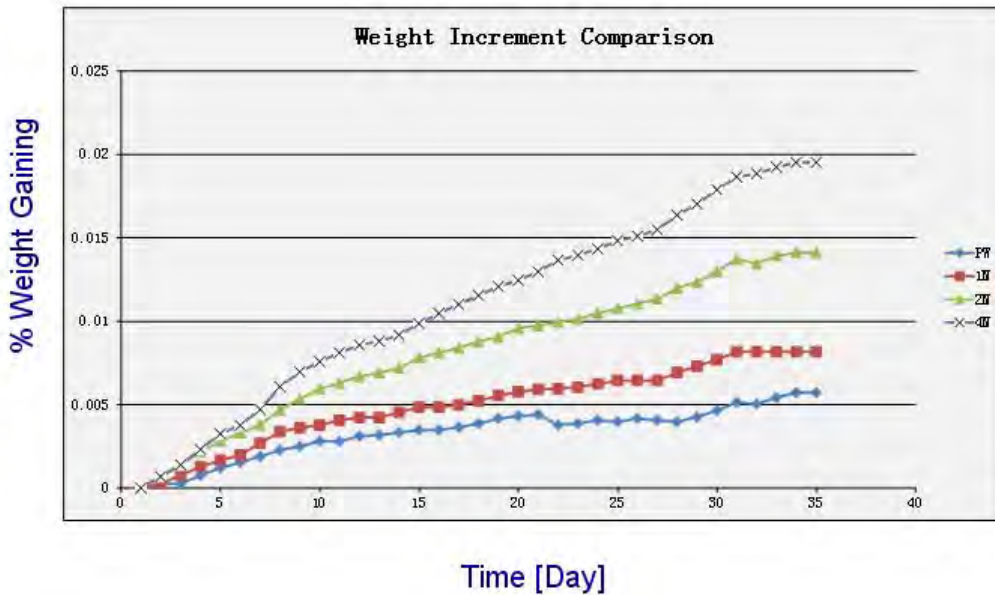


Fig. 4 Result of weight change with 0.33 w/c ratio

It is shown that samples immersed in the alkali solution slowly and continuously absorbed water. From this graph, it is seen that higher concentration enhances the amount of water absorbed by the sample. However, the result can be considered as initial weight gaining of the sample due to its slow water absorption and it shows that it is necessary to accelerate of the test by modifying experimental setup.

Result of Hydrated cement paste sample weight change with 0.5 w/c ratio

To accelerate the test speed and reach the plateau of the weight gaining result, some experimental conditions are modified. Firstly, water/cement ration increased from 0.33 to 0.5 for the sample to have more pores which are used as the path of water absorption. Secondly, hydrated cement paste samples were prepared by taking initial treatment procedure described by AASHTO T 303 where all samples are immersed in 80°C pure water for 24hours. Lastly, the variation range of concentration is changed to have finer increment step.

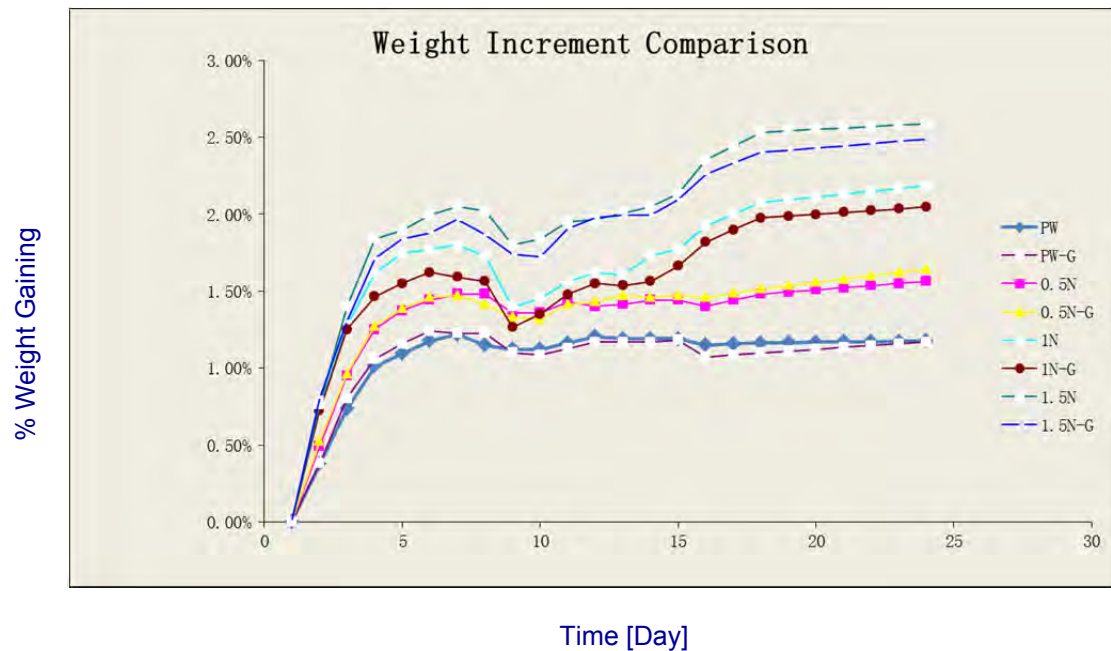


Fig. 5 Result of weight change with 0.5 w/c ratio

Fig. 5 shows the result of weight gaining test with respect to different concentration. Here, the sample whose name has 'G' stands for the one having a glass bead inside of the sample. Otherwise, samples do not have a glass bead; pure cement sample. It is seen that initial slope of the weigh gaining during the first 4 days varies with different concentration. Here the graph shows higher concentration solution has steeper slope. Moreover, the data sets reach saturation point in 18 days and it is interestingly seen that higher alkalinity induces more water absorption. Its reason is being sought for and will be explained in the next quarterly report.

Microscopy

The sample embedded in Alkali solution after 25 days and 60 days were cut to see cross-section. The microscopy specimens were then polished on a grinder/polisher to make the surface clearly visible. Digital images of the surface were taken.

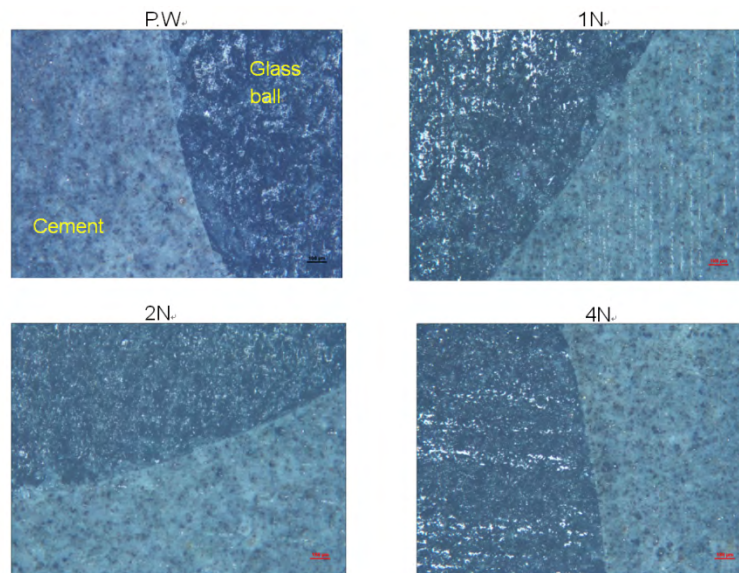


Fig. 6 Microscopy in the sample after 25days

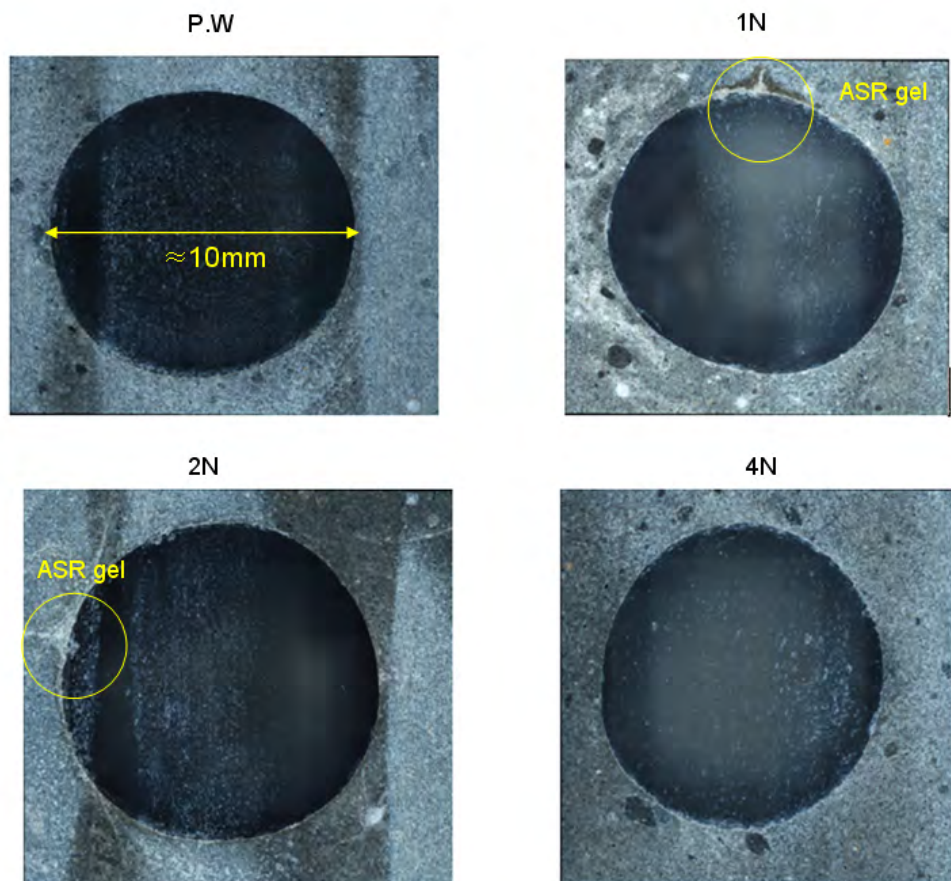


Fig. 7 Microscopy in the sample after 60 days

As shown in Fig 6, darker part is glass bead and brighter part is cement. ASR gels are hardly found with the samples after 25days of exposure. On the other hand, the cross sectional areas of

the samples immersed into the solution for 60 days show ASR gel produced around the surface of the glass bead as shown in Fig 7. As expected, the sample with pure water does not seem to have any ASR gel while alkali solution immersed sample has. From these figures of 1N, 2N and 4N, once ASR gel is produced, it begins to be diffused into pores by compensating the vacancy.

Glass bead weight change

In the same way, glass beads were also immersed in alkali solution. Fig. 8 shows the schematic diagram of weight loss measurement. 3 glass beads were put into the solution with the same set of concentration used for hydrated cement paste test and were taken out to check amount of weight loss periodically. Temperature of the test will increase from 50°C to 70°C and each solution has three glass beads. The results were plotted based on equation (2).

$$\frac{W_{\text{initial}} - W_{n^{\text{th}} \text{ day}}}{W_{\text{initial}}} \times 100(\%) \quad (2)$$

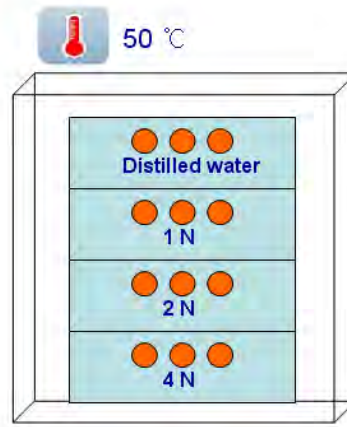


Fig. 8 Schematic diagram of glass bead weight measurement

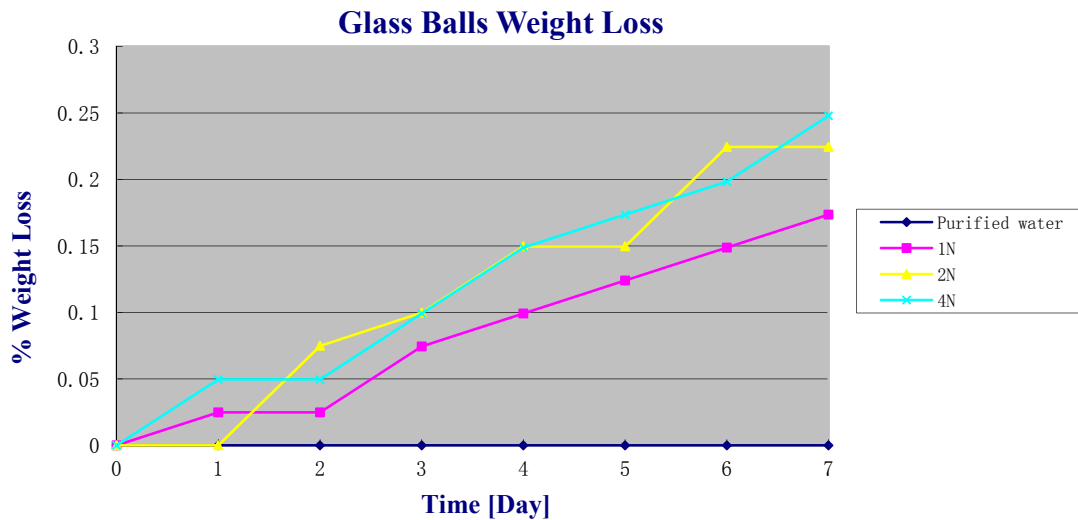


Fig. 9 Result of glass bead weight loss test

The result of a case with 50°C is shown in Fig. 9. The sample in pure water does not lose its

weight. It is seen that 2N and 4N solution samples have higher reactivity than 1N samples. However, the difference between 2N and 4N samples is hardly found because the normality of the 2 alkali solutions are high enough so that it can be beyond saturation point. So, it is needed to modify experimental set up by lowering concentration level and making an increment step finer. Fig. 10 shows the result of weight change with the other sets of solutions.

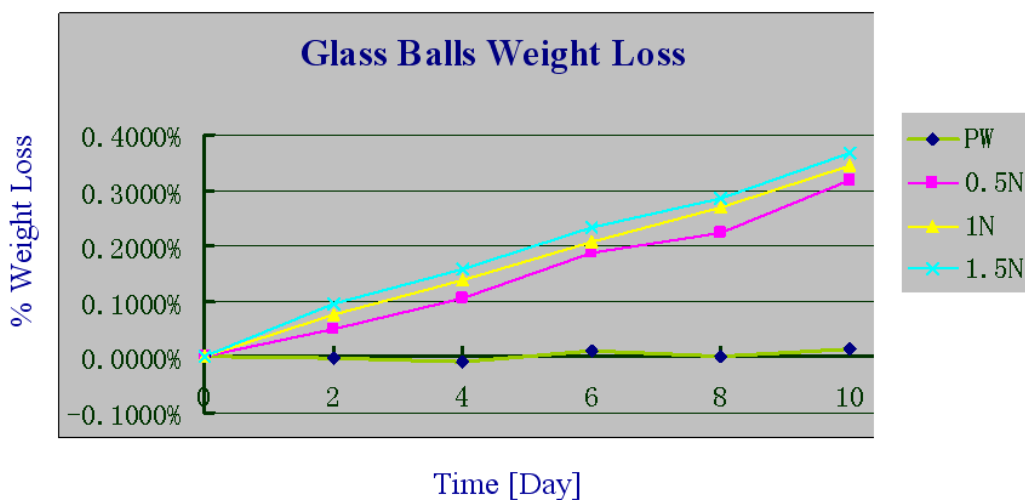


Fig. 10 Result of weight loss test with lower range of concentrations

As expected, the sample in pure water still does not lose its weight although tiny fluctuation is found due to experimental error. Of course, it is seen that higher alkali solution has higher reactivity with the glass beads. The test will be implemented with different temperatures and those results will be ultimately used to set the equation of activation condition as function of concentration and temperature

III.2.4 ASR Damage Evolution and Acoustic Nonlinearity Parameter

In this work, the following tasks were performed through conducting a parametric analysis.

1. Physics-based models that correlate the ANLP to ASR damage
2. Physics-based models for ASR damage evolution

Parametric analysis

The previously formulated and presented ASR-LDPM model is capable of replicating concrete damage due to ASR [Alnaggar 2013]. In the previous reports, the model was calibrated to replicate the expansions for small and large specimens.

While the Accelerated Mortar Bar Test (AMBT) specimens are tested in free expansion, real structural elements are in most cases experiencing ASR expansions under some case of stress or confinement. AMBT specifications don't require any assessment for stress effects on expansion and as mentioned before they don't require any strength testing. In this parametric analysis, the behavior of a mortar bar $50 \times 50 \times 100$ mm ($2 \times 2 \times 4$ in) is investigated. The same previously identified parameters are used. The AMBT test is simulated and both expansions and ultrasonic measurement simulations are presented. Two expansion cases are simulated for the bar, one with free expansion and the second with 10 MPa axial compression load. In addition, the compressive strength reduction for both cases is investigated. As the specimen now is much shorter (only 100 mm), two ultrasonic measurement locations are only feasible to avoid being close to the boundary, which were at the specimen center measuring in X-X direction and in Y-Y direction. The ANLP results of both directions are summed up and then normalized.

Figure 1a shows the different strain components of the volumetric expansion for the free expansion case, which is a unique feature of ASR-LDPM. The amount of ASR gel expansion estimated by the model is about 1 quarter of the total observed macroscopic expansion, leaving 3 quarters for cracking. In case of the 10 MPa axial compressive load, the amount of cracking was slightly reduced as can be seen from fig. 1b. On the other hand, ASR-LDPM was able to capture the redirection of cracking under loading as shown in fig 1c, where the crack pattern for free expansion case is almost random with no preferential directions while the 10 MPa forced the closure of horizontal cracks, which redirected the cracks in vertical direction. Figure 1d shows the ANLP evolution change for both free expansion and 10 MPa load case, where the loaded case response had a higher average value of ANLP in the early stages up to 10 days, then it started to be less than the free case. In the beginning, the load prevents cracking in the horizontal direction and this redirects the crack only in the vertical direction which means that at the same time, the crack openings in case of free expansions are smaller compared to the ones in loaded case, because the loaded case has to show almost the same crack volume but only in vertical direction. But as cracks grow, the chance for more cracking increases in the case of free expansion and result in more clear cracks which can lead to this increase. This can also be related to the fact that in early expansions, the cracks are localized, but as cracking propagates more, they coalesce and thus the effect of directionality reduces. Figure 1e shows the evolution of average crack volume and ANLP for the free expansion case. Here the average crack evolution serve seems to connect the maximas of the ANLP evolution curve or in other words, the ANLP is slightly under estimating the cracking, especially in the early stages. Again, such an effect seems to vanish towards later stages where cracks are not isolated anymore. The loaded case is shown in fig. 1f, where now the average crack volume evolution curve seems to represent a lower minima for the

ANLP evolution curve, or the ANLP is slightly overestimating the average cracking and again, such error minimizes towards late expansion stages. For both cases, figs 1e and f show that the ANLP evolution correlates very well with cracking as already discussed in the previous report.

Now, on the damage side, the effect of bar expansion on compressive strength reduction was simulated by testing the bar in compression uniaxially at 2 day intervals. Strength reduction is shown in fig. 1g. As can be expected from comparing the amount of cracking for both free and loaded cases (fig. 1a and b) the difference in strength reduction is very small as the average cracking strains are very close. To compare with ANLP evolution, the compressive strength evolutions in fig. 1g were used to compute normalized strength reduction evolutions given by $(f_c't - f_c'0) / (f_c'14 - f_c'0)$. Where $f_c't$ is the compressive strength at time t , $f_c'0$ is the original compressive strength before ASR effects (at day 0) and $f_c'14$ is the compressive strength at time 14 days. Figure 1h shows the correlation between compressive strength reduction and ANLP evolution for the free expansion case. Both almost coincide up to 4 days, then after that, the strength reduction seems to be above the ANLP evolution average line up to day 10. Finally, they come to agreement again towards the end. In fact, under uniaxial compression, horizontal cracks close up and transmit the compressive load and what really matter are vertical cracks (recall that horizontal cracks in /RC columns are usually considered safe that is why horizontal splices in columns are accepted). While this is the case for strength, both cracks contribute to the ANLP evolution, and this may cause this difference. To more emphasize this explanation, the loaded case strength reduction and ANLP evolution are shown in fig. 1i. It is clear that the correlation much better for the loaded case, that is because the preloading with 10 MPa closed the horizontal cracks pre-venting them from contributing to the ANLP evolution. This is a very important observation and should be considered in any ANLP correlation to the structural strength. As most structural components are under some type of loading, the strength reduction interpretation based on ANLP tested on free expansion should not be accurately reflective and it is much better to try mimicking the stress conditions of the structure when applying the ANLP testing. On the other hand, this shows also that the use of ANLP testing on the real structure, can give realistic evolution of its strength reduction.

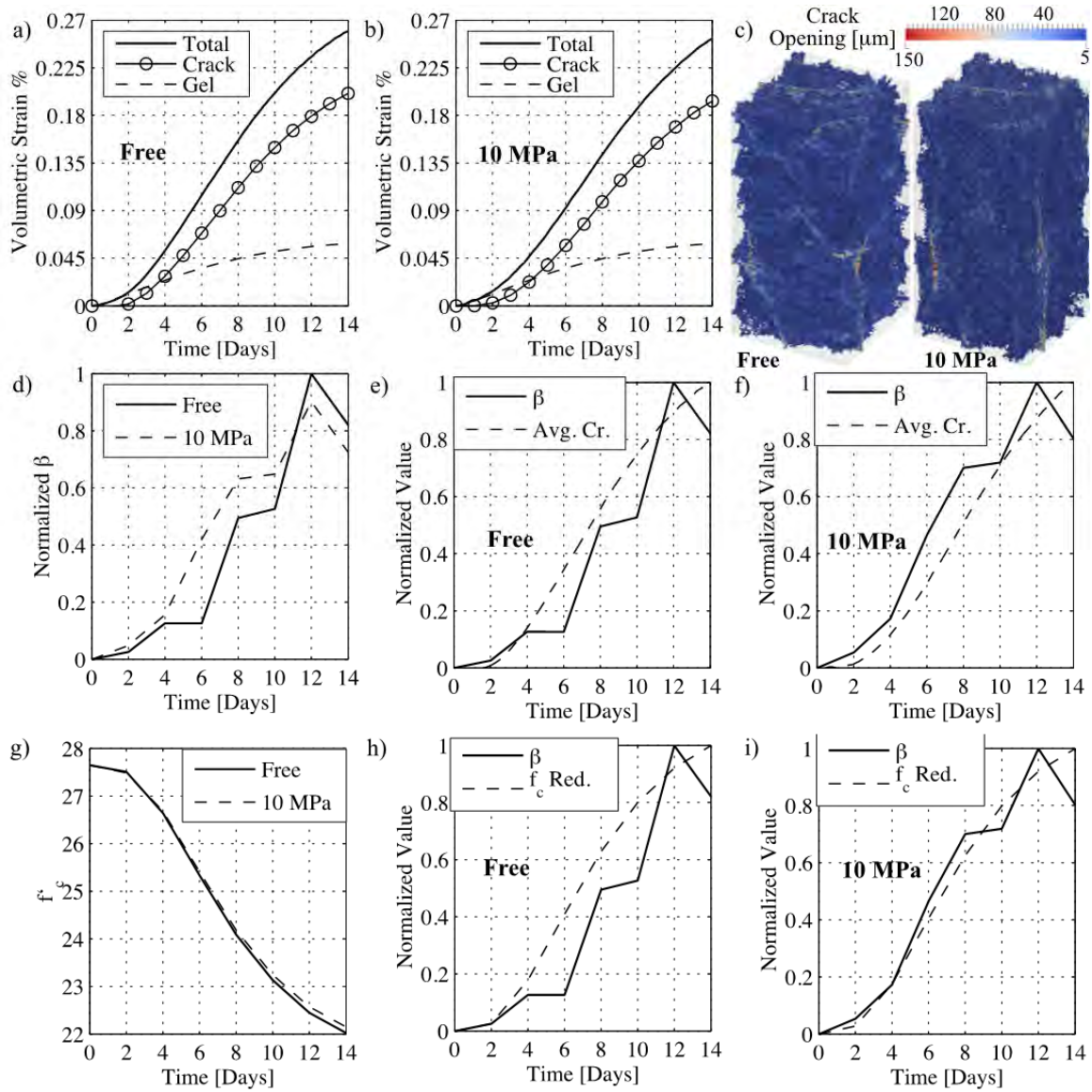


Figure 4: Parametric analysis specimens results for a) Different expansion components under free expansion. b) Different expansion components under 10 MPa axial loading. c) Crack patterns at 14 days in case of free expansion and 10 MPa axial loading. d) Simulated change in ANLP in case of free expansion and 10 MPa axial loading. e) ANLP evolution and average crack volume under free expansion. f) ANLP evolution and average crack volume under 10 MPa axial loading. g) Compressive strength evolution under free expansion and 10 MPa axial loading. h) ANLP evolution and compressive strength reduction under free expansion, and i) ANLP evolution and compressive strength reduction under 10 MPa axial loading.

III.2.5 Modeling ASR Gel Diffusion in Cement Pastes

Introduction

One purpose of present model is simulating, in a continuum constitutive model, the pressure of ASR gel extruded into pores of cement mortar as the ASR gel mass increasing as a function of time. To describe the production of the ASR gel in the mineral aggregate, the classical model of Bazant and Stefens (2000) is adopted. This model is considered as a given input, which predicts the gel mass extruded into the adjacent pores and into cracks developing in the matrix, as a function of time t .

As a result of equilibrating ASR gel pressure in a two-phase medium, the volumetric tensile stress also varies. The two-phase equilibrium equation relating volumetric stress σ_V and pore pressure p has the form:

$$(1 - n)\sigma_V - np = S_V \quad (1)$$

S_V = the total volumetric stress of element; n = porosity. If we consider that, e.g., the expanding element is restrained by an elastic frame of stiffness constant C , we simply have:

$$S_V = C\epsilon_V \quad (2)$$

ϵ_V = volumetric strain. If there is no restraint, then $C = 0$, which gives $S_V = 0$.

To reveal the main qualitative aspects of the problem, the one-dimensional problem of volumetric expansion is considered first. Some of the results for this case are summarized in the following.

Capability of model to simulate ASR gel pressure extruded into the pores of cement mortar surrounding the aggregate

The following figures show evolution of pressure p in the gel and the volumetric tensile stress in the solid phase cause by extruded gel mass increasing in time. Note the differences in stable evolution of post peak damage.

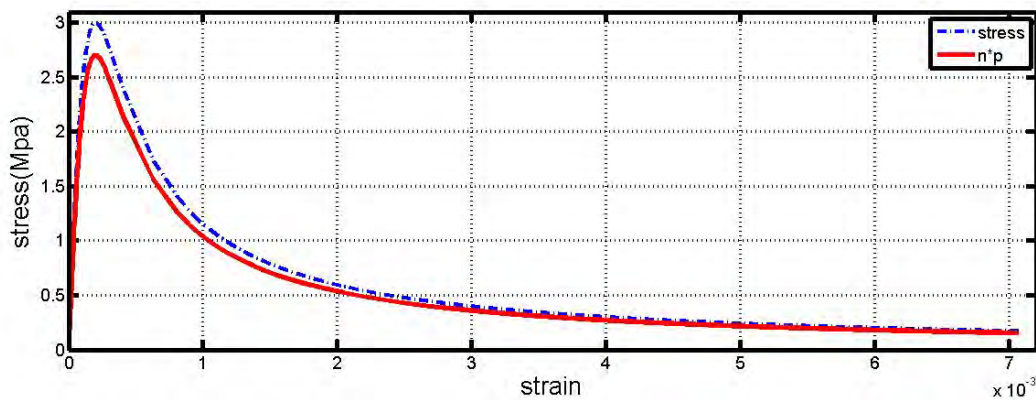


Fig.1 Stress-strain curve of unconfined material element

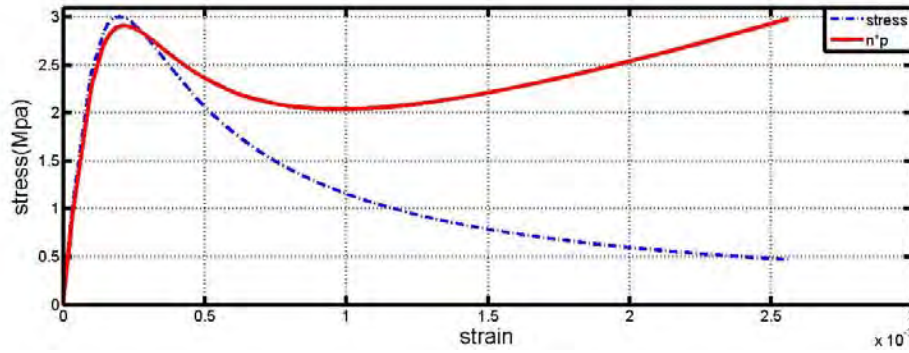


Fig2. Stress-strain curves of material element confined by soft elastic spring ($C=1000$ MPa)

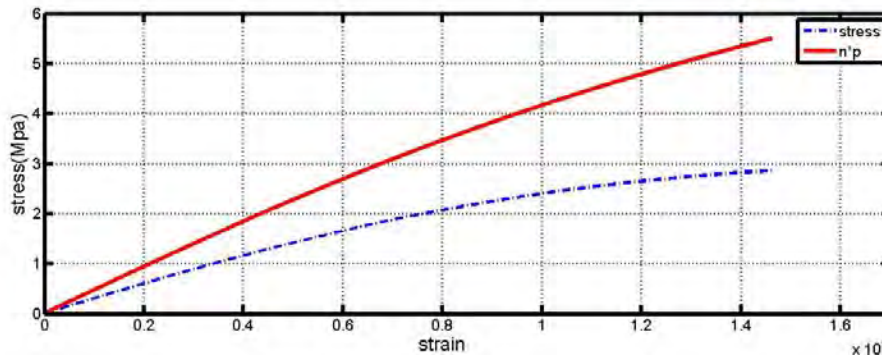


Fig3- Stress-strain curves of material element confined by stiff elastic spring ($C=20000$ MPa)

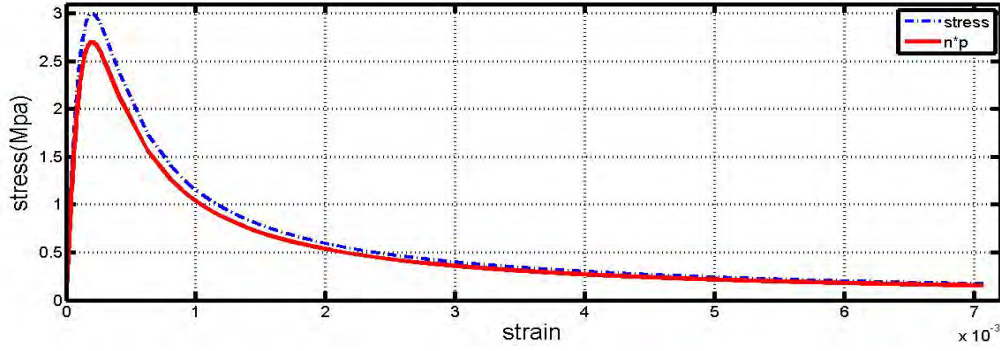
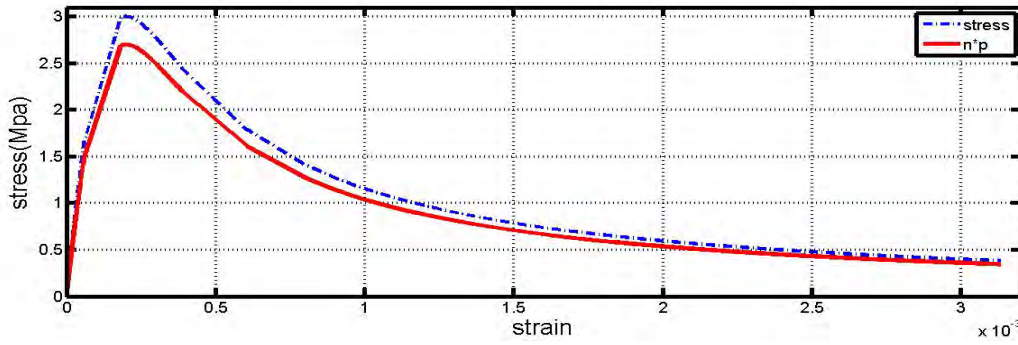
Discussion

As it can be seen in the Fig. 1, the present model can give qualitatively realistic evolutions of stress and strain both for prepeak hardening and postpeak softening. It is also obvious that a stable algorithm for postpeak damage has been achieved.

Fig. 2 and Fig. 3 show the effect of confinement. As it can be seen in these figures, by increasing the stiffness of confinement, the ASR gel pressure increases and the strain decreases. It should be noted that all the foregoing figures correspond to the same gel mass, but the maximum strains are very different. Therefore, it can be concluded, upon increasing the confinement, the gel cannot accommodate the gel simply by pore volume dilations and that, instead, the pressure increases.

Effect of freely accessible cracks

Expansion of ASR gel can be partly accommodated by its expulsion into the capillary pores in the hardened cement paste located very near the surface of the particle and small cracks in the particles. As long as these capillary pores are filling, no pressure gets induced in the gel, and the gel undergoes free expansion. Therefore, this freely accessible volume V_0 affects the starting time of ASR induced pressure. The following curves depict the effect of V_0 .

Fig4-stress - strain curve for V_0 (for small volume of freely accessible cracks)Fig 5-stress - strain curve for $2.5V_0$ (for large volume of freely accessible cracks)

Discussion

As it can be seen in the Fig. 4 and Fig. 5 this simply accessible volume has strong effect not only on the time when pressure starts to rise but also in the final strain. As it can be seen in above figures, for an element with a larger V_0 , the final strain is smaller. For the above cases, the final strain drops approximately from .007 to .003 when the easily accessible volume increases from V_0 to $2.5V_0$.

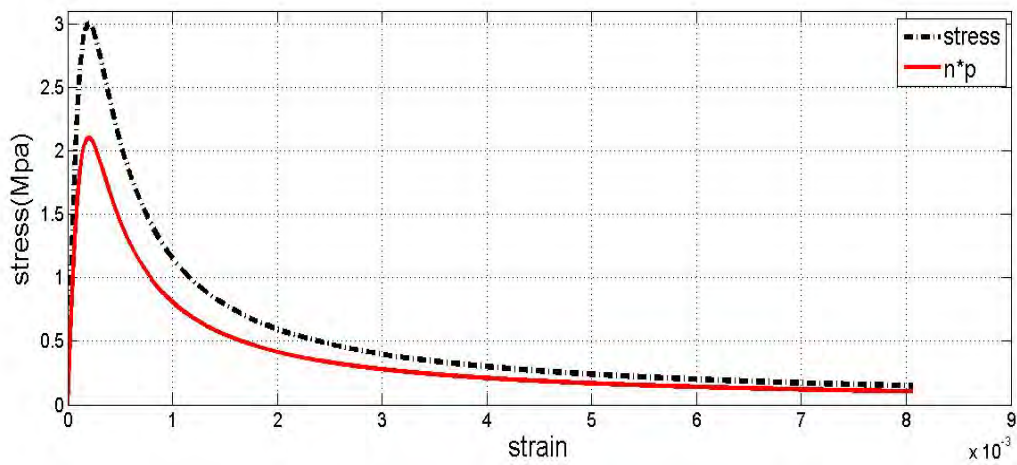
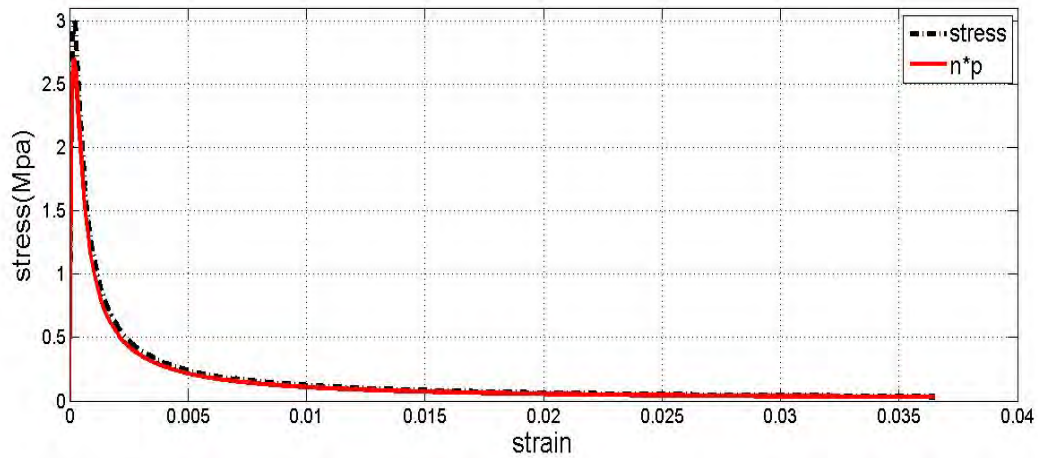
Effect of porosity

As it is expected porosity has big effect on ASR induced strain. If the gel can get accommodate in pore volume, the crack expansion is smaller. Another important aspect is the permeability. Basically it is a function of porosity, but the porosity is not constant during the process. For evaluating the porosity effect, the following state equation is considered:

$$\epsilon_V = (1 - n_0)\epsilon_S + (n - n_0) \quad (3)$$

ϵ_V is the volumetric strain of element, ϵ_S is volumetric strain of solid phase, n_0 is the initial porosity, n is time dependent porosity.

The following curves depict the effect of porosity on the strain evolution for the same gel mass evolution.

Fig 6- Stress- strain curve for $n_0=0.3$ Fig 7- stress-strain curve for $n_0=0.1$

Discussion

As Fig. 6 and Fig. 7 show, the initial porosity has a strong effect on the final strain. In the above cases, the final strain reduces approximately from 0.037 to 0.008 when the initial porosity increases from 0.1 to 0.3. Therefore, one can expect more ASR induced cracking in low porosity concretes.

III.2.6 ASR Activation Energy and Rate of Reaction

Introduction of Activation Energy Calculation

Activation energy is the energy which is required to start the chemical reaction. Therefore, it can represent reactivity of chemical reaction. To study reactivity of ASR, in this quarter, glass ball immersion tests in alkali solution were conducted taking into account the effects of temperature, concentration and time. Finally, the activation energy is obtained by plotting \ln (rate constant) with respect to $1/\text{temperature}$. The slope of this graph is equal to $-E_a/R$ where R is the universal gas constant.

Proposed method to calculate Activation Energy

To achieve the goals, one needs to have 4 batches of 3 glass beads as shown in Fig. 1. Each batch is filled with pure water, 0.5N, 1N and 1.5N NaOH solution respectively. The tests are conducted at 50 °C, 60 °C and 70 °C. The beads in each concentration are picked out every 2 days to measure their weight. From weight measurement, radius change of a glass ball is plotted, representing rate of reaction.

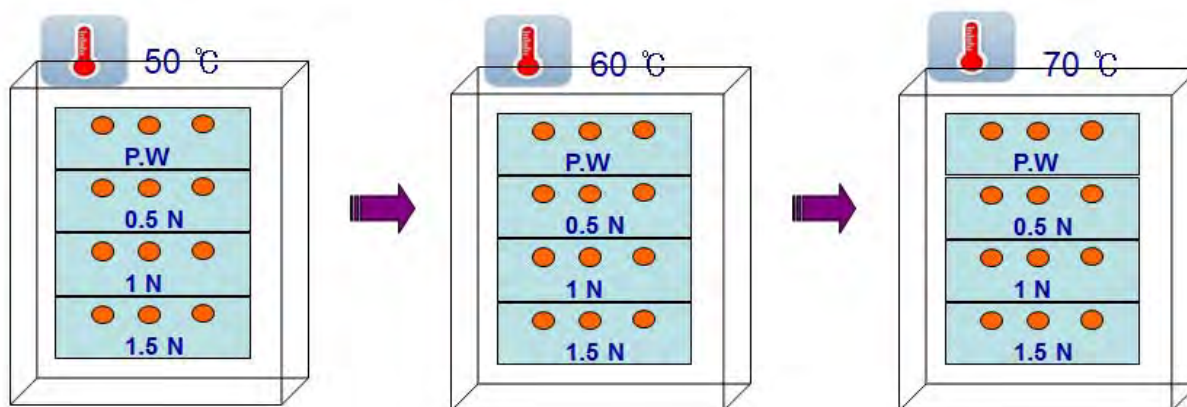


Fig. 1 Schematic diagram of glass ball weight measurement

The determination of the ASR activation energy (E_a) of a glass ball is accomplished through a series of steps. First, determine rate constant k from weight loss measurement. Since the weight measurement results are affected by its initial size, radius decrease of glass ball which does not depend on its original size is obtained from weight measurement test. Fig. 2 shows the schematic diagram of radius decrease and following equations shows the procedure of obtaining rate constant.

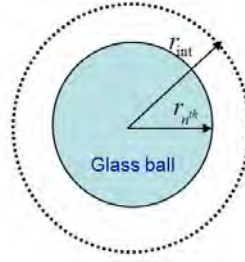


Fig. 2 Radius decrease of a glass ball by ASR

Initial weight and the weight on n-th day are expressed as

$$W_{\text{int}} = \frac{4}{3} \pi r_{\text{int}}^3 \cdot \rho; \quad W_{n^{\text{th}}} = \frac{4}{3} \pi r_{n^{\text{th}}}^3 \cdot \rho$$

Then, rate constant is derived as followings

$$r = \sqrt[3]{\frac{3W}{4\pi\rho}}$$

$$\varepsilon = \frac{\Delta r}{r_{\text{int}}} = \frac{r_{\text{int}} - r_{n^{\text{th}}}}{r_{\text{int}}} = 1 - \sqrt[3]{\frac{W_{n^{\text{th}}}}{W_{\text{int}}}}$$

$$\text{rate of reaction} = \frac{\partial \varepsilon}{\partial t} [\text{day}^{-1}] = k \cdot [\text{NaOH}]^m$$

$$k = \frac{\text{rate of reaction}}{(\text{concentration})^m}$$

where

r : Radius of the glass beads

W : Weight of the glass beads

ρ : Density of the glass beads

k : Rate Constant

Secondly, according to the Arrhenius equation, rate constant is expressed as

$$k = A e^{-E_a/(RT)}$$

Taking the natural logarithm of Arrhenius' equation yields

$$\ln(k) = \frac{-E_a}{R} \frac{1}{T} + \ln(A)$$

If $\ln(k)$ is plotted with respect $1/T$, the slope is $\frac{-E_a}{R}$ as shown in Fig. 3. As a result, ASR activation energy of a glass ball is determined.

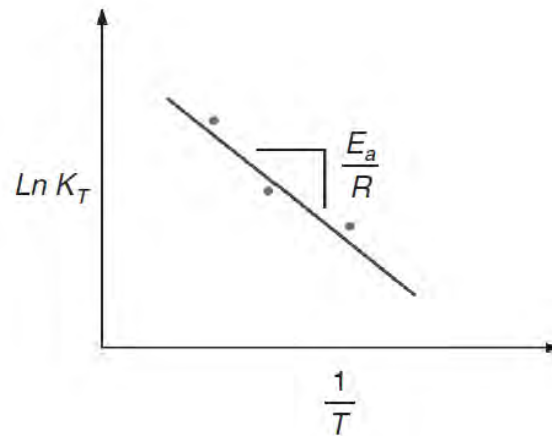
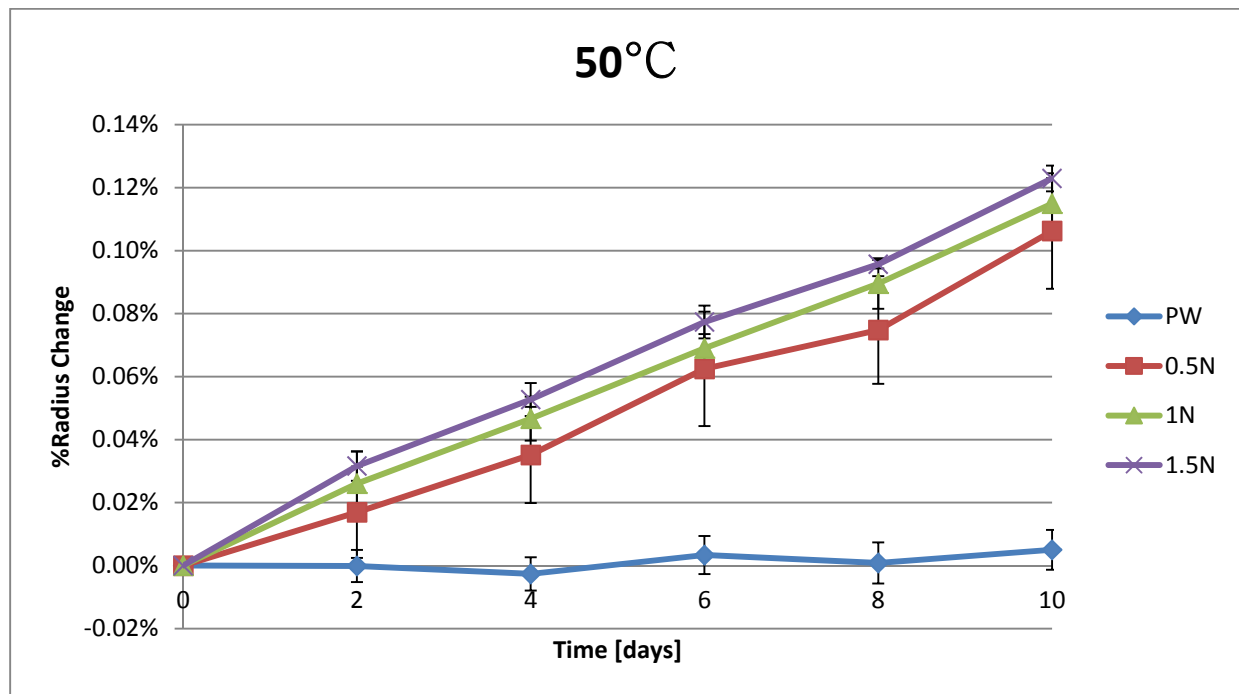


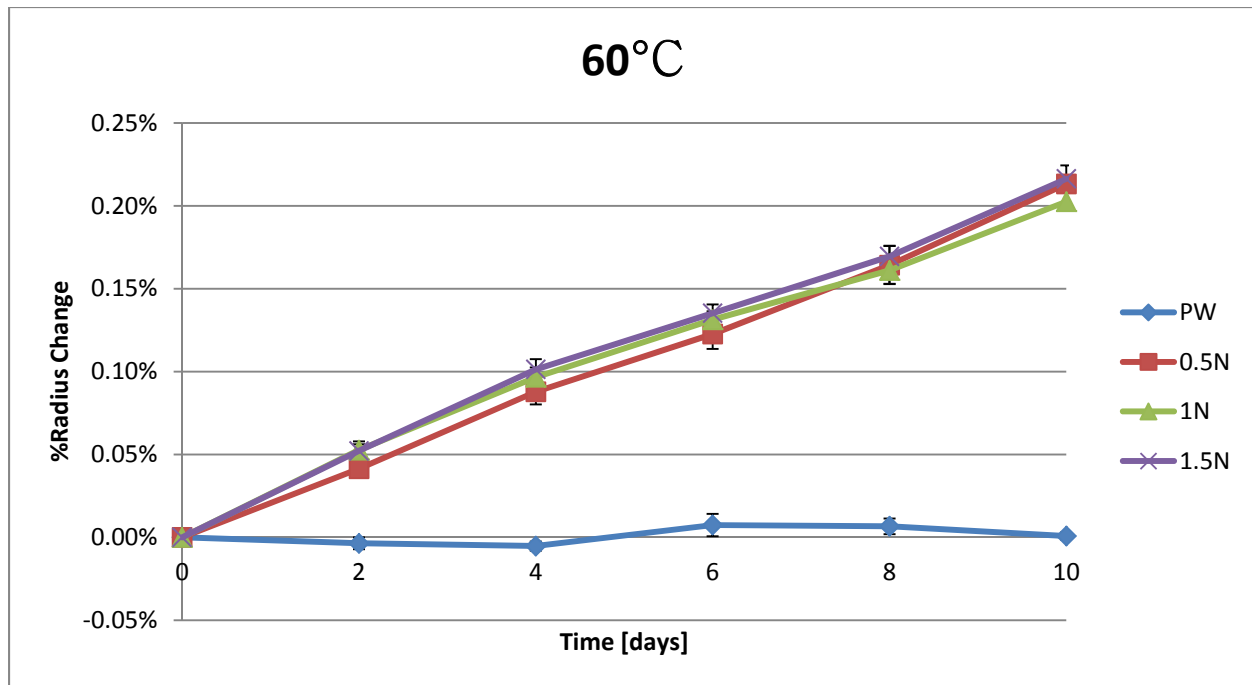
Fig. 3 Concept of activation energy calculation from the graph

Results

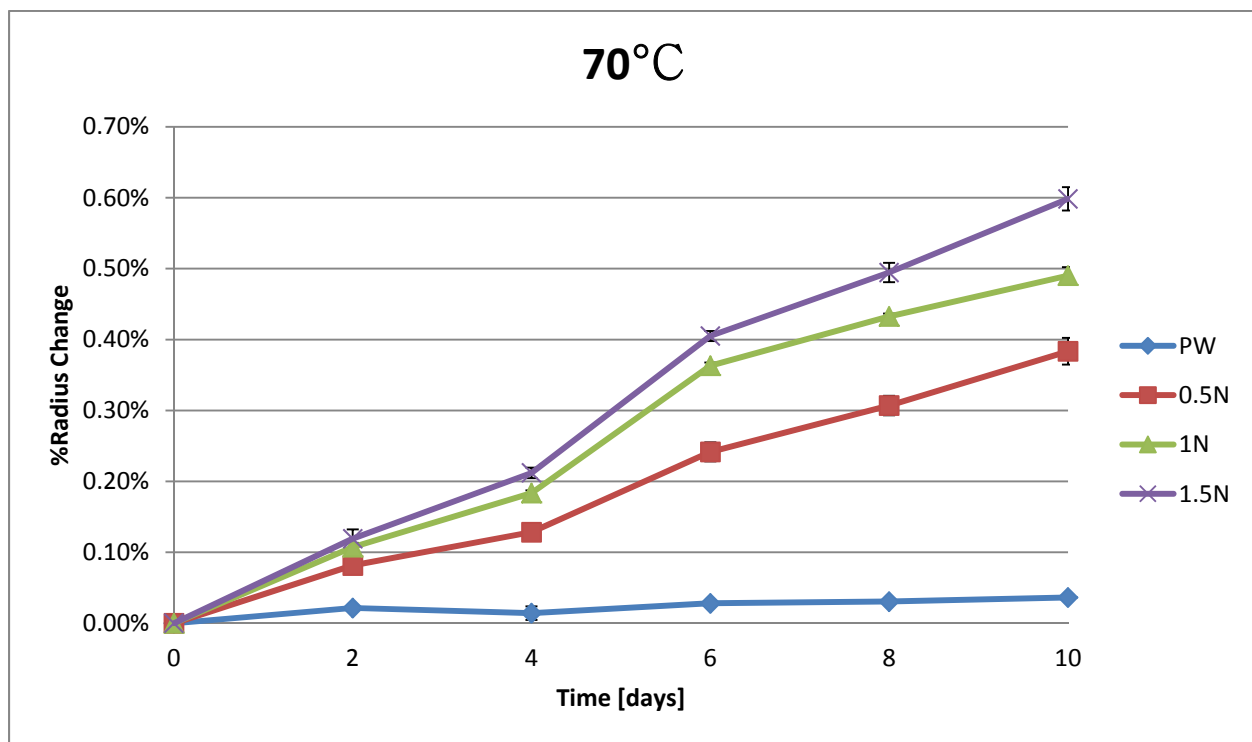
Fig. 4 shows the %radius change of a glass ball immersed in the different test solutions. It is seen that rate of ASR increases as the alkalinity of test solutions, temperature and time go up.



(a)



(b)



(c)

Fig. 4 %Radius Change (a) at 50°C, (b) 60°C and (c) 70°C

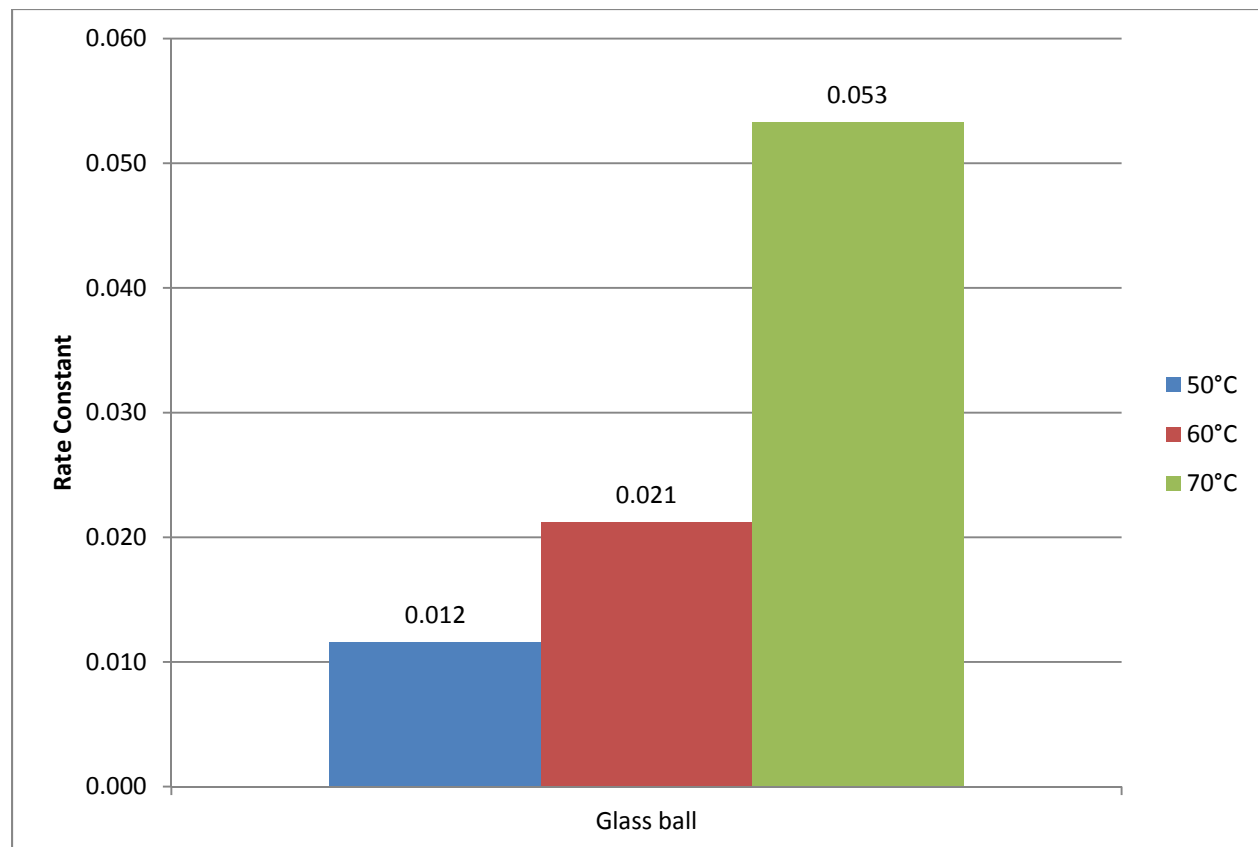


Fig. 5 ASR Rate Constant of a glass ball

In Fig. 5, ASR rate constant of a glass ball is shown.

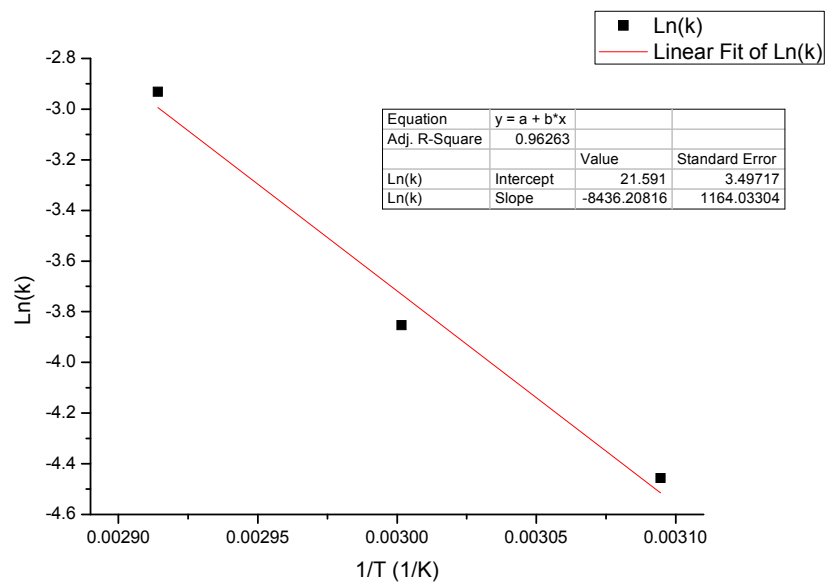


Fig. 6 Activation Energy calculation from the slope

The slope of the 3 data points is obtained by linear regression as shown in Fig. 6. Therefore,

ASR activation energy $E_a = 70.14 \text{ kJ} / \text{mol}$

This result will be used to understand the characteristics of samples with controlled ASR degree.

Linear Ultrasonic Measurements

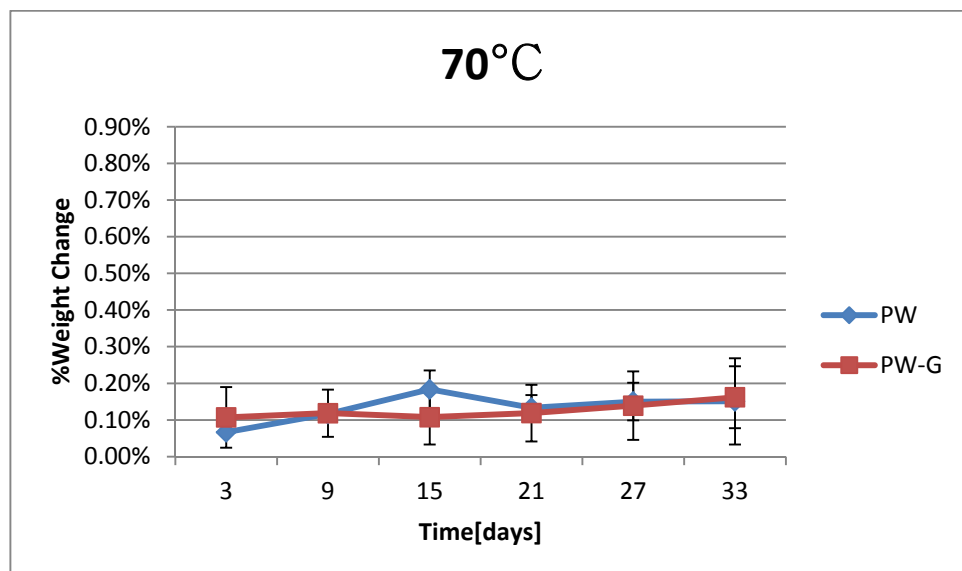
Introduction of ultrasonic wave measurement

It is assumed that if characteristics of concrete sample change with increase of gel and crack density, UT results should reflect its property change. Wave speed and attenuation coefficient are measured and compared with weight variation.

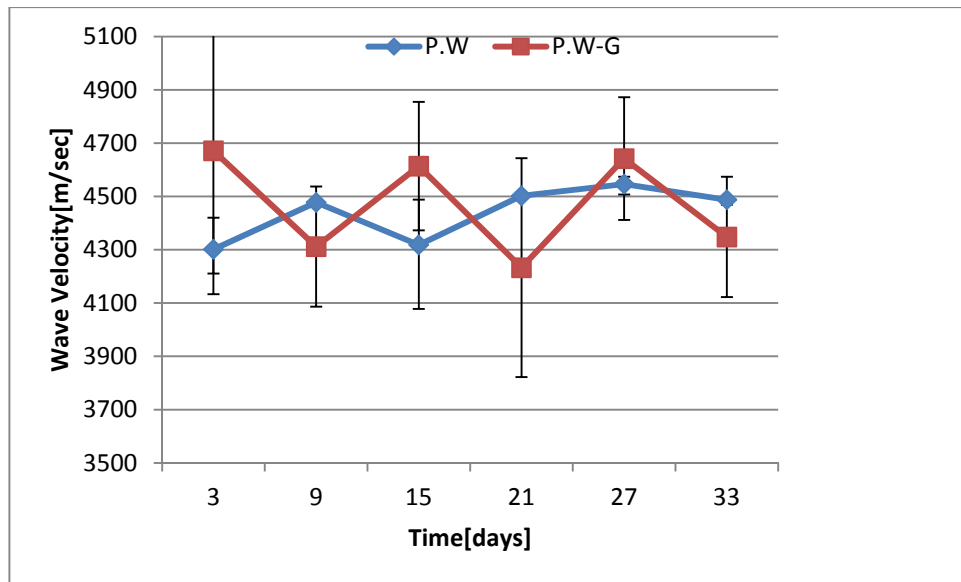
Experiment preparation

Four batches of different concentration solution were prepared which vary from 0N to 1.5N where 1N indicates 40g of NaOH per a liter of pure water. Prepared 6 samples were put into the batches. 6 samples were divided by two categories; 3 samples have the glass ball in its body and the other 3 do not have. Finally, 24 samples in total were immersed in the solutions and their weight changes were monitored every two days. 70°C was chosen. For the ultrasound test, through transmission test was used for wave speed calculation and pulse-echo method was conducted for attenuation coefficient measurement with 0.5MHz.

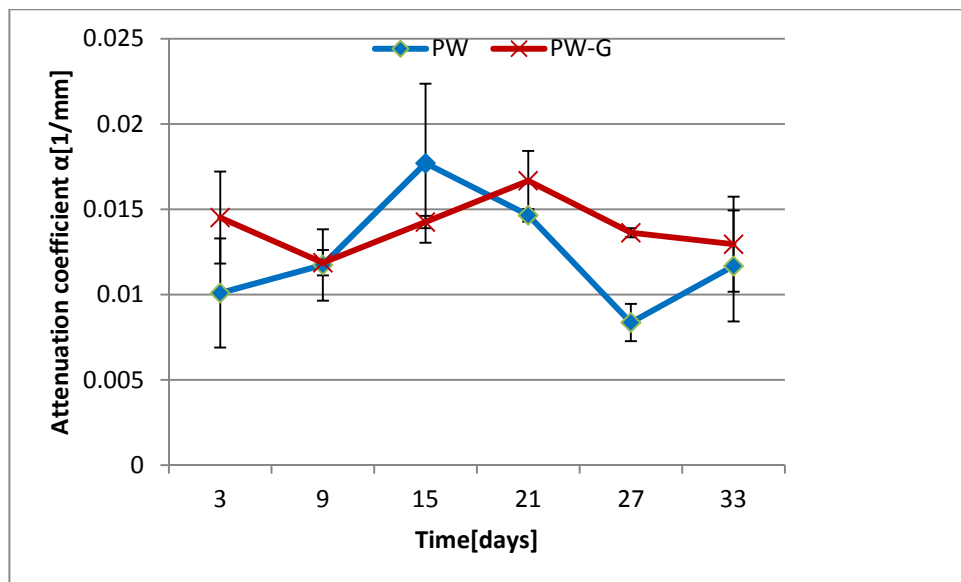
Results



(a)



(b)



(c)

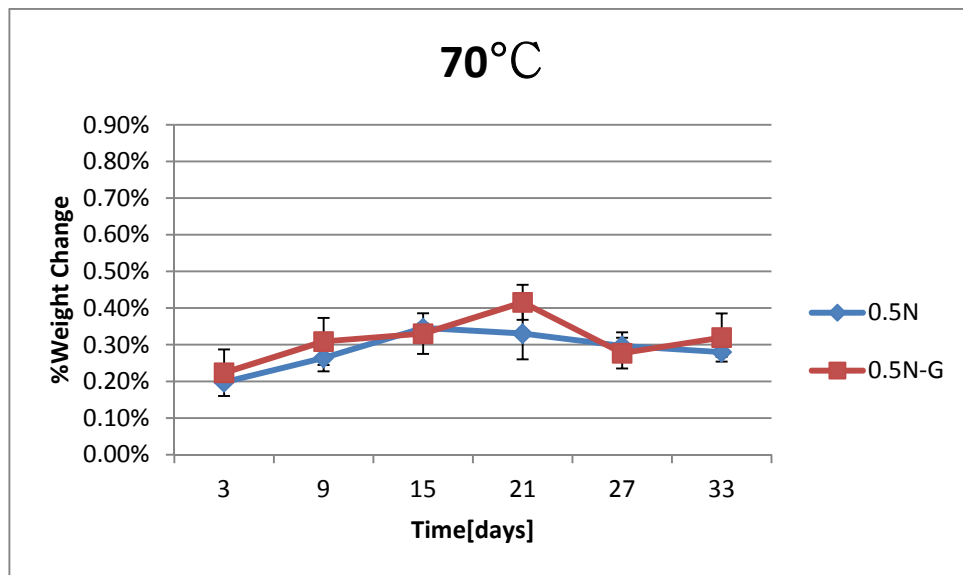
Fig. 7 Result of (a) %weight change, (b) Attenuation coefficient and (c) Wave velocity in pure water

The obtained attenuation coefficient is larger than the attenuation of normal Cement paste matrix 0.0085/mm

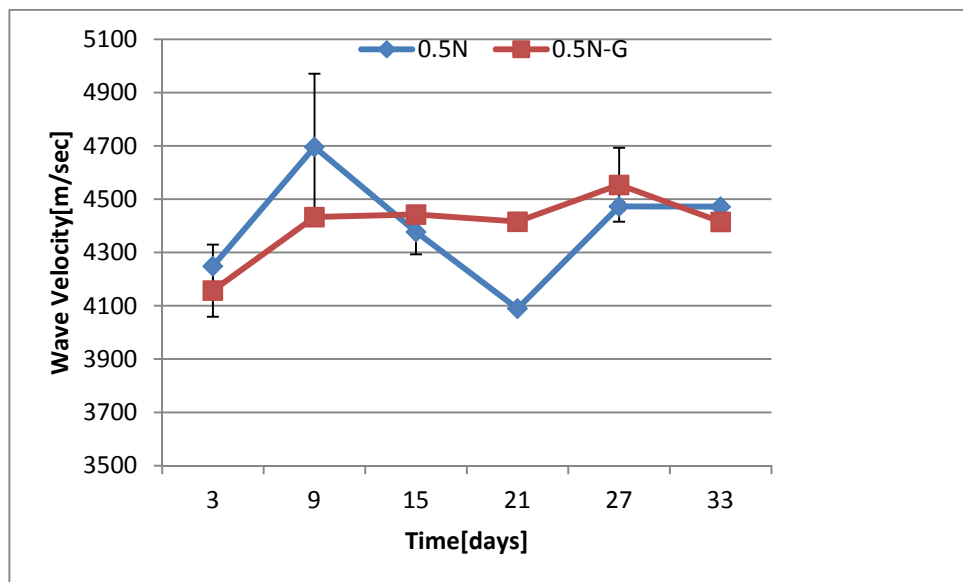
Weight change of samples in pure water varies between 0.07% and 0.18% that is a lot smaller than one in alkali solution.

Wave speed of sample without a glass ball(PW) is more or less than 4396.6m/sec and one with a glass ball(PW-G) is about 4413.7m/sec

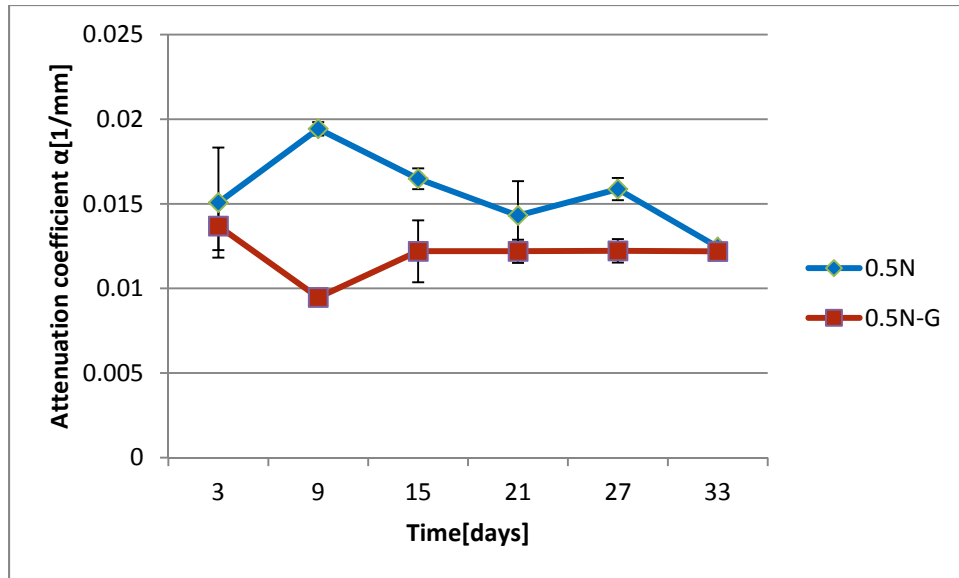
It is hard to find clear correlation between each of results.



(a)



(b)

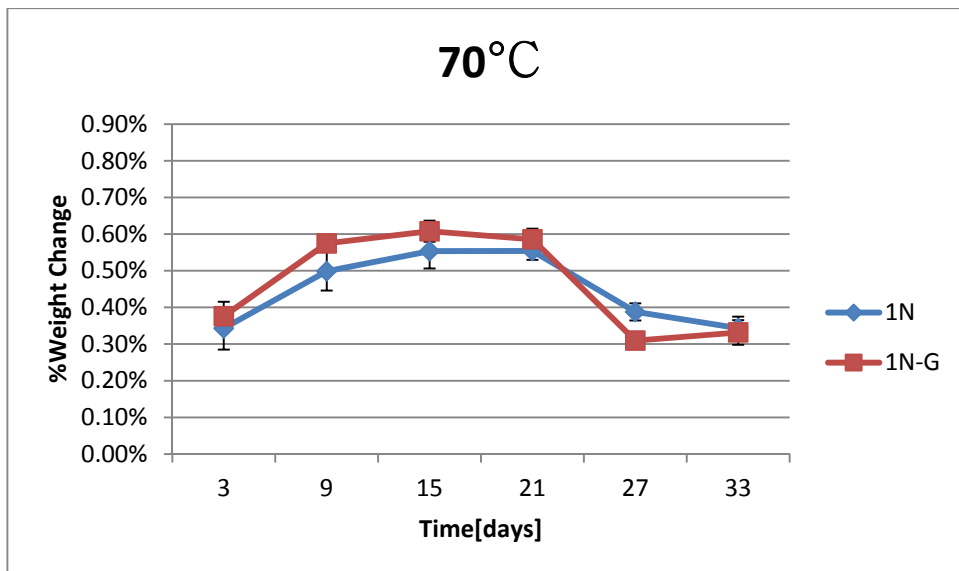


(c)

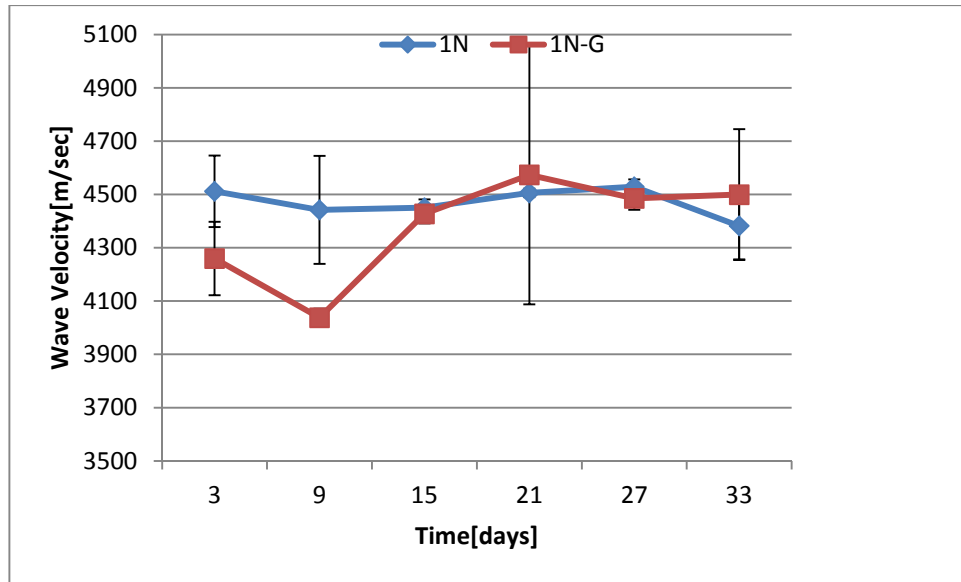
Fig. 8 Result of (a) %weight change, (b) Attenuation coefficient and (c) Wave velocity in 0.5N solution

From the wave velocity and attenuation coefficient graph, it is seen that wave velocity and attenuation coefficient of 0.5N have similar trend (when one increased, the other one has increasing trend) while those of 0.5N-G do not have.

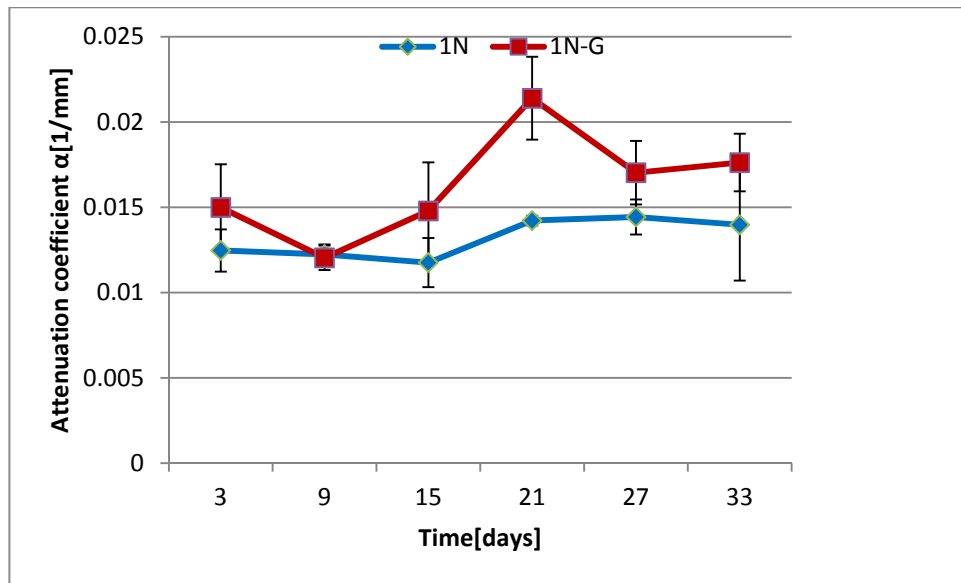
However, it does not make sense since higher attenuation coefficient should cause slower wave propagation. It is hard to find weight change effect to wave velocity and attenuation coefficient



(a)



(b)



(c)

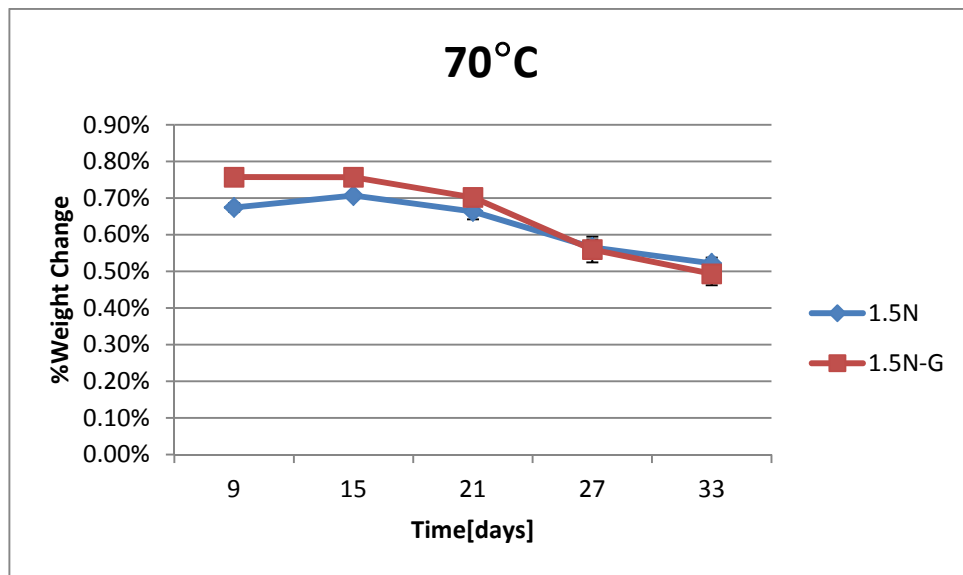
Fig. 9 Result of (a) %weight change, (b) Attenuation coefficient and (c) Wave velocity in 1N solution

From 21st day to 27th day, the sample lost its weight more than other days.

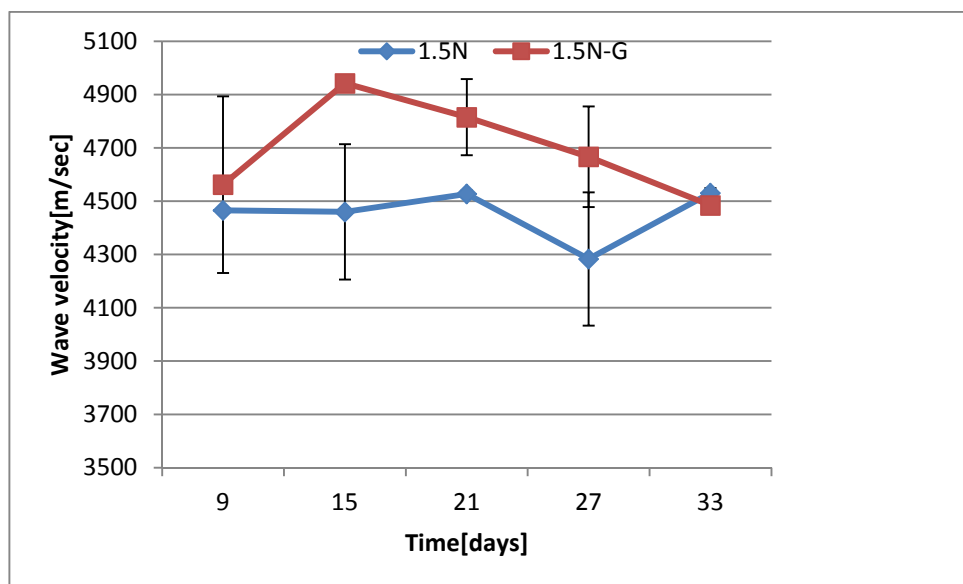
However, 1N sample does not have wave velocity and attenuation coefficient change as big as its weight change.

It is seen that once the sample is fully saturated with water, its additional weight change due to the ion diffusion does not directly affect its wave velocity and attenuation coefficient

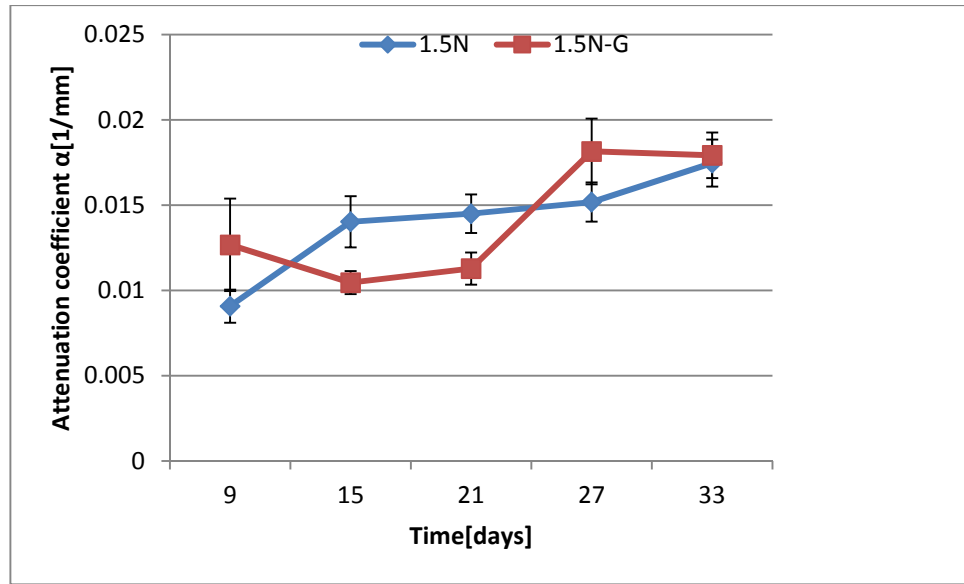
1N and 1N-G samples show that when wave velocity increases, attenuation coefficient also increases



(a)



(b)



(c)

Fig. 10 Result of (a) %weight change, (b) Attenuation coefficient and (c) Wave velocity in 1.5N solution

1.5N and 1.5N-G sample have the similar pattern of weight change. It is hardly found that the sample with a glass ball gains more weight than one without a glass ball as alkali-silica gel swells by absorbing water.

According to above graphs, it is concluded that conventional linear UT has not provided enough sensitivity toward property change of sample. As a result, nonlinear ultrasound measurement will be intensively conducted.

III.2.7 Constitutive Model for Continuum Analysis for ASR Damage in Concrete with Diffusion of Compressible Gel into Pores

Introduction

The excessive expansion and disintegration of some concrete made of cements of relatively high alkali content and of certain silica-containing aggregates can be explained by the so-called alkali-silica reaction (ASR). The ASR produces a soft viscous substance called the ASR gel, which has been observed to appear in pop-outs or to exude from cracks in concrete structures.

The eigenstrain caused by the alkali-silica reaction (ASR) is different from the thermal eigenstrain or shrinkage eigenstrain. The latter is simply additive to the stress-induced deformation and causes (or is assumed to cause) no damage to the solid. The ASR gel expands the pores and microcracks within the material and generates in the pores and microcracks fluid pressure p , which leads to material damage. It is actually an eigenstrain on a sub-scale of the material. For a porous solid with pressurized fluid in the pores, two different theories are well established: 1) Biot's (or Biot-Fillunger's) two-phase medium theory, and 2) Terzaghi's effective stress theory.

For three decades, these two theories were thought to be in conflict and were the subject of passionate polemics. One difference was that the latter assumed porosity $n < 1$ and the former $n = 1$ (for uplift in dam safety analysis). Another was that the elastic cross-stiffness between the solid and fluid has been missing from the latter. Today, however, it is clear that both are valid but have different applicability. The former applies to elastic or viscoelastic deformation of the porous medium, while the latter applies to failure and is an essential concept in soil mechanics.

This work explores a formulation that is an adaptation and combination of both (e.g., n increases, up to 1). The equality of macroscopic smeared-out deformation of both the solid and fluid phases is the same as in Biot's theory, but a major difference from Biot's theory is that the growth of fluid mass precludes applying the condition of equal strain in both phases. The model presented here should be applicable to any constitutive model for tensile softening damage but is here intended mainly for microplane model M7 (Caner and Bažant 2013).

ASR gel mass calculation

One purpose of present model is simulating the ASR gel pressure extruded into the porous phase (pores of cement mortar) when ASR gel mass increasing as a function of time. To describe the production of the ASR gel in the mineral aggregate, the model in Ref. [1] is adopted. This model is considered as a given input, which predicts the gel mass extruded into the adjacent pores and developing cracks in the matrix, as a function of time t . Fig.11 shows a sample result for the extruded gel mass for one spherical aggregate. The amount of extruded gel is depend on the diameter of the sphere; in this special case diameter assumed to be 20 mm. As it can be seen in this figure, the extruded gel mass is increasing function of time until the reaction front reaches the center of the aggregate (full reaction). After full reaction of the aggregate, extruded gel mass assumed to be constant.

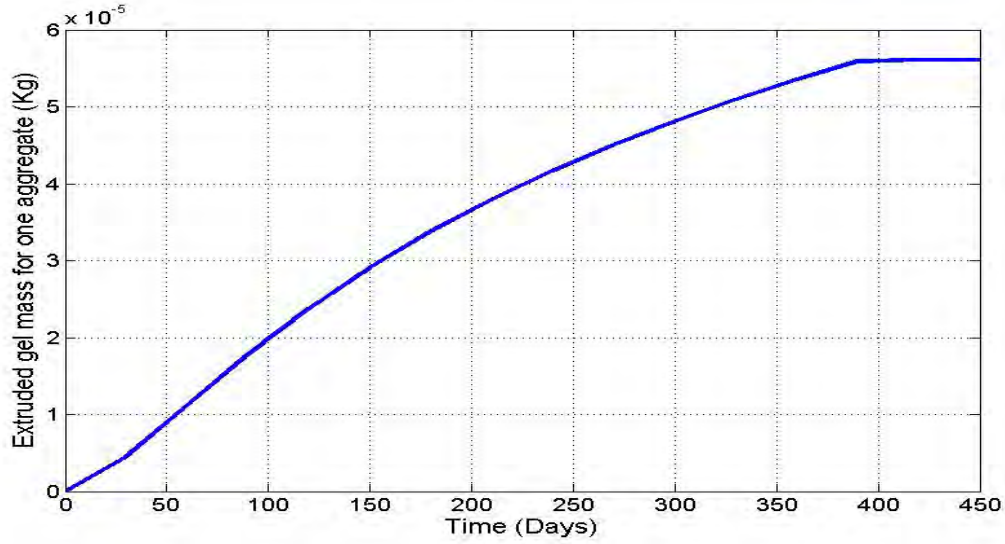


Fig. 11- Mass of extruded gel-time for one aggregate

ASR gel pressure evolution

Three different increments should be considered for ASR gel in each step. First increment is because of gel mass increment. Simultaneous gel mass increment can be accommodated only by elastic compression of the gel. This contribution can be formulated as following:

$$dp = \kappa \frac{dM}{M}$$

Where κ is the bulk modulus of ASR gel, and M is the mass of ASR gel.

Second contribution is because of diffusion of ASR gel When Gel Mass and Strain Are Constant. For calculating this pressure increment Darcy equation is used:

$$v = b \nabla p$$

Where v is the velocity and ∇ denotes the gradient and b = Darcy permeability (dimension $m^3 s / kg$)

In detailed analysis, one could now proceed to the point-wise differential equation for the diffusion in coordinate x . However, in view of all the uncertainties, it should suffice to replace v with the velocity dx/dt of the diffusion front at distance x from the aggregate surface, and the pressure gradient with the average pressure gradient $\bar{\nabla} p = p / x$. This leads to the simplified Darcy diffusion equation:

$$\frac{dx}{dt} = b \frac{p}{x}$$

By considering simplified Darcy equation and compressibility of ASR gel, the following equation can be derived:

$$\frac{dp}{\kappa} + \frac{p}{\eta} dt = 0$$

Where η is the effective viscosity.

Last contribution in pressure increment is because of the volumetric strain. By considering equal volumetric strain in solid part and porous part, this contribution can be calculated as following:

$$dp = -\kappa d\varepsilon_v$$

Where $d\varepsilon_v$ is volumetric strain increment.

Combining all the three pressure increments, the total pressure increment can be found as the following:

$$dp = \kappa \left(\frac{dM}{M} - \frac{p}{\eta} dt - d\varepsilon_v \right)$$

Equilibrium equations for two-phase solid-fluid continuum

The material with expanding gel is considered as a two-phase solid-fluid continuum with variable fluid fraction. Equilibrium between gel pressure p in the pores and the volumetric stress σ_v in the three-dimensional solid requires that:

$$S_v = (1 - n_0)\sigma_v - n_0 p$$

$$S_{ij} = \sigma_{ij} - (\sigma_v + p) n_0 \delta_{ij}$$

Here δ_{ij} = Kronecker delta (unit tensor); S_{ij} , S_v are the total stresses in the two-phase continuum and the total volumetric stress, which are used to calculate the nodal forces in an explicit finite element program (note that p is positive for compression, σ_v for tension).

Variation of Permeability and Effective Porosity

The permeability, b , is surely not constant. For $M < M_0$, the effective permeability is very high because the gel is filling bigger pores next to the ITZ. Later, the gel is forced under pressure into tighter and tighter pores. Thus the effective permeability b must sharply decrease with distance x to the diffusion front, or with M . Not being aware of any applicable characteristic length, we may logically assume that b decreases with M as a self-similar function, which is a power function; i.e.,

$$\text{for } M > M_0 \quad b = b_0 \left(\frac{M}{M_0} \right)^{-s}$$

where s ; b_0 are empirical constant (both ≥ 0). Probably $s \gg 1$, which reflects the fact that the very fine pores located farther from the aggregate piece beyond the ITZ are orders of magnitude harder to fill than the big pores in the ITZ.

According to the preceding simplified formulation, the gel pressure would be independent of the strains ε_{ij} in concrete. This is probably accurate enough only before the strength limit of concrete is reached. But once the ASR causes postpeak softening damage with large inelastic strain, microcracks will develop and serve as conduits greatly facilitating the flow of gel. This must be reflected in the increase of permeability, which may be assumed to depend on the inelastic volumetric strain:

$$\varepsilon_v'' = \varepsilon_v - \frac{\sigma_v}{3K}$$

Because, with increasing ε_v'' , the continuity of cracks is likely to increase, b ought to be an increasing function of ε_v'' . Combining the effects of pore tightening and crack widening, we may write:

$$\begin{aligned} \text{for } M < M_0 \quad b &= b_0 \\ \text{for } M > M_0 \quad b &= b_0 \left(\frac{M}{M_0} \right)^{-s} + b_1 \left(\frac{\varepsilon_v''}{\varepsilon_p} \right)^2 \end{aligned}$$

where $s; b_0; b_1$ = empirical constants.

Results of one dimensional simulation

(1) Stress-strain curves

Fig. 12 depicts a sample result of finite element simulation for unconfined condition. As it can be seen in this figure this model can capture the evaluation of stress and pressure very good. Also, as it can be seen in this figure, this model satisfy equilibrium equation greatly. Fig.13 shows the same result for confined condition, where the element is confined from all directions with elastic (spring) confinement. In this special case the stiffness of confinement assumed to be 1000 Mpa. As it can be seen in this figure after reaching the peak tensile strength of concrete, stress in solid part decreasing, but pressure is increasing. This behavior again is in complete agreement with equilibrium equation.

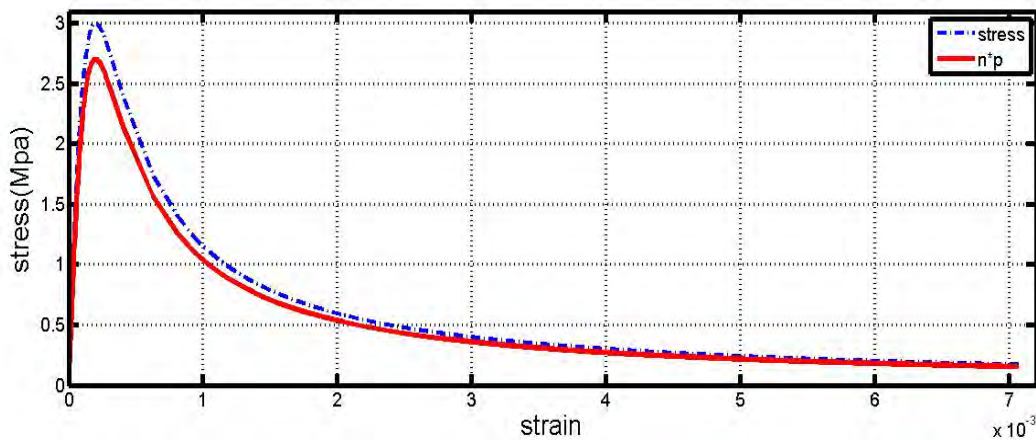


Fig. 12-Stress-strain curve of unconfined material element

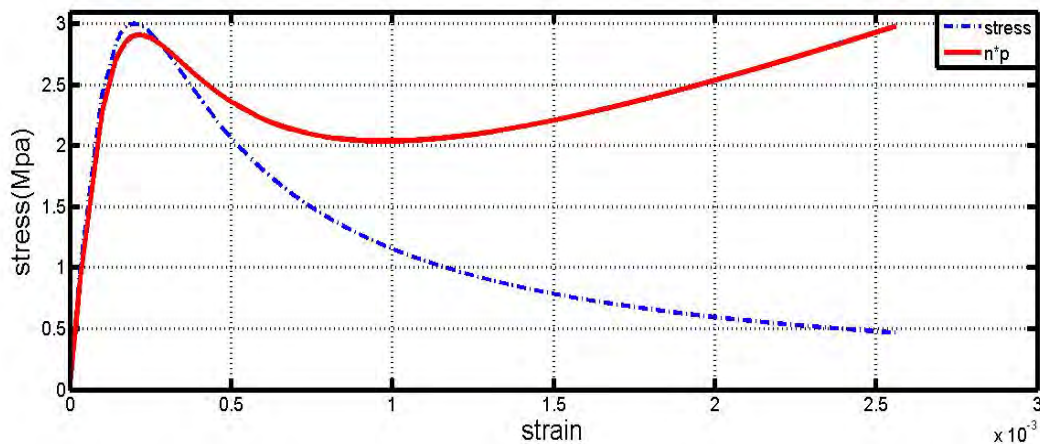
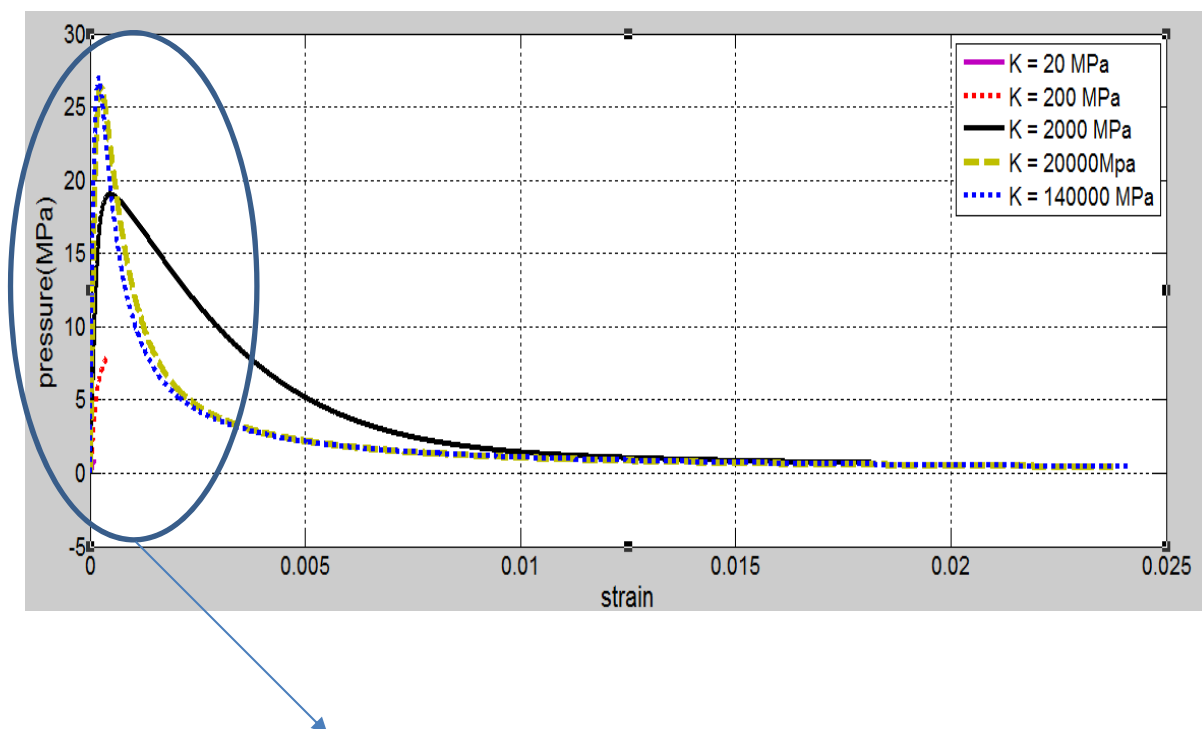


Fig. 13-Stress-strain curve of confined material element ($C=1000$ MPa)

(2) Effect of bulk modulus

One important issue that should be study is the bulk modulus of the gel. This property of the gel is not completely recognized, and there is some conflicts about this property. Fig. 14 illustrates how important is this property.



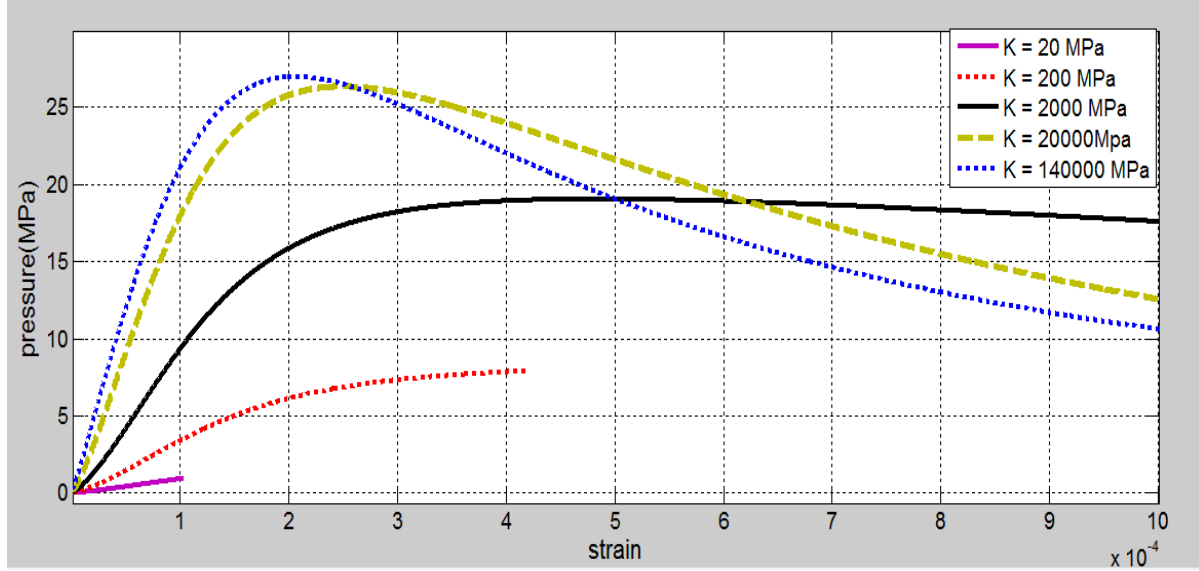


Fig. 14- Pressure- strain curves for different bulk moduli

As it can be seen in these figures, bulk modulus of the gel is significantly important in results. By increasing the bulk modulus, pressure increment increases. Therefore, for the same amount of extruded gel strain will increase more.

(3) Effect of effective Darcy coefficient

Another important parameter that should be calculated is Darcy coefficient. In order to find reasonable order for this parameter, it assumed the permeability of the gel is in the same order of concrete. In this study effective Darcy coefficient defines as following:

$$\bar{b} = b \left(6 \frac{v_D}{D} \right)^2$$

In above equation, b is Darcy coefficient and \bar{b} is the effective Darcy coefficient; v_D is volume fraction of aggregates of size D .

Fig. 15 depicts the effect of this value in finite results. At first glimpse, it may perceive this parameter is not that important, and it will not change the results that much, but it should be considered that the range of variation of this parameter is expansive. Therefore, this parameter is so important.

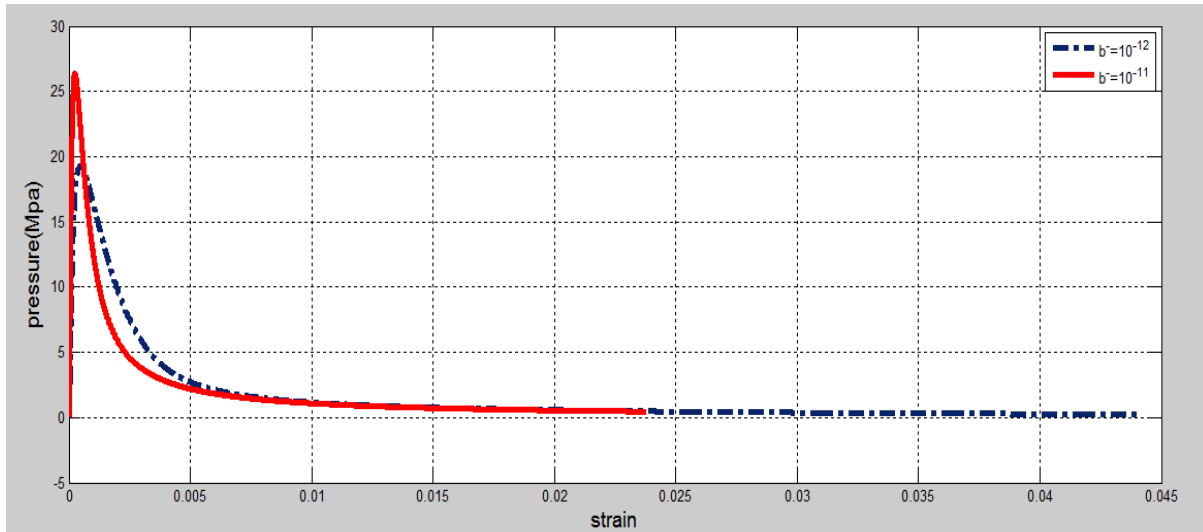


Fig. 15-Pressure- strain curve for different Darcy effective coefficients

Results for 3D simulation by using Microplane (M7) model

In this section Microplane model used as constitutive equation for solid part. In order to use this model, a simple finite element model considered. Fig.16 illustrate the considered model.

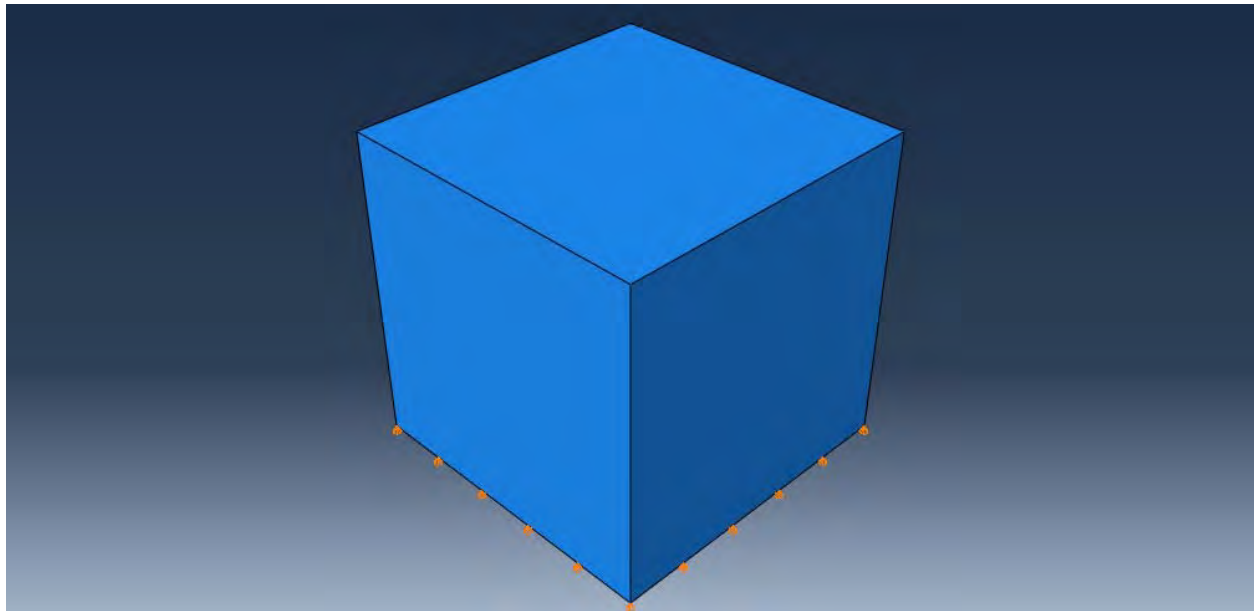


Fig. 16- Finite element model

ASR expansion applied to this model and evolutions of pressure and stress was calculated. Fig. 17 depicts the evolution of stress and Fig.18 shows the same for pressure. This model is for an unconfined condition and from equilibrium equation it expected these two figures be scaled of each other. As it can be seen in these figures, the results satisfy our expectation greatly, and these

two figures are scaled of each other. In this specific case porosity (n) considered equal to 0.1, thus from equilibrium equation pressure should be 9 times of stress, and it is.

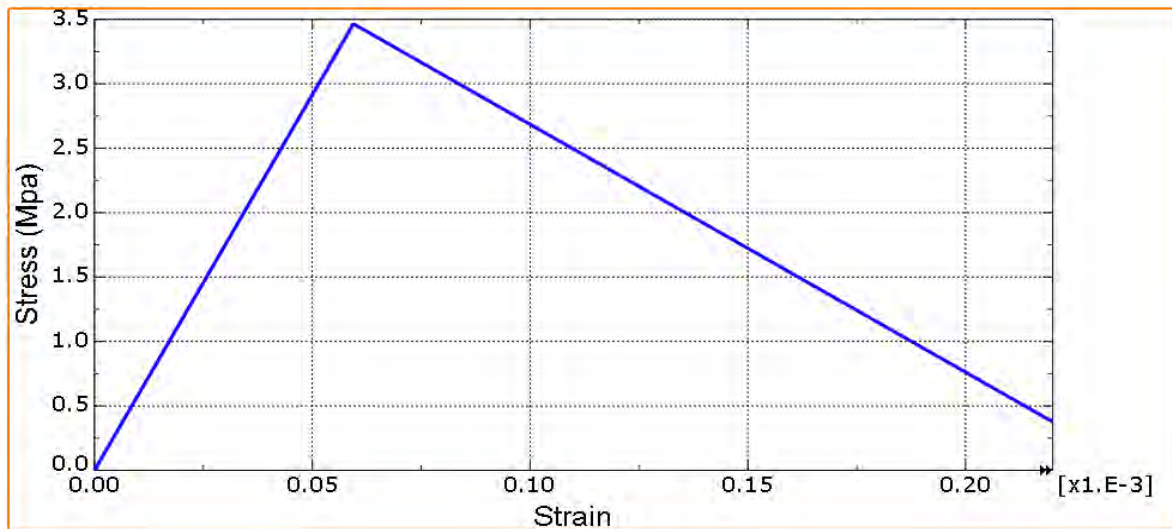


Fig. 17- Stress- strain curve

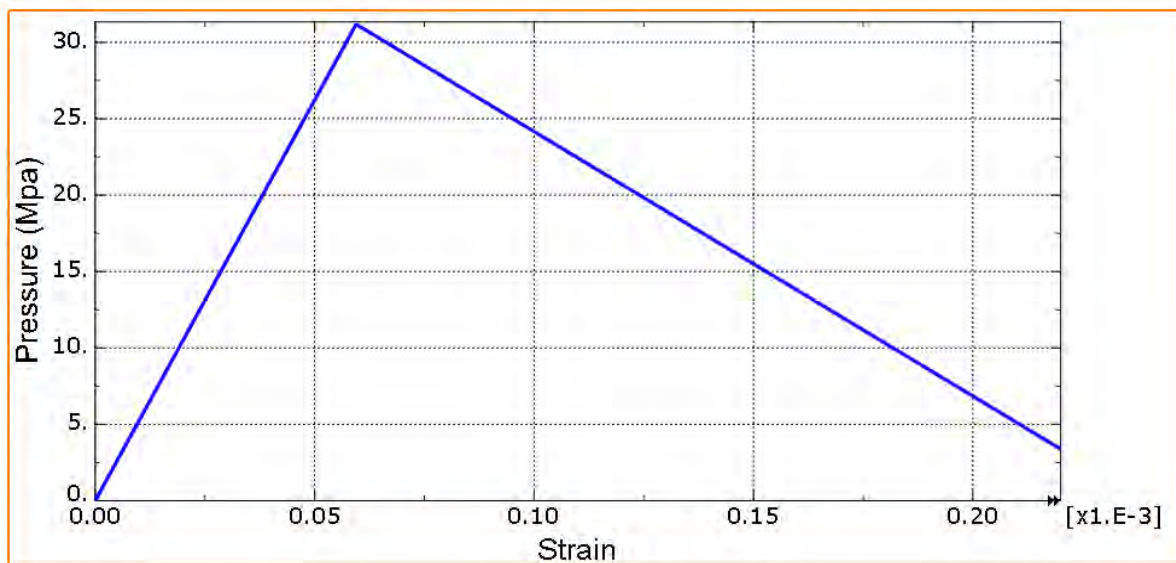


Fig. 18- Pressure-strain curve

References

- [1] Bažant, Z.P., and Stefens, A. (2000). “Mathematical model for kinetics of alkali-silica reaction in concrete.” *Cement and Concrete Research* 30 (3), 419{428 (disc. reply Vol. 31, 2001, 1111{1113).
- [2] Bažant, Z.P., Zi, G., and Meyer, C. (2000). “Fracture mechanics of ASR in concretes with waste glass particles of different sizes.” *J. of Engrg. Mechanics ASCE* 126 (3), 226{232.
- [3] Caner, F.C., and Bažant, Z.P. (2013). “Microplane Model M7 for Plain Concrete: I. Formulation. II. Calibration and Verification” *ASCE J. of Engrg. Mechanics* 139 (12), 1714-1723 and 1724-1735.

III.2.8 Effects of Moisture on Ultrasound Propagation in Cement Mortar

Introduction

Alkaline-silica reaction (ASR) is a major chemical degradation mechanism in concrete. In a humid environment, concrete may absorb moisture from the surrounding environment. As the absorbed moisture diffuses through the concrete, it dissolves the free alkaline ions in the cement and transports them to the aggregates. These alkaline ions then react with the amorphous silica in the aggregate. Such reaction produces a gel called ASR gel. The ASR gel expands its volume as it imbibes more water. Such volumetric expansion of the ASR gel induces large internal pressure, which may then cause microcracking of the concrete. For safe operation of concrete structures, nondestructive evaluation (NDE) techniques are needed to monitor and characterize ASR damage.

Ultrasound has been used extensively for NDE of cement-based materials [1-4]. Most of these applications are based on linear ultrasonic methods. In recent years, nonlinear ultrasonic techniques have also been developed [5-7]. A major challenge in using ultrasonic NDE methods for chemical degradation such as ASR is how to quantify the degree of damage in the early stages. To this end, it is critical to develop a fundamental understanding of how ultrasonic wave propagation is affected by the presence of moisture, gel and microcracks.

As a first step towards quantifying the relationship between ultrasonic measurements and chemical degradations, this study experimentally investigates the effects of moisture on the ultrasonic phase velocity and attenuation in cement mortar samples.

Sample Preparation

Four cement mortar cubic samples of 2X2X2 inches were made following the procedures described by AASHTO T303 [8]. The type I cement (potential Bogue composition 46.11% C₃S, 22.93% C₂S, 8.52% C₃A and 9.59% C₄AF and 0.83% Na₂O_{eq}) and sorted lime stone sand were used. Particle size distribution of the sand is given in Table 1. The water/cement ratio used is 0.5 and the sand/cement ratio is 2.25. After demolding, the samples were submerged in tap water at 80°C (176 °F) for 24 hours to cure.

TABLE 1. Sand proportion added to cement [8]

Sieve Size		Weight, %
Passing	Retained on	
4.75 mm (No. 4)	2.36 mm (No. 8)	10
2.36 mm (No. 8)	1.18 mm (No. 16)	25
1.18 mm (No. 16)	600 µm (No. 30)	25
600 µm (No. 30)	300 µm (No. 50)	25
300 µm (No. 50)	150 µm (No. 100)	15

Moisture Content Measurement

Water content measurements were carried out by measuring the weight change of the samples under drying conditions. Four samples were used in each measurement, and the reported data are the average of results from these four samples. The first weight measurement was taken immediately after the 24 hr curing in 80°C tap water. The samples were then placed in a drying oven set at 80°C until the samples were fully dried. During this drying process, weight measurements were taken periodically. The moisture contents is then computed using the standard formula,

$$\text{water content [\%]} = \frac{\text{weight(moist)} - \text{weight(dry)}}{\text{weight(dry)}} \times 100 \quad (1)$$

The water content so measured is plotted in Fig. I-1(a).

To investigate whether the moisture absorption and desorption are reversible, the fully dried samples were again submerged in tap water at 80°C for 2 days. After that, the samples were again placed in a drying oven set at 80°C until the samples were fully dried again. The weight measurements were taken again periodically during this second drying period. The moisture content so measured is plotted in Fig. I-1(b).

The similarity between Figs. I-1(a) and 1(b) seems to indicate that for samples well cured during the initial hydration process, additional moisture absorption and desorption are almost fully reversible.

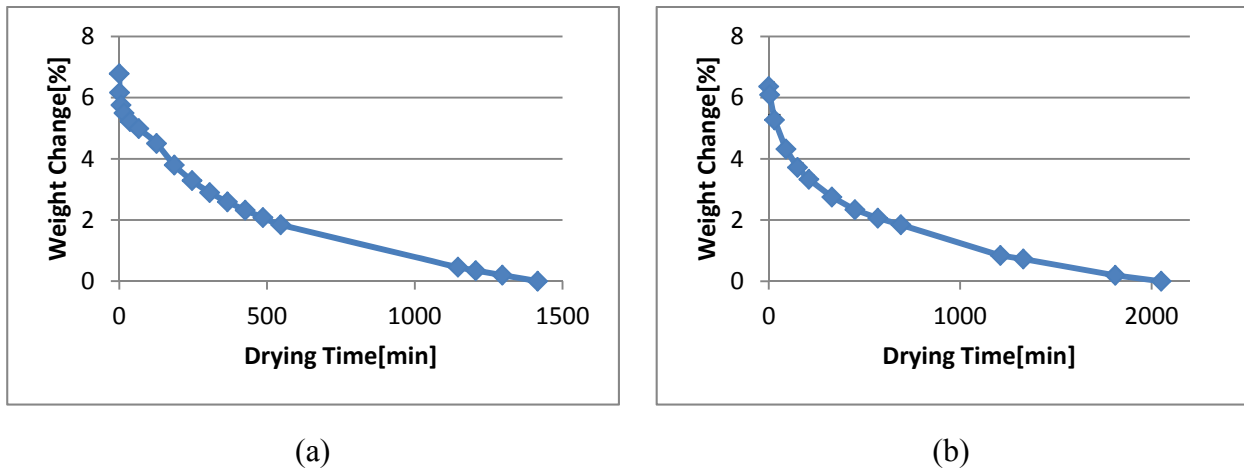


FIGURE I-9. (a) Moisture content during the first drying cycle after the samples were cured in 80°C tap water for 24 hours, (b) Moisture content during the second drying cycle after the samples were submerged in 80°C tap water for 2 days.

Ultrasonic wave measurement

Ultrasonic tests were conducted to measure the ultrasonic phase velocity and attenuation in the cement mortar samples at different levels of moisture content. The velocity was measured by carrying out through transmission tests as schematically illustrated in Fig. I-2(a). The attenuation was measured using a pulse-echo method as illustrated in Fig. I-2(b), where a diplexer was used to switch the transducer from transmitter mode to receiver mode. In both tests, the incident wave

consists of a 2-cycle tone burst centered at 250 kHz. High-vacuum grease was used as a couplant to attach the transducers to the mortar samples. For repeatability, measurements on each sample at each moisture content were repeated three times by completely detaching and re-attaching the transducers.

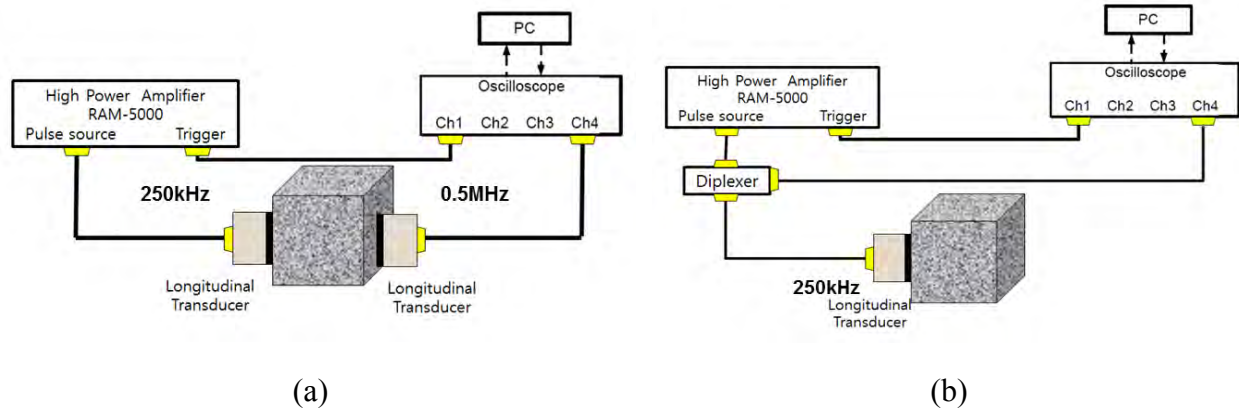


FIGURE I-10. Experiment setup for (a) phase velocity measurements and (b) attenuation coefficient measurements

The phase velocity was obtained by measuring the time of flight between the transducer and receiver. Showing in Fig. I-3(a) is the wave form received by the receiver when the transducers are directly attached to each other face-to-face without the sample in between them. Showing in Fig. I-3(b) is a typical waveform received by the receiver when a sample is placed between the transducer and receiver as illustrated in Fig. I-2(a). The difference between the arrival times of the highest peak in Figs I-3(a) and 3(b), i.e., $t_2 - t_1$, gives the time of flight for the ultrasound to travel through the sample. Knowing the time of flight and the distance between the transducers, the wave speed is obtained.

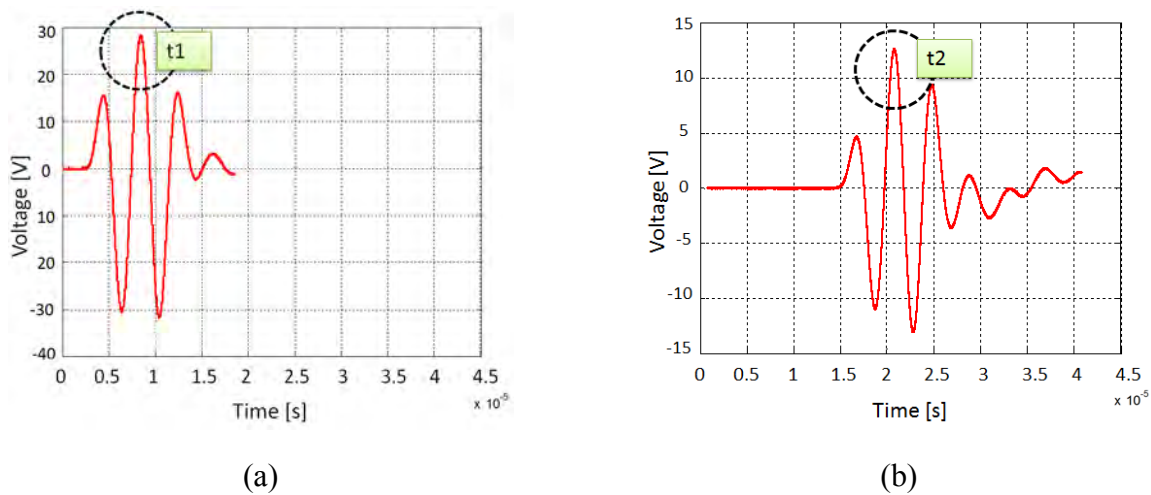


FIGURE I-11. Wave form received by the receiver when (a) the transmitter and receiver are placed face-to-face directly and (b) the transmitter and the receiver are placed on opposite sides of the sample as illustrated in Fig. I-2(a)

The wave speed so measured is plotted Fig. I-5 as a function of moisture content. Again, the results are the average values from four samples. It is seen that the wave speed increases almost linearly with increasing moisture content. However, the increase is so slight ($< 2\%$) that it is almost negligible. Previous studies, e.g., [4], have shown that wave speed could increase by as much as 12% when a concrete sample is fully saturated with moisture. It is thus speculated that such increase in wave speed in concrete is probably caused by the moisture stored in the aggregate/cement interfaces, since our results show that wave speed in cement mortar is not much affected by moisture.

To study the attenuation, the pulse-echo method as illustrated in Fig. I-2(b) was used. Shown in Fig. I-4 is a typical wave form received by the transducer, where the peaks with amplitude labeled A_1 and A_2 are, respectively, the first and second reflections from the far-side surface of the sample. The corresponding attenuation coefficient was then calculated from the following equation

$$\text{Attenuation Coefficient} = -\frac{20}{d} \log\left(\frac{A_2}{A_1}\right) \text{ [dB / mm]} \quad (2)$$

where d is the propagation distance (twice of the sample length).

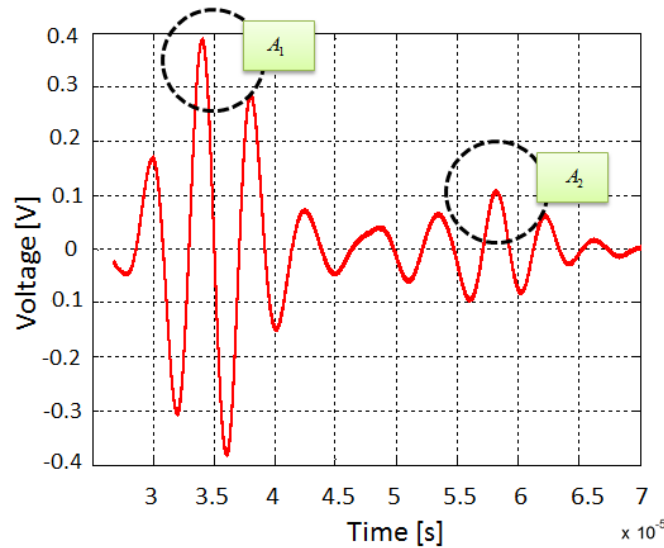


FIGURE I-12. Example of reflected signal obtained by pulse-echo method

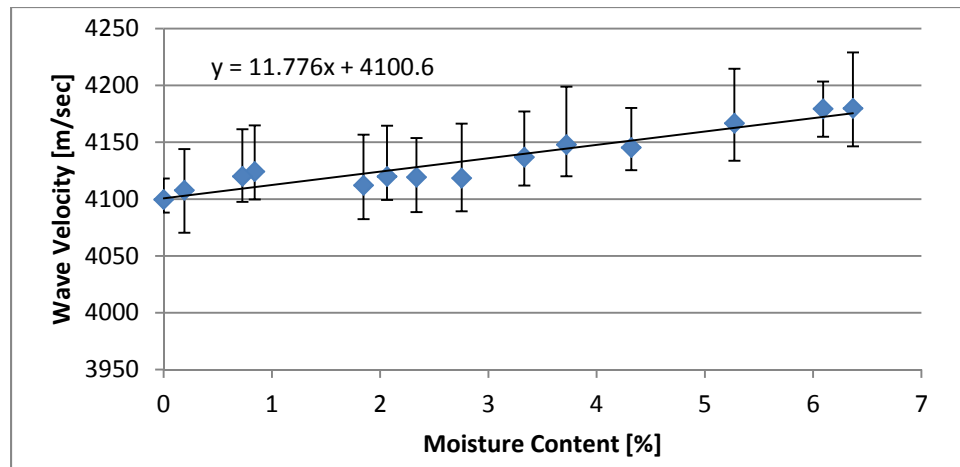


FIGURE I-13. Averaged wave velocity of all samples

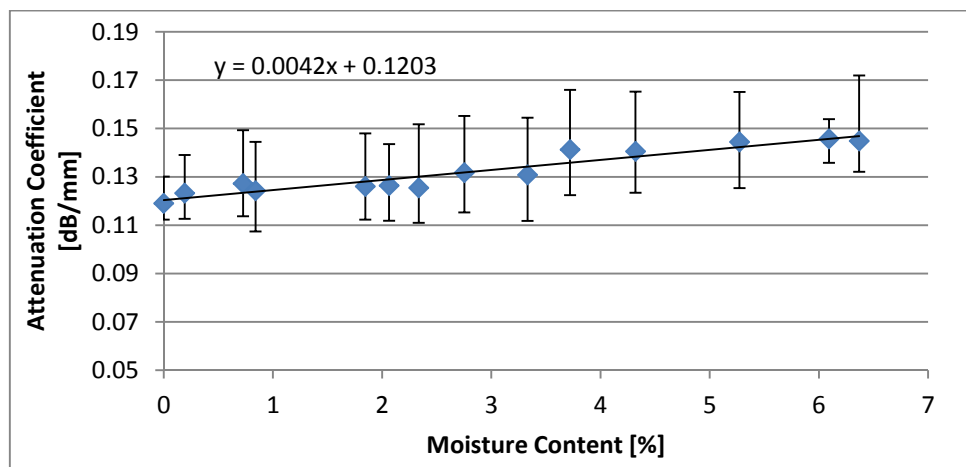


FIGURE I-14. Averaged attenuation coefficient of all samples

The measured attenuation coefficient is plotted in Fig. I-6. The data presented here are the average measurement from four samples. It is seen that the attenuation coefficient increases significantly with increasing moisture content. At full saturation, the attenuation coefficient is up more than 20%. Intuitively, this increase in attenuation might be attributed to the additional friction between the free water in the pores and the surrounding solid phase (cement).

Conclusions

This research has investigated experimentally the effects of moisture on ultrasonic phase velocity and attenuation in cement mortar samples. Several conclusions can be drawn from this study. First, moisture absorption and desorption are almost fully reversible in fully cured cement mortar samples. Second, moisture has negligible effects on the ultrasonic phase velocity in cement mortar samples. Finally, ultrasonic attenuation in cement mortar is strongly influenced by moisture. At full moisture saturation, the attenuation coefficient is more than 20% higher. It is because the effect of energy dissipation by liquid is more than that of stiffening medium.

References

1. Davis, A., F. Ansari, R. Gaynor, K. Lozen, T. Rowe, H. Caratin, F. Heidbrink, V. Malhotra, B. Simons, and N. Carino, *Nondestructive Test Methods for Evaluation of Concrete in Structures*. (American Concrete Institute, ACI, 1998), **228**.
2. Popovics, S. and J.S. Popovics, *Effect of stresses on the ultrasonic pulse velocity in concrete*. (Materials and Structures, 1991), **24**(1), pp. 15-23.
3. Ohdaira, E. and N. Masuzawa, *Water content and its effect on ultrasound propagation in concrete — the possibility of NDE*. (Ultrasonics, 2000), **38**(1–8), pp. 546-552.
4. Sturup, V., F. Vecchio, and H. Caratin, *Pulse velocity as a measure of concrete compressive strength*. (ACI Special Publication, 1984), **82**.
5. Liu, M., G. Tang, L.J. Jacobs, and J. Qu, *A nonlinear wave mixing method for detecting Alkali-Silica reactivity of aggregates*. (AIP Conference Proceedings, 2012), **1430**(1), pp. 1524-1531.
6. Antonaci, P., C.L.E. Bruno, A.S. Gliozzi, and M. Scalerandi, *Monitoring evolution of compressive damage in concrete with linear and nonlinear ultrasonic methods*. (Cement and Concrete Research, 2010), **40**(7), pp. 1106-1113.
7. Moradi-Marani, F., S.A. Kodjo, P. Rivard, and C.-P. Lamarche, *Nonlinear Acoustic Technique of Time Shift for Evaluation of Alkali-Silica Reaction Damage in Concrete Structures*. (ACI Materials Journal, 2014), **111**(1-6).
8. Officials, A.A.o.S.H.a.T., *Standard method of test for accelerated detection of potentially deleterious expansion of mortar bars due to alkali-silica reaction in Standard specifications for transportation materials and methods of sampling and testing Part 2B: Tests*. 2006, AASHTO: : Washington D.C.

III.2.9 Constitutive Model for Continuum Analysis for ASR Damage in Concrete with Diffusion of Compressible Gel into Pores

Introduction

The excessive expansion and disintegration of some concrete made of cements of a relatively high alkali content and of certain silica-containing aggregates can be explained by the so-called alkali-silica reaction (ASR). The ASR produces a soft viscous substance called the ASR gel, which has been observed to appear in pop-outs or to exude from cracks in concrete structures. The eigenstrain caused by the alkali-silica reaction (ASR) is different from the thermal eigenstrain or shrinkage eigenstrain. The latter is simply additive to the stress-induced deformation and causes (or is assumed to cause) no damage to the solid. The ASR gel expands the pores and microcracks within the material and generates in the pores and microcracks fluid pressure p , which leads to material damage. It is actually an eigenstrain on a sub-scale of the material. For a porous solid with pressurized fluid in the pores, two different theories are well established: 1) Biot's (or Biot-Fillunger's) two-phase medium theory, and 2) Terzaghi's effective stress theory. For three decades, these two theories were thought to be in conflict and were the subject of passionate polemics. One difference was that the latter assumed porosity $n < 1$ and the former $n = 1$ (for uplift in dam safety analysis). Another was that the elastic cross-stiffness between the solid and fluid has been missing from the latter. Today, however, it is clear that both are valid but have different applicability. The former applies to elastic or viscoelastic deformation of the porous medium, while the latter applies to failure and is an essential concept in soil mechanics.

This work explores a formulation that is an adaptation and combination of both (e.g., n increases, up to 1). The equality of macroscopic smeared-out deformation of both the solid and fluid phases is the same as in Biot's theory, but a major difference from Biot's theory is that the growth of fluid mass precludes applying the condition of equal strain in both phases. The model presented here should be applicable to any constitutive model for tensile softening damage but is here intended mainly for microplane model M7 (Caner and Bažant 2013).

ASR gel mass calculation

One purpose of present model is simulating the ASR gel pressure extruded into the porous phase (pores of cement mortar) when ASR gel mass increasing as a function of time. To describe the production of the ASR gel in the mineral aggregate, the model in Ref. [1] is adopted. This model is considered as a given input, which predicts the gel mass extruded into the adjacent pores and developing cracks in the matrix, as a function of time t . Fig.II-1 shows a sample result for the extruded gel mass for one spherical aggregate. The amount of extruded gel is depend on the diameter of the sphere; in this special case diameter assumed to be 20 mm. As it can be seen in this figure, the extruded gel mass is increasing function of time until the reaction front reaches the center of the aggregate (full reaction). After full reaction of the aggregate, extruded gel mass assumed to be constant.

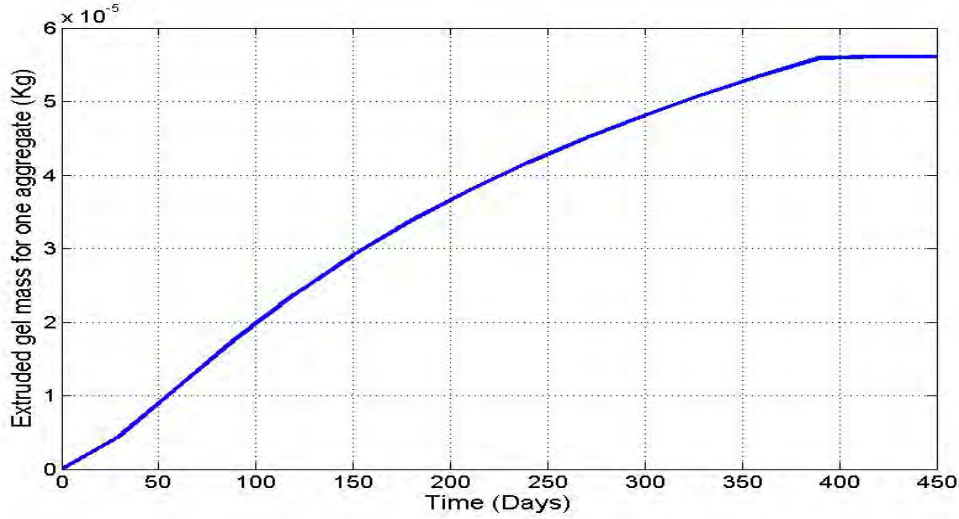


Figure II-15. Mass of extruded gel-time for one aggregate

ASR gel pressure evolution

Three different increments should be considered for ASR gel in each step. First increment is because of gel mass increment. Simultaneous gel mass increment can be accommodated only by elastic compression of the gel. This contribution can be formulated as following:

$$dp = \kappa \frac{dM}{M}$$

Where κ is the bulk modulus of ASR gel, and M is the mass of ASR gel.

Second contribution is because of diffusion of ASR gel When Gel Mass and Strain Are Constant. For calculating this pressure increment Darcy equation is used:

$$v = b \nabla p$$

Where v is the velocity and ∇ denotes the gradient and b = Darcy permeability (dimension $m^3 s / kg$)

In detailed analysis, one could now proceed to the point-wise differential equation for the diffusion in coordinate x . However, in view of all the uncertainties, it should suffice to replace v with the velocity dx/dt of the diffusion front at distance x from the aggregate surface, and the pressure gradient with the average pressure gradient $\bar{\nabla} p = p / x$. This leads to the simplified Darcy diffusion equation:

$$\frac{dx}{dt} = b \frac{p}{x}$$

By considering simplified Darcy equation and compressibility of ASR gel, the following equation can be derived:

$$\frac{dp}{\kappa} + \frac{p}{\eta} dt = 0$$

Where η is the effective viscosity.

Other pressure increment is because of the volumetric strain. By considering equal volumetric strain in solid part and porous part, this contribution can be calculated as following:

$$dp = -\kappa d\varepsilon_v$$

The last contribution that should be considered is the gradual filling of the pores. At early stages of the reaction, gel extruded into small volume around the particle. While, after reaction progress, concrete starts to crack and gel can extrude to further pores. Also it seems logical to assume aggregate will not have significant strains during process. Therefore, the area near particle undergo more strain than average strain. By solving equilibrium equations, an average strain for the element will be calculated, that this strain should be magnified to find the real strain in the part that gel extruded in. Fig. II-2, depicts this phenomena.

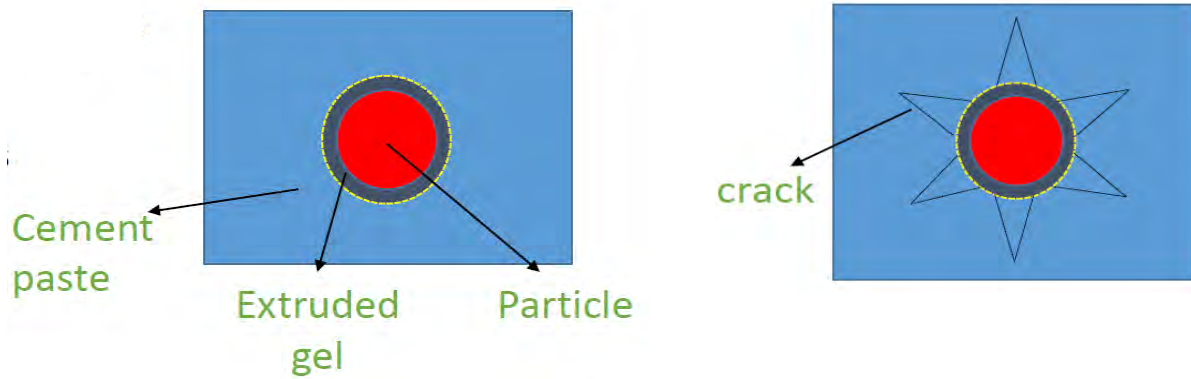


Figure II-16. Gel extrusion pattern

This phenomena is mostly important after cracking, since almost all of inelastic strain is due to the part that gel extruded to and other parts are free of inelastic strain. Simple equation for this phenomena can be written as following:

$$dp = -Ad\varepsilon_v''$$

Algorithm for ASR Gel Expansion Damage in a Finite Element System

In each time step $\Delta t = t_{r+1} - t_r$, in each integration point of each finite element of an explicit finite element program, the values of $\xi, \Delta\xi, \varepsilon_{ij}, \Delta\varepsilon_{ij}$ ($i, j = 1; 2; 3$) corresponding to the end of the time step known from the last run of the finite element program and from the calculation of gel mass increment.

For unconditional numerical stability, pressure increment can be found analytically in each step. By solving pressure differential equation following equations will be derived:

$$dp = (p_r - \eta q)e^{\frac{-dt}{\tau}} + \eta q - p_r$$

$$q = \frac{1}{\xi} \frac{d\xi}{dt} - \frac{d\varepsilon_v}{dt} - A \frac{d\varepsilon_v''}{dt}$$

Equilibrium equations for two-phase solid-fluid continuum

The material with expanding gel is considered as a two-phase solid-fluid continuum with variable fluid fraction. Equilibrium between gel pressure p in the pores and the volumetric stress σ_v in the three-dimensional solid requires that:

$$S_v = (1 - n_0)\sigma_v - n_0p$$

$$S_{ij} = \sigma_{ij} - (\sigma_v + p) n_0 \delta_{ij}$$

Here δ_{ij} = Kronecker delta (unit tensor); S_{ij} , S_v are the total stresses in the two-phase continuum and the total volumetric stress, which are used to calculate the nodal forces in an explicit finite element program (note that p is positive for compression, σ_v for tension).

Variation of Permeability and Effective Porosity

The permeability, b , is surely not constant. For $M < M_0$, the effective permeability is very high because the gel is filling bigger pores next to the ITZ. Later, the gel is forced under pressure into tighter and tighter pores. Thus the effective permeability b must sharply decrease with distance x to the diffusion front, or with M . Not being aware of any applicable characteristic length, we may logically assume that b decreases with M as a self-similar function, which is a power function; i.e.,

$$\text{for } M > M_0 \quad b = b_0 \left(\frac{M}{M_0}\right)^{-s}$$

where s ; b_0 are empirical constant (both ≥ 0). Probably $s \gg 1$, which reflects the fact that the very fine pores located farther from the aggregate piece beyond the ITZ are orders of magnitude harder to fill than the big pores in the ITZ.

According to the preceding simplified formulation, the gel pressure would be independent of the strains ε_{ij} in concrete. This is probably accurate enough only before the strength limit of concrete is reached. But once the ASR causes postpeak softening damage with large inelastic strain, microcracks will develop and serve as conduits greatly facilitating the flow of gel. This must be reflected in the increase of permeability, which may be assumed to depend on the inelastic volumetric strain:

$$\varepsilon_v'' = \varepsilon_v - \frac{\sigma_v}{3K}$$

Because, with increasing ε_v'' , the continuity of cracks is likely to increase, b ought to be an increasing function of ε_v'' . Combining the effects of pore tightening and crack widening, we may write:

$$\text{for } M < M_0 \quad b = b_0$$

$$\text{for } M > M_0 \quad b = b_0 \left(\frac{M}{M_0}\right)^{-s} + b_1 \left(\frac{\varepsilon_v''}{\varepsilon_p}\right)^2$$

where s ; b_0 ; b_1 = empirical constants.

Results of one dimensional simulation

1) Stress-strain curves

Fig. II-2 depicts a sample result of finite element simulation for unconfined condition. As it can be seen in this figure this model can capture the evaluation of stress and pressure very good. Also, as it can be seen in this figure, this model satisfy equilibrium equation greatly. Fig. II-3 shows the same result for confined condition, where the element is confined from all directions with elastic (spring) confinement. In this special case the stiffness of confinement assumed to be 1000 Mpa. As it can be seen in this figure after reaching the peak tensile strength of concrete, stress in solid part decreasing, but pressure is increasing. This behavior again is in complete agreement with equilibrium equation.

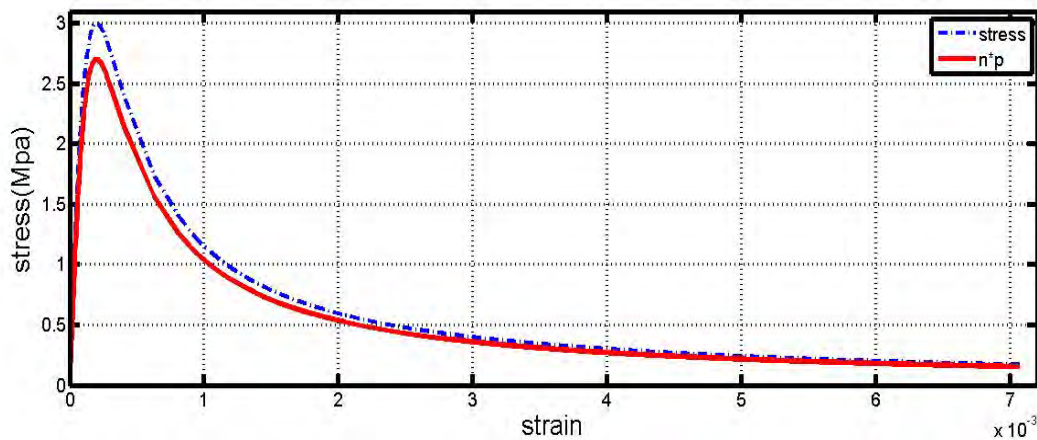


Figure II-17. Stress-strain curve of unconfined material element

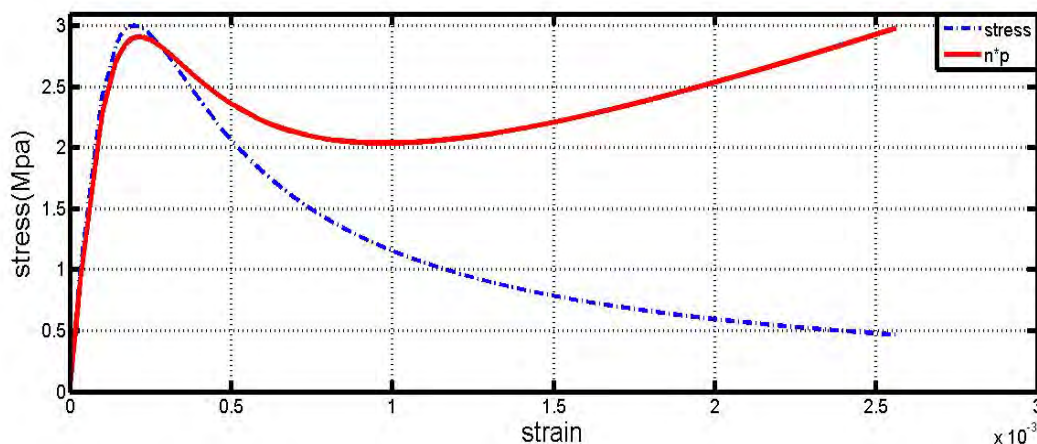


Figure II-18. Stress-strain curve of confined material element (C=1000 Mpa)

2) Free and restrained ASR expansion

To verify the ability of the model to predict correctly ASR-induced expansion under different loading conditions, this section presents the simulation of experimental results obtained by Multon and Toutlemonde [26]. Experiments were performed using sealed cylindrical specimens

(240 mm length and 130 mm in diameter). Three different cases were considered: (1) free expansion; 2) restrained expansion by using a 3 mm and thick steel ring; and (3) restrained expansion by using a 5 mm thick steel ring.

A) Unconfined condition

First, we consider free expansion test, without any external force and confinement. Fig. II-5 shows the mesh shape for this condition. Fig. II- 6 depicts the axial strain for simulation and experiment one. This figure shows good agreement between the results. Fig. II-7 depicts results for the radial strain. Also, it can be seen that the radial strain is also in good agreement with the experiment.

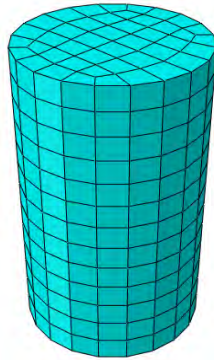


Figure II-19. Finite element mesh for unconfined condition

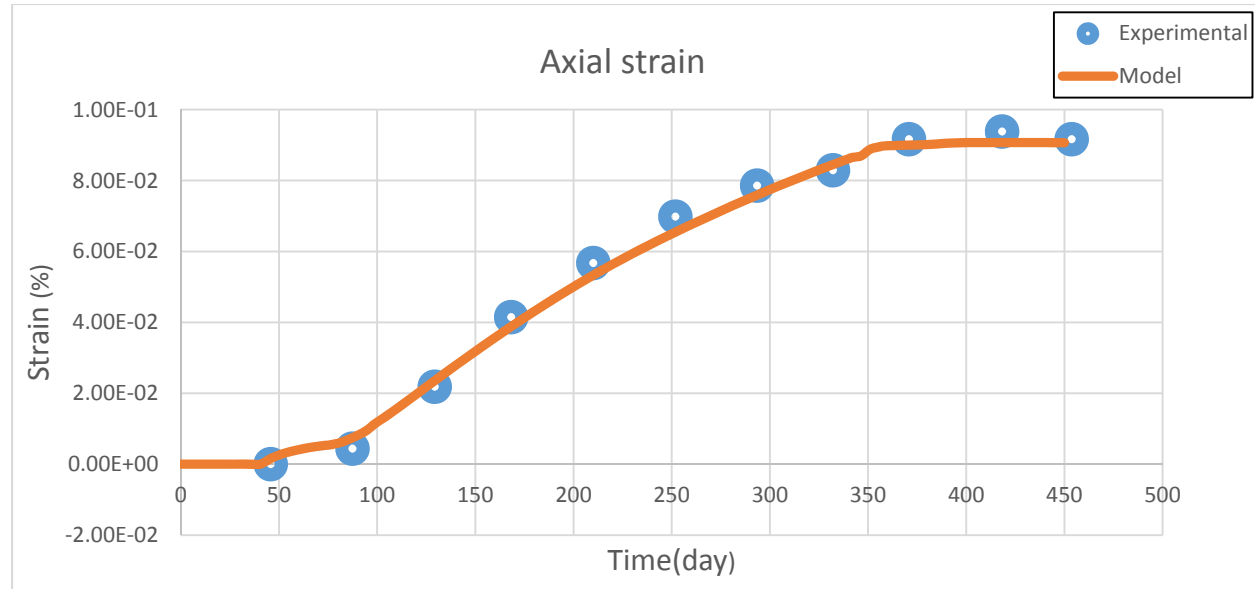


Figure II-20- Axial strain for unconfined condition

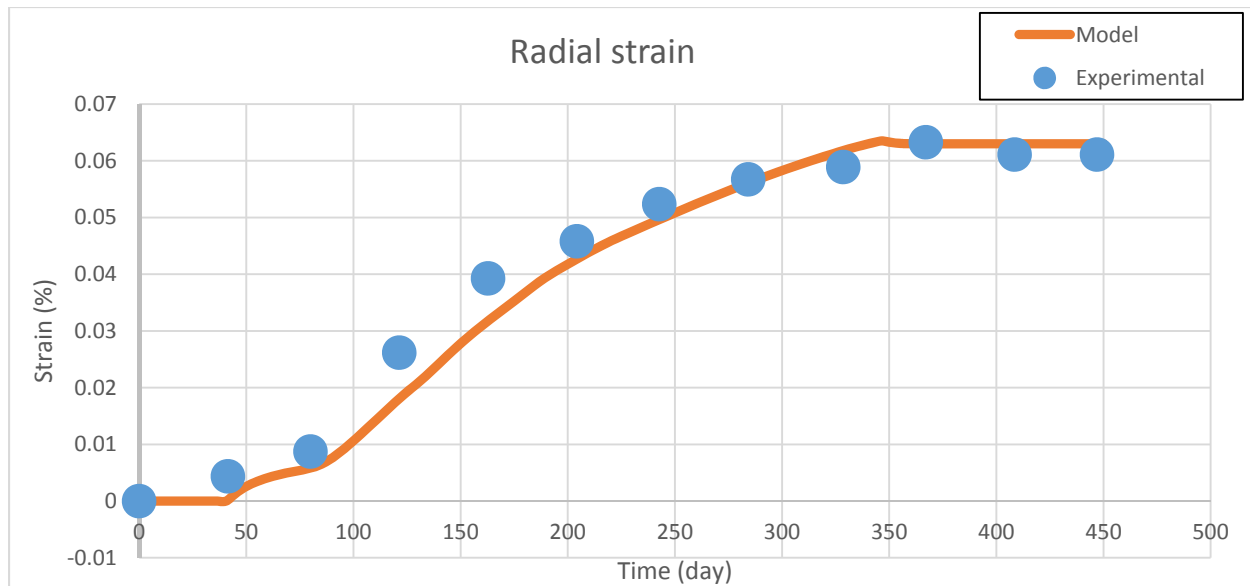


Figure II-21- Radial strain for unconfined condition

B) Confined condition for 3mm ring

This time concrete cylinder confined with 3 mm ring. Fig. II-8 shows finite element mesh for this condition.

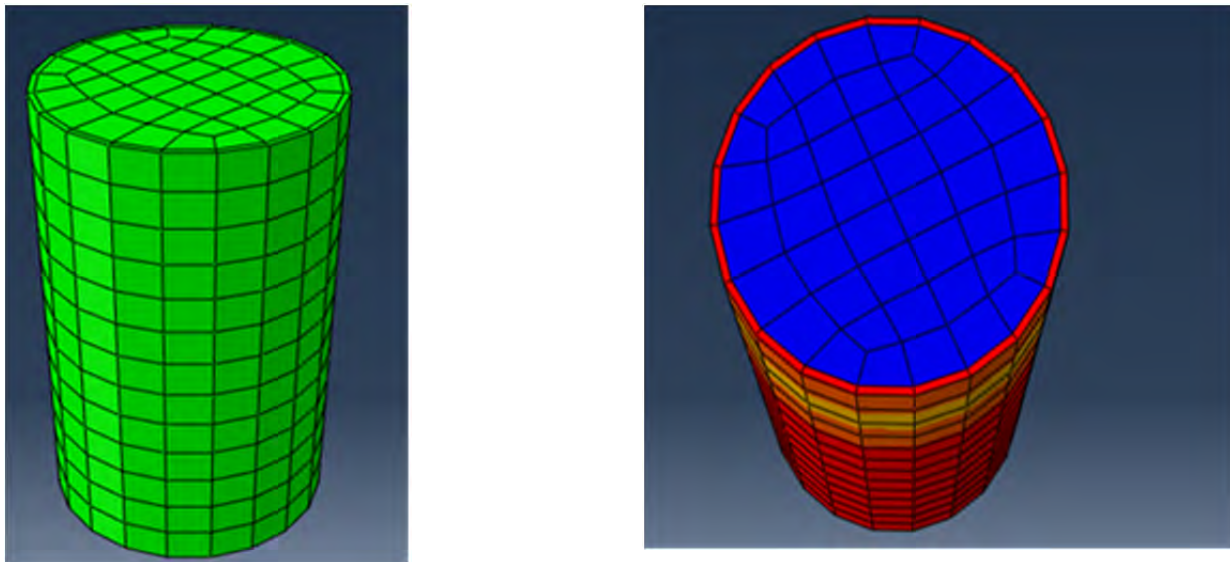


Figure II-22. Finite element mesh 3mm steel ring confinement

Fig. II- 9 and Fig. II-10 shows the results for this condition. As it can be seen results are in good agreement with experimental data.

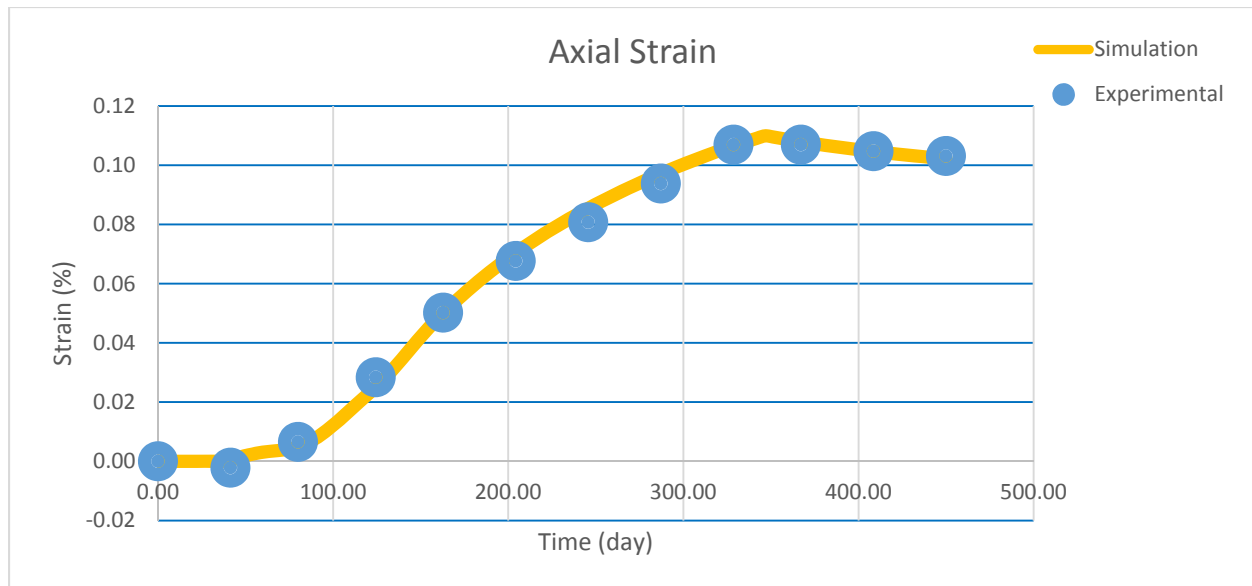


Figure II-23. Axial strain for 3mm steel ring confinement case

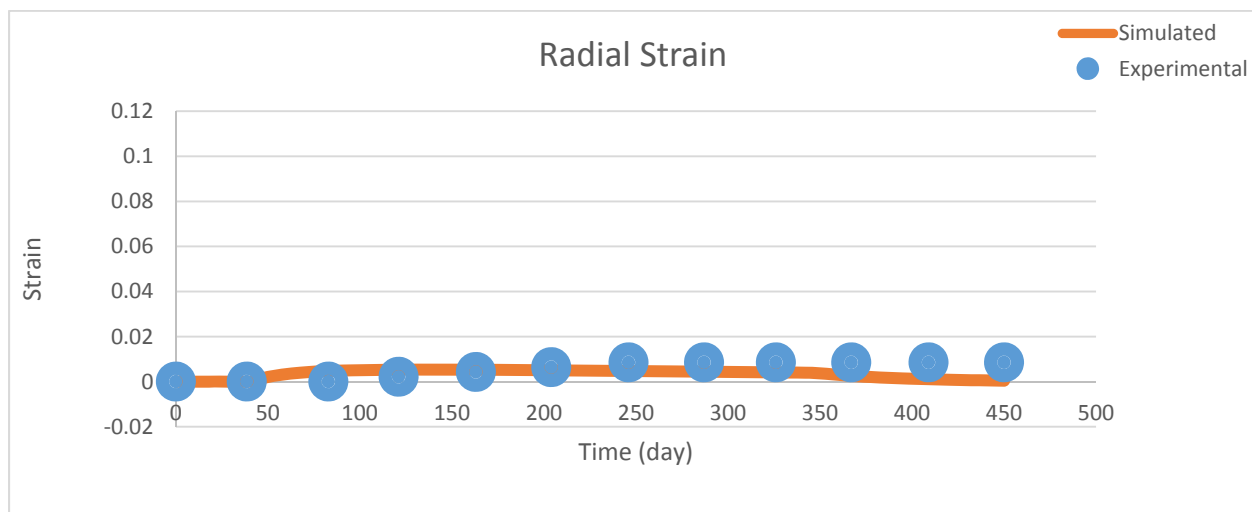


Figure II-24. Radial strain for 3mm steel ring confinement case

References

- [1] Bažant, Z.P., and Stefens, A. (2000). "Mathematical model for kinetics of alkali-silica reaction in concrete." *Cement and Concrete Research* 30 (3), 419{428 (disc. reply Vol. 31, 2001, 1111 {1113).
- [2] Bažant, Z.P., Zi, G., and Meyer, C. (2000). "Fracture mechanics of ASR in concretes with waste glass particles of different sizes." *J. of Engrg. Mechanics ASCE* 126 (3), 226{232.
- [3] Caner, F.C., and Bažant, Z.P. (2013). "Microplane Model M7 for Plain Concrete: I. Formulation. II. Calibration and Verification" *ASCE J. of Engrg. Mechanics* 139 (12), 1714-1723 and 1724-1735.
- [4] Multon S, Toutlemonde F. Effect of applied stresses on alkali - silica reaction induced expansions. *Cem Concr Res* 2006;36:912 - 20.

III.3 Report of the 3rd year

III.3.1 Effects of Moisture on Ultrasound Propagation in Cement Mortar

Introduction

Alkaline-silica reaction (ASR) is a major chemical degradation mechanism in concrete. In a humid environment, concrete may absorb moisture from the surrounding environment. As the absorbed moisture diffuses through the concrete, it dissolves the free alkaline ions in the cement and transports them to the aggregates. These alkaline ions then react with the amorphous silica in the aggregate. Such reaction produces a gel called ASR gel. The ASR gel expands its volume as it imbibes more water. Such volumetric expansion of the ASR gel induces large internal pressure, which may then cause microcracking of the concrete. For safe operation of concrete structures, nondestructive evaluation (NDE) techniques are needed to monitor and characterize ASR damage.

Ultrasound has been used extensively for NDE of cement-based materials [1-4]. Most of these applications are based on linear ultrasonic methods. In recent years, nonlinear ultrasonic techniques have also been developed [5-7]. A major challenge in using ultrasonic NDE methods for chemical degradation such as ASR is how to quantify the degree of damage in the early stages. To this end, it is critical to develop a fundamental understanding of how ultrasonic wave propagation is affected by the presence of moisture, gel and microcracks.

When moisture enters a mortar bar, free water diffuses through the entire bar with transporting free alkaline ions. So the governing equation of moisture diffusion can be expressed in terms of water concentration. Since diffusion of moisture is driven by the concentration gradient of free water, the governing equation is

$$\frac{dC}{dt} = \nabla \cdot (D \nabla C) \quad (1)$$

where C = water concentration, t = time and D = diffusion coefficient.

In this quarter, numerically obtained moisture diffusion coefficient is presented and its concentration-independency has been checked by comparing ABAQUS simulation results with experimentally obtained moisture diffusion results in mortar bars. Moreover, diffusivity of alkaline solution is compared with that of pure water.

Sample Preparation

Nine cement mortar cubic samples of 2X2X2 inches were made following the procedures described by AASHTO T303 [8]. The type I cement (potential Bogue composition 46.11% C₃S, 22.93% C₂S, 8.52% C₃A and 9.59% C₄AF and 0.83% Na₂O_{eq}) and sorted lime stone sand were used. Particle size distribution of the sand is given in Table 1. The water/cement ratio used is 0.5 and the sand/cement ratio is 2.25. After demolding, the samples were submerged in tap water at ambient room temperature for 14days to cure.

TABLE 1. Sand proportion added to cement [8]

Sieve Size		Weight, %
Passing	Retained on	
4.75 mm (No. 4)	2.36 mm (No. 8)	10
2.36 mm (No. 8)	1.18 mm (No. 16)	25
1.18 mm (No. 16)	600 μ m (No. 30)	25
600 μ m (No. 30)	300 μ m (No. 50)	25
300 μ m (No. 50)	150 μ m (No. 100)	15

ABAQUS simulation

This analysis is to simulate the diffusion of test solution into the mortar cube and calculate its concentration at each time. In ABQUS module, heat transfer has been used since its governing equation is mathematically identical. The “temperature” in this analysis is equivalent to concentration of diffusion equation. In the equation (1), Where C is concentration in mass diffusion and temperature in heat transfer. D is thermal diffusivity in heat transfer analysis and diffusivity in mass diffusion. The thermal conductivity we use in ABAQUS is not equivalent to thermal diffusivity but they are related by the formula:

$$\alpha = \frac{k}{\rho c_p} \quad (2)$$

where α is thermal diffusivity, k is the thermal conductivity used. c_p is specific heat and ρ is density, Therefore, when we use heat transfer analysis to simulate mass diffusion in ABAQUS, we should convert thermal conductivity into diffusivity. For this simulation, density and specific heat were assigned to be one so that they are equal.

Moisture Content Measurement

After the 14days curing in tap water at room temperature (25°C), nine samples were then placed in a drying oven set at 80°C until the samples were fully dried. Moisture content measurements were carried out by measuring the weight change of the samples under water-uptake conditions. Three samples over nine samples in total were submerged in pure water, 0.5N and 1N test solution respectively, and the reported data are the average of results from these three samples. The first weight measurement was taken when the samples were fully dried and weight measurements were taken periodically. The moisture contents is then computed using the standard formula,

$$\text{Solution Uptake [\%]} = \frac{\text{weight(moist)} - \text{weight(dry)}}{\text{weight(dry)}} \times 100 \quad (3)$$

The solution uptake measured is plotted in Fig. I-1.

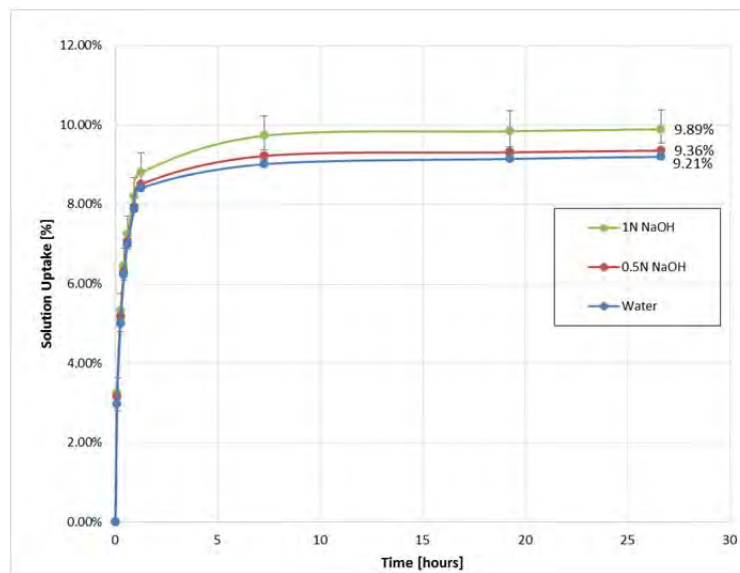


FIGURE I-25. Diffusion tests of three different solutions in the samples after fully dried in the drying oven at 80°C.

To investigate diffusion coefficient of three different test solutions, weight of the samples were measured as shown in Fig. I-1 and it is found that higher alkaline solution diffuses more than the other lower alkalinity solutions. This is because gradient of alkaline ions concentration serves as additional driving force. With these experimental data, ABQUS diffusion simulation has been implemented.

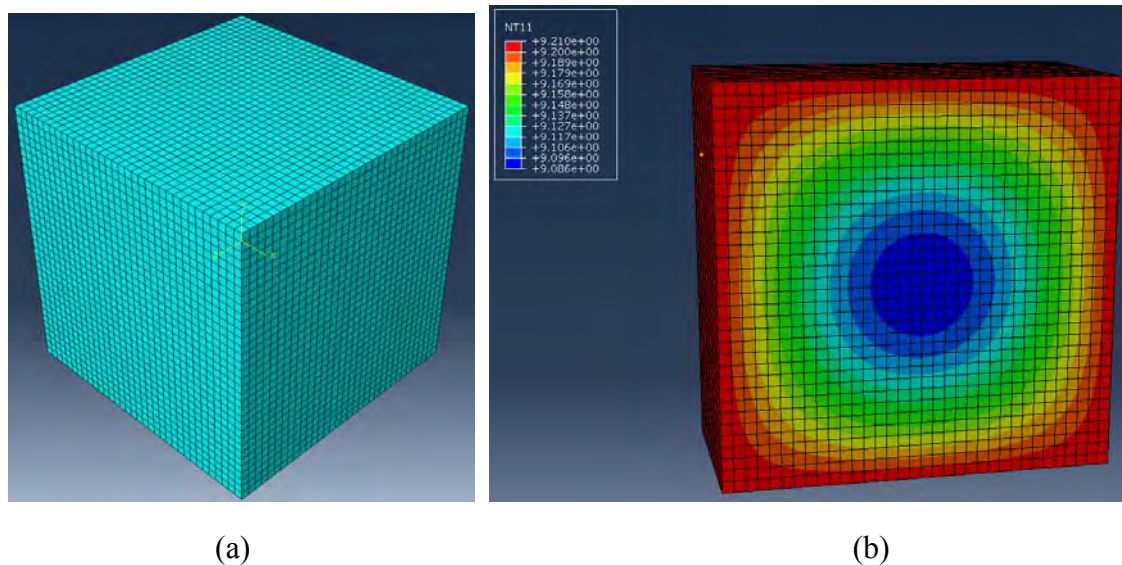


FIGURE I-2. (a) Uniform mesh of the mortar cube model (b) One frame of water diffusion process.

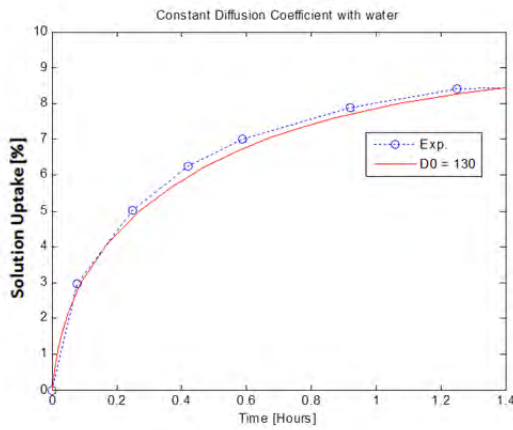
39304 uniform elements have been generated and the maximum solution uptake data from the experiment has been used as a boundary condition. The solution diffusion model was running for

28 hours in the simulation. Each corresponding numerically obtained data points were compared with the data from the experiment to find an optimized diffusion coefficient which makes the minimum error. Coefficient of determination method was used in order to determine appropriate value as followings,

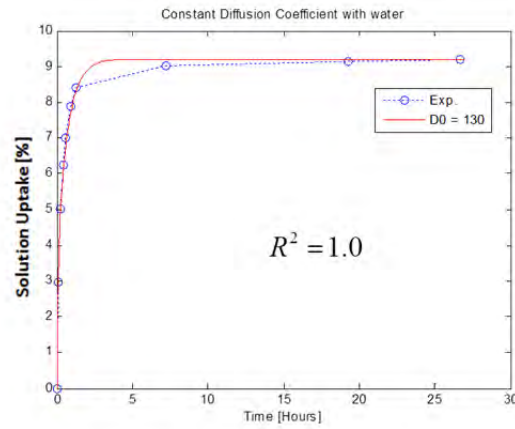
$$R^2 \equiv 1 - \frac{\sum_i (y_i - f_i)^2}{\sum_i (y_i - \bar{y})^2} \quad (4)$$

where y_i = experimental data, f_i = numerical data and \bar{y} = mean of experimental data

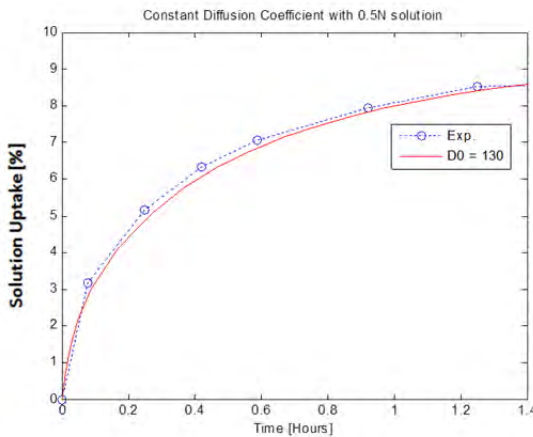
In fig. I-3, sub figures of (a), (c) and (e) present the numerical data over the first 1.4 hours and the rest of figures show the results during the entire 28 hours and it is seen that diffusion coefficient of $D=130 \text{ mm}^2 / \text{s}$ provides the best fit to the experiment results, having $R^2 \equiv 1.0$.



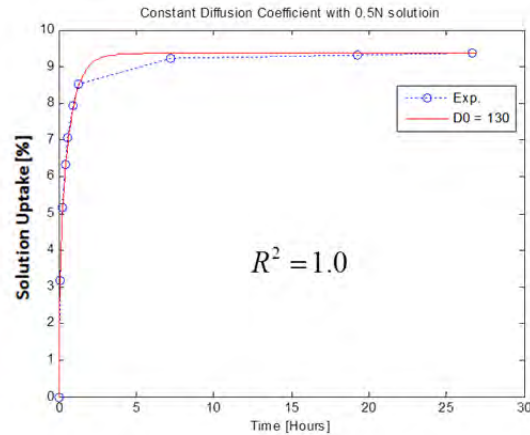
(a)



(b)



(c)



(d)

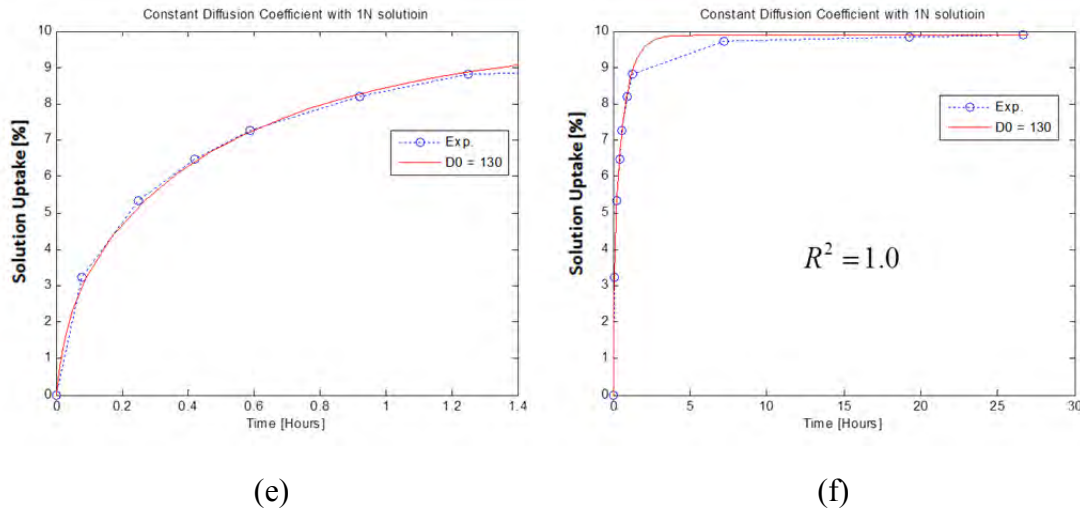


FIGURE I-3. Diffusion Simulation of (a)&(b) pure water, (c)&(d) 0.5N and (e)&(f) 1N solution

Conclusions

This study has numerically obtained the diffusion coefficient of test solutions. Several conclusions can be drawn from this study. First, for 2 inch mortar cube at room temperature, test solution diffusion occurs as constant diffusivity. Second, higher alkalinity solution makes the sample absorb more solution than lower one. Finally, although the maximum weight gain varies versus alkalinity of each solution, the diffusivity is comparable. It is because water diffusion is dominant over the entire diffusion regardless of alkaline ions.

References

1. Davis, A., F. Ansari, R. Gaynor, K. Lozen, T. Rowe, H. Caratin, F. Heidbrink, V. Malhotra, B. Simons, and N. Carino, *Nondestructive Test Methods for Evaluation of Concrete in Structures*. (American Concrete Institute, ACI, 1998), **228**.
2. Popovics, S. and J.S. Popovics, *Effect of stresses on the ultrasonic pulse velocity in concrete*. (Materials and Structures, 1991), **24**(1), pp. 15-23.
3. Ohdaira, E. and N. Masuzawa, *Water content and its effect on ultrasound propagation in concrete — the possibility of NDE*. (Ultrasonics, 2000), **38**(1–8), pp. 546-552.
4. Sturup, V., F. Vecchio, and H. Caratin, *Pulse velocity as a measure of concrete compressive strength*. (ACI Special Publication, 1984), **82**.
5. Liu, M., G. Tang, L.J. Jacobs, and J. Qu, *A nonlinear wave mixing method for detecting Alkali-Silica reactivity of aggregates*. (AIP Conference Proceedings, 2012), **1430**(1), pp. 1524-1531.
6. Antonaci, P., C.L.E. Bruno, A.S. Gliozzi, and M. Scalerandi, *Monitoring evolution of compressive damage in concrete with linear and nonlinear ultrasonic methods*. (Cement and Concrete Research, 2010), **40**(7), pp. 1106-1113.
7. Moradi-Marani, F., S.A. Kodjo, P. Rivard, and C.-P. Lamarche, *Nonlinear Acoustic Technique of Time Shift for Evaluation of Alkali-Silica Reaction Damage in Concrete Structures*. (ACI Materials Journal, 2014), **111**(1-6).

8. Officials, A.A.o.S.H.a.T., *Standard method of test for accelerated detection of potentially deleterious expansion of mortar bars due to alkali-silica reaction in Standard specifications for transportation materials and methods of sampling and testing Part 2B: Tests*. 2006, AASHTO: : Washington D.C.

III.3.2 A Micromechanics Model for the Acoustic Nonlinearity Parameter in Solids with Distributed Microcracks

Although the precise mechanisms of ASR formation are still under intensive investigation, it is generally accepted that there are four stages in ASR damage development: (1) gel formation, (2) internal pressure buildup, (3) microcrack initiation, and (4) crack growth. In our earlier report, we have shown that microcracking is the main contributor for the acoustic nonlinearity measured in the nonlinear ultrasonic testing. So, in this task, we try to develop a micromechanics-based model to simulate the effects of microcracks on the propagating ultrasound.

The first task is to estimate the tensile and compressive elastic moduli of elastic solids containing randomly distributed microcracks. The models are based on Eshelby (dilute crack density) model and the self-consistent model. Both static and frequency dependent cases are considered. Numerical simulations using the finite element method are conducted to validate the model. The model predicts that tensile and compressive moduli are different. Wave attenuation is also predicted by the model.

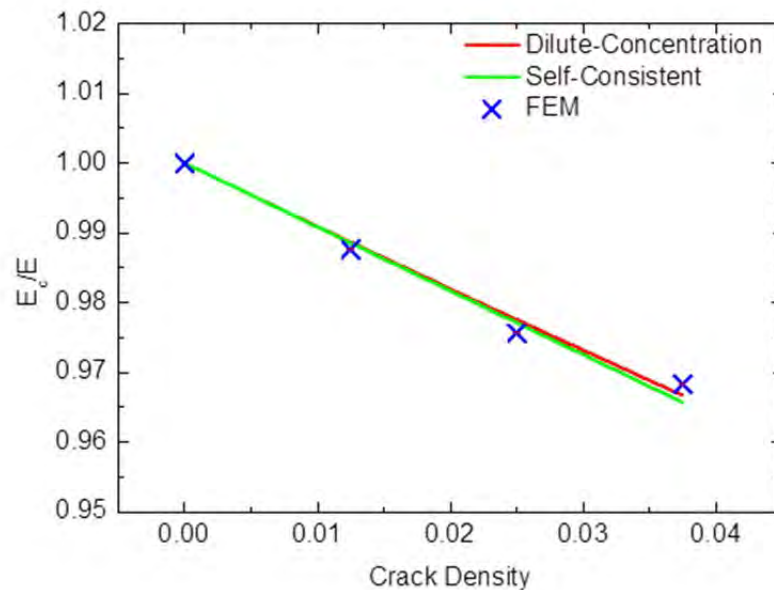


Fig. 3 Static compressive modulus versus crack density for plane strain case ($\mu = 0.5$). Solid lines are model predictions and symbols are from FEM.

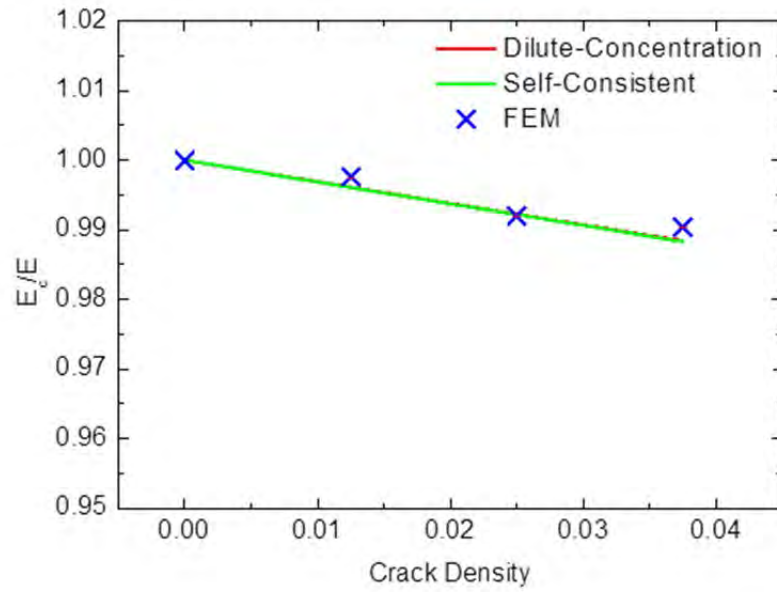


Fig. 4 Static compressive modulus versus crack density for plane strain case ($\mu = 1.0$). Solid lines are model predictions and symbols are from FEM.

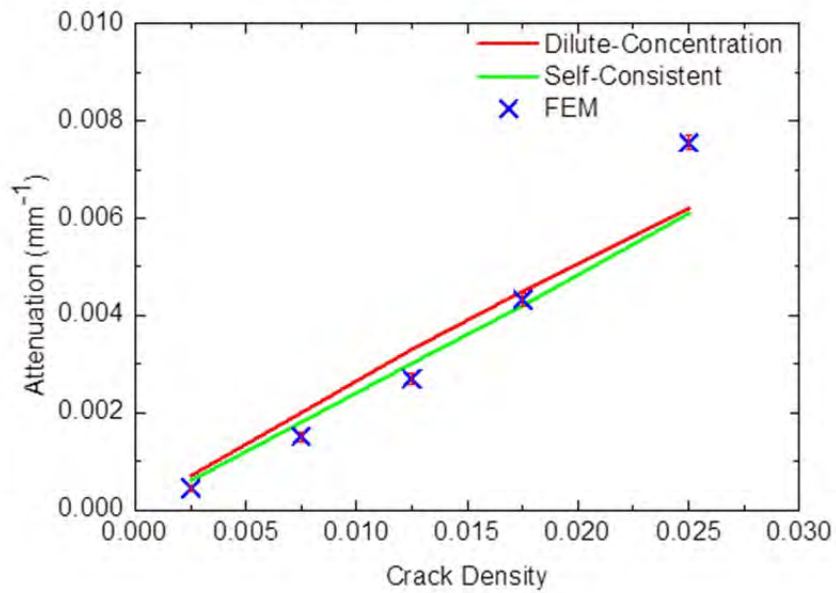


Fig. 5 Attenuation versus crack density for plane strain case ($\eta = 0.2516$). Solid lines are model predictions and symbols are from FEM.

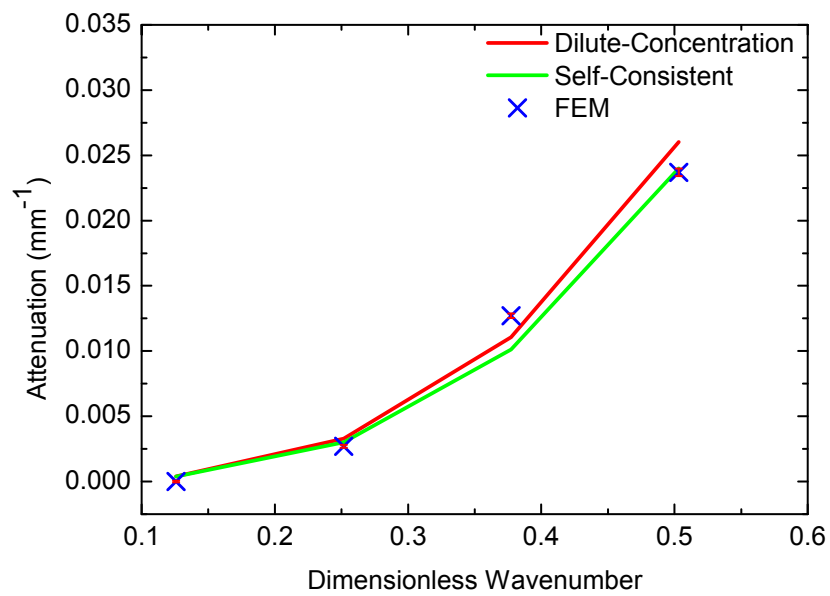
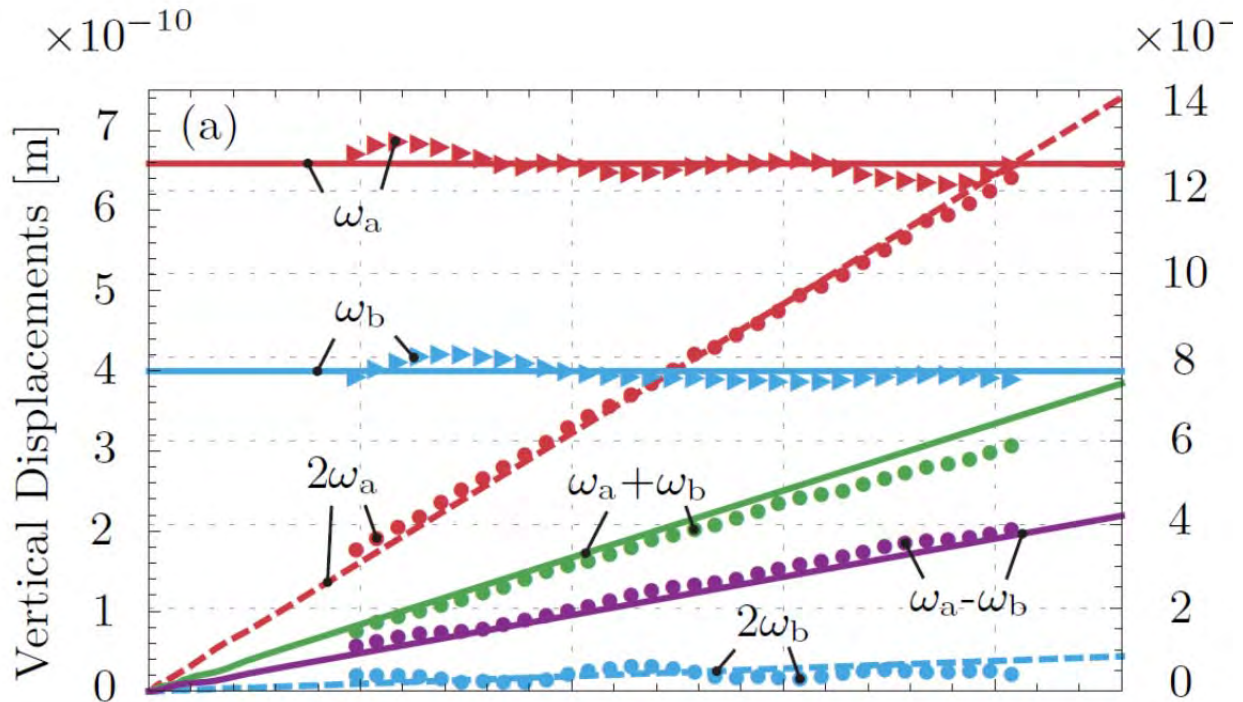


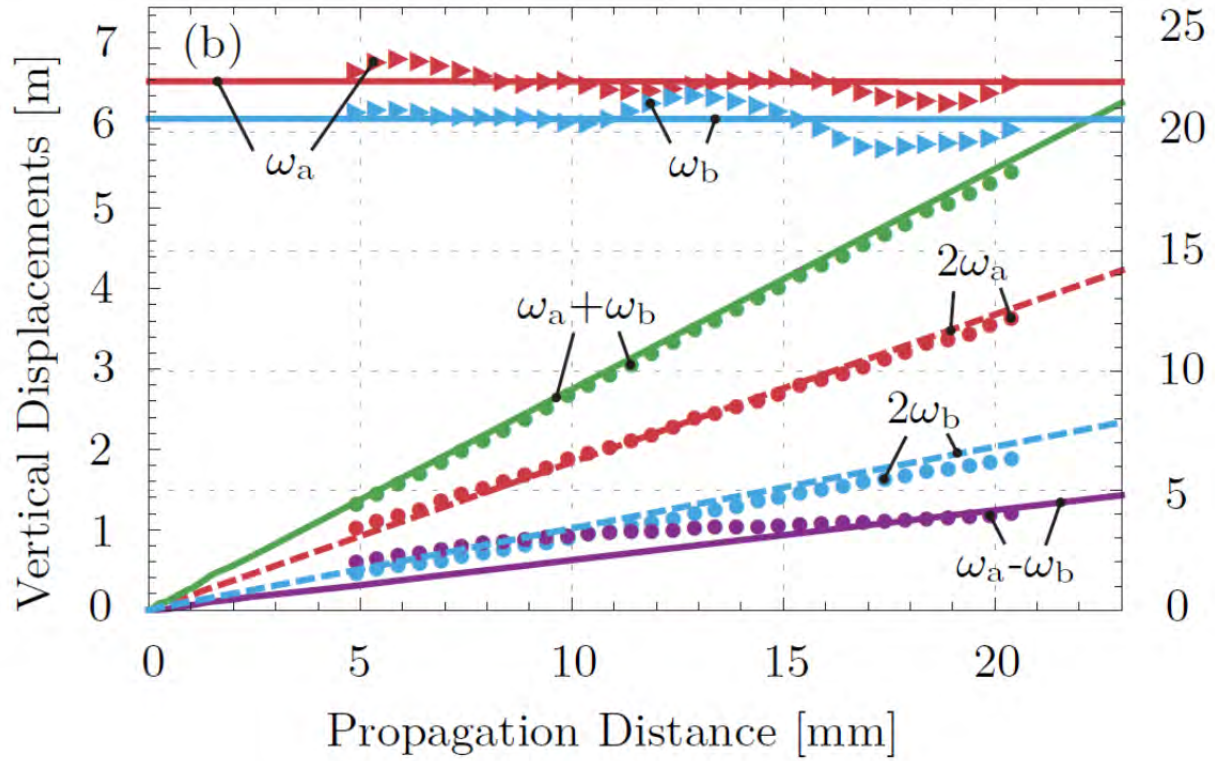
Fig. 6 Attenuation versus frequency for plane strain case ($c = 0.0125$). Solid lines are model predictions and symbols are from FEM.

III.3.3 Mixing of Two Co-Directional Rayleigh Surface Waves in a Nonlinear Elastic Material

The mixing of two co-directional, initially monochromatic Rayleigh surface waves in an isotropic, homogeneous and nonlinear elastic solid is investigated using analytical, finite element method and experimental approaches. The analytical investigations show that while the horizontal velocity component can form a shock wave, the vertical velocity component can form a pulse independent of the specific ratios of the fundamental frequencies and amplitudes that are mixed. This analytical model is then used to simulate the development of the fundamentals, second harmonics, and the sum and difference frequency components over the propagation distance. The analytical model is further extended to include diffraction effects in the parabolic approximation. Finally, the frequency and amplitude ratios of the fundamentals are identified which provide maximum amplitudes of the second harmonics as well as of the sum and difference frequency components, to help guide effective material characterization; this approach should make it possible to measure the acoustic nonlinearity of a solid not only with the second harmonics, but also with the sum and difference frequency components. Results of the analytical investigations are then confirmed using the finite element method and the experimental feasibility of the proposed technique is validated for an aluminum specimen.



Vertical displacements related to different frequencies of the analytical (curves) and the FE model (symbols) at the stress free surface. The fundamental frequencies are chosen as $\omega_a = 5\pi\text{MHz}$ and $\omega_b = 2\pi\text{MHz}$. The excitation of the mixed longitudinal wave in the wedge is conducted with two sine signals at amplitudes of $15 \times 10^{-10}\text{m}$.



Vertical displacements related to different frequencies of the analytical (curves) and the FE model (symbols) at the stress free surface. The fundamental frequencies are chosen as $\omega_a = 5\pi\text{MHz}$ and $\omega_b = 4\pi\text{MHz}$. The excitation of the mixed longitudinal wave in the wedge is conducted with two sine signals at amplitudes of $15 \times 10^{-10}\text{m}$.

III.3.4 Constitutive Model for Continuum Analysis for ASR Damage

Introduction

ASR experiments usually are done in long periods (more than 400 days). Also, these experiments are done under loading, and these loads can be high (20 Mpa). Therefore, for sure creep will be important part of their deformation and it should be considered in the model. Since loads are high, creep and damage should be considered in coupled manner. Also, some experiments show humidity change during experiment. In order to consider this humidity change, shrinkage should be added to the model.

In order to consider creep and shrinkage B3 model is applied. In order to find the stresses in each step from given strains, following steps are done.

First, as we know strain can be found by using compliance function by the following equation.

$$\varepsilon(t) = \sigma J(t, t') \quad (1)$$

From B3 model compliance function is given as

$$J(t, t') = q_1 + C_0(t, t') + C_d(t, t', t_0) \quad (2)$$

in which q_1 = instantaneous strain due to unit stress, $C_0(t, t')$ = compliance function for basic creep (creep at constant moisture content and no moisture movement through the material), and $C_d(t, t', t_0)$ = additional compliance function due to simultaneous drying.

The total basic creep compliance is obtained by integrating as follows:

$$C_0(t, t') = q_2 Q(t, t') + q_3 \ln[1 + (t - t')^n] + q_4 \ln\left(\frac{t}{t'}\right) \quad (3)$$

And drying creep compliance can be found as:

$$C_d(t, t', t_0) = q_5 [\exp\{-8H(t)\} - \exp\{-8H(t'_0)\}]^{1/2}, \quad t'_0 = \max(t', t_0) \quad (4)$$

t'_0 is the time at which drying and loading first act simultaneously; and

$$H(t) = 1 - (1 - h)S(t) \quad (5)$$

And q 's are constants that depend on the type of concrete. And they can be found from B3 model.

For considering shrinkage again B3 model is applied.

Mean shrinkage strain in the cross section:

$$\epsilon_{sh}(t, t_0) = -\epsilon_{sh\infty} k_h S(t) \quad (6)$$

Time dependence:

$$S(t) = \tanh\sqrt{\frac{t - t_0}{\tau_{sh}}} \quad (7)$$

Humidity dependence:

$$k_h = \begin{cases} 1 - h^3 & \text{for } h \leq 0.98 \\ -0.2 & \text{for } h = 1 \text{ (swelling in water)} \\ \text{linear interpolation} & \text{for } 0.98 \leq h \leq 1 \end{cases}$$

Size dependence:

$$\tau_{sh} = k_t (k_s D)^2 \quad (8)$$

where v/s = volume to surface ratio of the concrete member, $D = 2v/s$ = effective cross-section thickness which coincides with the actual thickness in the case of a slab, k_t is a factor and k_s is the cross-section shape factor. All of these factors can be found from B3 model.

Rheologic Chains

Rheologic models obtained by serial or parallel coupling of an elastic spring and a viscous dashpot are too simple to approximate viscoelastic behavior of real materials in a realistic manner. The deficiencies of such simple models are obvious: Maxwell model leads to a constant creep rate if the stress is kept constant, while the actual creep process slows down in time. Kelvin model cannot capture any instantaneous elastic strain and does not exhibit gradual relaxation of stress under constant strain. Each of these models has a certain intrinsic time scale, and on much shorter or much longer time scales does not behave as a truly viscoelastic model but degenerates either into a spring or into a dashpot. B3 model is in acceptance with kelvin chain. Therefore, in order to consider the problem as general, Kelvin aging chain will be considered.

Aging Kelvin Chain

For the Kelvin model, generalization to the case of aging is less straightforward, but still possible. Differential equation for the non-aging Kelvin model originates from the stress equivalence relation, $\sigma = \sigma_e + \sigma_v$. For an aging spring we cannot link the elastic stress to the current value of the elastic strain, and we must deal with their rates. Therefore, the stress equivalence relation must also be written in the rate form, $\dot{\sigma} = \dot{\sigma}_e + \dot{\sigma}_v$, so that the partial stress rates could be expressed in terms of the strain rate. The resulting differential equation is

$$\dot{\sigma}(t) = E(t)\dot{\epsilon}(t) + \frac{d}{dt} [\eta(t)\dot{\epsilon}(t)] \quad (9)$$

is then of the second order. It can be rewritten as

$$\dot{\sigma}(t) = D(t)\dot{\epsilon}(t) + \eta(t)\ddot{\epsilon}(t) \quad (10)$$

Where

$$\begin{aligned} \eta(t)/D(t) &= \tau \\ D(t) &= E(t) + \dot{\eta}(t) \end{aligned}$$

$D(t)$ is age dependent moduli that can be found by using so called continuous retardation spectrum. For this purpose Widder's formula is used.

For finding modulus by using retardation spectrum at least three times derivation of compliance function is needed. This can be done numerically or analytically. In this work this derivation has done analytically in order to be more reliable and exact.

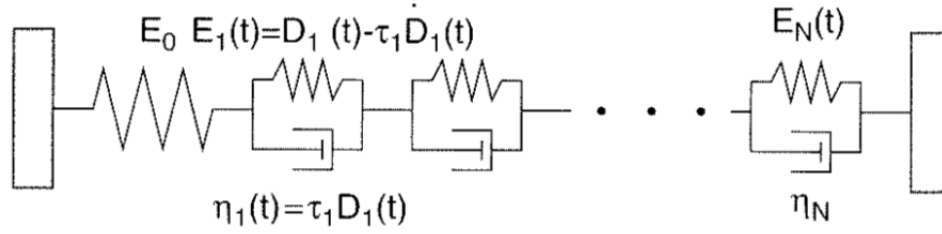


FIGURE II-26. Aging kelvin chain

By defining

$$\gamma_i = \tau_i \dot{\epsilon}_i \quad (11)$$

The differential equation will be simplified to,

$$\dot{\gamma}_i + \frac{1}{\tau_i} \gamma_i = \frac{\sigma_i(t)}{D_i(t)} \quad (12)$$

Since creep experiments are long in time and in order to be able to use large step times without going to unstability, Exponential algorithm will be applied in order to solve analytically differential equation in each step. By using this method we can find stress increment at the end of each time step for long step times. The final equations are as following,

$$\Delta \sigma = E'' G (\Delta \epsilon - \Delta \epsilon'') \quad (13)$$

Where

$$\beta_\mu = e^{-\frac{\Delta t}{\tau_\mu}}$$

$$\lambda_\mu = \tau_\mu (1 - \beta_\mu) / \Delta t$$

$$E''(t_{n-1/2}) = [E_0^{-1} + \sum_{\mu=1}^N D_\mu^{-1}]^{-1}$$

And at the end of each step internal variables can be updated by using the formula

$$\gamma_i^{(n+1)} = \frac{\lambda_i \bar{E}}{D_i^{(n+1/2)}} (\Delta \epsilon - \Delta \epsilon'') + \beta_i \gamma_i^{(n)} \quad (14)$$

Then by having stresses and internal variables at the end of each step we can go to next step.

Figure II-2 shows the results for unit compressive load by using B3 model and using finite element simulation by different number of chains in each kelvin unit. The results are totally very

good and also by increasing number of chain it comes closer to B3 model. Results shows that 21 chain gives almost exact results.

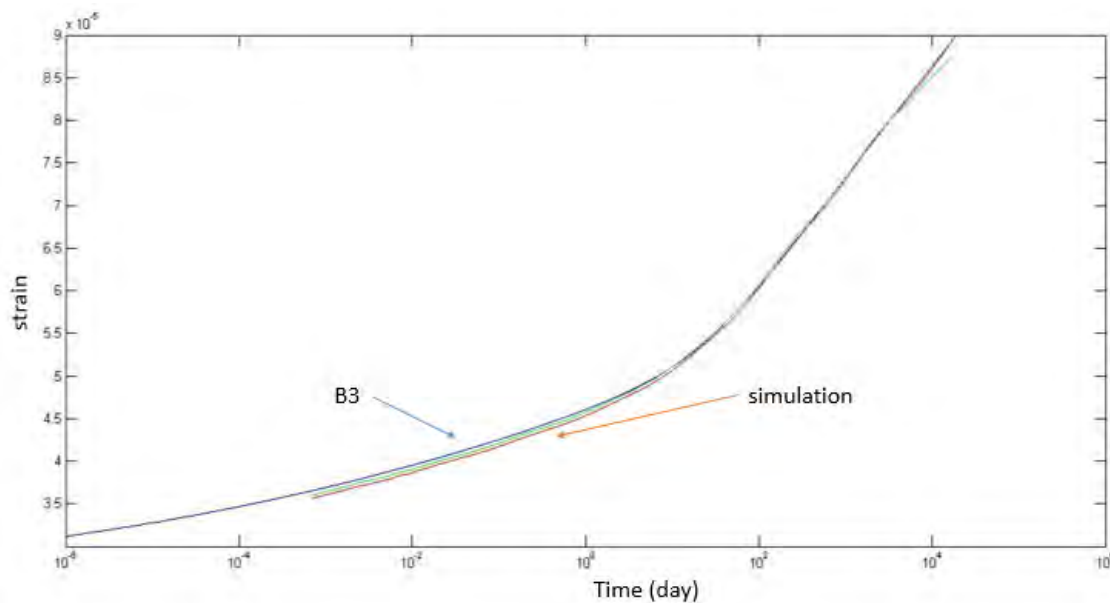


FIGURE II-27. Strain-time for unit compressive load

Figure II-3 shows the same results for the case that humidity is 75 percent. As it can be seen in this figure, also for this condition that we have drying creep results are in good agreement with B3 model in large interval of time.

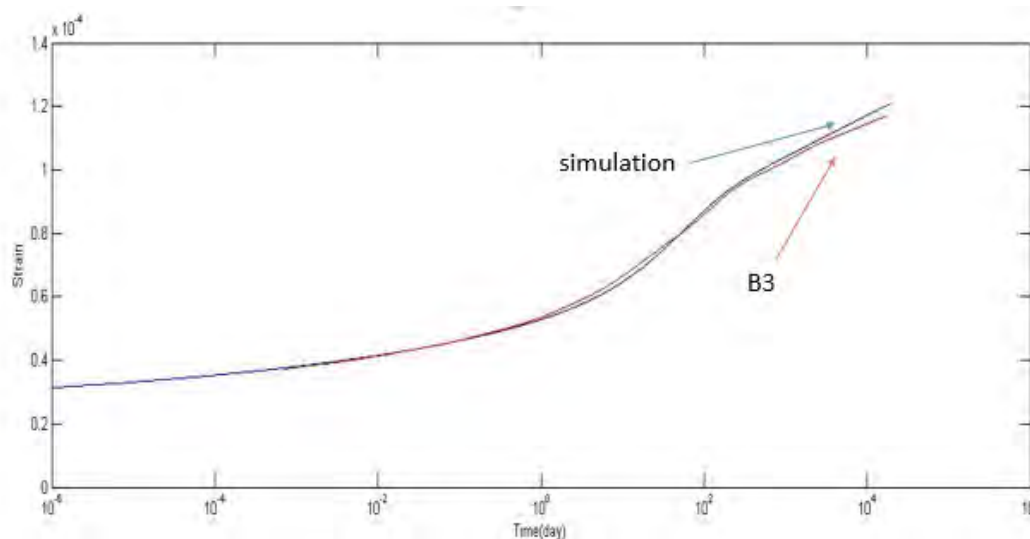


FIGURE II-28. Strain-time for unit compressive load and $h=75\%$

Figure II-4 shows the results for shrinkage. As it can be seen results are in good agreement.

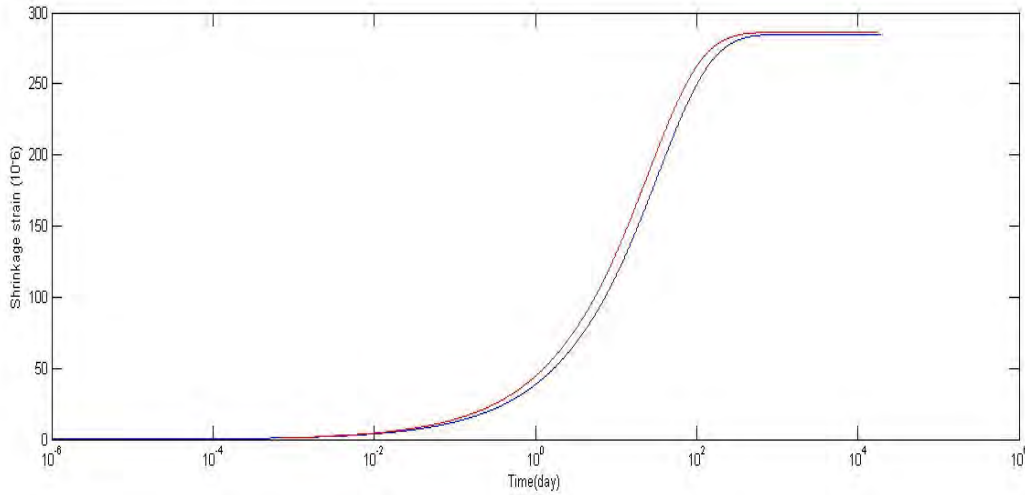


FIGURE II-29. Shrinkage for h=75%

Incorporation into Microplane Model

Until Now creep is considered without considering effect of damage. In order to model ASR reaction effect of damage should be considered and damage and creep should be considered coupled. In this study damage will be considered by using Microplane model. Thus, creep should be incorporated to this constitutive model.

In Microplane Model M7, the constitutive law is formulated in terms of the stress and strain vectors on each microplane.

On each microplane, the strain vector is decomposed into the volumetric strain, deviatoric strain, and shear strain. The trial stress can be found by changing young modulus by E'' (found from creep calculation). Then this stress will be relaxed because of creep.

The increments of the volumetric, deviatoric and shear stress components may be written as

$$\begin{aligned}
 \Delta \sigma_V &= E''_V (\Delta \varepsilon_V - \Delta \varepsilon''_V) \\
 \Delta \sigma_D &= E''_D (\Delta \varepsilon_D - \Delta \varepsilon''_D) \\
 \Delta \sigma_T &= E''_T (\Delta \varepsilon_T - \Delta \varepsilon''_T)
 \end{aligned} \tag{15}$$

In the next set up of figures results of simulation by considering creep without damage and creep coupled with damage will be compared. Figure II-5 shows the results for 0.1 Mpa compressive load. As it can be seen considering damage in this case doesn't have effect. This result is cogent, since the considered load is low and damage can't be expected.

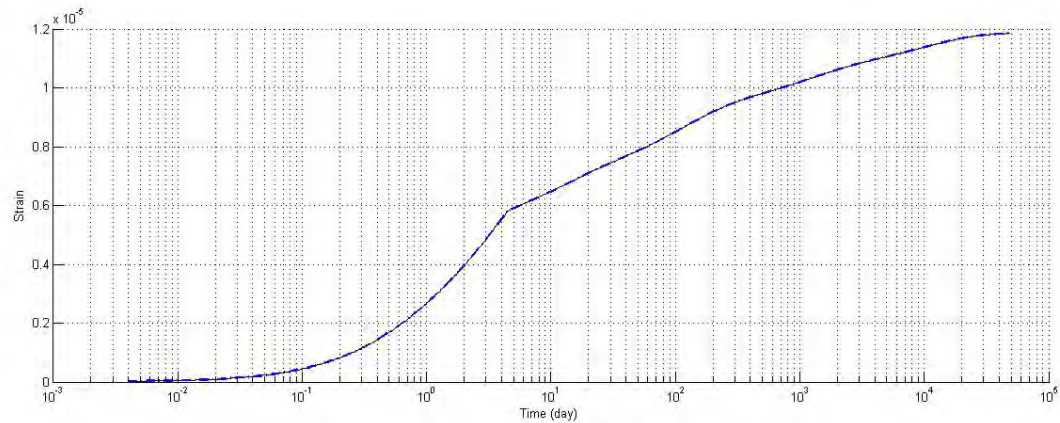


FIGURE II-30. Strain-time for 0.1 Mpa pressure by considering damage and without damage

Figure II-6 and II-7 show the same results for higher loads. As it can be seen, by increasing the load damage comes to play and we should consider that.

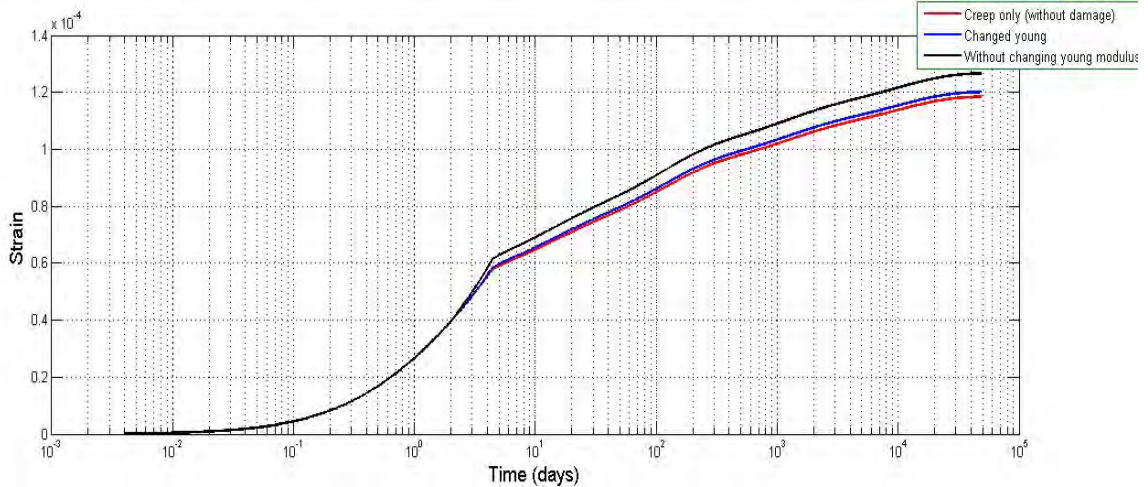


FIGURE II-31. Strain-time for 1 Mpa pressure by considering damage and without damage

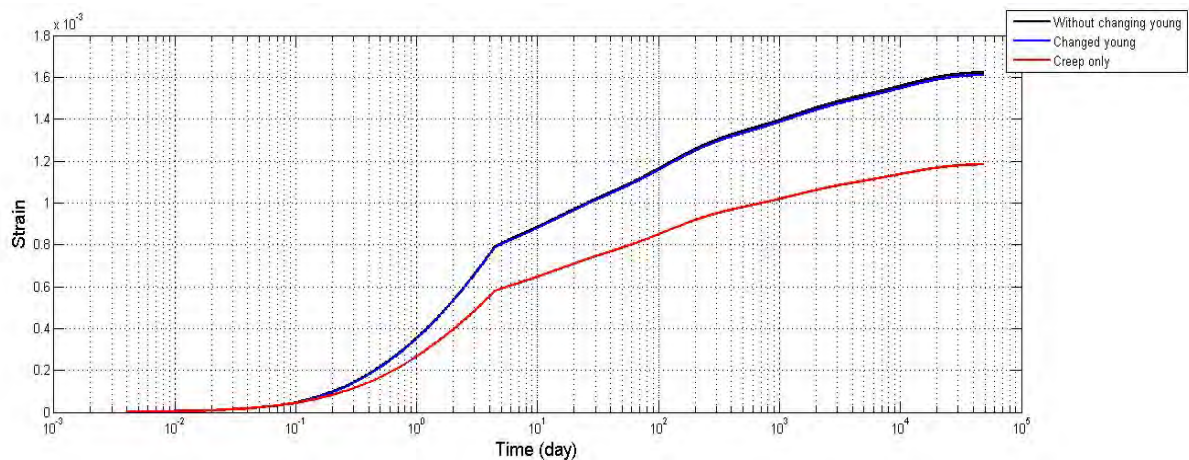


FIGURE II-32. Strain-time for 10 Mpa pressure by considering damage and without damage

References

1. Caner, F.C., and Bažant, Z.P. (2013). “Microplane Model M7 for Plain Concrete: I. Formulation. II. Calibration and Verification” *ASCE J. of Engrg. Mechanics* 139 (12), 1714-1723 and 1724-1735.
2. Bažant, Z. P., and Baweja, S. (2000) “Creep and shrinkage prediction model for analysis and design of concrete structures: Model B3— short form.” *Adam Neville Symposium: Creep and Shrinkage- Structural Design Effects*, ACI SP-194, A. Al-Manaseer, ed., American Concrete Institute, Farmington Hills, Mich., 85–100.
3. Zi, G., and Bažant, Z. P. (2001). “Continuous relaxation spectrum of concrete creep and its incorporation into microplane model M4.” *Creep, Shrinkage and Durability Mechanics of Concrete and Other Quasi-Brittle Materials, Proc., 6th Int. Conf., CONCREEP-6*, held at MIT, Cambridge F.-J. Ulm, Z. P. Bažant and F. H. Wittmann, eds. Elsevier, Amsterdam 2001, 239–243.
4. Bažant, Z. P., and Xi, Y. (1995). “Continuous retardation spectrum for solidification theory of concrete creep.” *J. Eng. Mech.*, 121(2), 281– 288.
5. Bažant, Z. P., and Xi, Y. (1995). “Continuous retardation spectrum for solidification theory of concrete creep.” *J. Eng. Mech.*, 121(2), 281–288.

III.3.5 Ultrasound Propagation in ASR Damaged Specimens

Introduction

Alkaline-silica reaction (ASR) is a major chemical degradation mechanism in concrete. In a humid environment, concrete may absorb moisture from the surrounding environment. As the absorbed moisture diffuses through the concrete, it dissolves the free alkaline ions in the cement and transports them to the aggregates. These alkaline ions then react with the amorphous silica in the aggregate. Such reaction produces a gel called ASR gel. The ASR gel expands its volume as it imbibes more water. Such volumetric expansion of the ASR gel induces large internal pressure, which may then cause microcracking of the concrete. For safe operation of concrete structures, nondestructive evaluation (NDE) techniques are needed to monitor and characterize ASR damage.

Ultrasound has been used extensively for NDE of cement-based materials [1-4]. Most of these applications are based on linear ultrasonic methods. In recent years, nonlinear ultrasonic techniques have also been developed [5-7]. A major challenge in using ultrasonic NDE methods for chemical degradation such as ASR is how to quantify the degree of damage in the early stages.

In this quarter, ASR damaged samples have been prepared for both volume expansion test and ultrasound measurements. To evaluate degree of early stage damage, the definition of nonlinear acoustic parameter for the method of mixing two longitudinal waves has been derived which can give information of nonlinearity of the specimens with lower frequency component of a longitudinal wave. The amplitude of this new wave is proportional to the acoustic nonlinear parameter which can then be obtained from the frequency spectrum of the newly generated longitudinal wave. Results of linear wave speed measurements for the prepared prisms will be shown.

Sample Preparation

Four plain concrete slabs were constructed and conditioned for the ASR portion of this project. An additional four small-scale matching prisms were cast with each slab specimen. Specimen dimensions were 1219 x 914 x 203 mm (48 x 36 x 8 in.) for the slabs and 102 x 76 x 406 mm (4 x 3 x 16 in.) for the matching prisms. ASR damage was characterized by expansion measurements for all specimens.

Materials

The materials used to create the reactive ASR specimens (ASR1, ASR2, and ASR3) included two reactive coarse aggregates from Wells, Maine (RCA1) and Bernalillo, New Mexico (RCA2), a highly-reactive fine aggregate from El Paso, Texas (RFA), and a Type I portland cement with a relatively high equivalent alkali content (Cement 1). Reactivity of all aggregates in this study was based on performance in the ASTM C1293 concrete prism test. Sodium hydroxide (NaOH) was added to the reactive mixtures to obtain a 1.25% equivalent alkali content, by mass of cement. The ASR control mixture (ASR0) consisted of one non-reactive coarse aggregate (NCA), a non-reactive fine aggregate (NFA), and a low-alkali Type II portland cement (Cement 2). Both the NCA and NFA were acquired from a source in Calera, Alabama. The w/cm was 0.50 for all mixtures. Relevant material properties for mixture proportioning are listed in Table I-

1; more extensive data on the materials can be found in Appendix B. Some of the listed materials were also used in the freeze-thaw specimens. Mixture proportions for the ASR specimens are shown in Table I-2.

Table I-1 Material properties for cements and aggregates for mixture proportioning.

<i>Material</i>	<i>Na₂O_{eq}, %</i>	<i>Absorption Capacity, %</i>	<i>Bulk Specific Gravity (Oven Dry)</i>
<i>Cement 1</i>	<i>1.10</i>	<i>-</i>	<i>3.15</i>
<i>Cement 2</i>	<i>0.53</i>	<i>-</i>	<i>3.15</i>
<i>RCA1</i>	<i>-</i>	<i>0.38</i>	<i>2.77</i>
<i>RCA2</i>	<i>-</i>	<i>0.60</i>	<i>2.64</i>
<i>NCA</i>	<i>-</i>	<i>0.70</i>	<i>2.74</i>
<i>RFA</i>	<i>-</i>	<i>1.10</i>	<i>2.57</i>
<i>NFA</i>	<i>-</i>	<i>1.00</i>	<i>2.70</i>

Table I.2 Mixture proportions for ASR specimens.

<i>Material</i>	<i>Quantity, kg/m³ (lb/yd³)</i>	
	<i>ASR Reactive</i>	<i>ASR Control</i>
<i>Cement 1</i>	<i>420 (708)</i>	<i>-</i>
<i>Cement 2</i>	<i>-</i>	<i>420 (708)</i>
<i>Water</i>	<i>210 (354)</i>	<i>210 (354)</i>
<i>RCA1 (oven dry)</i>	<i>429 (723)</i>	<i>-</i>
<i>RCA2 (oven dry)</i>	<i>429 (723)</i>	<i>-</i>
<i>NCA (oven dry)</i>	<i>-</i>	<i>1095 (1845)</i>
<i>RFA (oven dry)</i>	<i>818 (1379)</i>	<i>-</i>
<i>NFA (oven dry)</i>	<i>-</i>	<i>639 (1077)</i>
<i>NaOH</i>	<i>1.63 (2.74)</i>	<i>-</i>



Figure I-1 Steel mold for ASR matching prisms.

Fabrication

Three batches of concrete (A, B, and C) were required for each slab and its matching prisms. The batches were mixed and placed in rapid succession to avoid the formation of cold joints. Slabs were vibrated in two layers using an internal vibrator, and the sides of the formwork were tapped with a rubber mallet to ensure consolidation, particularly in the corners. Slump, unit weight, and air content were determined for each batch in accordance with ASTM C14, ASTM C29, and ASTM C231, respectively. Mixing temperatures were also recorded, and compressive strength tests were performed on 100 x 200 mm (4 x 8 in.) cylinders at 7 and 28 days following the guidelines of ASTM C39 for quality control. Values for these properties, including average compressive strength, for each batch are given in Table I-3.

Table I-3 Fresh concrete properties and average compressive strength for each ASR batch.

Batch	Unit Weight, kg/m ³ (lb/ft ³)	Slump, mm (in.)	Air Content, %	Mixing Temperature , °C (°F)	Compressive Strength, MPa (psi)	
					7 Days	28 Days
ASR1						
A	2336 (145.8)	240 (9.5)	1.4	22.0 (72)	30.6 (4440)	40.1 (5820)
B	2336 (145.8)	220 (8.75)	2.1	22.0 (72)	32.3 (4690)	41.9 (6080)
C	2281 (142.4)	230 (9.0)	1.6	22.0 (72)	28.6 (4150)	39.4 (5720)
ASR2						
A	2342 (146.2)	215 (8.5)	2.0	22.5 (73)	31.2 (4520)	40.6 (5890)
B	2339 (146.0)	230 (9.0)	1.7	22.5 (73)	29.2 (4240)	38.6 (5600)
C	2336 (145.8)	215 (8.5)	2.0	22.5 (73)	28.9 (4190)	38.1 (5520)
ASR3						

A	2350 (146.8)	205 (8.0)	1.7	21.5 (71)	32.5 (4720)	40.3 (5840)
B	2348 (146.6)	205 (8.0)	1.9	21.0 (70)	31.4 (4550)	39.9 (5790)
C	2332 (145.6)	215 (8.5)	1.9	22.0 (72)	33.9 (4910)	39.7 (5760)
ASR0						
A	2425 (151.4)	190 (7.5)	1.75	21.5 (71)	37.6 (5450)	40.3 (5840)
B	2409 (150.4)	215 (8.5)	0.8	21.0 (70)	38.2 (5540)	45.1 (6540)
C	2406 (150.2)	180 (7.0)	0.8	21.0 (70)	37.2 (5400)	43.1 (6250)

Specimen	Compressive Strength, MPa (psi)	
	7 Days	28 Days
ASR3		
A		
1	30.1 (4360)	-
2	33.8 (4900)	40.8 (5920)
3	33.8 (4900)	39.7 (5760)
B		
1	31.6 (4580)	40.1 (5820)
2	32.0 (4640)	38.5 (5590)
3	30.5 (4420)	41.1 (5960)
C		
1	33.4 (4850)	37.6 (5450)
2	34.0 (4930)	41.1 (5960)
3	34.1 (4950)	40.5 (5880)
ASR0		
A		
1	37.5 (5440)	30.8 (4470)
2	38.1 (5520)	45.6 (6620)
3	37.2 (5400)	44.3 (6430)
B		
1	38.1 (5530)	45.4 (6590)
2	38.8 (5630)	44.8 (6500)
3	37.6 (5450)	45.0 (6530)
C		
1	37.6 (5460)	44.1 (6400)
2	37.0 (5370)	20.2 (2930)
3	37.1 (5380)	42.1 (6100)

An epoxy resin was used to attach four DEMEC target discs to the top of each slab 500 mm (19.7 in) apart in a square pattern for expansion measurements. Three DEMEC discs were attached to each side of each ASR prism; one disc was centered with the other two discs spaced at 150 mm (5.9 in) from the center disc. A finished slab and its matching prisms are shown in Figs. I-2 and I-3, respectively.



Figure I-2 A finished slab showing anchor bolts protruding from the sides (top) and DEMEC discs attached to the top surface in a square pattern (bottom).



Figure I-3 Finished matching ASR prisms with DEMEC discs attached to each side.

Conditioning

To induce ASR in the reactive slabs, temperature and relative humidity in the environmental chamber were maintained at 27°C (80.6°F) and 65%. This conditioning regime was less severe than standard accelerated laboratory tests; it was selected in order to prevent excessive expansions in the slabs because the aggregate combination had the potential to be extremely reactive. Temperature within the chamber was increased to 32°C (89.6°F) after taking readings on January 15, 2014 (Day 93) but was returned back to 27°C (80.6°F) after taking readings on January 29, 2014 (Day 107) because expansions in the slabs increased rapidly during that time. Slabs were draped with wet burlap and wrapped in plastic once per week after each expansion reading to maintain a supply of sufficient moisture. All matching prisms were kept in a moist curing room at 23°C (73°F) and 100% relative humidity. The non-reactive control slab remained in the concrete laboratory at a constant 23°C (73°F) and was draped in wet burlap once weekly after expansion readings were taken on all ASR slabs.

Expansion Monitoring

Expansion measurements for the slabs and prisms were taken once a week on the same day. Expansions on the top of the slabs were measured with the person taking measurements kneeling on top of the slab in the center of the DEMEC disc square. For reference purposes, each side of the slab was assigned a compass direction (i.e. north, south, east, and west). Measurements of the sides of the slabs were taken as shown in I-4 (top). The prisms were measured with the north end to the left of the person conducting the measurements, as shown in Fig. I-4 (bottom).

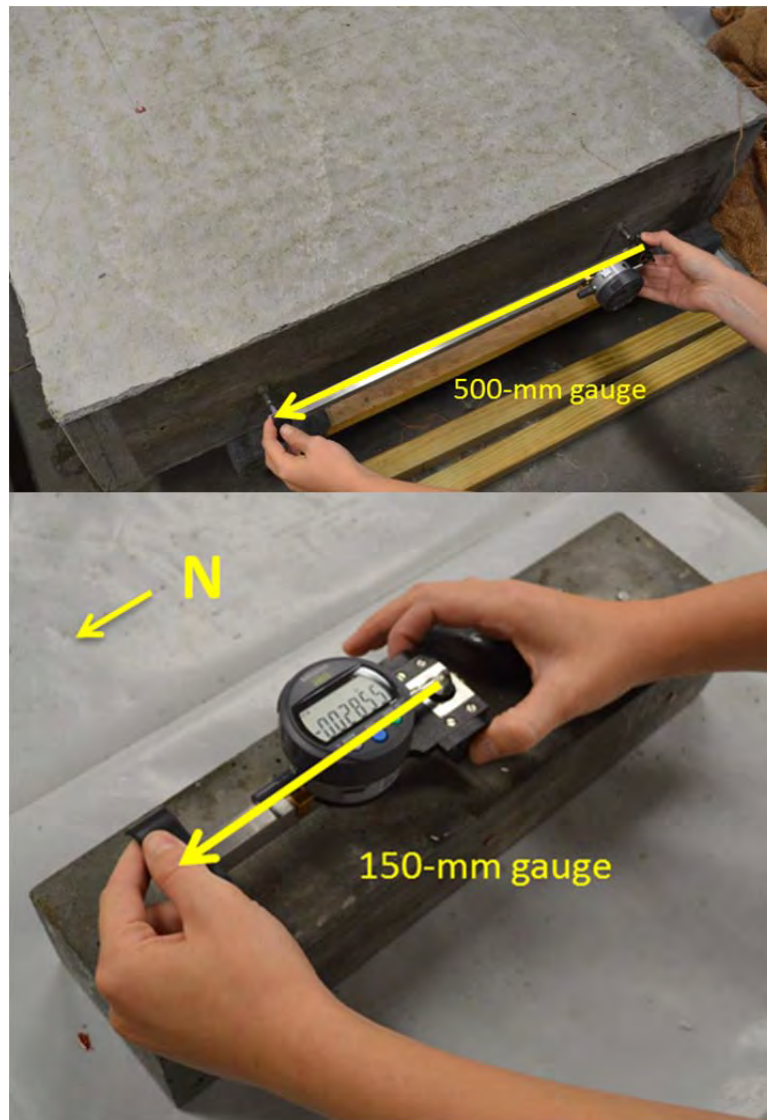


Figure I-4 Measuring orientation of slabs (top) and ASR matching prisms (bottom).

The frequency of the readings increased as damage began reaching the desired levels. Values from each face of each specimen were averaged and reported as the overall percent expansion of that particular specimen. Target average expansions for the reactive slabs were 0.05, 0.10, and 0.20% ($\pm 0.02\%$). Once the desired average expansion value was reached on a slab, the slab and its matching prisms were removed from their conditioning locations. Fig. I-5 illustrates the expansions of the ASR slabs (top) and the matching prisms (bottom) over time.

As expansions increased in the reactive slabs, some map cracking and efflorescence could be seen on the surfaces, as illustrated in Fig. I-6. Reactive prisms also exhibited cracking and efflorescence over time, as shown in Fig. I-7.

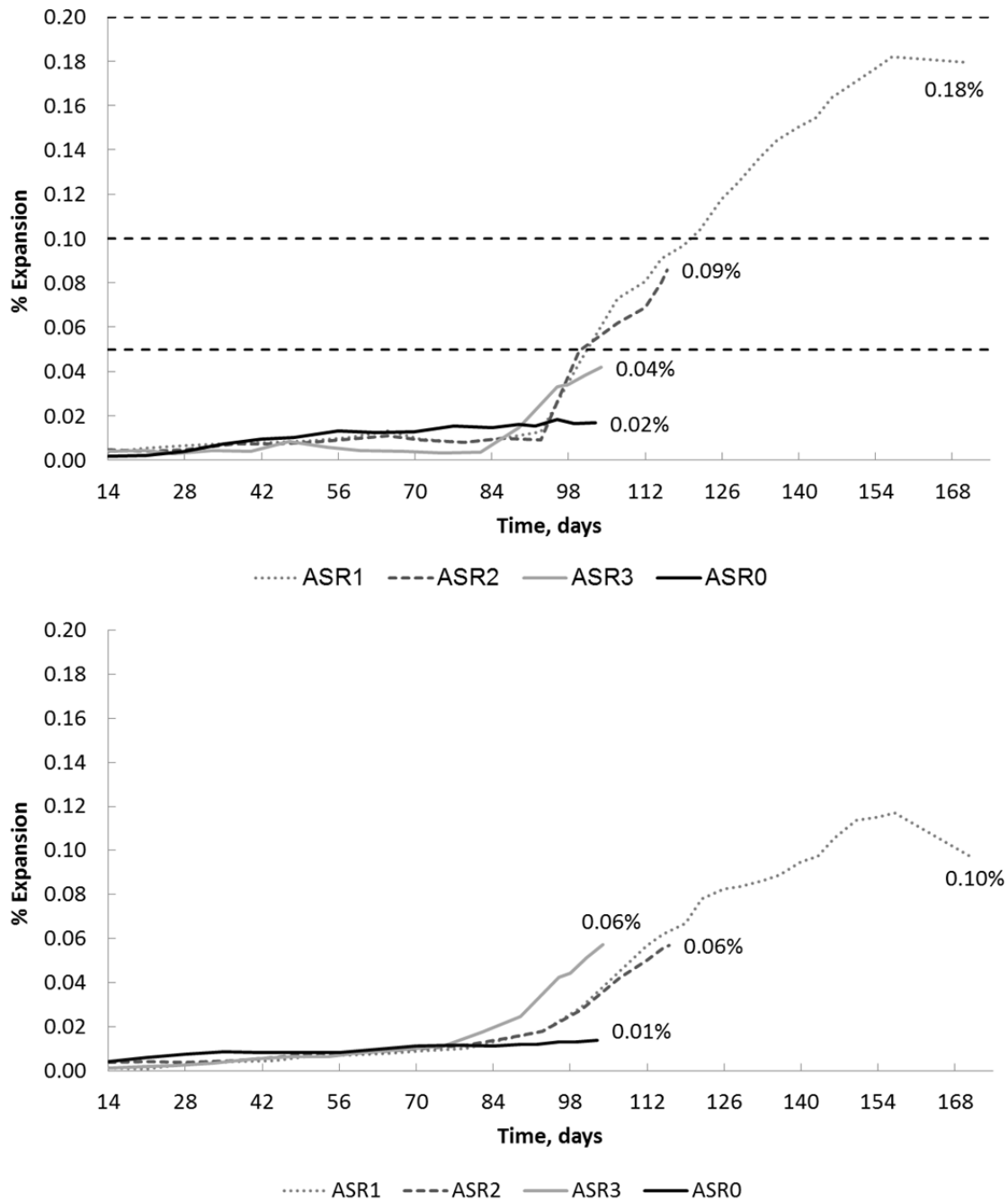


Figure I-5 ASR expansions for slabs (top) and matching prisms (bottom). Horizontal dashed lines indicate target expansions for the reactive slabs.

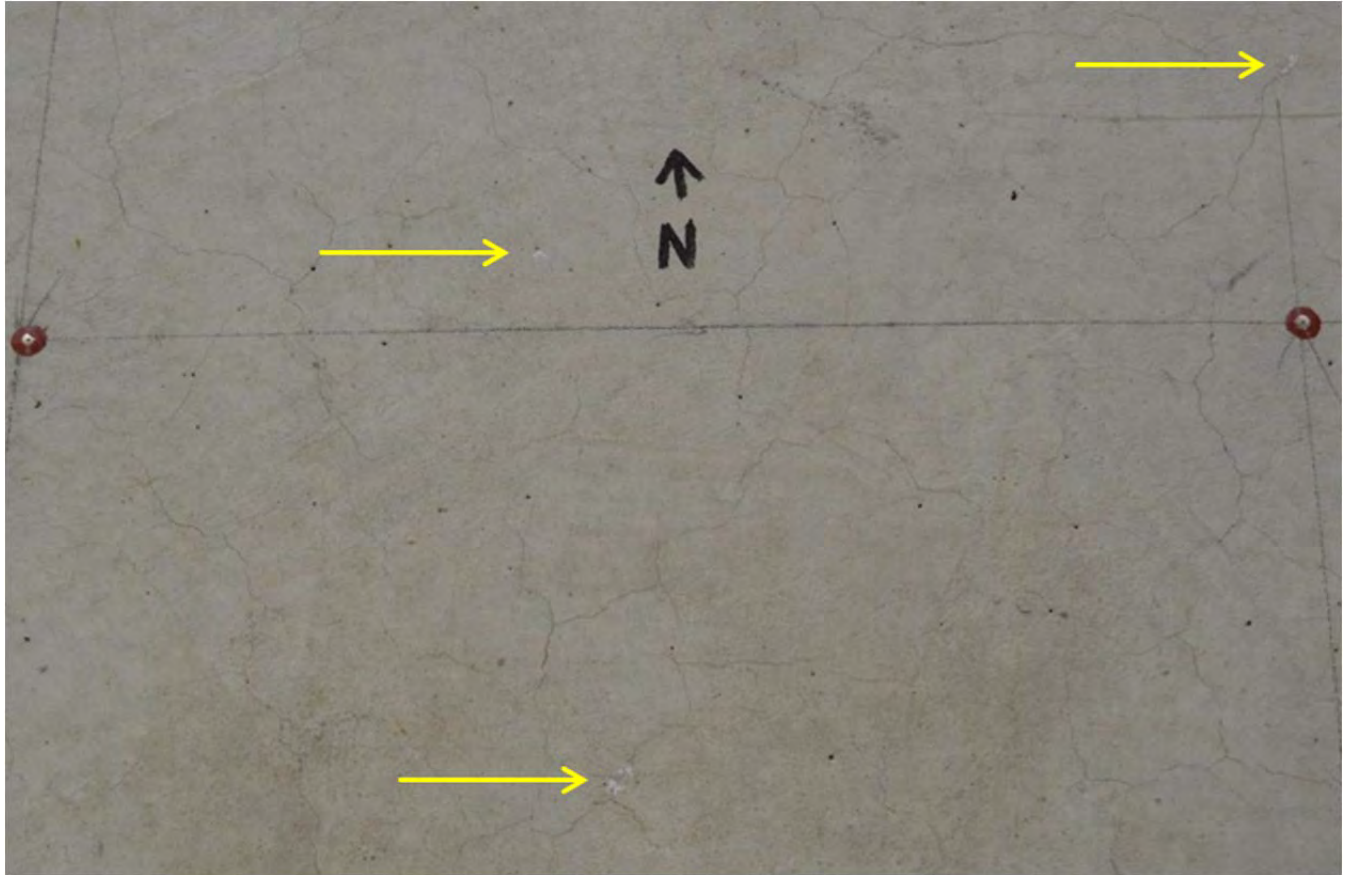


Figure I-6 Map cracking and efflorescence on the top of an ASR slab. Yellow arrows indicate areas of efflorescence.



Figure I-7 Cracking and efflorescence on an ASR prism.

Ultrasound Measurements

Acoustic nonlinearity

Since one needs to related the measured acoustic nonlinearity with the degree of ASR damage, acoustic nonlinear parameter in attenuated media is needed.

From the earlier research [8], the wave equation with frequency dependent attenuation has the form of

$$\frac{\partial^2 u}{\partial t^2} - c^2 \frac{\partial^2 u}{\partial x^2} - K \frac{\partial^3 u}{\partial t \partial x^2} = \beta c^2 \frac{\partial u}{\partial x} \frac{\partial^2 u}{\partial x^2} \quad (1)$$

To use perturbation method, solution of the equation is set as $u = u_1 + u_2$ (2)

Plug (2) into (1) and use the condition (3)

$$\frac{\partial^2 u_1}{\partial t^2} - c^2 \frac{\partial^2 u_1}{\partial x^2} - K \frac{\partial^3 u_1}{\partial t \partial x^2} = 0 \quad (3)$$

We get

$$\frac{\partial^2 u_2}{\partial t^2} - c^2 \frac{\partial^2 u_2}{\partial x^2} - K \frac{\partial^3 u_2}{\partial t \partial x^2} = \beta c^2 \frac{\partial u_1}{\partial x} \frac{\partial^2 u_1}{\partial x^2} \quad (4)$$

To find solution of (4) it is assumed that $u_1 = Ue^{(-\alpha_1 x)} \cos((\omega_1(t - \frac{x}{c}))) + Ve^{(-\alpha_2 x)} \cos((\omega_2(t - \frac{x}{c})))$

and we need to substitute this in (3) and then we find

$$\alpha_1 = \frac{K\omega_1^2}{2c^3}, \alpha_2 = \frac{K\omega_2^2}{2c^3} \quad (5)$$

c is the phase velocity of longitudinal wave, K represents the attenuation coefficient.

The term on the right hand side with frequency difference component becomes

$$\beta c^2 \frac{\partial u_1}{\partial x} \frac{\partial^2 u_1}{\partial x^2} = \frac{1}{2c^3} \beta e^{-(\frac{\omega_1^2 + \omega_2^2}{2c^3})x} UV\omega_1\omega_2 [K(\omega_1^2 - \omega_1\omega_2 + \omega_2^2) \cos(\omega_-(t - \frac{x}{c})) - c^2(\omega_1 - \omega_2) \sin(\omega_-(t - \frac{x}{c}))] \quad (6)$$

To find the coefficient of second order solution, we put

$$u_2 = e^{-(\alpha_1 + \alpha_2)x} [A \cos[\omega_-(t - \frac{x}{c})] + B \sin[\omega_-(t - \frac{x}{c})]] \quad (7)$$

and assume

$$\frac{\partial^2 u_2}{\partial t^2} - c^2 \frac{\partial^2 u_2}{\partial x^2} - K \frac{\partial^3 u_2}{\partial t \partial x^2} = \frac{-2\omega_1\omega_2(\omega_1 - \omega_2)K}{c^2} e^{-(\frac{\omega_1^2 + \omega_2^2}{2c^3})x} [B \cos(\omega_-(t - \frac{x}{c})) - A \sin(\omega_-(t - \frac{x}{c}))] \quad (8)$$

$$A = \frac{\beta c UV}{4K}, B = -\frac{\beta UV(\omega_1^2 - \omega_1\omega_2 + \omega_2^2)}{4c(\omega_1 - \omega_2)} \quad (9)$$

To satisfy the boundary condition, $u_2(0, t) = 0$

$$u_{2-} = (e^{-(\frac{\omega_1^2 + \omega_2^2}{2c^3})x} - e^{-(\frac{(\omega_1 - \omega_2)^2}{2c^3})x}) \frac{\beta c UV}{4K} \cos[\omega_-(t - \frac{x}{c})] \quad (10)$$

$$\lim_{K \rightarrow 0} \|u_2\| = -\frac{UV\beta\omega_1\omega_2}{4c^2} x = -\frac{UV\beta\omega_1\omega_2}{4c^2} x \quad (\text{from undamped system})$$

$$\text{Since } e^{-(\frac{\omega_1^2 + \omega_2^2}{2c^3})x} \ll e^{-(\frac{(\omega_1 - \omega_2)^2}{2c^3})x}$$

$$\|u_{2-}\| = e^{-\frac{(\omega_1 - \omega_2)^2 K}{2c^3} x} \frac{\beta c UV}{4K} \quad (11)$$

$$\text{So, } \beta = \frac{4K \|u_{2-}\|}{cUV} \exp\left[\frac{(\omega_1 - \omega_2)^2 K}{2c^3} x\right] \quad (12)$$

Wave Speed Measurements

To observe linear behavior of ultrasound propagation in the prepared prism samples, through-transmission method has been used to obtain longitudinal wave velocity of each sample as shown in fig. I-8.

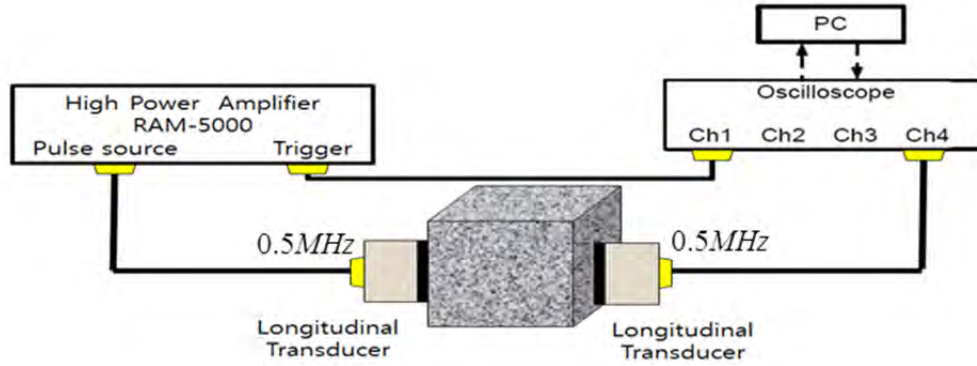


Figure I-8. Experimental setup for wave speed measurement.

The size for the matching prisms is 102 x 76 x 406 mm (4 x 3 x 16 in.).

Here, ASR1,2 and 3 (ASR samples) have huge attenuation due to micro cracks inside, shorter path and smooth surface for the contact of sensors were needed. By taking into account those factors, 4inch path has been selected. By simply recording the arrival time of primary wave at the receiver, one can calculate the ultrasonic velocity change in each ASR specimen. The values have been obtained by averaging 6 measurements.

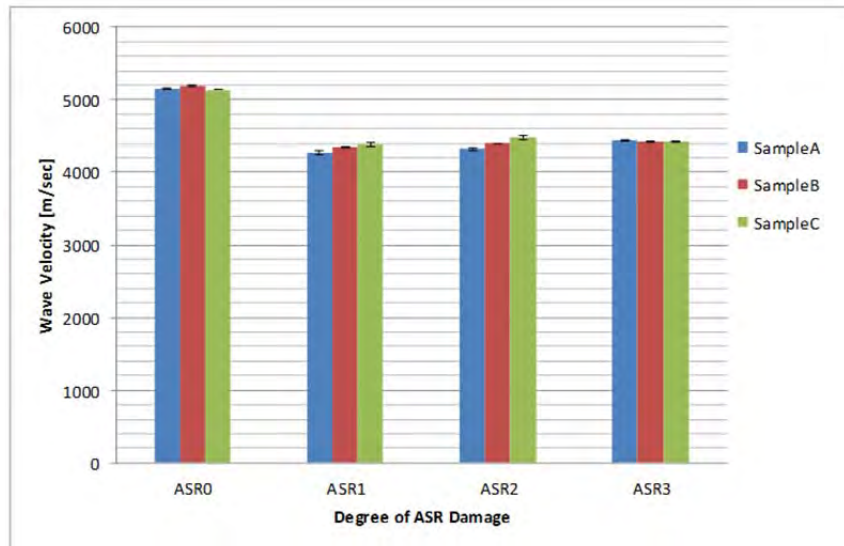


Figure I-9. Results of longitudinal wave velocity

Fig I-9 shows that non ASR specimen, ASR0, has the faster wave speed than the other ASR damaged samples. It is because ASR samples have higher level of crack density due to ASR induced stresses and having more micro cracks results in the change of strength and density of the specimens. However, it is still hard to determine which ASR sample has higher degree of crack density among ASR damaged samples. To this end, nonlinear ultrasound test has been being conducted now and the experimental results will be discussed in the next report.

References

1. Davis, A., F. Ansari, R. Gaynor, K. Lozen, T. Rowe, H. Caratin, F. Heidbrink, V. Malhotra, B. Simons, and N. Carino, *Nondestructive Test Methods for Evaluation of Concrete in Structures*. (American Concrete Institute, ACI, 1998), **228**.
2. Popovics, S. and J.S. Popovics, *Effect of stresses on the ultrasonic pulse velocity in concrete*. (Materials and Structures, 1991), **24**(1), pp. 15-23.
3. Ohdaira, E. and N. Masuzawa, *Water content and its effect on ultrasound propagation in concrete — the possibility of NDE*. (Ultrasonics, 2000), **38**(1–8), pp. 546-552.
4. Sturup, V., F. Vecchio, and H. Caratin, *Pulse velocity as a measure of concrete compressive strength*. (ACI Special Publication, 1984), **82**.
5. Liu, M., G. Tang, L.J. Jacobs, and J. Qu, *A nonlinear wave mixing method for detecting Alkali-Silica reactivity of aggregates*. (AIP Conference Proceedings, 2012), **1430**(1), pp. 1524-1531.
6. Antonaci, P., C.L.E. Bruno, A.S. Gliozzi, and M. Scalerandi, *Monitoring evolution of compressive damage in concrete with linear and nonlinear ultrasonic methods*. (Cement and Concrete Research, 2010), **40**(7), pp. 1106-1113.
7. Moradi-Marani, F., S.A. Kodjo, P. Rivard, and C.-P. Lamarche, *Nonlinear Acoustic Technique of Time Shift for Evaluation of Alkali-Silica Reaction Damage in Concrete Structures*. (ACI Materials Journal, 2014), **111**(1-6).
8. Officials, A.A.o.S.H.a.T., *Standard method of test for accelerated detection of potentially deleterious expansion of mortar bars due to alkali-silica reaction in Standard specifications for transportation materials and methods of sampling and testing Part 2B: Tests*. 2006, AASHTO: : Washington D.C.
9. Holm, S. and R. Sinkus (2010). "A unifying fractional wave equation for compressional and shear waves." The Journal of the Acoustical Society of America **127**(1): 542-548.

III.3.6 The constitutive model for continuum analysis of ASR induced damage

Introduction

Numerous concrete structures, such as dams and bridges, are suffering from deterioration due to alkali-silica reaction (ASR). ASR is a chemical reaction between alkalis in Portland cement paste and certain amorphous silica in a variety of natural aggregate. The ASR produces a soft viscous substance called the ASR gel. ASR gel can expand in time by imbibing water from cement paste and exerts pressures on the surrounding matrix, causing extensive cracking in concrete. Thus, the strength and stiffness of concrete can be reduced substantially.

Once ASR gel migrates from the reacted aggregate and reaches the cement paste, it takes up calcium and loses alkali thus its composition approaches the one of C-S-H gel and thus loses its potential for expansion. (Katayama, 2008). Therefore, produced ASR gel can be divided to two part. First, part of gel that reaches cement paste and it will not cause expansion. Second, part of gel that accumulate in aggregate or interfacial transition zone (ITZ) and it can be expansive. Preceding argument can be illustrated as following,

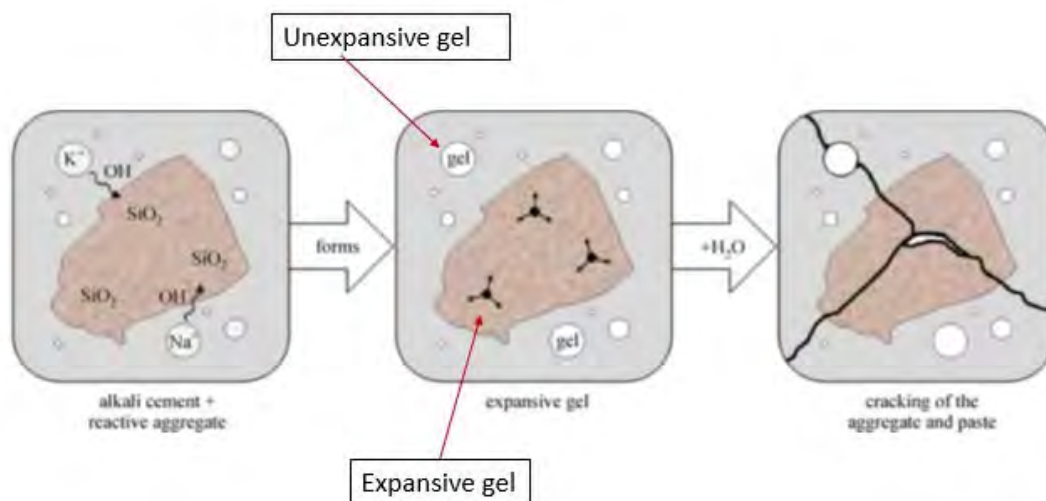


Figure II- 1.ASR reaction process

Following picture from experiment supports stated argument. As it can be seen in this figure, gel accumulate in some regions, and from that regions it starts to enforce pressure on concrete. Finally, this pressure will go so high that it will crack aggregate and mortar.

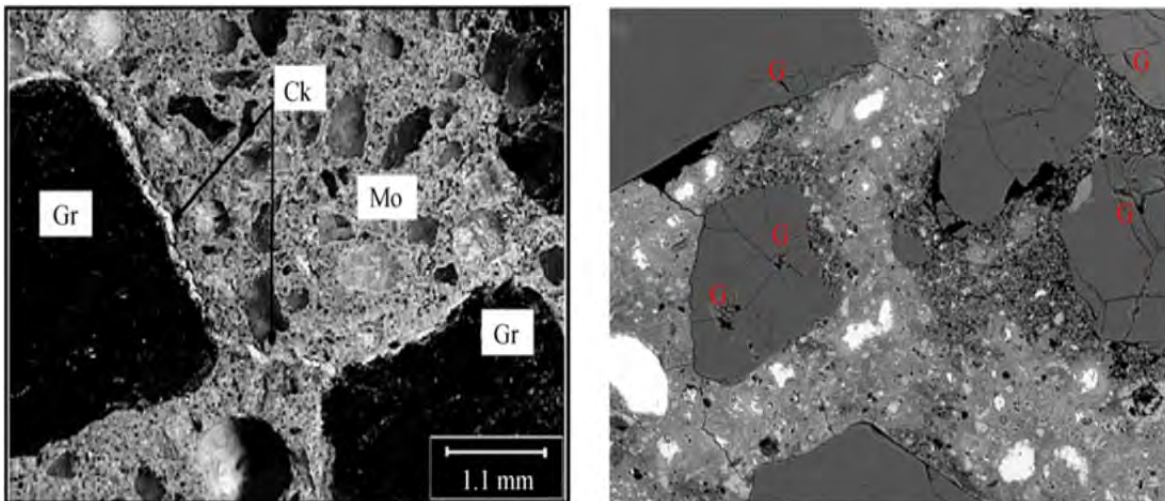


Figure II- 2. ASR induced cracking pattern

Simulation Method

Accumulated ASR gels can be called gel regions. In terms of simulation, first specimen discretized to small parts, and some parts are considered as gel regions and others are considered as normal concrete. Volume of gel regions can be increased either by production of new gel or expansion of old gel by imbibing water. Thus, gel regions undergo expansion and this expansion can cause damage in concrete. Figure II-3 illustrate this method. Yellow regions in this figure are gel regions and orange ones are normal concrete.

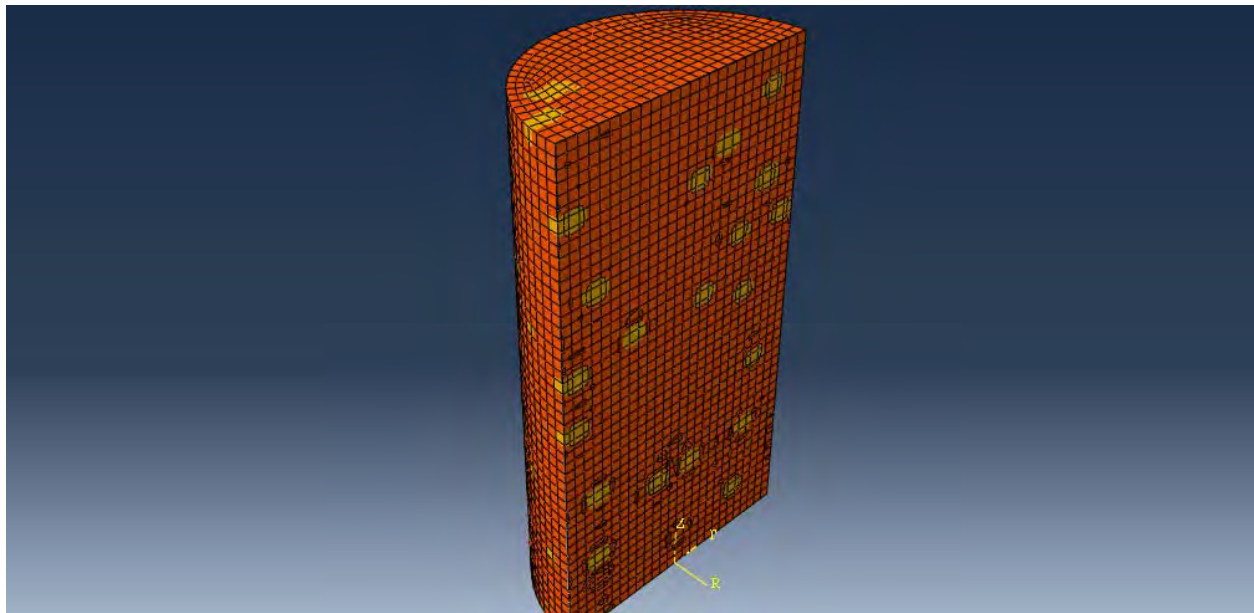


Figure II- 3. Selecting gel regions

Calculating ASR induced pressure and cracking

According to the model proposed by Bazant and Steffens and its modification by Alnaggar and Cusatis, ASR gel production can be simulated in time. This produced gel can migrate from reacted aggregate or remain in or near the aggregate. The part that migrate is not important for swelling. Thus, throughout simulation only part of gel that accumulate near or inside of aggregate will be considered. Expansion of accumulated gel in gel regions cause damage in concrete. ASR gel can also extrude to damage regions and it will reduce pressure in gel regions. Therefore, total volume increment of gel and induced pressure because of this increment can be calculated as,

$$dV_{eff} = dV_{gel} - dV_{in} \quad (1)$$

$$dp = \frac{dV_{eff}}{\kappa} \quad (2)$$

Where dV_{gel} is total volume of produced gel, and dV_{in} represents extruded gel into damaged regions that is the only unknown of equations. κ is bulk modulus of gel and p is pressure in gel regions. In this study properties of gel considered as same as water ones. In order to Model concrete and its damage Microplane model (M7) is used. Damaged volume can be calculated by exploiting Principal inelastic strains. Inelastic strain increments can be defined as,

$$d\epsilon''_{ij} = d\epsilon_{ij} - \frac{1+\nu}{E} d\sigma_{ij} - \frac{\nu}{E} d\sigma_{kk} \delta_{ij} \quad (3)$$

where ν and E are Poisson ratio and young modulus of concrete, and $d\epsilon''_{ij}$ represent inelastic strain. In calculating these strains unloading in each increment assumed to be linear. Principal inelastic strains then can be calculated using these inelastic strains. Finally, using principal inelastic strains and volume of elements, inelastic volume increment and current empty inelastic volume can be calculated.

$$dV'' = V_{element} (d\epsilon''_1 + d\epsilon''_2 + d\epsilon''_3) \quad (4)$$

$$V''_{new} = V''_{old} + dV'' \quad (5)$$

Where $d\epsilon''_1, d\epsilon''_2, d\epsilon''_3$ are principal inelastic strains, and V'' represent current empty inelastic volume. Word empty is used since some parts of produced inelastic volume have been already filled by gel in previous increments.

Accumulated gel will move to inelastic volume regions and will fill them. Amount of gel that will extrude depend on gel regions pressure and partition of inelastic volume that is empty. Thus, extruded gel into damaged regions can be calculated as,

$$dV_{in} = V'' \exp(-\beta p) \quad (6)$$

Where m represents pressure in gel regions and β is a constant.

Duration of ASR experiments is long and usually specimen is under external pressure. Therefore, creep and shrinkage will be significant source of deformation. In this study for considering creep and shrinkage, B3 model is adopted combined with Microplane model. These models should be considered together because usually external loads are big and creep and damage will occur

simultaneously. Usually this important phenomena has been neglected in other models in literature. Therefore, other models can't fit properly experiments for different external loading.

Results

To verify the ability of the model to predict correctly ASR-induced expansion under different loading and confining conditions, experimental results obtained by (Multon and Toutlemonde) was simulated. Experiments were performed using sealed cylindrical specimens (240 mm length and 130 mm in diameter).

Figure II-4 (a) to (d) shows four different experiments. This figures show comparison for axial stresses. As it can be seen in figures simulation results are in good agreement with simulation results.

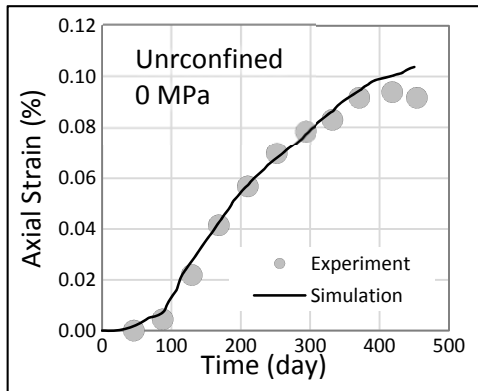


Figure II-4 (a)

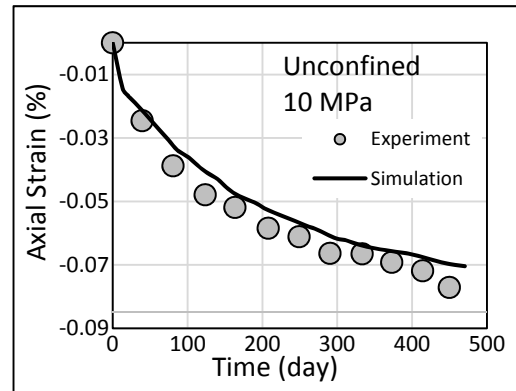


Figure II-4 (b)

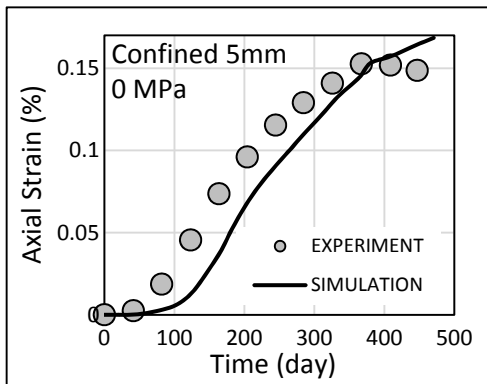


Figure II-4 (c)

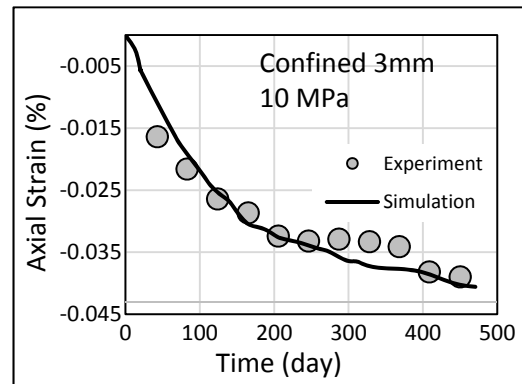


Figure II-4 (d)

Figure II- 4

Figure II-5 shows comparisons for radial strains. As it can be seen results are in good agreement with experiments.

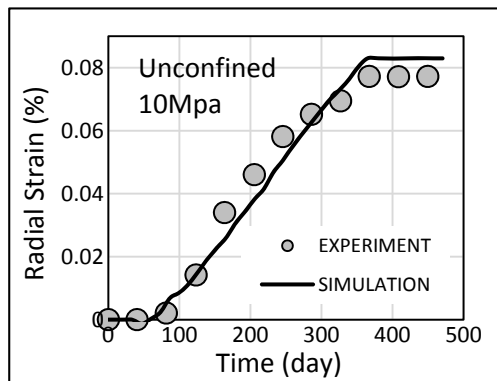


Figure II-5 (a)

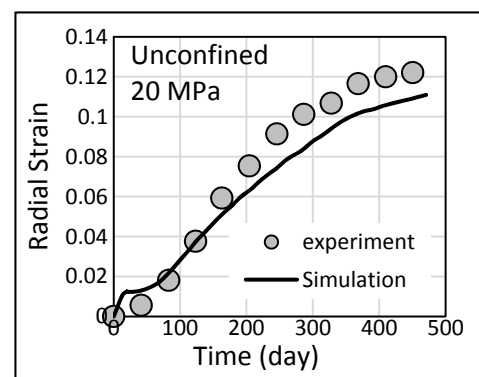


Figure II-5 (b)

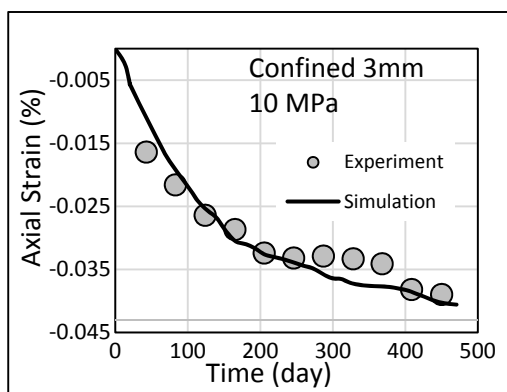


Figure II-5 (c)

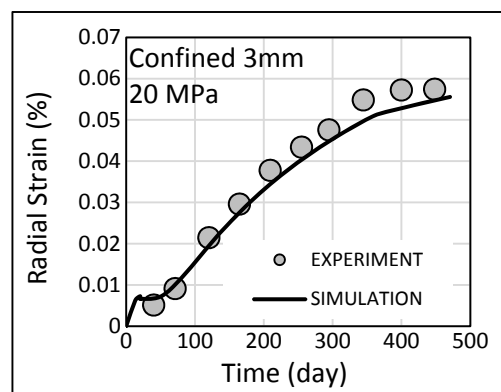


Figure II-5 (d)

Figure II- 5

References

- [1] Bažant, Z.P., and Stefens, A. (2000). "Mathematical model for kinetics of alkali-silica reaction in concrete." *Cement and Concrete Research* 30 (3), 419{428 (disc. reply Vol. 31, 2001, 1111{1113).
- [2] Bažant, Z.P., Zi, G., and Meyer, C. (2000). "Fracture mechanics of ASR in concretes with waste glass particles of different sizes." *J. of Engrg. Mechanics ASCE* 126 (3), 226{232.
- [3] Caner, F.C., and Bažant, Z.P. (2013). "Microplane Model M7 for Plain Concrete: I. Formulation. II. Calibration and Verification" *ASCE J. of Engrg. Mechanics* 139 (12), 1714-1723 and 1724-1735.
- [4] Multon S, Toutlemonde F. Effect of applied stresses on alkali-silica reaction induced expansions. *Cem Concr Res* 2006;36:912-20.
- [5] Bazant Z, Baweja S. Creep and shrinkage prediction model for analysis and design of concrete structures, the Adam Neville symposium, SP-194. Akthem Al-Manaseer; 2000. p. 1-83.
- [6] Multon S, Seignol J-F, Toutlemonde F. Structural behavior of concrete beams affected by alkali-silica reaction. *ACI Mater J* 2005;102(2):67-76.

III.3.7 Linear and Nonlinear Ultrasonic Test in ASR Damaged Concrete Prisms

Introduction

Alkaline-silica reaction (ASR) is one of many undesirable degradation mechanisms in concrete. Although this reaction has not been fully understood yet, it can be briefly explained by several chemical reactions [1, 2]. First, alkali cations and hydroxyl ions (OH^-) from concrete pore solution attack the siloxane chain (Si-O-Si) in reactive aggregates. It releases SiO^- molecules and then this molecules start forming a gel by attracting the alkali cations in the pore solution. This corss-linked gel is called ASR gel. Next, the ASR gel absorbs moisture from the surrounding environment and expands its volume as it imbibes water. Such volumetric expansion of the ASR gel induces large internal pressure, which may then cause microcracking of the concrete[3]. To assess this ASR inducing damage, people in the industry drill a core from an existing concrete structure and conduct microcopy on the drilled core. However, that drilling task can cause additional damage to the structures and it is not practical to inspect an entire structure. For safe operation of concrete structures, nondestructive evaluation (NDE) techniques are needed to monitor and characterize ASR damage.

There have been many researches carried out to characterize ASR damage. One of the most well-known methods is expansion test method such as the accelerated mortar bar test (AMBT), the concrete prism test (CPT) and the accelerated prism test (ACPT). All of these methods rely on volume expansion of a specimen. Therefore, they have their own drawbacks, e.g., 1) the tests are bulk assessment of ASR damage over an entire specimen so that they cannot provide spatial variation of ASR damage, 2) once the sample has expansion in volume, it can be considered that the sample has already been in crack initiation and crack growth damage stage although early stage of damage detection is needed.

To overcome those shortcomings, there have been many methods tried to characterize ASR damage with the aid of linear ultrasonic technique such as pulse velocity measurement and acoustic attenuation test. However, these linear ultrasonic methods are showing inconsistent results each other and not sensitive to microcarck detection at early damage stage in materials[4-7]. On the other hand, it is shown in many papers that nonlinear ultrasonic methods have more sensitivity to detect the early stages damage [8, 9]. One of the most well-known nonlinear ultrasonic techniques is second harmonic test. This test uses the double frequency component generated by the interaction of fundamental incident wave with a damaged material. However, for the media which has huge attenuation like a concrete, it would be less efficient to monitor double frequency component which has higher attenuation level.

Another nonlinear ultrasonic method called nonlinear wave mixing technique mixes two fundamental frequency components within a material and generates difference frequency component of two fundamental ones[10]. [10] shows that nonlinear parameter in a mortar bar changes with respect to the exposure time to alkali solution but it ignored the attenuation in the mortar bar. Therefore, in this study, nonlinear mixing wave technique is used to assess a degree of ASR damage in prepared concrete prisms, taking into account the attenuation. To this end, asymptotic solution of a wave equation in a damped media will be derived later in this paper. Finally, experimentally measured acoustic nonlinear parameter will be plotted to see if the acoustic nonlinearity is related to the degree of ASR damage.

Nonlinear Mixing Wave Theory in Damped Media

Since the material nonlinear parameter β is proportional to amplitude of second order wave, we derive β in nonlinear wave mixing technique. As shown in Figure I-1, two longitudinal primary waves are transmitted into the sample and the interaction of these two incident waves generates new longitudinal waves.

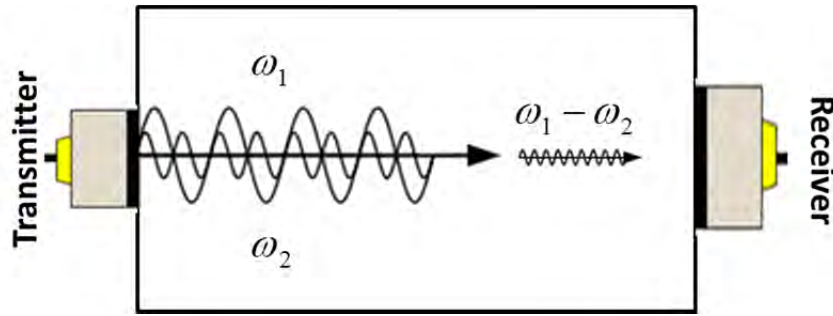


Figure I-33 Two longitudinal wave mixing in a sample

Consider the 1D wave equation governing the pure longitudinal wave propagation in x direction

From the earlier research [11, 12], we set the following wave equation

$$\frac{\partial^2 u}{\partial t^2} - c_L^2 \frac{\partial^2 u}{\partial x^2} - K \frac{\partial^3 u}{\partial t \partial x^2} = \beta c_L^2 \frac{\partial u}{\partial x} \frac{\partial^2 u}{\partial x^2} \quad (7)$$

where c_L , K and β are longitudinal wave velocity, damping coefficient and acoustic nonlinear parameter respectively. A prescribed displacement with two frequency components, ω_1 and ω_2 , at $x=0$ is

$$u_1(0, t) = U \cdot \exp[-\alpha_1 x] \cos(\omega_1 t) + V \cdot \exp[-\alpha_2 x] \cos(\omega_2 t) \quad (8)$$

where U and V are the amplitude of the incident wave before attenuated for each frequency component. By using the perturbation method with assumption of $u = u_1 + u_2$ where u_1 and u_2 are the first order and second order solution respectively, we have two sets of wave equation,

$$\frac{\partial^2 u_1}{\partial t^2} - c_L^2 \frac{\partial^2 u_1}{\partial x^2} - K \frac{\partial^3 u_1}{\partial t \partial x^2} = 0 \quad (9)$$

and

$$\frac{\partial^2 u_2}{\partial t^2} - c_L^2 \frac{\partial^2 u_2}{\partial x^2} - K \frac{\partial^3 u_2}{\partial t \partial x^2} = \beta c_L^2 \frac{\partial u_1}{\partial x} \frac{\partial^2 u_1}{\partial x^2} \quad (10)$$

The solution of e.q. (3) is

$$u_1 = U e^{(-\alpha_1 x)} \cos((\omega_1(t - \frac{x}{c})) + V e^{(-\alpha_2 x)} \cos((\omega_2(t - \frac{x}{c})) \quad (11)$$

where $\alpha_1 = \frac{K \omega_1^2}{2c_L^3}$ and $\alpha_2 = \frac{K \omega_2^2}{2c_L^3}$.

The solution of (4) has several terms of frequency components and in this study, we will focus on the term with frequency difference component, $\omega_1 - \omega_2$.

To satisfy the boundary condition, $u_2(0, t) = 0$, the solution with $\omega_1 - \omega_2$ is

$$u_{2-} = (e^{-\frac{(\omega_1^2 + \omega_2^2)K}{2c_L^3}x} - e^{-\frac{(\omega_1 - \omega_2)^2 K}{2c_L^3}x}) \frac{\beta c_L UV}{4K} \cos[\omega_-(t - \frac{x}{c_L})] \quad (12)$$

where u_{2-} is the amplitude of displacement at $\omega_1 - \omega_2$ and ω_- represents $\omega_1 - \omega_2$. If K goes to zero, u_{2-} becomes the same as the one from undamped system.

$$\lim_{K \rightarrow 0} \|u_{2-}\| = -\frac{UV \beta \omega_1 \omega_2}{4c_L^2} x \quad (13)$$

Since $e^{-\frac{(\omega_1^2 + \omega_2^2)K}{2c_L^3}x} \ll e^{-\frac{(\omega_1 - \omega_2)^2 K}{2c_L^3}x}$, e.q (5) can be simplified to

$$\|u_{2-}\| = e^{-\frac{(\omega_1 - \omega_2)^2 K}{2c_L^3}x} \frac{\beta c_L UV}{4K} \quad (14)$$

Finally, acoustic nonlinear parameter is defined as

$$\beta = \frac{4K \|u_{2-}\|}{c_L UV} \exp[\frac{(\omega_1 - \omega_2)^2 K}{2c_L^3}x] = \frac{4K \|u_{2-}\|}{c_L \|U^*\| \|V^*\|} \exp[(-\alpha_1 - \alpha_2 + \frac{(\omega_1 - \omega_2)^2 K}{2c_L^3})x] \quad (15)$$

where $\|U^*\|$ and $\|V^*\|$ are the attenuated amplitude of displacement for each fundamental frequency obtained in frequency domain.

Experimental Method

Sample Preparation

12 concrete prisms with four types of the different levels of ASR damage were constructed and conditioned. Specimen dimensions were 102 x 76 x 406 mm (4 x 3 x 16 in.) for the samples. The materials used to create the reactive ASR specimen group (ASR1, ASR2, and ASR3) included two reactive coarse aggregates from Wells, Maine (RCA1) and Bernalillo, New Mexico (RCA2), a highly-reactive fine aggregate from El Paso, Texas (RFA), and a Type I portland cement with a relatively high equivalent alkali content (Cement 1). Reactivity of all aggregates in this study was based on performance in the ASTM C1293 concrete prism test [13]. Sodium hydroxide (NaOH) was added to the reactive mixtures to obtain a 1.25% equivalent alkali content, by mass of cement. The ASR control mixture (ASR0) consisted of one non-reactive coarse aggregate (NCA), a non-reactive fine aggregate (NFA), and a low-alkali Type II portland cement (Cement 2). Both the NCA and NFA were acquired from a source in Calera, Alabama. The w/cm was 0.50 for all mixtures. Relevant material properties for mixture proportioning are listed in Table 1. Some of the listed materials were also used in the freeze-thaw specimens. Mixture proportions for the ASR specimens are shown in Table 2. Finally, each of four groups had three samples and we had 12 samples in total. Figure I-2 shows the mold used to produce the prisms and Figure I-3 shows the produced samples.

Table 1: Material properties for cements and aggregates for mixture proportioning.

Material	Na ₂ O _{eq} , %	Absorption Capacity, %	Bulk Specific Gravity (Oven Dry)
Cement 1	1.10	-	3.15
Cement 2	0.53	-	3.15
RCA1	-	0.38	2.77
RCA2	-	0.60	2.64
NCA	-	0.70	2.74
RFA	-	1.10	2.57
NFA	-	1.00	2.70

Table 2: Mixture proportions for ASR specimens.

Material	Quantity, kg/m3 (lb/yd3)	
	ASR Reactive	ASR Control
Cement 1	420 (708)	-
Cement 2	-	420 (708)
Water	210 (354)	210 (354)
RCA1 (oven dry)	429 (723)	-
RCA2 (oven dry)	429 (723)	-
NCA (oven dry)	-	1095 (1845)
RFA (oven dry)	818 (1379)	-
NFA (oven dry)	-	639 (1077)
NaOH	1.63 (2.74)	-



Figure I-34 Steel mold for ASR matching prisms



Figure I-35 ASR reactive concrete prisms

To induce ASR in the reactive samples, all prisms were kept in a moist curing room at 23°C (73°F) and 100% relative humidity. The non-reactive control samples were remained in the concrete laboratory at a constant 23°C (73°F). The samples in the group of ASR1, ASR2 and ASR3 have been conditioned for 170days, 117days and 104days respectively in order that the degree of ASR damage is changed in the order of ASR1>ASR2>ASR3>ASR0.

Ultrasonic Measurements

To see the relation between each ultrasonic measurement results and the degree of ASR damage, longitudinal wave velocity, acoustic attenuation and the amplitude at the frequency difference were measured. Those parameters were used to calculate acoustic nonlinear parameter later on. The measurements were conducted twice at 6 different points on each sample so that we can obtain averaged value over 36 data for each ASR damage level, ASR0, ASR1, ASR2 and ASR3. Figure I-4 shows the position for 6 different measurements on the sample.

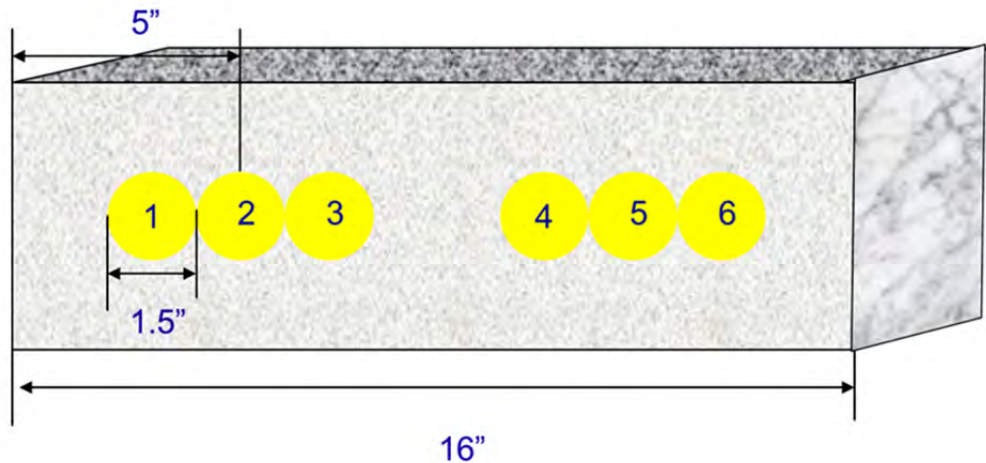


Figure I-36 Six different location of the measurement in concrete prisms

Pulse Velocity Measurement

Ultrasonic tests were conducted to measure the ultrasonic pulse velocity (UPV), attenuation and acoustic nonlinear parameter in the concrete prism samples with different levels of ASR damages. All data were obtained by carrying out through transmission tests as schematically illustrated in Figure I-5. A high-vacuum grease were used as a couplant to attach the transducers to the samples. For repeatability, measurements on each point at each sample were repeated two times by completely detaching and re-attaching the transducers so that each sample has 12 data over 6 different locations.

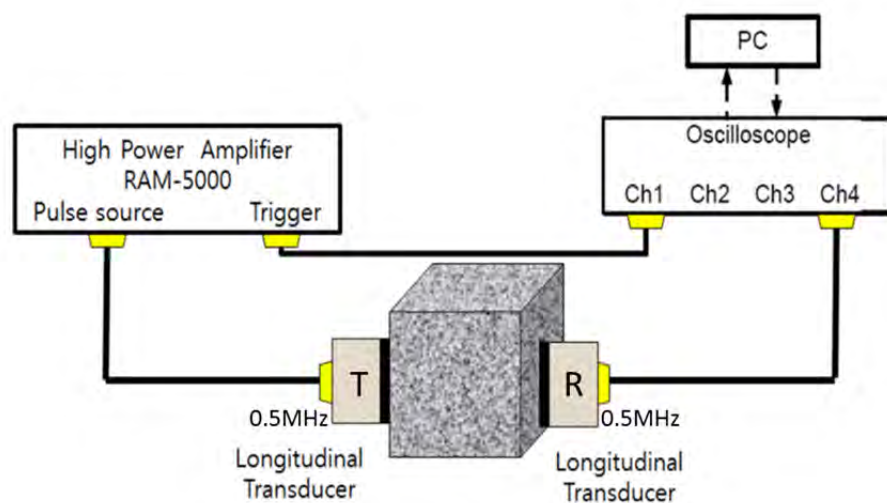


Figure I-37 Experiment setup for wave velocity measurement

For the UPV, 9 cycles of incident wave at 0.5MHz propagate by a longitudinal wave PZT transducer with the central frequency of 0.5MHz which was put on the one side of the sample. On the other side of the sample, another longitudinal wave PZT transducer whose central frequency was 0.5MHz is used as a receiver. A time domain were recorded by a Tektronix TDS 5034B oscilloscope to see traveling time in 4".

Attenuation Measurement

To obtain the attenuation coefficient, the amplitude changes were monitored. In case of less damped media, attenuation coefficients were measured by pulse-echo method[14]. However, the pulse-echo method is not useful for the sample used in this study due to huge attenuation where the incident waves seem to be totally decayed before returning back to a receiver. In this study, therefore, through-transmission approach was used instead of pulse and echo method. Although some researches simply compared the amplitudes received with and without the sample between a transmitter and a receiver[15, 16], it is still necessary to consider additional attenuation factor due to contact losses[17]. So the attenuation coefficient was measured as follows. First, a transmitter and a receiver whose central frequency are 0.5MHz and 0.1MHz respectively were attached face to face as shown in Figure I-6 (a) and signals in a time domain were recorded by a Tektronix TDS 5034B oscilloscope. The recorded signals were then converted to a frequency domain by FFT. Here, amplitudes of 0.35MHz and 0.25MHz were denoted by A_0 and B_0 respectively. Next, the concrete sample was placed between the transmitter and the receiver at this time and amplitudes corresponding to 0.35MHz and 0.25MHz were recorded in the same way as the previous measurements. The obtained amplitudes were named A_1 and B_1 . Figure I-7 shows the example of FFT result for four different amplitudes.



195

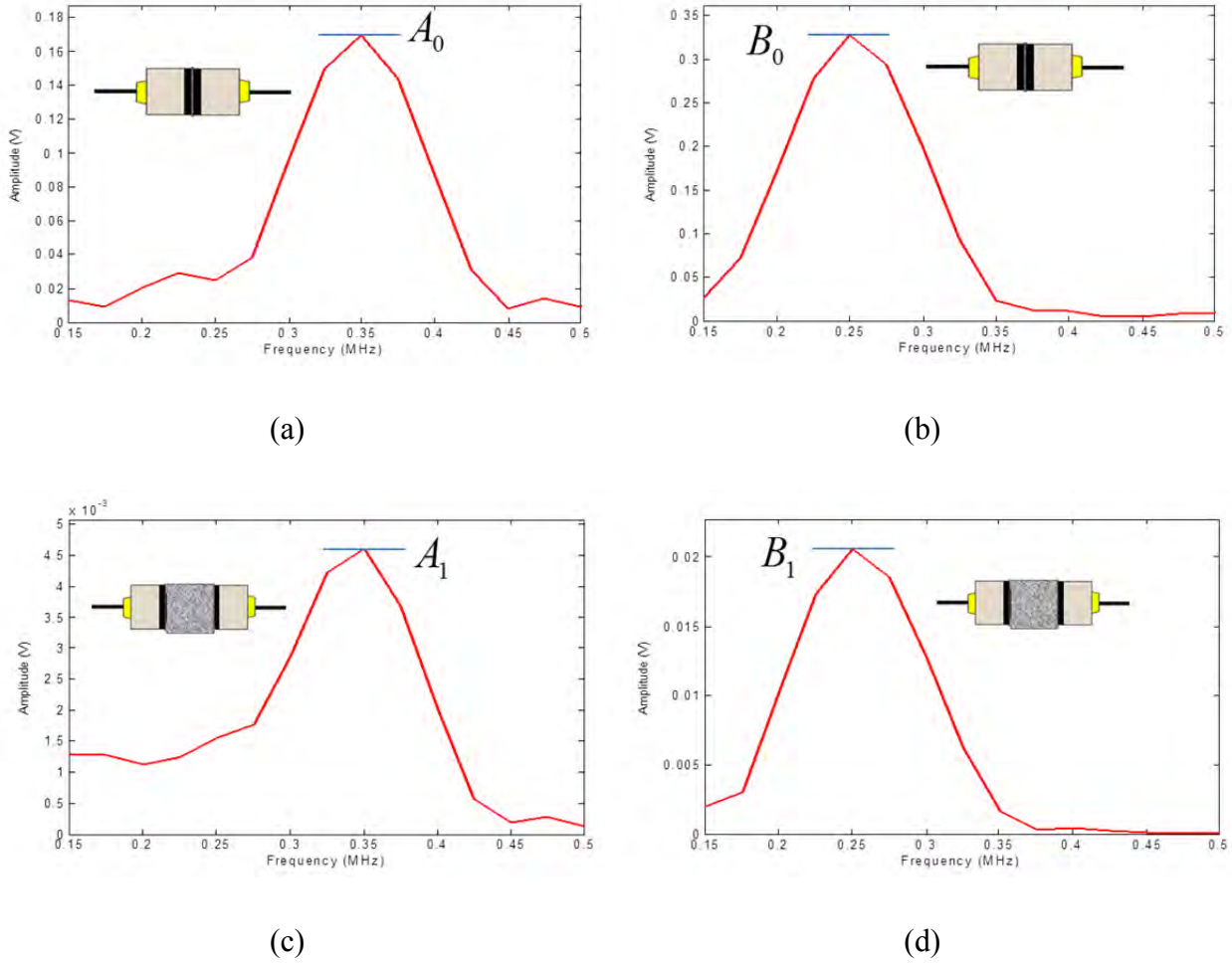


Figure I-39 Amplitude Analysis at (a) 0.35MHz and (b) 0.25MHz without the sample and at (c) 0.35MHz and (d) 0.25MHz with the sample

[17] recalls there is additional energy loss of incident waves when transmitter contacts with the sample due to impedance difference and set the following relations,

$$A_1 = A_0 \cdot K_c \cdot \exp[-\alpha_1 x], \quad B_1 = B_0 \cdot K_c \cdot \exp[-\alpha_2 x] \quad (16)$$

where the amplitudes of incident waves are decreased due to the factor K_c which is additional attenuation factor due to contact losses. From e.q (5), we know

$$\frac{2\alpha_1 c_L^3}{\omega_1^2} = \frac{2\alpha_2 c_L^3}{\omega_2^2} \quad (17)$$

Thus, we can calculate α_1 and α_2 from e.q (10) and (11).

Acoustic Nonlinear Parameter Measurement

A schematic of the nonlinear wave mixing measurement setup is shown in Figure I-8.

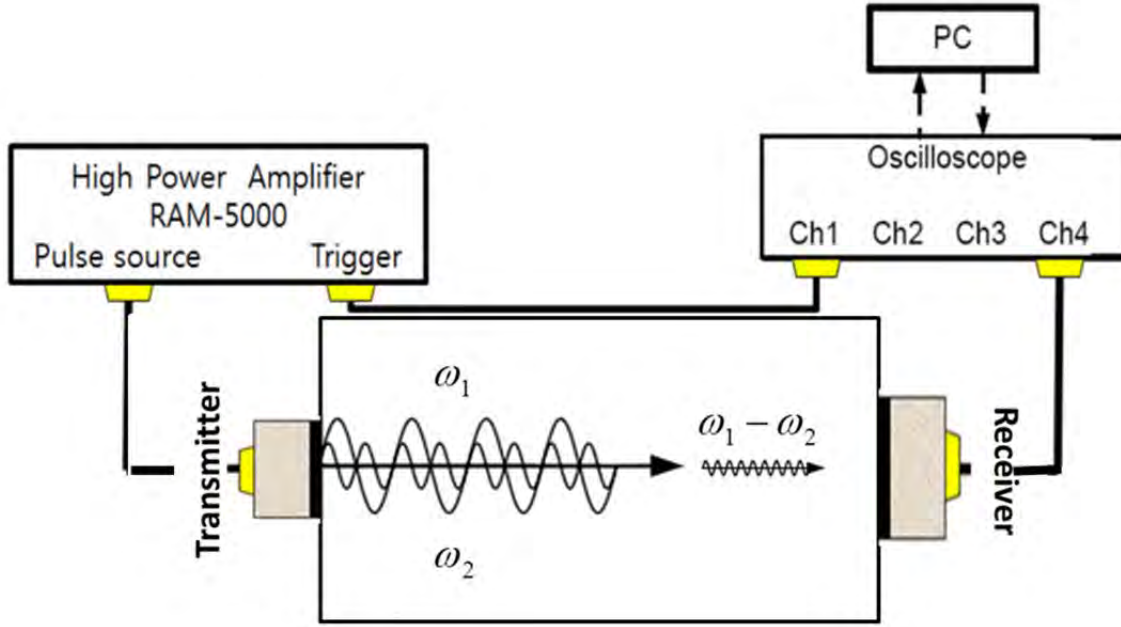


Figure I-40 Experiment setup for nonlinear wave mixing technique

The two frequency components in the incident wave were generated by a 1.0 in diameter broadband transmitter with a central frequency of 0.5MHz. The mixed waves were received by a 1.5 in diameter broadband receiver with a central frequency of 0.1MHz. To match the pulse duration as $18 \mu\text{sec}$, 6.3 cycles of 0.35MHz and 4.5 cycles of 0.25MHz were generated by RAM-5000 function generator. Since the transmitter and the receiver have already been attached to each side of the sample for the attenuation test, nonlinear parameter measurement was conducted while the sensors kept attached to the sample. In this way, nonlinear parameter can be calculated based on the attenuation measured having the same contact condition. The frequency spectrum of incidents waves in the frequency domain is shown in Figure I-9 (a) measured by putting the transmitter and the receiver face to face, which tells us the two frequency components were properly generated. Since mixing two primary longitudinal waves generates new longitudinal wave at difference frequency of two primary frequencies, received signal through the sample provides information of second order wave's amplitude. So, $\|U^*\|$, $\|V^*\|$ and $\|u_{2-}\|$ in e.q. (9) were experimentally measured.

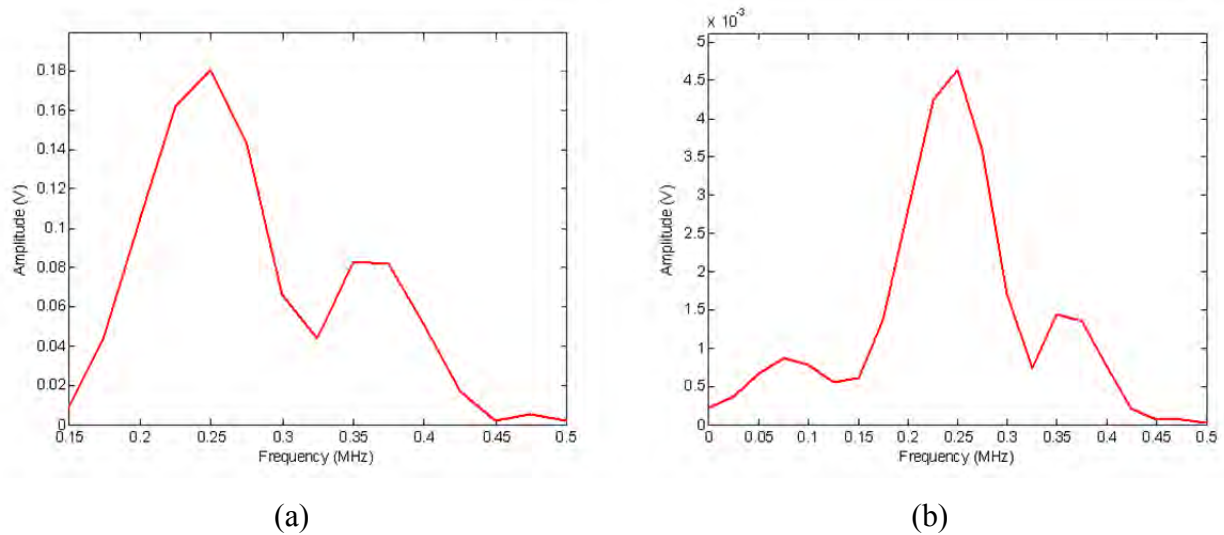


Figure I-41 Frequency spectrum of (a) two incident waves and (b) received signal through the sample

Ultrasonic Measurement Results

With the aid of linear and nonlinear ultrasonic experiments, variation of the ultrasonic velocity, attenuation and nonlinear parameter β were monitored with the samples at different ASR damage. For all ultrasonic tests, each sample was measured twice at the same position and it has six different locations. Since each ASR damage group has 3 samples, total 36 data in each group (ASR0, ASR1, ASR2 and ASR3) were experimentally obtained and averaged. Next, the averaged values of each group were normalized by the averaged value of ASR0.

Figure I-10 shows normalized ultrasonic pulse velocity graph by plotting averaged values. The error bar indicates the standard error of 36 measurements. It is seen that control specimen (ASR0), has the faster wave speed than the other ASR damaged samples (ASR1, ASR2, ASR3) and the maximum difference is about 17%. It is because ASR damaged samples have higher level of crack density due to ASR inducing stresses and having more micro cracks results in the change of strength and density of the specimens. However, there is no clear trend for the velocity change in ASR reactive samples and is still hard to determine which sample has higher degree of crack density among ASR damaged samples.

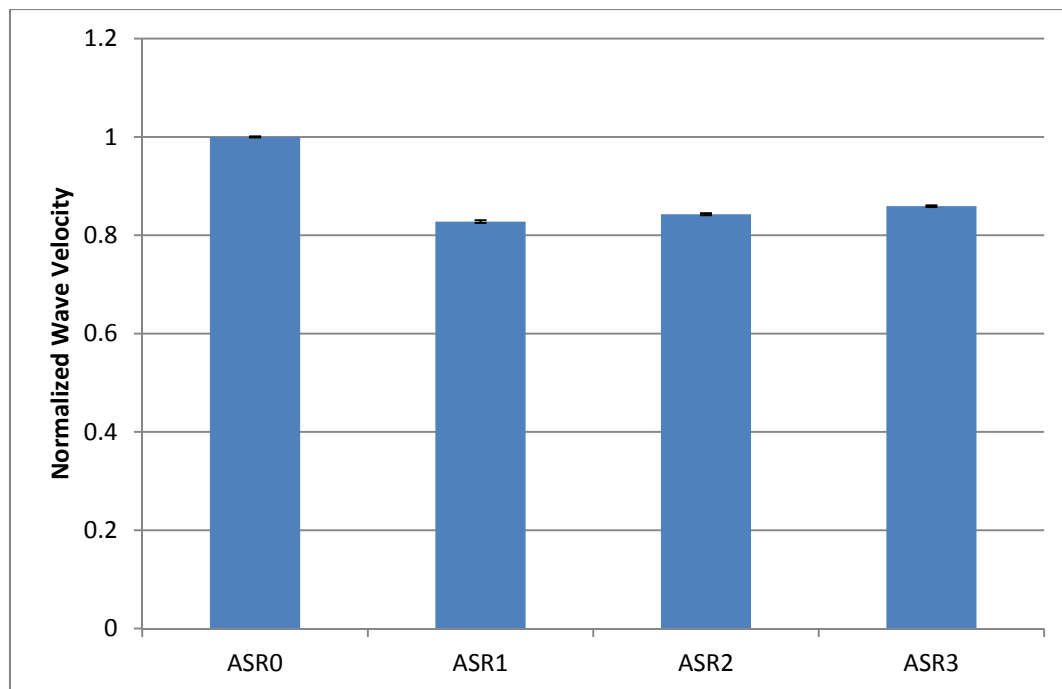


Figure I-42 Normalized wave velocity

Figure I-11 shows the normalized attenuation. It is found that the attenuation of ASR damaged samples were bigger than the control samples but it is hard to see the difference of each ASR damaged sample like wave velocity measurement. Through two types of linear ultrasonic measurement, linear method has sensitivity to macrocracks but is not efficient to assess microcrack density.

Finally, normalized nonlinear parameter β is plotted in Figure I-12. As shown in this graph, we can see distinguishable change for β even from each ASR damaged sample. We note that β was calculated based on contributions from the amplitude of mixed wave at 0.1MHz, wave velocity and attenuation.

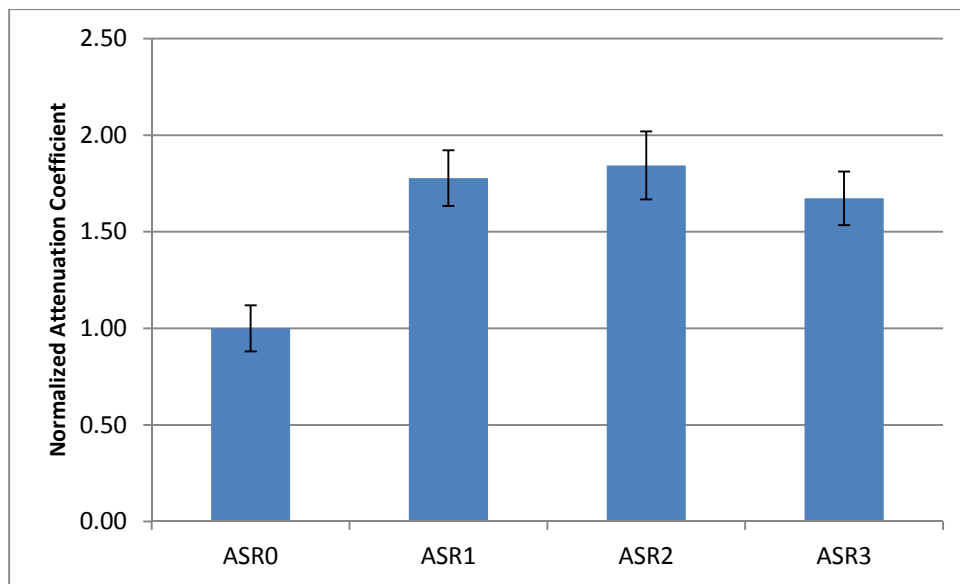
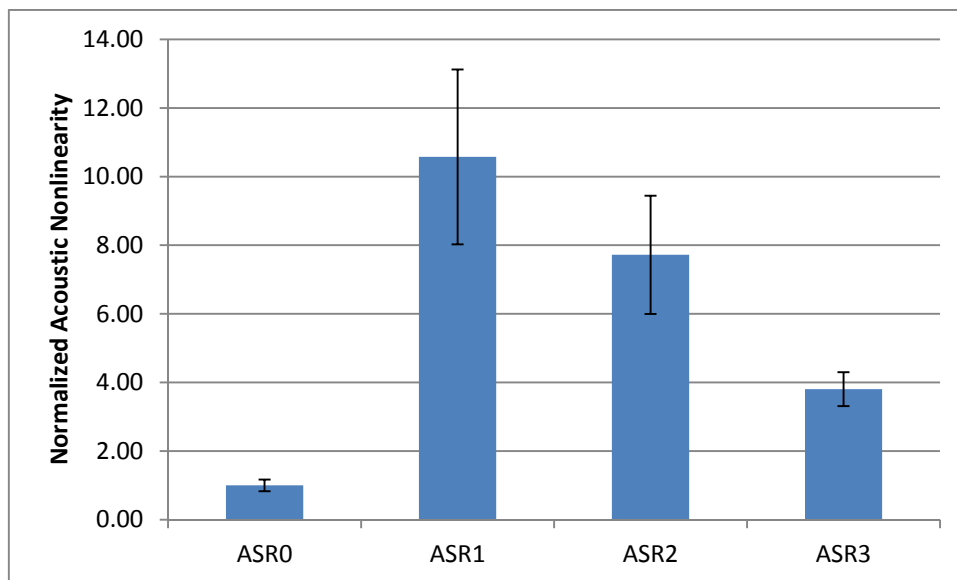


Figure I-43 Normalized Attenuation Coefficient

Here, it is clearly shown that nonlinear parameter of each ASR damage group was different from the others, i.e., control samples has the least β and ASR1 which was designed to have the most damages shows the biggest β . Therefore, we found that (1) nonlinear ultrasonic mixing technique yields consistent and repeatable results, (2) β increases with higher level of ASR damage, and (3) β has better sensitivity to ASR damage than wave velocity and attenuation change.

Figure I-44 Normalized β

Destructive Method

Microscopy

To conduct both microscopy and compressive strength test, four 1.5" X 1.5" X 3" samples were taken from each prism by using a low speed saw (IsoMet) and ethanol as a lubricant. Therefore, each ASR group had 12 samples. The samples were then polished on a grinder/polisher down to 240 grit size with water. Digital images were taken on each sample using a stereomicroscope at magnifications of 6.5X. Micrographs are shown in Figure I-13. It is found that first, ASR control sample (ASR0) does not have gel or cracks as a product of ASR as shown in Figure I-13-(a) while ASR damaged samples have gel that looks like a white rim around an aggregate shown in (b) and (c) and even cracks in (d) and second, all cracks found by microscopy exist only in the aggregate.

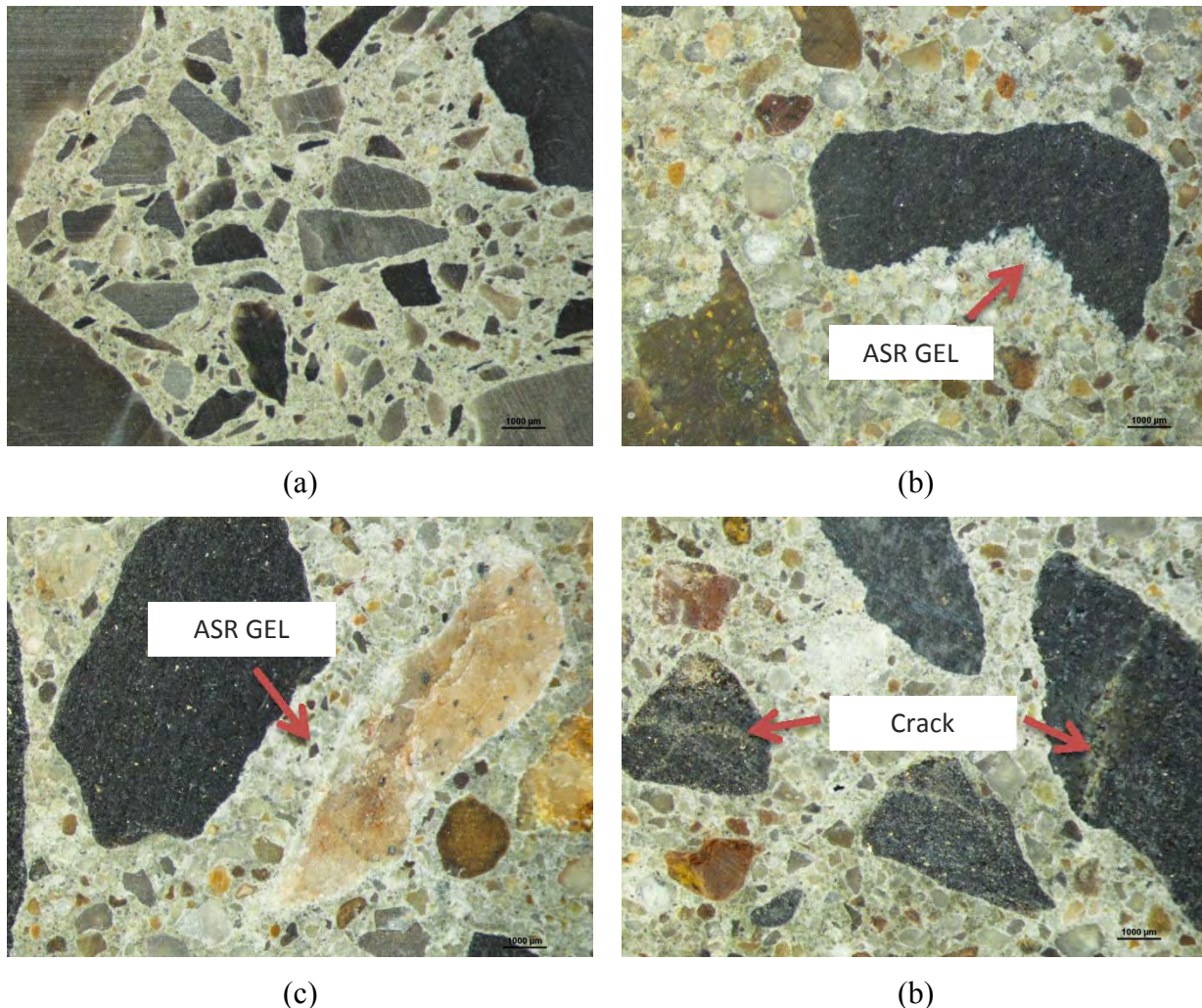


Figure I-45 Microscopy of (a) ASR Control sample and (b), (c) and (d) ASR damaged sample

Through this work, one can see a process of crack evolution. Firstly, ASR gel is produced at an interface between cement past and aggregate. Second, once this gel is formed much enough, it starts to penetrate the interface and grows into the aggregate. Lastly, these cracks are propagated through cement paste after breaking aggregate completely.

Visualization of ASR product

The micrographs showed that ASR damaged samples have silica gel and micro cracks. However, in many photos, it is still difficult to determine which one is gel and how much gel is produced. To this study, an image analysis algorithm was coded in MATLAB language based on an assumption that ASR gel has a certain color, e.g. white as shown in Figure I-14-(a) and the number of pixels in white color can be counted by the code. First, a color image (Figure I-14-(a)) from microscope is converted to a gray image (b) based on brightness of each pixel. Second, a histogram of the gray image with respect to the brightness is plotted in range from 0 (black) to 255 (white). Here, one can determine what each bar in the histogram represents as shown in Figure I-14-(c) and which threshold value in the brightness scale is chosen to filter the image. In the case of Figure I-14-(c), 200 was chosen as the threshold value and any pixels whose brightness is less than the threshold value are filtered to become a black pixel. Figure I-14-(d) shows all pixels but pixels in ASR gel become black. Finally, a position of the ASR gel is drawn as red rim as Figure I-14-(e). It is seen that the image analysis algorithm successfully found ASR gel. As the next step, this algorithm was applied to the photos taken by the microscope as shown in Figure I-15. Since the majority of pixels are from cement paste, bars beyond 8000 pixels in Fig. 15-(c) were considered as cement paste. Therefore, a value of 198 was chosen as the threshold value through an analysis of the image histogram in Figure I-15-(c). Figure I-15-(e) shows the algorithm can work for a micrograph as well. To quantify the amount of ASR gel in each micrograph, the fraction of the number of white pixels in Figure I-15-(d) over the number of total pixels was calculated.

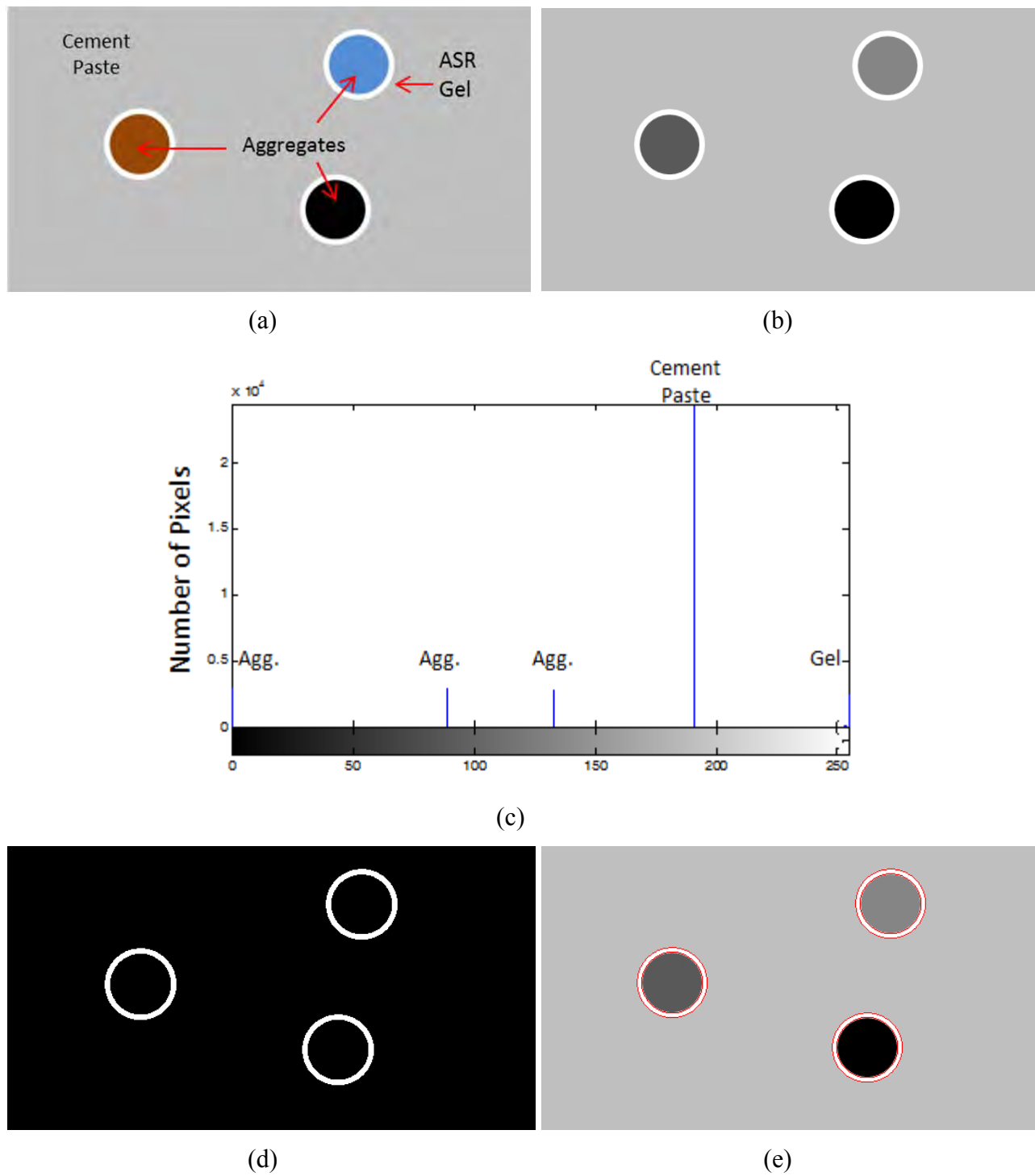
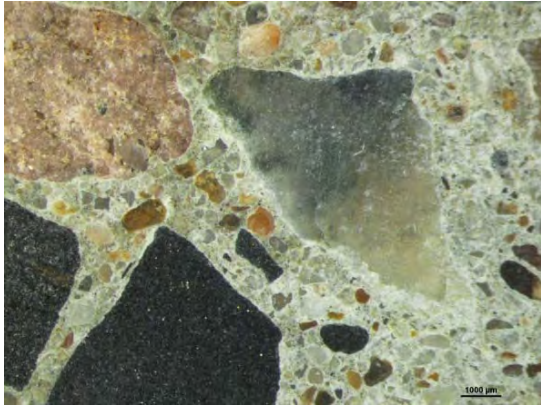
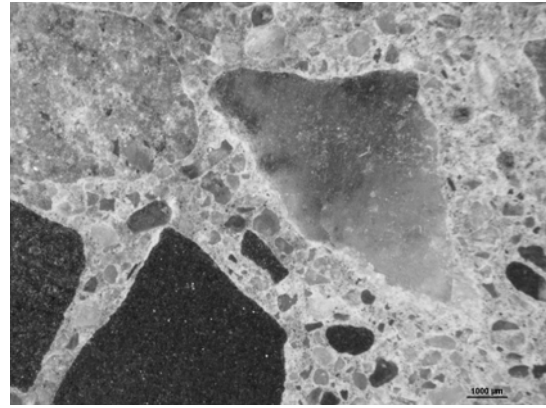


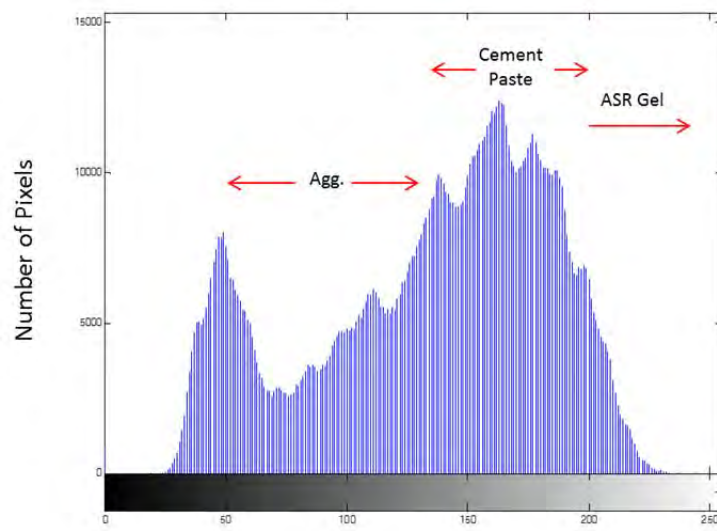
Figure I-46 A concept of Image analysis



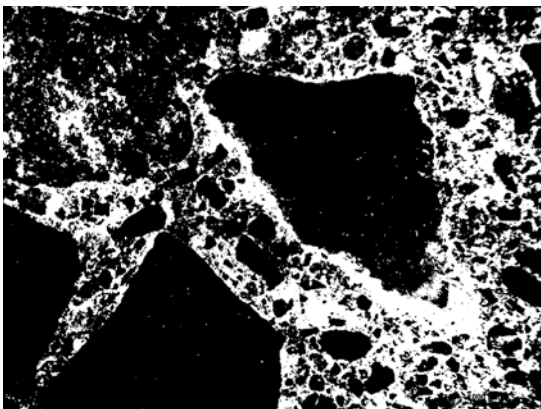
(a)



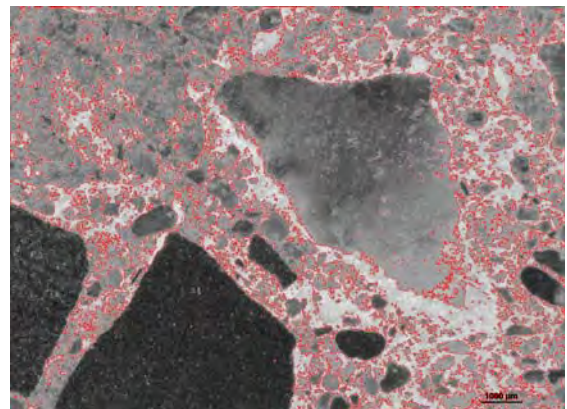
(b)



(c)



(d)



(e)

Figure I-47 Observation of ASR Gel through image analysis

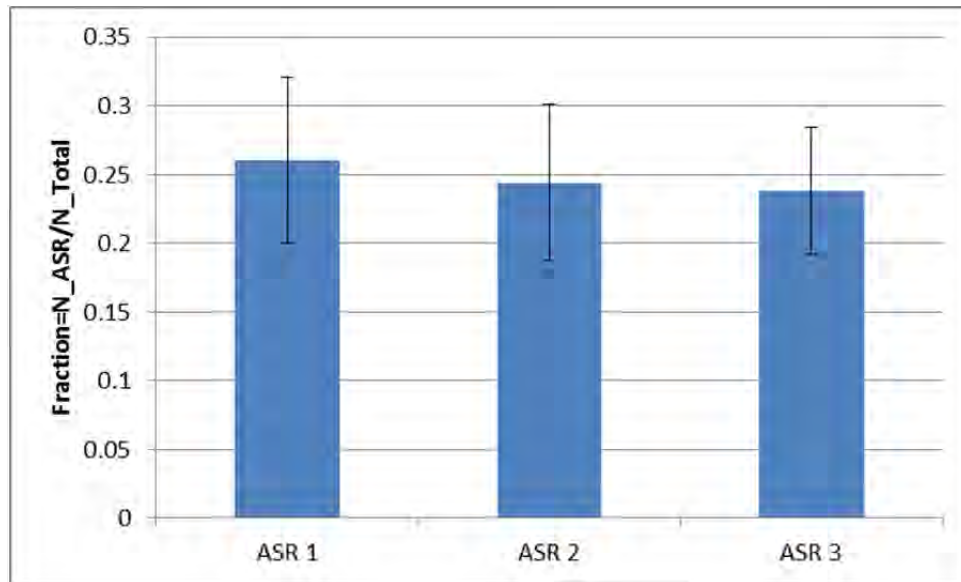


Figure I-48 Quantification of ASR gel from microscopy and image analysis

12 fraction values in each ASR group through an image analysis are averaged. It shows that the sample in most damage group, ASR 1, has the largest fraction values and the algorithm found the least ASR-guessed pixels in the least ASR damage group, ASR 3.

Compressive Strength Measurement

After taking a microscopy for 36 samples, compressive strengths of all samples used for the microscopy were measured by using MTS Axial/Torsion Material Test System as shown in Figure I-17. The machine applied compressive load on the top of samples with rate of 0.006mm/sec.



Figure I-49 Compressive Strength Measurement



Figure I-50 Sample failure after compression

The maximum force applied to the sample until failure was recorded. The broken sample is shown in Fig. 18. Averaged compressive strength over 12 samples per each ASR group is plotted in Figure I-19. From this chart, one can find 1) the compressive strengths of all ASR damaged samples are decreased compared to that of fresh concrete and 2) the most damaged sample group, ASR 1, has the most degradation from the reference strength. Therefore, we can conclude the order of ASR damage is $ASR\ 1 > ASR\ 2 > ASR\ 3$ through Figure I-16 and Figure I-18.

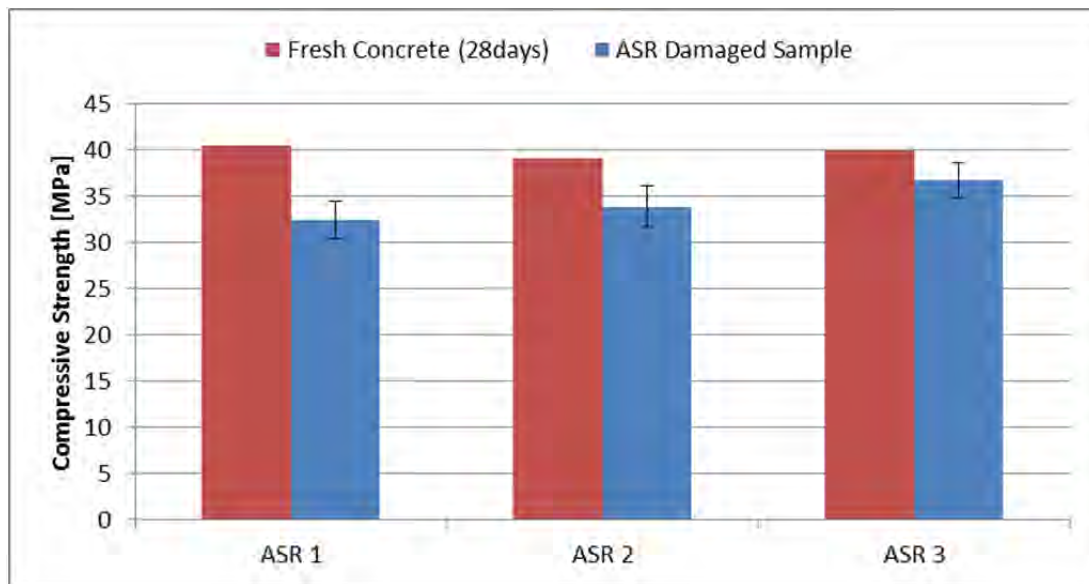


Figure I-51 Results of Compressive Strength Measurement

Conclusion

First, linear and nonlinear ultrasonic measurements have been carried out to see the variations of wave velocity, acoustic attenuation and acoustic nonlinear parameter with respect to the different ASR damage level. For the wave velocity measurement, it is seen that non-damaged sample has higher speed than ASR damaged samples because ASR damaged samples have higher level of crack density due to ASR inducing stresses and having more micro cracks and it results in the change of strength and density of the specimens. However, this measurement results were not able to show distinguished difference among three different levels of ASR damaged samples. Results of acoustic attenuation measurement show that ASR damaged samples have larger attenuation than control samples but it is still hard to determine the level of ASR damage among three groups of ASR damaged samples. Finally, with the aid of nonlinear mixing wave method, it is found that nonlinear ultrasonic measurement results have higher sensitivity to the density of ASR damages while the other linear measurements were not able to show the difference among damaged samples, i.e., the more damaged samples have the larger acoustic nonlinearity.

Second, microscopy has been carried out and the image analysis was implemented to quantify amount of ASR gel. Through this study, one can see the feasibility of image processing method to quantify this and it showed meaningful data by providing the order of ASR pixels as ASR 1 > ASR 2 > ASR 3.

Lastly, compressive strengths of 1.5" X 1.5" X 3" samples from the prepared prisms were measured. This measurement shows that ASR damage degraded concrete samples and the order of ASR damage is also well matched with previous two results.

From all studies done in this quarter, it is seen that measuring acoustic nonlinearity can be a good tool to assess the ASR damage level of concretes.

References

1. Saouma, V. and L. Perotti, *Constitutive model for alkali-aggregate reactions*. (ACI materials journal, 2006), **103**(3).
2. Glasser, L.D. and N. Kataoka, *Chemistry of "alkali-aggregate" reaction*.
3. Smaoui, N., B. Bissonnette, M. Bérubé, and B. Fournier, *Stresses induced by alkali-silica reactivity in prototypes of reinforced concrete columns incorporating various types of reactive aggregates*. (Canadian Journal of Civil Engineering, 2007), **34**(12), pp. 1554-1566.
4. Rivard, P. and F. Saint-Pierre, *Assessing alkali-silica reaction damage to concrete with non-destructive methods: From the lab to the field*. (Construction and Building Materials, 2009), **23**(2), pp. 902-909.
5. Saint-Pierre, F., P. Rivard, and G. Ballivy, *Measurement of alkali-silica reaction progression by ultrasonic waves attenuation*. (Cement and Concrete Research, 2007), **37**(6), pp. 948-956.
6. Nogueira, C.L. and K.J. Willam, *Ultrasonic testing of damage in concrete under uniaxial compression*. (ACI Materials Journal, 2001), **98**(3).
7. Warnemuende, K. and H.-C. Wu, *Actively modulated acoustic nondestructive evaluation of concrete*. (Cement and Concrete Research, 2004), **34**(4), pp. 563-570.
8. Nagy, P.B., *Fatigue damage assessment by nonlinear ultrasonic materials characterization*. (Ultrasonics, 1998), **36**(1), pp. 375-381.
9. Cantrell, J.H., *Substructural organization, dislocation plasticity and harmonic generation in cyclically stressed wavy slip metals*. (Proceedings of the Royal Society of London. Series A: Mathematical, Physical and Engineering Sciences, 2004), **460**(2043), pp. 757-780.
10. Liu, M., G. Tang, L.J. Jacobs, and J. Qu, *A nonlinear wave mixing method for detecting Alkali-Silica reactivity of aggregates*. (AIP Conference Proceedings, 2012), **1430**(1), pp. 1524-1531.
11. Holm, S. and R. Sinkus, *A unifying fractional wave equation for compressional and shear waves*. (The Journal of the Acoustical Society of America, 2010), **127**(1), pp. 542-548.
12. Holm, S. and S.P. Näsholm, *A causal and fractional all-frequency wave equation for lossy media*. (The Journal of the Acoustical Society of America, 2011), **130**(4), pp. 2195-2202.
13. International, A., *Standard Test Method for Determination of Length Change of Concrete Due to Alkali-Silica Reaction*. 2008, ASTM International: West Conshohocken, PA.
14. International, A., *Standard Test Method for Measurement of Ultrasonic Attenuation Coefficients of Advanced Ceramics by Pulse-Echo Contact Technique*. 2013, ASTM International: West Conshohocken, PA.
15. Philippidis, T. and D. Aggelis, *Experimental study of wave dispersion and attenuation in concrete*. (Ultrasonics, 2005), **43**(7), pp. 584-595.

16. Mažeika, L., R. Šliteris, and A. Vladišauskas, *Measurement of velocity and attenuation for ultrasonic longitudinal waves in the polyethylene samples*. (Ultrasound, 2010), **65**(4).
17. Tharmaratnam, K. and B. Tan, *Attenuation of ultrasonic pulse in cement mortar*. (Cement and Concrete Research, 1990), **20**(3), pp. 335-345.

III.3.8 The constitutive model for continuum analysis of ASR induced damage

Introduction

In this study, till now simulations was based on condition that there is no drying from surface. Thus, the effect of environment conditions was neglected. This is usual assumption for modeling ASR reaction in literature, but in reality and for practical purposes, environmental condition is very important. The most important environmental condition that should be considered is, environmental humidity. Humidity can have very important effect in progress of ASR reaction. Water has different roles in ASR reaction. Some of the reasons are,

1. The pore water acts as the necessary transport medium for the mass transport of hydroxyl and alkali ions required by the reaction.
2. The expansion of the gel is essentially governed by the imbibition of water.
3. For the reaction to continue, water must be supplied by macro-diffusion through the pores of concrete.

As it can be seen, effect of water is so important that it can change rate of reaction significantly and even in low humidity it would stop the reaction. In order to consider this effect, different parts of model should be modified. First, produced mass of gel should be modified in order to can consider effect of humidity. Second, water diffusion should be considered. This diffusion can be outward if the humidity of the environment be less than humidity of the specimen, and it would be inward if the humidity condition be opposite. Also, in order to consider correct humidity profile, effect of self-desiccation should be considered. Self-desiccation should be considered since hydration process would use water and this water usage would decrease humidity.

Change of humidity in addition to changing rate of ASR reaction, would cause shrinkage. It would cause both drying and autogenous shrinkage. In order to consider these shrinkages B4 would be used. These refinements would be discussed in detail in different section of this report.

Effect of humidity on gel mass production

Producing ASR gel is highly related to presence of water. In order to consider this effect equations should be modified in the way that they can consider this important effect. This modification can be considered easily as following,

$$\dot{M}_{gel}(h) = \dot{M}_{gel} \cdot f(h)$$

where \dot{M}_{gel} is gel increment in full humidity, and function $f(h)$ is a function for correcting gel increment. This function will start from unity in full humidity and will decrease rapidly with decrease of

humidity and in humidity near 75% it would be almost zero. Fig. 1 illustrate some of necessary properties of this function.

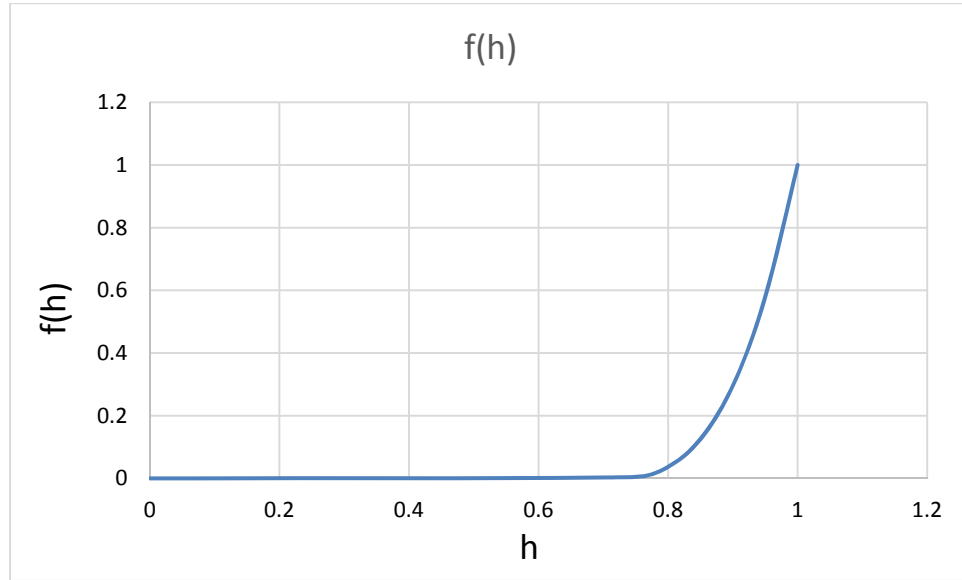


Figure II-1 Effect of relative humidity on produced gel

Different functions can satisfy these conditions. Thus, an empirical equation that can satisfy these conditions would be considered and calibrated based on experimental results. A sample function for considering this effect can have the following form

$$f(h) = \begin{cases} \frac{(h - .7)^n}{(1 - .7)^n} & , \quad h > .7 \\ 0 & , \quad h < .7 \end{cases}$$

Where n is a parameter that should be found from calibrating experimental results.

Diffusion

Usually concrete structures are exposed to the environment that its humidity is less than 100%. Thus, water would diffuse from specimen. This drying and water loss is very important and should be considered in order to found humidity profile respect to time and hydration degree (as it can be seen in last section humidity can have great effect on ASR evolution). Other important concept in order to find humidity profile is finding humidity loss because of the self-desiccation. Self-desiccation can be very important, because lots of experiment has shown that only because of this phenome humidity can decrease to about 75%. Therefore, humidity change because of hydration itself can be very important. Fig. 2 shows this effect. As it can be seen in this figure in long time by continuing hydration process humidity would decrease to low values that this decrease would decelerate ASR reaction significantly.

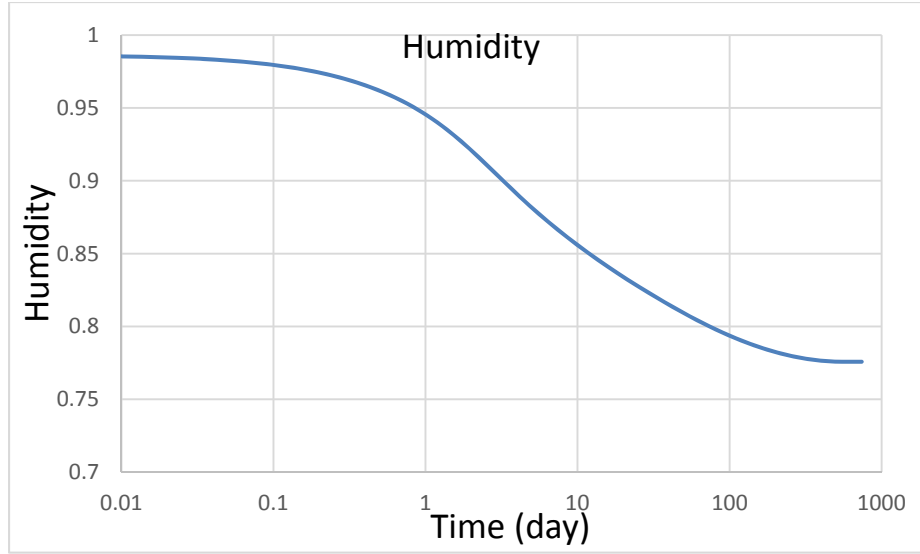


Figure II-2 Effect of self-desiccation on humidity

In order to consider transport of water through concrete, it is very important to consider right diffusivity. Concrete is very complex material in terms of diffusion. This complexity comes from the fact that, by decreasing humidity first big pores of the concrete will deplete and after that smaller pores will start to deplete. Thus, by decreasing humidity and depleting big pores, continuous humidity path between big pores will loose and because of that diffusion will decrease drastically.

In order to find equation for water transport one should start with mass balance of water. The mass of moisture per unit volume corresponds to the total water content, w_t . Mass conservation requires that the net water gain be equal to the time derivative of the total water content. If the total flux of moisture is denoted as j_w , the resulting equation reads

$$\dot{w}_t = -\nabla \cdot j_w$$

After defining water change because of flux, flux itself should be found. Bazant and Najjar (1971) proposed and Bazant and Najjar (1972) elaborated a model for moisture transport in concrete, with the pore relative humidity h as the primary unknown. Their model, which has been embodied in the fib Model Code (Federation internationale de beton 2013), directly postulates that, under constant temperature, the total moisture flux is driven by the gradient of pore relative humidity. Mathematically, such a transport law is written as

$$j_w = -c_p \nabla h$$

where c_p is the moisture permeability [kg/m·s], to be determined experimentally. Combining two above equations and using sorption-desorption isotherm, equation will become,

$$\dot{h} = K(h) \nabla \cdot (c_p(h) \nabla h)$$

where K is reciprocal moisture capacity (reciprocal slope of the sorption isotherm). This equation is valid for the case that humidity change because of self-desiccation is neglected. Humidity change because of

hydration, can be considered as source term and it can be added to above equation. Thus, governing equation would become,

$$\dot{h} = k(h)\nabla \cdot (c_p(h)\nabla h) + h_s^*$$

Where h_s^* is humidity loss because of self-desiccation. In order to find humidity change because of self-desiccation, complete hydration model should be considered. There are lots of models for predicting hydration degree in literature, but none of them are both exact and fast. Thus, in this study a new hydration model is developed. In general, the moisture permeability c_p depends on the equivalent age, too, because the hydration process results into changes of porosity, tortuosity and hydraulic permeability. Identification of the specific form of functions k , c_p and h_s^* is quite tedious and requires extensive experimental data. In order to simplify equation let's combine two parameters by multiplying them and define a new parameter that can be named moisture diffusivity,

$$C(h) = kc_p(h)$$

For mature good quality concretes, its values are very low—roughly 10 to 20 mm²/day at saturation ($h = 1$), and for high-strength concrete even less.

For concrete, the dependence of diffusivity on pore relative humidity is very strong (as noticed already by Carlson (1937)) and cannot be ignored in computations. A jump in diffusivity to roughly 5% of its value at full saturation occurs mainly between 85% and 60% humidity. This fact, established by Bazant and Najjar (1971) on the basis of experimental data on the evolution of pore humidity distributions in cylinders and slabs, is illustrated in Figs.3. The dotted curves, representing optimum fits by the linear diffusion theory, are in blatant disagreement with the data of Abrams and Orals (1965). The solid curves, which fit much better, are the result of optimization of the function $C(h)$, which established that the humidity dependence of concrete diffusivity may be approximately described by the empirical law (Bazant and Najjar 1971)

$$C(h) = C_1 \left(\alpha_0 + \frac{1 - \alpha_0}{1 + \left(\frac{1 - h}{1 - h_c} \right)^r} \right)$$

where $C_1 = C(1)$ is the diffusivity at full saturation, α_0 is the ratio $C(0)/C(1)$, h_c is the pore relative humidity at which $C(h_c) = [C(0) + C(1)]/2$, and r is a parameter affecting the shape of the curve;

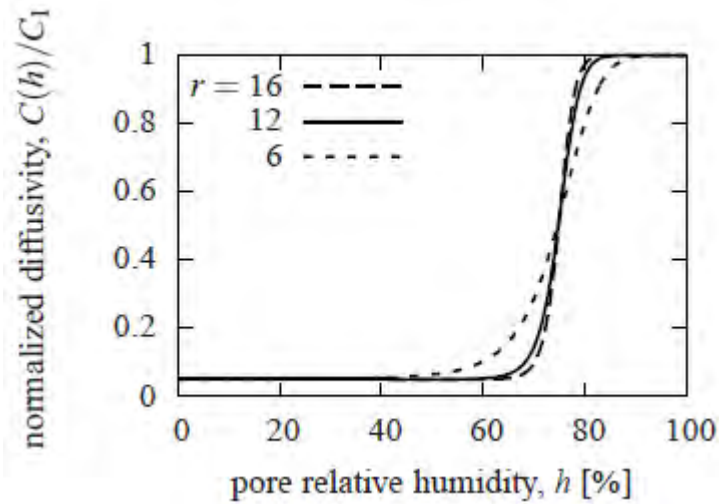


Figure II-3 Dependence of normalized diffusivity $C(h)/C_1$ on relative humidity h

Turk 1967) analyzed by Bazant and Najjar (1971) and Bazant and Najjar (1972), the optimum value is $r = 16$, and according to some other classical data (Hanson 1968), the optimum is $r = 6$. In some calculations of structures (in which, of course, many phenomenon other than drying intervened), various intermediate values of r seemed optimum. In absence of more recent precise measurements, it is recommended to use $r = 12$.

Autogenous and drying shrinkage

When the structure is exposed to the environment, and also there is humidity decrease because of self-desiccation, structure would go under shrinkage. This shrinkage can be both drying and autogenous shrinkage. By considering moisture diffusion (that is discussed in last chapter) it is possible to find complete humidity profile in each step, thus it is more reasonable to use more exact definition for shrinkage than just using proposed average shrinkage equations. This can be done using following equation

$$\epsilon_{sh} = K(\alpha)\nabla h$$

In this equation α is the hydration degree that in the next section a new way to find that would be described. Also, in that equation K is a parameter that shows how much the material aged, and because of this aging how much the much material is stronger. In order to see how this model is working a simple simulation is done. Fig. 4 shows comparison between the experiment and simulation. As it can be seen in this figure, this model combined with diffusion that discussed last chapter, can predict shrinkage in good precision.

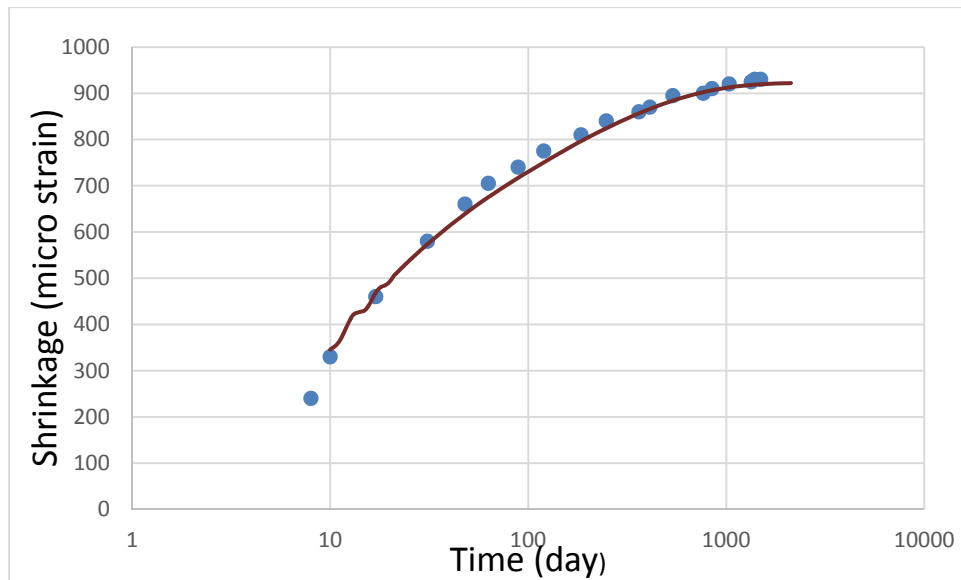


Figure II-4 Shrinkage comparison with Hanson experiment (dotted experiment, full line simulation)

Hydration

In order to consider humidity change and aging of the material, a comprehensive model for considering hydration should be developed. This model would have different stages. In first stage that would happen in first day after mixing concrete, nucleation and growth mechanism is important and after that important mechanism is transport of water through already made paste. Different steps for hydration can be described as it can be seen in figure. 5. As it can be seen in this figure in part (a), first model just include anhydrated cement with water. After very short time, water will act with cement and a thin layer of calcium leached zone will be produced around the cement. Then, nucleation would happen on boundary of cement and by continuing hydration, C-S-H gel will grow from these zones. After almost one day of hydration, a complete barrier of gel will be produced around anhydrated cement. After composing this complete barrier, controlling mechanism would be transport of water through this barrier.

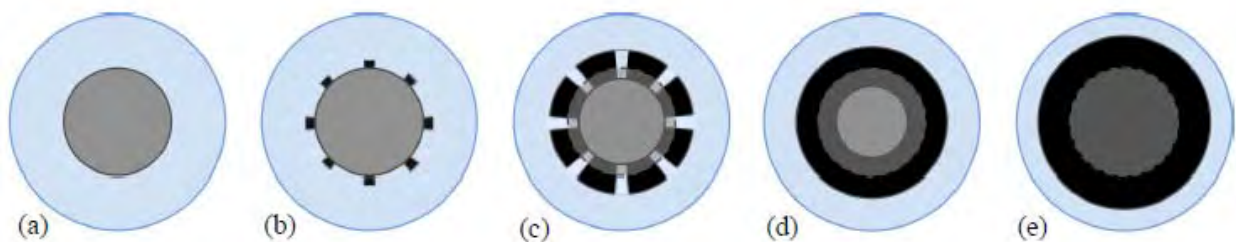


Figure II-4 Different stages for hydration

References

- [1] Bažant, Z.P., and Stefens, A. (2000). “Mathematical model for kinetics of alkali-silica reaction in concrete.” *Cement and Concrete Research* 30 (3), 419{428 (disc. reply Vol. 31, 2001, 1111{1113).
- [2] Bažant, Z.P., Zi, G., and Meyer, C. (2000). “Fracture mechanics of ASR in concretes with waste glass particles of different sizes.” *J. of Engrg. Mechanics ASCE* 126 (3), 226{232.
- [3] Caner, F.C., and Bažant, Z.P. (2013). “Microplane Model M7 for Plain Concrete: I. Formulation. II. Calibration and Verification” *ASCE J. of Engrg. Mechanics* 139 (12), 1714-1723 and 1724-1735.
- [4] Multon S, Toutlemonde F. Effect of applied stresses on alkali-silica reaction induced expansions. *Cem Concr Res* 2006;36:912–20.
- [5] Bazant Z, Baweja S. Creep and shrinkage prediction model for analysis and design of concrete structures, the Adam Neville symposium, SP-194. Akthem Al-Manaseer; 2000. p. 1–83.
- [6] Multon S, Seignol J-F, Toutlemonde F. Structural behavior of concrete beams affected by alkali-silica reaction. *ACI Mater J* 2005;102(2):67–76.
- [7] Bažant, Z.P., and Najjar, L. J. (1971). “Drying of concrete as a nonlinear diffusion problem.” *Cement and Concrete Research*, 1, 1971, 461–473.
- [8] BAŽANT, Z., et al. "Progress in creep and shrinkage prediction engendered by alarming bridge observations and expansion of laboratory database." *Mechanics and Physics of Creep, Shrinkage, and Durability of Concrete: A Tribute to Zdenek P. Bažant: Proceedings of the Ninth International Conference on Creep, Shrinkage, and Durability Mechanics (CONCREEP-9)*. 2013.

III.3.9 Nonlinear Ultrasonic Test in ASR Damaged Concrete prisms

Introduction

Alkaline-silica reaction (ASR) is one of many undesirable degradation mechanisms in concrete. Although this reaction has not been fully understood yet, it can be briefly explained by several chemical reactions [1, 2]. First, alkali cations and hydroxyl ions (OH^-) from concrete pore solution attack the siloxane chain (Si-O-Si) in reactive aggregates. It releases SiO_2 molecules and then these molecules start forming a gel by attracting the alkali cations in the pore solution. This cross-linked gel is called ASR gel. Next, the ASR gel absorbs moisture from the surrounding environment and expands its volume as it imbibes water. Such volumetric expansion of the ASR gel induces large internal pressure, which may then cause microcracking of the concrete [3]. To assess this ASR inducing damage, people in the industry drill a core from an existing concrete structure and conduct microscopy on the drilled core. However, that drilling task can cause additional damage to the structures and it is not practical to inspect an entire structure. For safe operation of concrete structures, nondestructive evaluation (NDE) techniques are needed to monitor and characterize ASR damage.

There have been many researches carried out to characterize ASR damage. One of the most well-known methods is expansion test method such as the accelerated mortar bar test (AMBT), the concrete prism test (CPT) and the accelerated prism test (ACPT). All of these methods rely on volume expansion of a specimen. Therefore, they have their own drawbacks, e.g., 1) the tests are bulk assessment of ASR damage over an entire specimen so that they cannot provide spatial variation of ASR damage, 2) once the sample has expansion in volume, it can be considered that the sample has already been in crack initiation and crack growth damage stage although early stage of damage detection is needed.

To overcome those shortcomings, there have been many methods tried to characterize ASR damage with the aid of linear ultrasonic technique such as pulse velocity measurement and acoustic attenuation test. However, these linear ultrasonic methods are showing inconsistent results each other and not sensitive to microcrack detection at early damage stage in materials [4-7]. On the other hand, it is shown in many papers that nonlinear ultrasonic methods have more sensitivity to detect the early stages damage [8, 9]. One of the most well-known nonlinear ultrasonic techniques is second harmonic test. This test uses the double frequency component generated by the interaction of fundamental incident wave with a damaged material. However, for the media which has huge attenuation like a concrete, it would be less efficient to monitor double frequency component which has higher attenuation level.

Another nonlinear ultrasonic method called nonlinear wave mixing technique mixes two fundamental frequency components within a material and generates difference frequency component of two fundamental ones[10]. [10] shows that nonlinear parameter in a mortar bar changes with respect to the exposure time to alkali solution but it ignored the attenuation in the mortar bar. Therefore, in this study, nonlinear mixing wave technique is used to assess a degree of ASR damage in prepared concrete prisms, taking into account the attenuation. To this end, asymptotic solution of a wave equation in a damped media will be derived later in this paper. Finally, experimentally measured acoustic nonlinear parameter will be plotted to see if the acoustic nonlinearity is related to the degree of ASR damage.

QUADRATIC NONLINEARITY AND DAMPING

Recently, collinear mixing of nonlinear waves has been studied and employed for nondestructive evaluation (NDE) in several studies [11-13]. In this section, we will derive the necessary equations pertinent to this work for the mixing of two longitudinal waves in an elastic solid with quadratic nonlinearity and damping. To be definitive, we consider the configuration illustrated in Fig. 1. Two longitudinal plane waves of frequencies ω_1 and ω_2 are induced into the sample by a transmitter attached to the left end of the sample. Without losing generality, one can assume that $\omega_1 > \omega_2$. The waves will propagate in the positive x-direction. A receiver is attached to the right end of the sample. The distance between the transmitter and the receiver is L . As the two primary waves propagate, they interact with each other due to the nonlinearity in the medium. Such interaction generates a third longitudinal wave of frequency $\omega_d = \omega_1 - \omega_2$. This third wave will be called the mixing wave. Since all three waves have the same phase velocity, they will arrive at the receiver the same time. However, they can be distinguished by their frequency components. In addition to mixing, the amplitude of all three waves will decay due to material damping. Since damping is generally frequency dependent, the rate of amplitude decay for each wave is different. In what follows, we carry out the derivation to understand how each wave decays as they propagate through the medium.

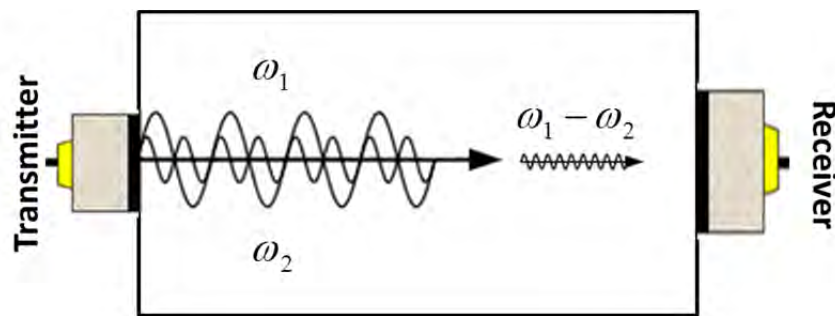


Fig. 1 Two longitudinal wave mixing in a sample

We start by considering the one-dimensional wave equation for the longitudinal wave motion

$$\frac{\partial^2 u}{\partial t^2} - c_L^2 \frac{\partial^2 u}{\partial x^2} - K \frac{\partial^3 u}{\partial t \partial x^2} = \beta c_L^2 \frac{\partial u}{\partial x} \frac{\partial^2 u}{\partial x^2} , \quad (96)$$

where c_L is the longitudinal phase velocity, β is the acoustic nonlinearity parameter [14], and K is the damping coefficient [15, 16]. The total incident wave can be expressed as

$$u_0(x, t) = \sum_{n=1}^2 U_n \exp(-\alpha_n x) \cos[\omega_n(t - \frac{x}{c})] , \quad (97)$$

where U_n is the amplitude at $x=0$ for the primary wave with frequency ω_n , and α_n is the corresponding coefficient of attenuation.

Assuming that the nonlinearity is much weaker, one may write the total wave field as $u = u_0 + v$, where $\|v\| \ll \|u_0\|$ so that terms of higher ordered than v can be neglected. Under these assumption, the governing equation for u_0 and v can be derived from

DisplayText cannot span more than one line!

$$\frac{\partial^2 u_0}{\partial t^2} - c_L^2 \frac{\partial^2 u_0}{\partial x^2} - K \frac{\partial^3 u_0}{\partial t \partial x^2} = 0 , \quad (98)$$

$$\frac{\partial^2 v}{\partial t^2} - c_L^2 \frac{\partial^2 v}{\partial x^2} - K \frac{\partial^3 v}{\partial t \partial x^2} = \beta c_L^2 \frac{\partial u_0}{\partial x} \frac{\partial^2 u_0}{\partial x^2} . \quad (99)$$

Substituting (97) into

DisplayText cannot span more than one line! yields the relationship between the damping coefficient and the coefficient of attenuation,

$$\alpha_n = \frac{K\omega_n^2}{2c_L^3} . \quad (100)$$

The solution to (4) has several frequency components. This work focuses on the frequency component, $\omega_d = \omega_1 - \omega_2$. The corresponding wave that satisfies the homogeneous boundary conditions $v(0, t) = 0$ is

$$v(x, t) = -A \cos\left[\omega_d \left(t - \frac{x}{c_L}\right)\right] , \quad (101)$$

where

$$A = \frac{\beta c_L U_1 U_2}{4K} e^{-\frac{\omega_d^2 K}{2c_L^3} x} (1 - e^{-\frac{\omega_1 \omega_2 K}{c_L^3} x}) \quad (102)$$

gives the amplitude of $v(x, t)$. For values of practical interest, $\exp(-\frac{\omega_1 \omega_2 K}{c_L^3} x) \ll 1$. Thus, Eq. (102)

can be simplified to

$$A = \frac{U_1 U_2 \beta \omega_1 \omega_2 x}{4c_L^2} e^{-\frac{\omega_d^2 K}{2c_L^3} x} . \quad (103)$$

Obviously, in the limit of $K \rightarrow 0$, the amplitude A reduces to that of the undamped system [11-13], i.e.,

$$\lim_{K \rightarrow 0} A = \frac{U_1 U_2 \beta \omega_1 \omega_2}{4c_L^2} x . \quad (104)$$

It follows from (103) that the acoustic nonlinearity parameter can be expressed as

$$\beta = \frac{4c_L^2 A}{U_1 U_2 \omega_1 \omega_2 x} e^{\frac{\omega_d^2 K}{2c_L^3} x} . \quad (105)$$

Once A is measured at x , the acoustic nonlinearity parameter β can be evaluated from (105) assuming that the incident waves (U_n and ω_n) used and the material parameters (c_L and K) are known. In practice, a more convenient form to use is

$$\beta = \frac{4c_L^2 A}{U_1^* U_2^* \omega_1 \omega_2 x} \exp\left[\left(\frac{\omega_d^2 K}{2c_L^3} - \alpha_1 - \alpha_2\right)x\right] , \quad (106)$$

where U_n^* is the amplitude of the wave component with frequency ω_n measured at x , and α_n is the coefficient of attenuation that is related to K through (100). Although U_n^* can be related to U_n through

$$U_n^* = U_n e^{-\alpha_n x} , \quad (107)$$

it is usually more convenient to measure U_n^* directly in practice.

Experiment

Sample Preparation

NDE field test has been implemented at EPRI on July 22nd ~23rd for both ASR damaged concrete slabs and prisms. For the test, four plain concrete slabs were constructed. Three were designed and conditioned to expand as from ASR; the fourth slab was constructed to serve as a non-expansive control specimen. Each slab had three small-scale accompanying prisms. The slab dimensions were 1219 x 914 x 203 mm (48 x 36 x 8 in.) and the prism dimensions were 102 x 76 x 406 mm (4 x 3 x 16 in.). Results for the slab samples will be discussed in the next appendix.

For assessment on ASR damage, 12 concrete prisms with four types of the different levels of ASR damage were constructed and conditioned. Specimen dimensions were 102 x 76 x 406 mm (4 x 3 x 16 in.) for the samples. The materials used to create the reactive ASR specimen group (ASR1, ASR2, and ASR3) included two reactive coarse aggregates from Wells, Maine (RCA1) and Bernalillo, New Mexico (RCA2), a highly-reactive fine aggregate from El Paso, Texas (RFA), and a Type I portland cement with a relatively high equivalent alkali content (Cement 1). Reactivity of all aggregates in this study was based on performance in the ASTM C1293 concrete prism test [17]. Sodium hydroxide (NaOH) was added to the reactive mixtures to obtain a 1.25% equivalent alkali content, by mass of cement. The ASR control mixture (ASR0) consisted of one non-reactive coarse aggregate (NCA), a non-reactive fine aggregate (NFA), and a low-alkali Type II portland cement (Cement 2). Both the NCA and NFA were acquired from a source in Calera, Alabama. The w/cm was 0.50 for all mixtures. Relevant material properties for mixture proportioning are listed in Table 1. Some of the listed materials were also used in the freeze-thaw specimens. Mixture proportions for the ASR specimens are shown in Table 2. The reactive prisms were demolded the day after casting and cured in a fog room at 23 °C and 100% relative humidity. After the seven-day curing period, the reactive slabs and prisms were placed in the environmental chambers set to 38 °C and 98% relative humidity to rapidly induce the ASR reaction. The

environmental chamber conditions were changed to 23 °C and 50% relative humidity on days of expansions. To prevent the prisms from drying out, they were covered in wet burlap during while the chambers were at the lower temperature and relative humidity conditions. The control prisms were left in the concrete lab set to 23 °C and 50 % relative humidity.

The prisms were kept in the high temperature and relative humidity environment until they were shipped to EPRI. Finally, each of four groups had three samples and we had 12 samples in total for the test.

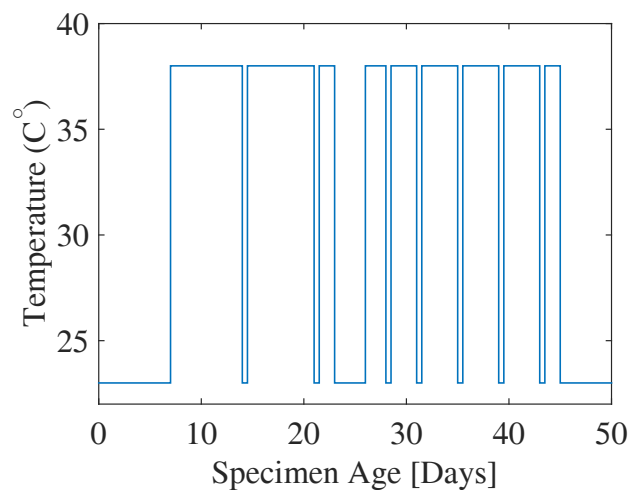


Figure I-1 Sample conditioning

Table 1: Material properties for cements and aggregates for mixture proportioning.

Material	Na2Oeq, %	Absorption Capacity, %	Bulk Specific Gravity (Oven Dry)
Cement 1	1.10	-	3.15
Cement 2	0.53	-	3.15
RCA1	-	0.38	2.77
RCA2	-	0.60	2.64
NCA	-	0.70	2.74
FA	-	1.10	2.57
NFA	-	1.00	2.70

Table 2: Mixture proportions for ASR specimens.

Material	Quantity, kg/m3 (lb/yd3)	
	ASR Reactive	ASR Control
Cement 1	420 (708)	-
Cement 2	-	420 (708)
Water	210 (354)	210 (354)
RCA1 (oven dry)	429 (723)	-
RCA2 (oven dry)	429 (723)	-
NCA (oven dry)	-	1095 (1845)
RFA (oven dry)	818 (1379)	-
NFA (oven dry)	-	639 (1077)

Ultrasonic Measurements

To see the relation between nonlinear ultrasonic measurement results and the volume expansion of the specimen, the amplitude at the frequency difference were measured. This amplitude was used to calculate acoustic nonlinear parameter. The measurements were conducted at 6 different points on each sample so that we can obtain averaged value over 36 data for each ASR damage level, ASR0, ASR1, ASR2 and ASR3. Figure I-2 shows the position for 6 different measurements on the sample.

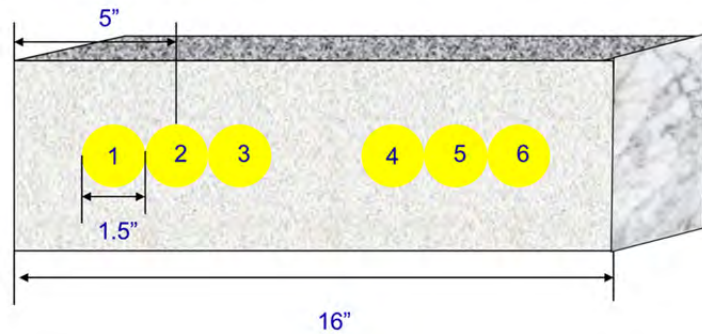


Figure I-2 Six different location of the measurement in concrete prisms

Acoustic Nonlinear Parameter Measurement

A schematic of the nonlinear wave mixing measurement setup is shown in Figure I-3.

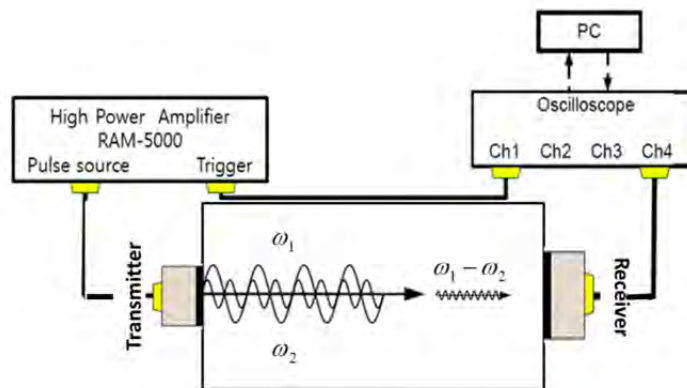


Figure I-3 Experiment setup for nonlinear wave mixing technique

The two frequency components in the incident wave were generated by a 1.5 in diameter broadband transmitter with a central frequency of 225 kHz. The mixed waves were received by a 1.5 in diameter broadband receiver with a central frequency of 0.1MHz. To match the pulse duration as $18 \mu\text{sec}$, 6.3 cycles of 0.35MHz and 4.5 cycles of 0.25MHz were generated by RAM-5000 function generator. Since mixing two primary longitudinal waves generates new longitudinal wave at difference frequency of two primary frequencies, received signal through the sample provides information of second order wave's amplitude. So, $\|U^*\|$, $\|V^*\|$ and $\|u_{2-}\|$ in e.q. (9) were experimentally measured.

Volume Expansion Measurement Results

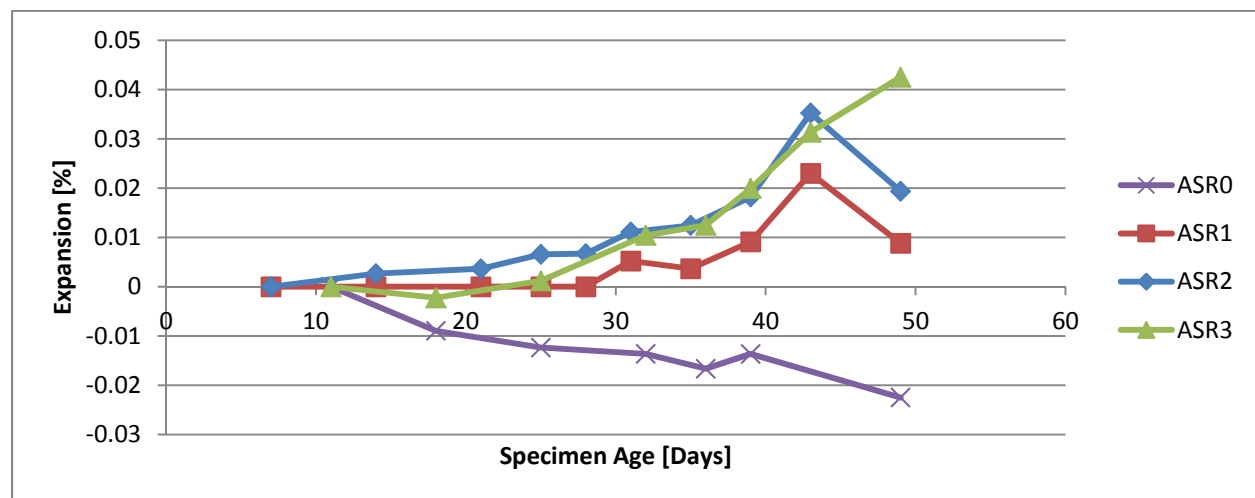


Figure I-4 Averaged Specimen Expansion Results over 49 days

Figure I-4 shows the averaged values of expansion in three prisms (Sample A, B and C) and the last data points were obtained three days before the nonlinear ultrasonic measurements. According to the graph, it is seen that ASR 3 has the most expansion, ASR 2 has less and ASR3 has even less expansion while the control sample, ASR0, did not have any expansion at all. The other findings are that expansion for ASR1 and ASR2 began to decrease at 43 days of aging since all samples had been taken out from environmental chamber after 40days of exposure to 38°C and 98 % RH and shrinkage in volume was made. However, ASR3 reached to the largest expansion by 0.043 % and began shrinkage due to more reaction.

Comparison of Ultrasonic Measurement Results with Expansion Results

Acoustic nonlinearity parameter, β , was measured in the samples at different ASR damage. For all ultrasonic tests, each sample was measured twice at the same position and it has six different locations. Since each ASR damage group has 3 samples, total 18 data in each group (ASR0, ASR1, ASR2 and ASR3) were experimentally obtained and averaged. Figure I-5 shows the measured acoustic nonlinearity parameter.

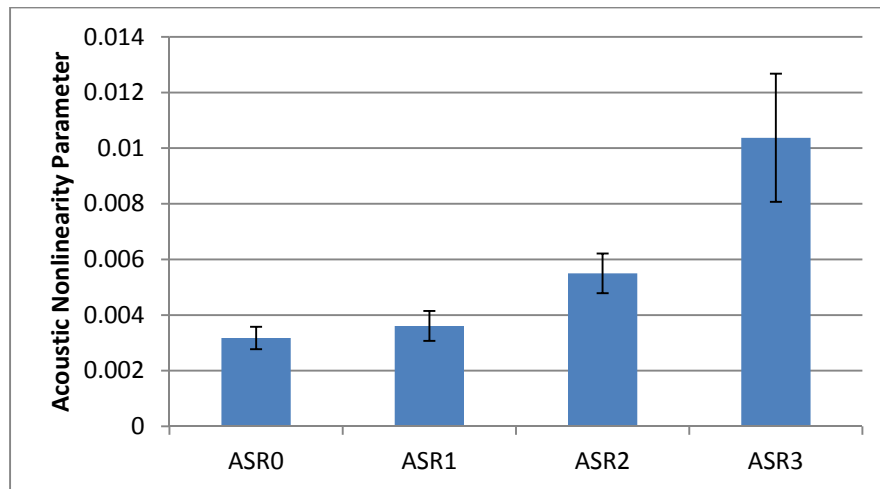


Figure I-5 Averaged Acoustic Nonlinearity at 55th days

To compare the acoustic nonlinearity with longitudinal wave velocity and expansion results, the corresponding results were normalized by the averaged value of ASR1 as shown in Figure I-6.

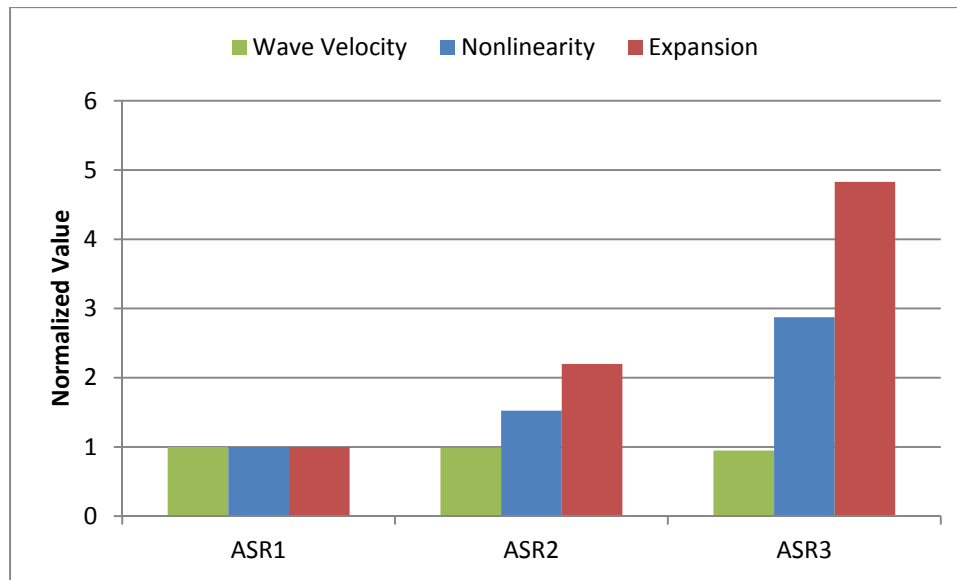


Figure I-6 Normalized Nonlinearity and Expansion of ASR damaged Prisms

Figure I-6 shows that more alkali-silica reaction resulted in more expansion in volume and it is followed by higher level of acoustic nonlinearity parameter. Acoustic nonlinearity parameter was increased by 187% while wave velocity was decreased by 5 %. Thus, it would be concluded that longitudinal wave velocity was not able to capture change on the level of micro damage induced by ASR but acoustic nonlinearity parameter is more sensitive parameter to assess ASR damage.

In addition, if one looks at the entire expansion results, it is found that ASR 3 has more irreversible damage than ASR1 and ASR2 as shown in Figure I-7. It would be concluded that silica gel and its expansion made contribution to the volume expansion but some of those effects could be recovered by loss of moisture. However, if volume expansion exceeds a certain level, micro damage is produced which is not fully recovered. That is why ASR 3 has shown much more nonlinearity.

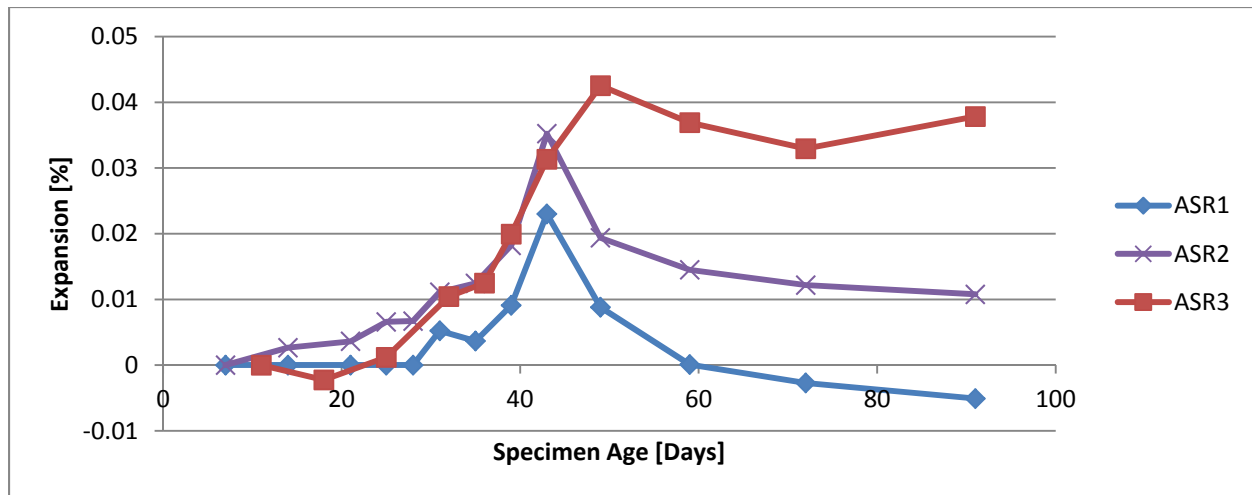


Figure I-7 Expansion results of prism over the entire test period

Conclusion

First, linear and nonlinear ultrasonic measurements have been carried out to see the variations of wave velocity and acoustic nonlinear parameter with respect to the different ASR damage level. For the wave velocity measurement, it is seen that non-damaged sample has higher speed than ASR damaged samples because ASR damaged samples have higher level of crack density due to ASR inducing stresses and having more micro-cracks and it results in the change of strength and density of the specimens. However, this measurement results were not able to show distinguished difference among three different levels of ASR damaged samples. Finally, with the aid of nonlinear mixing wave method, it is found that nonlinear ultrasonic measurement results have higher sensitivity to the density of ASR damages while the other linear measurements were not able to show the difference among damaged samples, i.e., the more damaged samples have the larger acoustic nonlinearity.

Third, the prisms which have the highest level of acoustic nonlinearity (ASR3) showed quite different expansion history over the entire expansion test period. Their expansion was remained at about 0.04% while ASR1 was contracted from its original volume and ASR 2 shrank by expansion of 0.01%. It would infer that there was further damage mode occurring in ASR 3 so that accompanying expansion was not reduced as much as ASR1 and AS2 did.

From all studies done in this quarter, it is seen that measuring acoustic nonlinearity can be a good tool to assess the ASR damage level of concretes.

References

1. Saouma, V. and L. Perotti, *Constitutive model for alkali-aggregate reactions*. ACI materials journal, 2006. **103**(3).
2. Glasser, L.D. and N. Kataoka, *Chemistry of "alkali-aggregate" reaction*.
3. Smaoui, N., et al., *Stresses induced by alkali-silica reactivity in prototypes of reinforced concrete columns incorporating various types of reactive aggregates*. Canadian Journal of Civil Engineering, 2007. **34**(12): p. 1554-1566.
4. Rivard, P. and F. Saint-Pierre, *Assessing alkali-silica reaction damage to concrete with non-destructive methods: From the lab to the field*. Construction and Building Materials, 2009. **23**(2): p. 902-909.
5. Saint-Pierre, F., P. Rivard, and G. Ballivy, *Measurement of alkali-silica reaction progression by ultrasonic waves attenuation*. Cement and Concrete Research, 2007. **37**(6): p. 948-956.
6. Nogueira, C.L. and K.J. Willam, *Ultrasonic testing of damage in concrete under uniaxial compression*. ACI Materials Journal, 2001. **98**(3).
7. Warnemuende, K. and H.-C. Wu, *Actively modulated acoustic nondestructive evaluation of concrete*. Cement and Concrete Research, 2004. **34**(4): p. 563-570.
8. Nagy, P.B., *Fatigue damage assessment by nonlinear ultrasonic materials characterization*. Ultrasonics, 1998. **36**(1): p. 375-381.
9. Cantrell, J.H., *Substructural organization, dislocation plasticity and harmonic generation in cyclically stressed wavy slip metals*. Proceedings of the Royal Society of London. Series A: Mathematical, Physical and Engineering Sciences, 2004. **460**(2043): p. 757-780.
10. Liu, M., et al., *A nonlinear wave mixing method for detecting Alkali-Silica reactivity of aggregates*. AIP Conference Proceedings, 2012. **1430**(1): p. 1524-1531.
11. Chen, Z., et al., *Mixing of collinear plane wave pulses in elastic solids with quadratic nonlinearity*. Journal of the Acoustical Society of America, 2014. **136**(5): p. 2389-2404.
12. Liu, M., et al., *Measuring acoustic nonlinearity parameter using collinear wave mixing*. Journal of Applied Physics, 2012. **112**(2).
13. Tang, G., et al., *Detecting Localized Plastic Strain by a Scanning Collinear Wave Mixing Method*. Journal of Nondestructive Evaluation, 2014. **33**(2): p. 196-204.
14. Kim, J.Y., et al., *Acoustic nonlinearity parameter due to microplasticity*. Journal of Nondestructive Evaluation, 2006. **25**(1): p. 29-37.
15. Holm, S. and R. Sinkus, *A unifying fractional wave equation for compressional and shear waves*. The Journal of the Acoustical Society of America, 2010. **127**(1): p. 542-548.
16. Holm, S. and S.P. Näsholm, *A causal and fractional all-frequency wave equation for lossy media*. The Journal of the Acoustical Society of America, 2011. **130**(4): p. 2195-2202.
17. International, A., *Standard Test Method for Determination of Length Change of Concrete Due to Alkali-Silica Reaction*. 2008, ASTM International: West Conshohocken, PA.

III.3.10 Nonlinear Ultrasonic Test in ASR Damaged Concrete slabs

Sample Preparation

Table 1 shows the detailed mixture contents of the prepared concrete slab. The freshly mixed concrete (91×122×20 cm) is cast, and cured, then the demolded slab is transferred into an environmental chamber where the temperature and relative humidity (RH) are controlled. The reactive slab is then conditioned in the chamber at 38°C and 98 % RH for the ASR damage. Note that the environmental chamber is controlled to keep 23°C and 50 % RH during both the ultrasonic measurements and expansion testing as shown in Fig. II-1(a) and (b) shows the measured expansion during the measurements period.

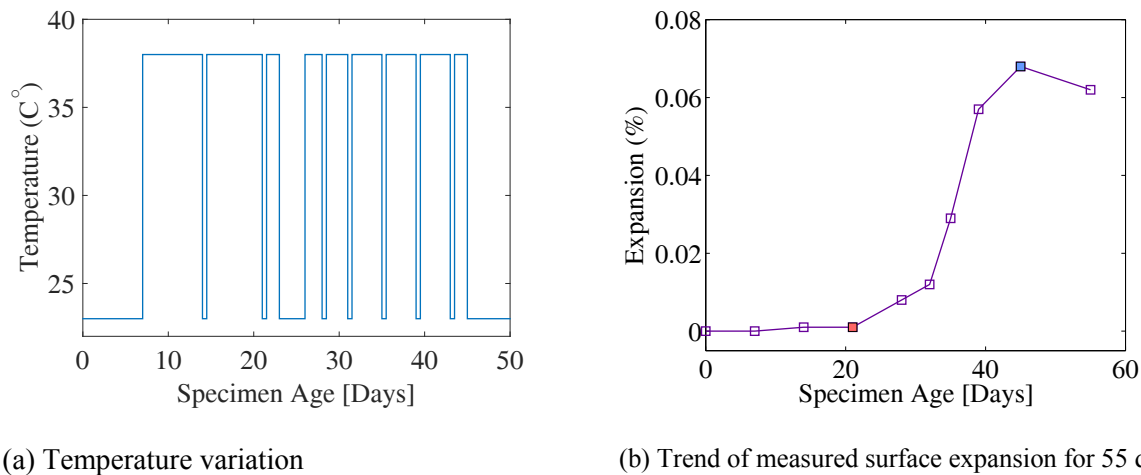


Figure II-1. Sample preparation and controlled temperature

TABLE 1. Mixture design of concrete and mortar mixtures, kg/m³ (lb/yd³).

	Source	Concrete Slab
Water	Tuscaloosa Water Supply	210 (354)
Cement	Leeds, AL Type II	420 (708)
Coarse Aggregate	Calera, AL (Vulcan)	1095 (1845)
Reactive Fine Aggregate	El Paso, TX (Cement/Jobe)	608 (1025)
Water-to-cement ratio (w/c)		0.5

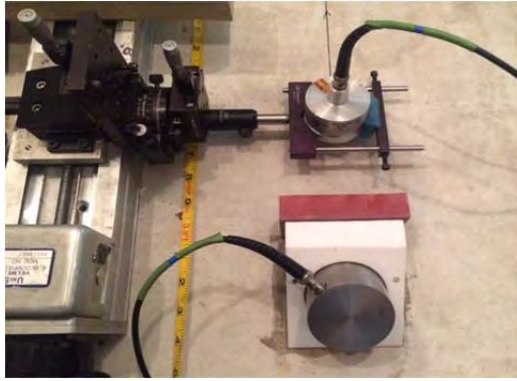
Alkali-Silica Reaction in Concrete

Alkali-silica reaction (ASR) is one of the deleterious mechanism that can induce the serious durability problems of in-service concrete structures. Recently, a summary of the current state of understanding in regard to the ASR mechanism and the accompanying aggregate properties is reported by [1] and the nondestructive evaluation (NDE) method using nonlinear impact resonance acoustic spectroscopy (NIRAS) is also applied to characterize the ASR damage in concrete [2]. This paper introduces new NDE approach [3-6] using nonlinear Rayleigh surface waves for the assessment of the ASR damage in concrete slab and thus it is expected that the evolution of microcracks concentrated near the surface can be sensitively quantified.

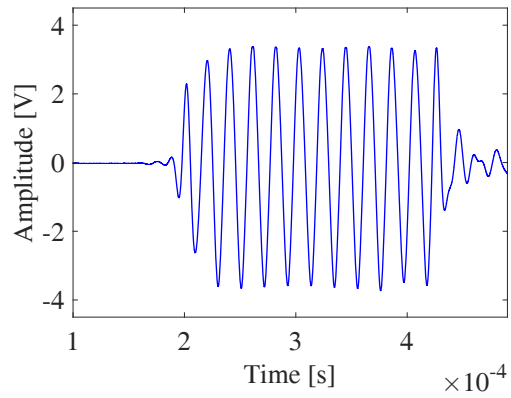
Nonlinear Ultrasound - Second Harmonic Generation (SHG)

A sinusoidal signal at 48 kHz frequency is excited by a function generator (AGILENT 33250A) with 260 mV of a peak to peak voltage. The high enough acoustic energy is then obtained from a power amplifier and the amplified signal is fed to the 50 kHz transmitting transducer (Ultrasonics GRD 50). For the generation of the Rayleigh surface waves, the transmitting transducer is coupled with the Teflon wedge by vacuum grease. The contact angle between the transmitter and the wedge is fixed to 36.3 degrees according to Snell's law and then the wedge is tightly connected to the surface area. Figure II- 2(a) shows the wedge to

air-coupled configuration. The 100 kHz air-coupled transducer (Ultran GRD 100) is used to detect the propagating waves and tilted by approximately 8° to only receive the Rayleigh surface waves. The detected signal is then recorded in an oscilloscope (Tektronix TDS 5034B Digital) and averaged over 256 times to increase the signal-to-noise ratio (SNR) as shown in Figure II- 2(b). The entire NLU measurement system is synchronized by an internal signal from the function generator. In this nonlinear ultrasonic measurement, the propagation distance varies from 13.5 cm to 17 cm by an incremental step of 5 mm. It is experimentally confirmed that second harmonic amplitude no longer increases beyond 17 cm due to the effect of the attenuation. Concerning the previous results [3-6], it is important to note that the propagating Rayleigh wave is relatively free from the distortion by the boundary reflected waves within the propagation distances since the geometry of large scale concrete slab highly guarantees the time delay of the propagating reflected waves. Most importantly, it is observed that the measured A2 tends to monotonically increase with propagation distance while A1 shows the decreasing trend with propagation distance. The acoustic nonlinearity parameter is then determined by taking the slope of the linear fit of A2 to A12 versus propagation distance as shown in Figure II- 3. Note that the linear fits for all averaged nonlinearity parameter of each damage level have R2 correlation coefficients higher than 98%. Accordingly, it is validated that the SHG theory can be applicable to the characterization of full-scale concrete slab.



(a) Air-coupled detection setup for detecting Rayleigh waves



(b) The averaged time-domain signal (256 times).

Figure II-2. The obtained time-domain and windowed signals

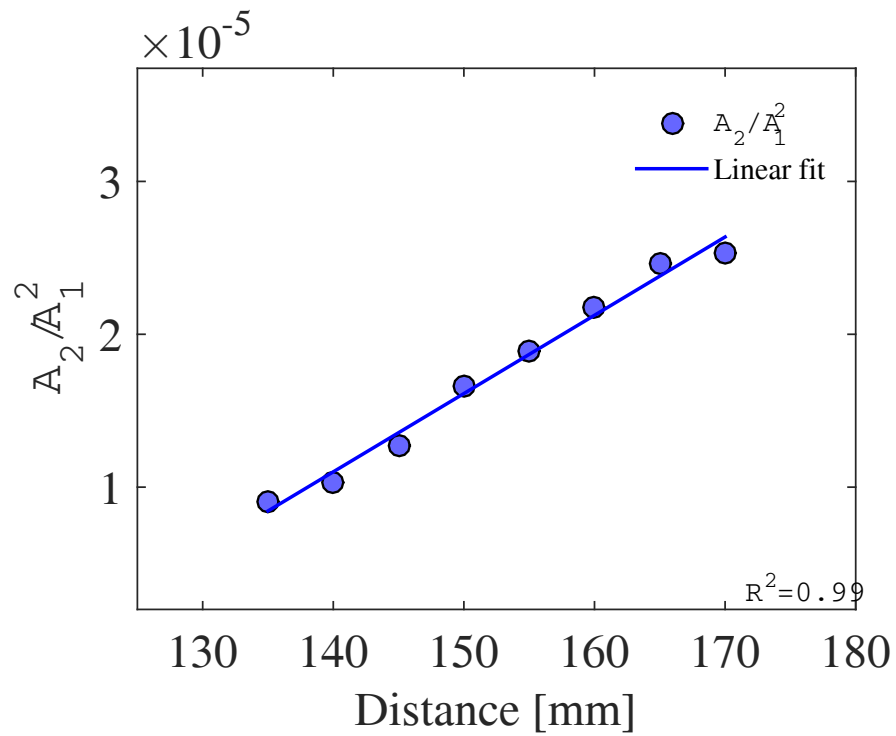


Figure II-3. A_2/A_{12} versus propagation distance.

Results and discussion

The measurement of the SHG in nonlinear Rayleigh waves is performed on a single concrete slab as it exposed to the ASR damages in the environmental chamber for 55 days. First, the NLU measurement is performed after 21 days of exposure for the reference and then is repeated right after the expansion of surface area reaches its peak by 45 days of exposure. The measurements are repeated 4 to 5 times for each exposure level. Figure II- 4 shows averaged acoustic nonlinearity parameter for each damage level. The value of the nonlinearity parameter for the reference is 4.75×10^{-7} , indicating that the measured nonlinearity parameter is relatively small, compared to previous experimental results [3-6]. It can be therefore interpreted that the concrete slab has less inherent microcracks. Importantly, it is mostly likely that the decrease in the nonlinearity parameter is attributed to the fact that the concrete slab is cured at consistent temperature in the environmental chamber, and therefore the effect of drying shrinkage on the microcracks is significantly reduced. Most importantly, it is demonstrated that the measured acoustic nonlinearity parameter is increased by 346% (2.12×10^{-6}) after 45 days of exposure. The error bars shown in the Figure II- 7 indicate the variability of the repeated measurements, where the wedge transmitter and the air-coupled receiver are re-setup.

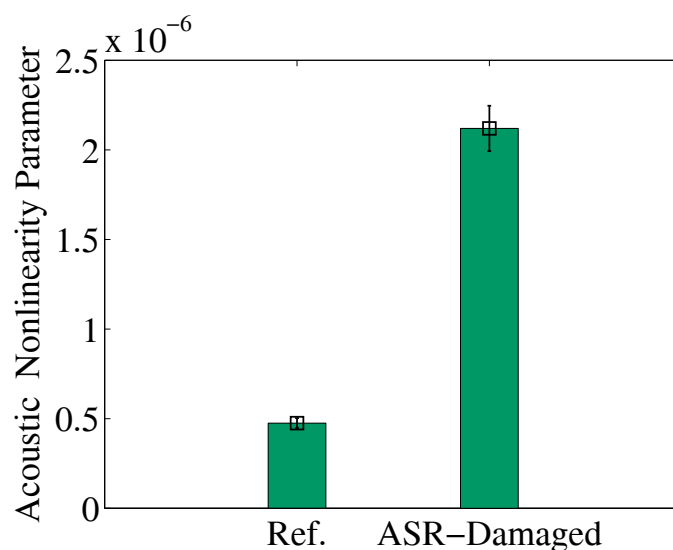


Figure II-4. The measured relative nonlinearity parameter and the effect of ASR-damage on acoustic nonlinearity parameter.

To characterize the sensitivity of the acoustic nonlinearity parameter on the ASR-induced microstructural behavior, the Rayleigh phase velocity are also measured simultaneously. First, the expansion on the surface is increased by 67% while the Rayleigh phase velocity is decrease by a maximum of 17% (2081.48 m/s). Therefore, it can be concluded that the expansion data provide more sensitive results for the effect of ASR damage than the Rayleigh phase velocity. However, the measured expansion is much less sensitive than the acoustic nonlinearity parameter. Overall, the experimental results clearly show that acoustic nonlinearity parameter is greatly sensitive to the ASR-induced microstructural behavior than conventionally used methods and, most importantly, this research demonstrates the applicability of the SHG technique using Rayleigh surface waves to the large scale concrete slab.

Conclusion

This paper validates the potential possibility of the SHG technique using Rayleigh surface waves to evaluate the full-scale concrete slab. The experimental results show that the trends of the measured fundamental and second harmonic amplitudes versus the propagation distance are in a good agreement with previous experimental results [1-3] and further demonstrate that the reliable and repeatable acoustic nonlinearity parameter can be obtained on the concrete slab. With the objective of characterizing the effect ASR damage on the microstructures, significant increase of the acoustic nonlinearity parameter is observed due to the ASR. Interestingly, the sensitivity of the nonlinearity parameter to the ASR-induced damage shows far greater than that of any conventional parameters used for evaluation of ASR damage. Overall, this research clearly shows that the SGH technique using Rayleigh surface waves is efficient method to assess surface concentrated damage in full-scale concrete and can provide the reliable index for damage characterization in concrete.

References

- F. Rajabipour, E. Giannini, C. Dunant, J.H. Ideker, and M.D.A. Thoams, *Cement and Concrete Research* 76, 130–146 (2015).
- K.J. Leśnicki, J.-Y. Kim, K.E. Kurtis, and L.J. Jacobs, *Materials and Structures* 46, 497–509 (2013).
- G. Kim, J.-Y. Kim, K.E. Kurtis, L.J. Jacobs, Y. Le Pape, and M. Guimaraes, *Materials and Structures*, DOI 10.1617/s11527-014-0506-1 (2014).
- G. Kim, C.-W. In, J.-Y. Kim, K.E. Kurtis, and L.J. Jacobs, *NDT & E International* 67, 64–70 (2014).
- G. Kim, J.-Y. Kim, K.E. Kurtis, and L.J. Jacobs, *AIP Conference Proceedings* 1650, 1431–1439 (2015), DOI 10.1063/1.4914759.
- G. Kim, C.-W. In, J.-Y. Kim, L.J. Jacobs, and K.E. Kurtis, *AIP Conference Proceedings* 1581, 805–813 (2014), DOI 10.1063/1.4864904.

Diffusion-Controlled and Creep-Mitigated ASR Damage via Microplane Model: I. Mass Concrete

Zdeněk P. Bažant² and Saeed Rahimi-Aghdam³

Abstract: A diffusion- and creep-based chemo-mechanical model for calculating the evolution of damage caused in concrete and concrete structures by the alkali-silica reaction (ASR) is developed. First the model of Bažant and Steffens for the diffusion controlled kinetics of ASR is outlined, to be used for calculating the rate of production of the ASR gel within the aggregate. The next step is the formulation of a nonlinear diffusion model for the penetration of gel into the micro- and nanopores in mineral aggregate grain, into the interface transition zone (ITZ) and into the microcracks created in the cement paste of mortar. The gel that penetrates the pores and cracks in cement paste is considered to calcify and stop expanding. A novel point, crucial for unconditional numerical stability of time step algorithm, is that the diffusion analysis is converted to calculating the pressure relaxation at constant gel mass during the step. The gel expansion in the aggregate and the ITZ causes fracturing damage in the concrete, which is analyzed by microplane model M7, into which the aging creep of broad retardation spectrum is incorporated. The gel and the damaged concrete are macroscopically treated as a two-phase (solid-fluid) medium, which is non-standard because of load-bearing but mobile water in nanopores. The condition of equilibrium between the phases is what mathematically introduces the fracture producing load into the concrete. Depending on the stress tensor in the solid phase, the cracking damage is oriented and the expansion is directional. The creep is found to have a major mitigating effect on multi-decade evolution of ASR damage, and is important even for interpreting laboratory experiments. A stable explicit algorithm of time integration of the ASR problem is formulated. Finally, to validate the model, successful fits of various test data from the literature are demonstrated.

Introduction

The alkali-silica reaction (ASR) afflicts mineral aggregates in concrete if they contain imperfectly crystalline silica. The reaction produces a gel that can imbibe enormous amount of water. The swelling that results, typically after 20 to 60 years, is often causing severe strength degradation and fracturing in concrete structures. Since drying arrests the ASR, the worst damage has occurred in massive structures such as dams, large bridges and nuclear power plant structures. To prevent the ASR damage is one important goal of sustainable design.

The damage due to alkali-silica reaction (ASR) (also called the alkali-aggregate reaction, AAR) was first identified by Stanton in 1940 [48]. Since that time a vast body of literature on this pernicious problem has been accumulated [4, 7, 41, 2, 44, 31, 47, 48, 28, 52, 16, 24, 25, 55, 51, 37, 35, 36, 38, 33, 34, 19, 50, 43, 18, 1, e.g.]. Comprehensive literature reviews have recently been given by Saouma and Xi [47] and Pan et al. [41]. The chemical relations involved in ASR have been presented and discussed in [4, 2, 41, 46, 47].

A review relevant to mathematical modeling of the chemical reaction kinetics prior to 1999 appears in the introduction of [4]. An excellent recent review relevant to the ASR damage

²McCormick Institute Professor and W.P. Murphy Professor of Civil and Mechanical Engineering and Materials Science, Northwestern University, 2145 Sheridan Road, CEE/A135, Evanston, Illinois 60208; z-bazant@northwestern.edu; corresponding author.

³Graduate Research Assistant, Northwestern University.

simulation is found in the introduction of Cusatis and Alnaggar’s paper [2]. This paper was also the first to provide a general structural analysis of a creep-mitigated ASR damage based on Cusatis’ lattice discrete particle model (LDPM). All of the ASR gel expansion was assumed to occur in the interparticle contacts, with no delay due to gel diffusion. Lumping all of the expansion into the interparticle contacts is a effective simplification but it implies that, in a perfectly regular lattice, the expansions would cause no stresses and no damage, although in reality they surely would.

A comprehensive model for structural analysis of ASR capturing the essential physical phenomena involved seems unavailable. The present objective is to formulate such a model, which must include a realistic but manageably simple characterization of various types of pores and cracks, the calcification of gel expelled in the hardened cement paste, the diffusion control of gel expansion, the evolution of material damage with its anisotropy, the stress relaxation and damage mitigation by creep, the porosity effects, the effects of selfdesiccation and external drying, and the formulation of an effective and stable numerical algorithm. The objective is a continuum, rather than discrete, model, since this is still the only way to analyze large three-dimensional structures. Among various constitutive models in existence, the microplane model is particularly suitable because it can capture different degrees of damage on planes of different orientations.

The eigenstrain caused by the ASR is different from the thermal eigenstrain or shrinkage eigenstrain. The latter is simply additive to the stress-induced deformation and causes (or is assumed to cause) no damage unrestrained concrete. The ASR gel expansion into the pores and microcracks loads the porous solid skeleton of material from within, producing material damage. It is actually an eigenstrain on a sub-scale of the material.

The objective of the present work is to present a new comprehensive continuum model capable of capturing the main physics of ASR damage, including: 1) delay of the ASR due to diffusion of ASR gel into the pores and expanding cracks within and very near aggregate grains; 2) fracturing of the solid framework of concrete as a two-phase medium caused by fluid expansion in the pores and cracks; 3) oriented character of damage; 4) mitigation by creep (with chemical aging) of the stresses created by gel expansion; and 5) control of ASR process by variation of pore humidity due to selfdesiccation or external drying. A challenging though essential objective is to formulate an unconditionally stable computational algorithm permitting long time steps. To create a model permitting the analysis ASR in large structures, a macroscopic continuum model (with a localization limiter preventing instability of softening damage) is sought. To capture the oriented character of ASR damage under general (non-hydrostatic) stress states, the microplane constitutive damage [20] model is best and its latest version M7 is used, although the aspects of the present model are applicable to any constitutive damage model.

To describe the production of the ASR gel in the mineral aggregate, the model of Bažant and Steffens (2000) is adopted. This model is considered as a given input, which predicts the gel mass $M(t)$ per unit area of aggregate surface (kg/m^2) extruded into the adjacent pores and developing cracks in the matrix, as a function of time t . The coupling with the penetration of ASR gel into the pores of the mortar surrounding the aggregate piece is considered to be one-way, i.e., the evolution of gel mass $M(t)$ is considered to be independent of pressure $p(t)$ developed in the pores surrounding the aggregate piece. This is, of course, a simplification, although probably not a major one since the pore pressures sustainable by concrete cannot be large enough to slow down the alkali-silica reaction appreciably.

The fracturing model of Bažant, Zi and Meyers (2000) is not used since it is materials science type approach which deals with local micromechanics of fracture driven by pore pressure. This

analytical approach worked well for determining the pessimum size of non-crystalline silica particles that causes maximum damage. But it seems too unwieldy to upscale and include in a continuum model.

Review of Simplified Model for Kinetics of ASR Gel Production

First we need to introduce a model for the kinetics of gel production in mineral aggregates. To this end, the simplified model of Bažant and Steffens [4], as improved by Alnaggar, Cusatis and de Luzio [2], and slightly modified here, is adopted. Since the shape of aggregate grains is not too important, spherical grains of diameter D are considered.

The ASR reaction occurs at various randomly located discrete sources inside the grain. Those near the grain surface will be activated first and the time to activate the deeper sources will grow with the depth. Thus, as an average behavior of many aggregate grains, we introduce a smeared continuum model in which water to diffuse radially into a spherical aggregate grain, with a spherical at which the ASR takes place in a smeared continuum way. The ASR reaction is assumed to take place instantly at the front of water penetration, which forms a spherical surface of decreasing radius z (Fig. 1c). The reaction is slowed down by the diffusion of water through the aggregate piece, and particularly through the layer of ASR gel already formed. Like in hydration modeling [45], the radial diffusion of water through the barrier of the previously formed ASR gel is what controls the rate of ASR. This diffusion control captures the effect of grain size on the reaction rate, typical of all diffusion phenomena.

For the sake of simplicity, the radial profile of water concentration ξ_w (water mass per unit volume of aggregate) is considered to be fixed and is assumed to be the solution of the steady-state linear diffusion equation in spherical coordinates [4]. For the proper boundary conditions, this assumption yields the profile:

$$\xi_w = w_s F(\bar{x}), \quad F(\bar{x}) = \frac{1 - \bar{z}/\bar{x}}{1 - \bar{z}}, \quad \bar{x} = \frac{2x}{D}, \quad \bar{z} = \frac{2z}{D} \quad (1)$$

where x = radial coordinate (Fig. 1c), \bar{x} = dimensionless radial coordinate, w_s = water concentration at the surface of aggregate grain (kg of water per m³ of aggregate), and $F(\bar{x})$ = dimensionless concentration profile obtained as solution of Laplace equation for spherical geometry [4]. The condition of mass balance at the reaction front $x = z$ requires that

$$r_{ws} c_s dz = -a_s [d\xi_w/dx]_{x=z} dt \quad (2)$$

where r_{ws} = water-to-silica stoichiometric ratio (mass conversion ratio) ; a_s = permeability of water through ASR gel (whose dependence on temperature follows the Arrhenius equation); and c_s = reactive silica concentration (mass of reactive silica per unit volume of aggregate). The reactive silica typically is only a part of silica content (here assumed as 1/3). Since two water molecules are necessary to dissolve one silica atom, $r_{ws} = 2m_w/m_s$; where $m_w = 18$ g/mole and $m_s = 60.09$ g/mole are the molar masses of water and silica. The gel as produced at the reaction front z is called the basic gel. Its total mass in one aggregate grain of diameter D is

$$w_{bg} = \frac{\pi}{6} (D^3 - (2z)^3) c_s f_a \frac{m_g}{m_s} \quad (3)$$

where f_a = parameter specifying the availability of alkali (sodium and potassium ions); $f_a = 1$ when the alkali content a in permeating water is high enough to give the maximum gel production (the ASR experiments are usually carried out under such conditions).

Furthermore, the mass of imbibed water, w_i , needs to be calculated. Its increment is, approximately,

$$\dot{w}_i = \frac{A_i}{\tau_i}, \quad A_i = k_i w_{bg} - w_i, \quad \tau_i = \frac{\delta_w^2}{C_i} \quad (4)$$

where k_i, δ_w = empirical constants, A_i = thermodynamic affinity (proportional to the difference in chemical potentials), τ_i = time characterizing the imbibition rate and C_i = diffusivity of cement mortar around the aggregate, which depends on the relative humidity h in the pores. The humidity depends on 1) water imbibition by ASR gel, 2) self-desiccation of concrete, and 3) external drying. These effects are not additive.

The humidity decrease due to self-desiccation is usually given as a function of time but should correctly be calculated as a function of the local degree of hydration [45]. The external drying may be calculated according to the nonlinear diffusion equation in [12]. In absence of external drying and selfdesiccation, the humidity decrease caused by ASR at the gel source may be calculated as

$$dh_{ASR} = -k_g w_i \quad (5)$$

where w_i = mass of water imbibed in the gel; and k_g = empirical constant representing the slope of the sorption isotherm of the gel.

The diffusion of water in the aggregate must pass through nanopores, same as in concrete and cement paste. Therefore, like in concrete, diffusivity $C_i(h)$ must be expected to decrease sharply with pore humidity h . For this reason, based on Bazant-Najjar model [12] we propose,

$$C_i(h) = C_i^0 \left[1 + \left(\frac{1-h}{1-h^*} \right)^k \right]^{-1} \quad (6)$$

where C_i^0 = diffusivity at saturation and k, h^* = empirical constants. Eq. 6 is similar to that for concrete [12] except that, for a large exponent k (which is typically 6 to 16), the C_i value at $h = 0$ is almost zero, rather than a small finite value.

Production of the basic ASR gel is assumed to cause no volume increase. Rather, the increase of gel volume, or swelling, is attributed solely to water imbibition into the gel. The volume increase of ASR gel per aggregate grain, due to imbibing volume V_i of water of mass density ρ_w , may be calculated as

$$V_i = w_i / \rho_w \quad (7)$$

In what follows, all the quantities will preferably be given as the content fractions (or densities), per unit volume of concrete. The increase of gel volume fraction in concrete above the initial volume of silica and reacted water is

$$v = V_i \xi_{ac} \quad (8)$$

where ξ_{ac} = volume fraction of aggregate in concrete; v as a function of time t is used in the following as the input into the ASR damage analysis.

To simplify the equation system, Eqs. (1) and (2) may be combined to yield the differential equation

$$d\bar{t} = (\bar{z}^2 - \bar{z})d\bar{z} \quad \text{where} \quad \bar{t} = \frac{4a_s w_s}{D^2 r_w s C_s} \quad (9)$$

Integration with the initial condition $\bar{z} = 1$ at $\bar{t} = 0$ gives the cubic equation $2\bar{z}^3 - 3\bar{z}^2 = 6\bar{t} - 1$, which can be solved for \bar{z} either analytically or numerically to obtain the function $\bar{t}(\bar{z})$.

Alternatively, one can use Alnagar et al.'s approximation [2]: $\bar{z} = 1 - k_m \bar{t}^{0.6}$ for $\bar{t} < 1/12$ and $\bar{z} = k_m(1/6 - \bar{t})^{0.6}$ for $1/12 < \bar{t} < 1/6$ with $k_m = 12^{0.6}/2$.

Combining Eqs. (3), (4), (6), one gets

$$\dot{w}_i = \frac{C_i(h)}{\delta^2} [C_1(1 - \bar{z}^3)D^3 - w_i] \quad \text{where} \quad C_1 = \frac{\pi}{6} k_i f_a c_s \frac{m_g}{m_s} \quad (10)$$

Diffusion of ASR Gel into Pores in Aggregate and Concrete

The expulsion of gel from a gel source into adjacent pores is another mechanics controlling the rate of ASR. It may be treated as a diffusion flow obeying the Darcy law. The flow velocity $\dot{z} = b_D \nabla p$ where ∇ denotes the gradient and b_D = Darcy permeability (dimension $\text{m}^3\text{s/kg}$). In detailed analysis, one could now proceed to a point-wise differential equation for the diffusion in coordinate x . However, in view of all the uncertainties and inevitable simplifications, it should suffice to replace \dot{z} with the velocity dx/dt of the diffusion front at distance x from the gel source, and the pressure gradient with the average pressure gradient $\bar{\nabla} p = p/x$. This leads to the simplified Darcy diffusion equation:⁴

$$\frac{dx}{dt} = b_D \frac{p}{x} \quad (12)$$

Note that if p at the gel source were constant, integration of this differential equation would yield $x = \sqrt{2b_D p t}$, which is the well known penetration depth x of the filling front at constant pressure. Thus it is verified that this fundamental feature of diffusion theory is exhibited by the simplified Darcy equation.

The ASR gel first enters the pores, of volume fraction v_0 , that are empty and easily accessible at virtually zero pressure p . They are of three kinds: 1) Pores inside the aggregate, whose amount depends strongly on the aggregate type; 2) Pores inside the cement paste, which always contains empty pores, because of self-desiccation (caused by the chemical reactions during hydration); and 3) pores in the interface transition zone (ITZ) of typical thickness $0.1 \mu\text{m}$, surrounding each aggregate grain, which is a thin layer of cement paste of lower mass density and higher porosity. The filling of empty pores of volume fraction v_0 can take years or even decades. After they get filled, further imbibition of water will cause the gel to develop a significant pressure p and to diffuse into adjacent voids and cracks.

Part of the gel will also enter the pores and cracks in the cement paste or mortar beyond the ITZ. However, the gel intruded in these pores, of volume fraction v_{ca} , will become inactive. It will not further imbibe water and swell, and the pressure in the these pores will vanish. The reason is that calcium hydroxide (C-O, or CaOH) crystals are plentiful in cement paste [24, 25, 23]. The ASR gel will inevitably react with them and form a solid compound similar to C-S-H, which does not swell. So the calcified volume fraction v_{ca} of the gel produced must be omitted from the pressurized pore volume fraction v .

⁴The pressure profile over the gel penetration zone $x' \in (0, x)$ is doubtless nonlinear. What matters is the flux of mass into the pores at the penetration front, $x = 0$. Generally, it is a good approximation to consider the pressure distribution within $(0, x)$ to be a power law, proportional to $(x - x')^u$ (where u = positive constant). Then the pressure gradient at the front ($x' \rightarrow x$), is $\nabla p = p/ux$. Thus Eq. (12) may be generalized as

$$\frac{dx}{dt} = b'_D \frac{p}{x}, \quad b'_D = \frac{b_D}{u} \quad (11)$$

So the form remains the same for every fixed profile of p , and the fact that the permeability b_D changes to b'_D does not matter since its value is a fitting parameter anyway. Frequently considered is a parabolic profile, for which $u = 2$.

One or several basic gel sources are imagined to develop in each aggregate grain with reactive silica. From each source, the gel diffuses in several directions (Fig. 1, Fig. 2) into pores, interfaces and micro-cracks in the aggregate grain, and into the ITZ (the gel expelled into cracks in the surrounding cement paste will not imbibe water and swell because it will calcify). The distances x_n ($n = 1, 2, \dots, n_t$) from the numerous gel sources to the fronts of all these diffusion paths vary randomly (Fig. 2). But their average must grow in proportion the volume fraction $v - v_{ca}$ of the active gel. So, replacing in Eq. (12) x with $v - v_{ca}$, we introduce a modified Darcy law

$$\frac{dv}{dt} = b \frac{p}{v - v_{ca}} \quad (13)$$

where p = average gel pressure, and b = effective Darcy permeability (dimension m^2/Ns or m s/kg) which is proportional to actual Darcy permeability b_D . From the volume fraction v of gel-filled pores we subtract here the volume fraction v_{ca} of calcified gel which is not a fluid, does not swell and does not communicate pressure p . The gel calcification in these pores is one reason why decades would pass before the ASR damage would become noticeable.

During the initial filling of empty, easily accessible, pores, the pressure is nearly zero. Thus the initial condition for ASR gel diffusion is

$$p = 0 \quad \text{for} \quad v = v_0 \quad (14)$$

Diffusion at Constant Total Gel Mass in Time Step

An explicit computational algorithm for damage in structures can be based directly on Eq. (13), but then very short time steps are required to ensure numerical stability and convergence. Such a limitation becomes a serious problem when the creep is taken into account. The creep proceeds rapidly at first, which requires short time steps on the order of minutes at the beginning. But to reach durations such as 50 years, the time steps need to be increased greatly in time, which is possible since the pressure evolution becomes very slow. For this reason, an analog of the unconditionally stable exponential algorithm [8, 30] for creep must be introduced for the gel diffusion equation.

Based on an analogy with the unconditionally stable exponential algorithm for creep, we assume the volume fraction of fluid (non-calcified) gel to be held constant during the time step Δt ; i.e., $\rho(v - v_{ca}) = \text{const.}$ or

$$z\rho dv + (v - v_{ca}) d\rho = 0 \quad (15)$$

where ρ = mass density of gel ($dv_{ca} = 0$). To express $d\rho$, it is necessary to take into account the bulk compressibility, κ , of the gel, which is probably about the same as that of water, and thus about 20-times higher than the compressibility of concrete as a whole, with its pores. Since the volume compression must be elastic, we have

$$p = \kappa \left(\frac{\rho}{\rho_0} - 1 \right) \quad (16)$$

or, conversely, $\rho = \rho_0(1 + p/\kappa)$, where ρ_0 = mass density of the gel at $p = 0$. So, $d\rho = \rho_0 dp/\kappa$. Substituting this and the expression for dv from Eq. (12) into the constant mass condition in Eq. (15), we get a differential equation for pressure relaxation due to diffusion at constant gel mass:

$$\frac{dp}{dt} + \frac{p}{\tau} = 0 \quad (17)$$

$$\text{where} \quad \tau = \frac{(v - v_{ca})^2}{B(p + \kappa)} \quad (18)$$

where τ plays the role of characteristic time. The initial condition is $v = v_0$ when $t = 0$ and $p = 0$.

Eq. (17) describes pressure relaxation at constant gel mass. It is nonlinear since τ depends on v and p . However, in forward-stepping algorithm, we may calculate τ assuming v and p to remain during the time step equal to the values at the end of the previous time step, v_{old} and p_{old} ; i.e.

$$\tau = \frac{(v_{old} - (v_{ca})_{old})^2}{B(p_{old} + \kappa)} \quad (19)$$

which is a constant. This allows Eq. (17) to be integrated by separation of variable, which yields the pressure increment:

$$\Delta p = -p_{old} (1 - e^{-\Delta t/\tau}) \quad (20)$$

The advantage of this exponential form is that, for arbitrarily long time steps, the numerical integration can never yield unbounded p .

From Eq. (12), the new value of the gel volume fraction at the end of the time step is

$$v = v_{old} + \frac{b_0 p}{v_{old} - (v_{ca})_{old}} \Delta t, \quad p = p_{old} + \Delta p \quad (21)$$

The new value of the volume fraction v_{ca} of the inactive calcified gel is obtained as

$$v_{ca} = (v_{ca})_{old} + \frac{(b - b_0) p}{v_{old} - (v_{ca})_{old}} \Delta t + \Delta v'' \quad (22)$$

where $\Delta v''$ = increase of inelastic pore volume fraction cause by fracturing. Why is all of $\Delta v''$ included in the calcified gel volume?—Since the aggregate is expanding against the surrounding concrete, it should be under compression and so the cracks should form mainly in the surrounding mortar rather than in the aggregate itself. Ignoring the delay in gel calcification is, of course, a simplification, but surely a negligible one, compared to the decades of ASR evolution.

Constitutive Law for the Solid Part of Concrete: Microplane Model M7

In most structures undergoing ASR, the concrete is subjected to multiaxial stress states. Therefore, anisotropic damage must be expected. The anisotropic damage of quasibrittle materials, concrete included, may be most effectively described by the microplane constitutive model. Its basic idea is to express the constitutive law in terms of the vectors of stress and strain acting on a generic plane of any orientation in the material microstructure, called the microplane. The use of vectors, rather than tensors, is analogous to the Taylor models used for plasticity of polycrystalline metals, but with important conceptual differences.

Firstly, to avoid model instability in post-peak softening, a kinematic constraint must be used instead of a static one [20]. Thus, the strain (rather than stress) vector on each microplane is the projection of the macroscopic strain tensor, i.e.,

$$\epsilon_N = \epsilon_{ij} N_{ij}, \quad \epsilon_M = \epsilon_{ij} M_{ij}, \quad \epsilon_L = \epsilon_{ij} L_{ij} \quad (23)$$

where ϵ_N , ϵ_M and ϵ_L are the magnitudes of the three strain vectors corresponding to each microplane, and $N_{ij} = n_i n_j$, $M_{ij} = (n_i m_j + m_i n_j)/2$ and $L_{ij} = (n_i l_j + l_i n_j)/2$ ($i, j = 1, 2, 3$);

n_i , m_i , and l_i are three unit, mutually orthogonal, normal and tangential vectors characterizing that microplane.

Secondly, the principle of virtual work is used to relate the stresses on the microplanes (σ_N , σ_M and σ_L) to the macro-continuum stress tensor σ_{ij} , to ensure equilibrium. This gives [10, 20]:

$$\sigma_{ij} = \frac{3}{2\pi} \int_{\Omega} (N_{ij}\sigma_N + M_{ij}\sigma_M + L_{ij}\sigma_L) d\Omega \quad (24)$$

where Ω is a unit hemisphere, over which the integration is carried out numerically, by an optimum Gaussian integration formula.

Microplane model M7 [20] uses an explicit constitutive relation which delivers the microplane stress vector from the microplane strain vector. It involves stress-strain boundaries (or strain-dependent strength limits) within which the behavior is elastic or damaged-elastic. When the elastic increment exceeds the boundary, the state point drops at constant strain to the boundary, the drop representing an inelastic (or damage) stress increment. There are three types of boundaries: 1) The tensile normal boundary captures progressive tensile fracturing; 2) The compressive volumetric boundary simulates pore collapse under extreme pressures; 3) The compressive deviatoric boundary simulates compression softening at low confinement, together with a normal-shear stress envelope.

In combination with some localization limiter with a material characteristic length, microplane model M7 has been proven to give rather realistic predictions of the constitutive and behavior of quasi-brittle materials over a broad range of loading scenarios, including uniaxial, biaxial and triaxial loadings with post-peak softening, compression-tension load cycles, opening and mixed mode fractures, compression-shear failure and axial compression followed by torsion (or vertex effect) [20, 21].

Incorporation of Creep with Aging and Shrinkage

The ASR damage in structures evolves over decades, and so the creep and shrinkage must play a major role. Even the laboratory experiments with ASR have a long enough duration for creep and shrinkage to be important. Here the creep and shrinkage are calculated according to model B4 [29, 57], which was combined with the microplane damage constitutive model M7 [20]. Combining B4 with M7 is important because the ASR damage in presence of external loads causes fracturing, which cannot be captured well by the classical tensorial constitutive models.

The linear viscoelastic aging creep occurs in undamaged concrete between the cracks, while the fracturing (or damage) strain occur in the cracks. Therefore the creep strain is additive to the fracturing strain. Since the ASR, pore humidity and fracturing damage all evolve in time and affect the constitutive law, the rate-type creep model, rather than hereditary integral-type, must be used [6]. The rate-type creep model can be based on the Kelvin or Maxwell chain. The former is more convenient since model B4 specifies the compliance, rather than relaxation, function.

The spring and dashpots moduli of the Kelvin units in the chain are obtained by discretizing the continuous retardation spectrum [5]. Because of aging, the spectrum is different for every time step and every integration point. The retardation times are selected to form a geometric progression with quotient 10 and must cover the entire time range of interest. The time integration requires the exponential algorithm [8], which is unconditionally stable and allows arbitrarily increasing the time step as the creep rate decays. On the tensorial lever, this

algorithm leads to the incremental stress-strain relation

$$\Delta\sigma_{ij} = \bar{E}(\Delta\epsilon_{ij} - \Delta\epsilon''_{ij}) \quad (25)$$

$$\Delta\epsilon''_{ij} = \Delta\epsilon_{ij}^{cr} + \delta_{ij}(\Delta\epsilon^{sh} + \alpha\Delta T) \quad (26)$$

in which ϵ_{ij}^{cr} = creep strain increment tensor calculated from the exponential algorithm for Kelvin chain model, \bar{E} = incremental modulus obtained from the exponential algorithm, ϵ^{sh} = shrinkage strain increment, and $\alpha\Delta T$ = thermal strain.

When the microplane model is used, the creep strain increments should properly be introduced within the microplane algorithm because they affect the stress changes differently on microplanes of different orientations, thus creating incremental anisotropy. To this end, tensor ϵ_{ij}^{cr} is projected as a creep strain vector on each microplane, with the normal and shear components

$$\epsilon''_N = \epsilon''_{ij}N_{ij}, \quad \epsilon''_M = \epsilon''_{ij}M_{ij}, \quad \epsilon''_L = \epsilon''_{ij}L_{ij} \quad (27)$$

Based on the microplane elastic stiffness scaled for aging, the trial microplane stress increments gets changed from $\Delta\sigma_N = \bar{E}_N\Delta\epsilon_N$, etc., to

$$\Delta\sigma_N = \bar{E}_N(t)(\Delta\epsilon_N - \Delta\epsilon''_N) \quad (28)$$

$$\Delta\sigma_M = \bar{E}_T(t)(\Delta\epsilon_M - \Delta\epsilon''_M) \quad (29)$$

$$\Delta\sigma_L = \bar{E}_T(t)(\Delta\epsilon_L - \Delta\epsilon''_L) \quad (30)$$

where \bar{E}_N and \bar{E}_T are the elastic moduli for the normal and shear components. If these stress increments exceed the stress boundary, a drop to the boundary is executed at constant strain. The microplane elastic moduli at age t are calculated as

$$\bar{E}_N = E_N \frac{\bar{E}}{E}, \quad \bar{E}_T = E_T \frac{\bar{E}}{E} \quad (31)$$

where $E(t)$ = Young's modulus, increasing with concrete age t due to chemical hydration of cement and microprestress relaxation, E_N, E_T = elastic normal and shear moduli for the microplane calculated from Young's modulus at the reference age (28 days) and the Poisson ratio.

Dependence of Permeability on Crack Opening

The permeability, b , is sure to increase with the opening δ_c of the cracks. According to the crack band model [10, 11], $\delta_c \approx l_0\epsilon''$ where l_0 is the material characteristic length and ϵ'' is the inelastic part of strain across (assuming it is tensile). Since the gel-created cracks run in all directions, we consider the volumetric inelastic strain ϵ_V'' . The flow of gel in the cracks must be viscous and laminar, in which case the volume flux is proportional to δ_c^3 (as between two parallel plates). Thus, the effect of inelastic strain on the gel permeability may be introduced as

$$\text{for } v \leq v_0 : \quad b = b_0 \quad (32)$$

$$\text{for } v > v_0 : \quad b = b_0 \left(1 + \beta \langle \epsilon_{(i)}^{fr} \rangle^n\right) \quad (33)$$

where b_0 = initial permeability for filling the empty pores, β = empirical dimensionless constant, and $\langle x \rangle = \max(x, 0)$ (Macauley brackets); $n = 3$ if the flow of gel in the crack is considered as viscous; and $\epsilon_{(i)}^{fr}$ ($i = 1, 2, 3$) are the principal values of the fracturing strain tensor

$$\epsilon_{ij}^{fr} = \epsilon_{ij} - \epsilon_{ij}^{cr} = C_{ijkl}(t)\sigma_{kl} \quad (34)$$

where C_{ijkl} = current elastic compliance tensor based on current $E(t)$.

Note that the opening of the cracks in the surrounding paste or mortar do not matter for permeability. The gel in these cracks quickly calcifies and ceases to be a fluid.

Two-Phase Medium for Loading of Concrete by Pressure in Pores and Cracks

Concrete is a nonstandard two-phase slid-fluid medium—nonstandard because much of evaporable is contained as hindered adsorbed water in nanopores with the width of only a few atoms. Such water behaves simultaneously as a load-bearing solid. Thus it would be incorrect to use the classical Biot-type equilibrium relation between the phases, which applies to materials such as saturated sand and reads $S_V = (1 - v)\sigma_V - vp$; here σ_V = volumetric stress in the solid, calculated from the constitutive model for concrete; S_V = total volumetric stress in the two-phase medium, which is used in finite element analysis to calculate the nodal forces. The gel volume fraction v is here used instead of porosity.

An important point is that, because of the water adsorbed in the nanopores, the stiffness of the solid, especially its damage and fracture, is not very sensitive to the volume fraction of water (indeed, the water content has usually been ignored in the nonlinear triaxial modeling of concrete damage). Consequently, σ_V in the solid phase should not be multiplied by $(1 - v)$. So we use the following incremental volumetric and tensorial two-phase equilibrium conditions and their incremental forms:

$$\Delta S_V = \Delta \sigma_V - \Delta(vp) \quad (35)$$

$$\Delta S_{ij} = \Delta \sigma_{ij} - \delta_{ij} \Delta(vp) \quad (36)$$

$$\Delta(vp) = v \Delta p + p \Delta v \quad (37)$$

where $i, j = 1, 2, 3$ are Cartesian tensorial subscripts; δ_{ij} = Kronecker delta (unit tensor), and $\sigma_V = \sigma_{kk}/3$. Although Eq. (35) has the form of Terzaghi's effective stress, it should not be physically interpreted as such because the effective stress, based on the so-called boundary porosity, is appropriate only for failure criterion, while this equation applies at all stages of loading.

Stable Algorithm for a Time Step of Explicit Finite Element Analysis

1. For concrete age $t_{old} + \Delta t/2$ at the middle of the current time step, use Widders' formula for inverse Laplace transform to calculate from the compliance function of concrete the current continuous, and then discrete, retardation spectra.
2. For each integration point of each finite element, use the exponential algorithm for aging linear creep to calculate for each microplane the inelastic strains and incremental moduli according to Eqs. (28), (29) and (30).
3. In the current time step, at each integration point of each finite element, compute the pressure change due to diffusion at constant gel mass from Eq. (20) using the old values of v and p . Then update p , v and v_{ca} according to Eqs. (20), (21) and (22).
4. Using the new nodal displacements and strains furnished by the finite element analysis of the previous time step, calculate the new σ_V -value for each integration point from the constitutive law for the solid (based here on microplane model M7).
5. Calculate the total volumetric stress S_V and its increment for each integration point of each finite element from Eq.(35) and its old value.

6. Use the total stress tensor S_{ij} as the input for an explicit finite element program, to calculate from S_{ij} the equivalent nodal forces according to the principle of virtual work. Then, solve the finite element system for these forces and applied loads to obtain the new strain tensors ϵ_{ij} and their increments at all integration points, which are needed to begin the analysis of the next time step.

Calibration and Verification by Laboratory Experimental Data

ASR induced expansion

The present model is now calibrated and validated by published experimental data. Important data were reported by Multon and Toutlemonde [36]. These tests had the duration of 450 days, but because the ASR was accelerated ASR the deformation and deterioration corresponded to 5–50 years in actual structures. The specimens were cylinders of diameter 130 mm and height 240 mm. The water-cement ratio w/c was 0.5, and cement content of concrete was 410 kg/m³. To accelerate the ASR, potassium hydroxide was dissolved in the mixing water (up to 1.25% of the mass of cement)

Since moisture content has a large effect on ASR [40, 31], all the specimens were kept sealed under a watertight cover to achieve a homogeneous moisture state and thus homogeneous ASR-induced strains. Nevertheless, about 0.5% of water mass leaked after 450 days. After 28 days of curing, the cylinders were subjected 9 different homogeneous stress states of 3 different types: 1) free expansion; 2) expansion under confinement by a 3 mm thick steel ring, and 3) a 5 mm thick steel ring (the yield stress of steel was 206 MPa and Young’s modulus 193,000 MPa). For each type of loading, three levels of axial compressive load were used: 0, 10 and 20 MPa. The simulations of these tests are presented in Fig. 3.

The damage and cracking patterns for the three different stress states were rather different, as seen in Fig. 4 which shows the differences in the cracking patterns that occur for these different stress states. For the unconfined load-free specimens, there is no preferred direction of crack propagation (Fig. 4a). But when an axial compressive load is superposed, damage in the loading direction is prevented and the ASR damage zones and cracks grow mainly radially (Fig. 4b).

Fig. 4c demonstrates the cracking pattern for the case of radial confinement without axial loading. As expected, the confinement directs the ASR expansion in the axial direction and thus the cracks propagate mainly horizontally. Finally, for the case of both strong radial confinement and a large compressive axial stress, there is only micro-cracking in all directions (Fig. 4d). All of these cracking patterns are in agreement with the experiments [31].

Fig. 5 compares the axial strains and Fig. 6 the radial strains. For the free expansion case with no external loading, there is no preferred direction for damage and cracking growth, but after damage the radial and axial strains are often unequal and scattered. To minimize this scatter, Fig. 7 shows the evolution of the volumetric strain, i.e., $\epsilon_V = \epsilon_{axial} + 2\epsilon_{radial}$. Fig. 7.

Generally, the predicted curves are in satisfactory agreement with the experimental ones, even though only a single aggregate size was considered. In reality, the aggregate size followed a specified granulometric curve. The aggregate size distribution could nevertheless be taken into account in future work, which may be expected to lead to further improvement in data fits.

Conclusions

1. Analysis of the ASR gel diffusion into pores and cracks in the aggregate and the surrounding cement paste and mortar leads to realistic model for the ASR damage in concrete. The model can match published experimental data quite well.
2. The diffusion analysis must distinguish empty pores fillable at no pressure, pores requiring high pressures to penetrate, cracks whose opening reduces the required pressure, and pores in cement paste beyond the interface transition zone in which the gel combines quickly with calcium hydroxide and solidifies.
3. In view of the complexities and uncertainties involved, the partial differential equation for diffusion may be replaced by an approximate ordinary differential equation for the evolution of the average depth of gel penetration front, characterized by the gel volume fraction in concrete.
4. To achieve an unconditionally stable explicit algorithm for time step integration permitting long time steps, the diffusion problem is inverted to pressure relaxation during the time step at constant gel mass. The gel mass is then increased suddenly at the end of time step.
5. The directionality of damage when ASR evolves under various triaxial stress states can be captured by using the microplane model.
6. Although concrete with the ASR gel represents a two-phase medium, the standard Biot's form is eschewed because the evaporable adsorbed water in the nanopores, while mobile, is load-bearing and acts as part of the solid skeleton.
7. The creep of concrete, which significantly reduces the stresses produced by ASR, may be incorporated into the microplane model as additional inelastic strains on microplanes of various orientations.

Acknowledgment: Financial support from the NEUP Program of the U.S Department of Energy under grant DE-AC07-05/D14517 to Northwestern University is gratefully acknowledged. The authors also wish to thank professors Jianmin Qu and Gianluca Cusatis of Northwestern University, and professor Mohammed Alnaggar of Rensselaer Polytechnic Institute, for valuable discussions.

References

- [1] ASTM 129301 AC. Standard test method for concrete aggregates by determination of length change of concrete due to alkalisilica reaction. Annual Book of ASTM Standards, vol. 04.02 (Concrete and Aggregates), Philadelphia (PA); 2002.
- [2] Alnaggar, M., Cusatis, G., and Di Luzio, G. (2013). "Lattice discrete particle modeling (LDPM) of alkali silica reaction (ASR) deterioration of concrete structures." *Cement and Concrete Composites* 41, 45–29.
- [3] Al-Asali, S. a. (1988). "Engineering properties of concrete affected by alkali silica reactions." *ACI Materials Journal*. vol. , pp. 367-374.
- [4] Bažant, Z.P., and Steffens, A. (2000). "Mathematical model for kinetics of alkali-silica reaction in concrete." *Cement and Concrete Research* 30 (3), 419–428..
- [5] Bažant, Zdenek P., and Yunping Xi. "Continuous retardation spectrum for solidification theory of concrete creep." *Journal of Engineering Mechanics* 121.2 (1995): 281-288.

⁵Planned to be completed and inserted by November 30, 2015

- [6] Bazant, Zdenek P., Qiang Yu, and Guang-Hua Li. "Excessive long-time deflections of prestressed box girders. I: Record-span bridge in Palau and other paradigms." *Journal of Structural Engineering* 138.6 (2012): 676-686.
- [7] Bažant, Z.P., Zi, G., and Meyer, C. (2000). "Fracture mechanics of ASR in concretes with waste glass particles of different sizes." *J. of Engrg. Mechanics* ASCE 126 (3), 226–232.
- [8] Bažant, Z.P. (1971). "Numerically stable algorithm with increasing time steps for integral-type aging creep." *Proc., First Intern. Conf. on Struct. Mech. in Reactor Tech. (SMIRT-1)* (org. by BAM, Berlin, and Commission of Eur. Communities), ed. by T.A. Jaeger, West Berlin, Vol. 4, Part H, 119–126.
- [9] Caner, F.C., and Bažant, Z.P. (2013). "Microplane model M7 for plain concrete: I. formulation." *ASCE J. of Engrg. Mechanics* 139 (12), Dec., 1714–1723.
- [10] Bažant, Z.P., and Oh, B.-H. (1983). "Crack band theory for fracture of concrete." *Materials and Structures* (RILEM, Paris), 16, 155–177.
- [11] Bažant, Z.P., and Planas, J. (1998). *Fracture and Size Effect in Concrete and Other Quasibrittle Materials*. CRC Press, Boca Raton and London.
- [12] Bažant, Z.P., and Najjar, L. J. (1972). "Nonlinear water diffusion in nonsaturated concrete." *Materials and Structures* (RILEM, Paris), 5, 3–20 (used in Model Code 2010).
- [13] Biot, M.A. (1942). "General theory of three-dimensional consolidation." *J. of Appl. Phys.* 12 (2), 155–164.
- [14] Biot, M.A. (1962). "Mechanics of deformation and acoustic propagation in porous media." *J. of Appl. Phys.* 33 (4), 1482-1498.
- [15] Biot, M.A. (1957). "The elastic coefficients of the theory of consolidation." *ASME J. of Applied Mechanics* 24, 594–601.
- [16] Clark L.A. Modeling the structural effects of alkalisilica reactions on reinforced concrete. *ACI Mater J* 1991;88:2717.
- [17] Clark L.A (1990). "Structural aspects of alkali-silica reaction." *Structural engineering review* 2: pp. 121-125.
- [18] CSA A23.225A00 C. Detection of alkali-silica reactive aggregate by accelerated expansion of mortar bars. CSA A23.200: Methods of Test for Concrete, Canadian Standards Association, Mississauga, Ont..
- [19] Berra M, Faggiani G, Mangialardi T, Paolini AE. Influence of stress restraint on the expansive behaviour of concrete affected by alkalisilica reaction. *Cem Concr Res* 2010; 40(9):14039.
- [20] Caner, F.C., and Bažant, Z.P. (2013). "Microplane model M7 for plain concrete: I. formulation." *ASCE J. of Engrg. Mechanics* 139 (12), Dec., 1714–1723.
- [21] Caner, F.C., and Bažant, Z.P. (2013). "Microplane model M7 for plain concrete: II. calibration and verification." *ASCE J. of Engrg. Mechanics* 139 (12), Dec., 1724–1735.
- [22] Coussy, O. (1995). *Mechanics of Porous Continua*, J. Wiley & Sons, Chichester, U.K.
- [23] Diamond S. Chemistry and Other Characteristics of ASR Gels. Proceedings of the 11th International Conference on Alkali-Aggregate Reaction in Concrete, Quebec City, Canada. 2000, 31– 40.
- [24] Dron R, Brivot F. Thermodynamic and kinetic approach to the alkalisilica reaction: Part 1. *Cem Concr Res* 1992;22(5):9418.
- [25] Dron R, Brivot F. Thermodynamic and kinetic approach to the alkalisilica reaction: Part 2. *Cem Concr Res* 1993;23(1):93103.
- [26] Farage M, Alves JLD, Fairbairn EMR. Macroscopic model of concrete subjected to alkaliaggregate reaction. *Cem Concr Res* 2004;34(3):495505.
- [27] Herrador MF, F M-A, Fernandez-Gago RH. Mechanical behavior model for ASR affected dam concrete under service load: formulation and verification. *Mater Struct* 2009;42(2):20112.
- [28] Hobbs DW. Alkalisilica reaction in concrete. London: Thomas Telford; 1988.
- [29] Hubler, M.H., Wendner, R., and Bažant, Z.P. (2015). "Statistical justification of model B4 for drying and autogenous shrinkage of concrete and comparisons to other models." *Materials and Structures* 48 (4), 797-814.
- [30] Jirásek, M., and Bažant, Z.P. (2002). *Inelastic Analysis of Structures*. J. Wiley & Sons, London and New York.
- [31] Larive C. (1988). Rapports combinées de l' experimentation et de la modélisation à la compréhension de l'alcali-réaction et de ses effets mécaniques. Doctoral Dissertation, Laboratoire Central des Ponts et Chaussées, Paris.
- [32] Monette L.J, G. N. J., Grattan-Bellew P.E, (2000). "Structural effects of the alkali aggregate reactions on non-loaded and loaded reinforced concrete beams." *Proc., 11th Intern. Conf. on Alkali Aggregate Reaction*: pp. 999-1008.

- [33] Multon S, Cyr M, Sellier A, Leklou N, Petit L. Coupled effects of aggregate size and alkali content on ASR expansion. *Cem Concr Res* 2008;38(3):3509.
- [34] Multon S, Cyr M, Sellier A, Diederich P, Petit L. Effects of aggregate size and alkali content on ASR expansion. *Cem Concr Res* 2010;40(4):50816.
- [35] Multon S, Sellier A, Cyr M. Chemomechanical modeling for prediction of alkali silica reaction (ASR) expansion. *Cem Concr Res* 2009;39(6):490500.
- [36] Multon, S., and F. Toutlemonde. "Effect of applied stresses on alkali-silica reaction-induced expansions." *Cement and Concrete Research* 36.5 (2006): 912-920.
- [37] Multon S, Seignol JF, Toutlemonde F. Chemo-mechanical assessment of beams damaged by alkalisilica reaction. *J Mater Civ Eng* 2006;18(4):5009
- [38] Multon S, Toutlemonde F. Effect of moisture conditions and transfers on alkali silica reaction damaged structures. *Cem Concr Res* 2010;40(6):92434.
- [39] Ono K (1990). "Strength and stiffness of alkali silica reaction concrete and concrete members." *Structural Engineering Review* 2: pp. 121-125.
- [40] H. Olafsson, The effect of relative humidity and temperature on alkali expansion of mortar bars, *Proc. 7th Int. Conf. on AAR*, Ottawa, Canada, 1986, pp. 461-465.
- [41] Pan, J.W., Feng, Y.T., Wang, J.T, Sun, Q.C., Zhang, C.H., and Owen, D.R.J. (2012). "Modeling of alkali-silica reaction in concrete: a review." *Front. Struct. Civ. Eng.* 6 (1). 1-18.
- [42] Pietruszczak S. On the mechanical behaviour of concrete subjected to alkali aggregate reaction. *Comput Struct* 1996;58(6):10937.
- [43] Poyet S, Sellier A, Capra B, Thvenin-Foray G, Torrenti JM, Tournier-Cognon H, et al. Influence of water on alkalisilica reaction: experimental study and numerical simulations. *J Mater Civ Eng* 2006;18(4):58896.
- [44] RILEM Technical Committee TC-242-MDC (Z.P. Bažant, chair) (2015). "Model B4 for creep, drying shrinkage and autogenous shrinkage of normal and high-strength concretes with multi-decade applicability (RILEM draft recommendation: TC-242-MDC multidecade creep and shrinkage of concrete: material model and structural analysis). *Materials and Structures* 48 (4), 753-750.
- [45] Rahimi S, Abdolhosseini M, Bažant Z.P. " Modeling long term hydration based on diffusion." Under publication.
- [46] Saouma V, Perotti L. Constitutive model for alkali-aggregate reactions. *ACI Mater J* 2006;103:194202.
- [47] Saouma V, Xi Y. Literature review of alkali aggregate reactions in concrete dams. Report cu/sa-xi-2004/001. Department of Civil, Environmental, & Architectural Engineering University of Colorado; 2004.
- [48] Stanton TE. Expansion of concrete through reaction between cement and aggregate. *Proc Am Soc Civ Eng* 1940;66:1781811.
- [49] Siemes T, V. J. (2000). "Low tensile strength in older concrete structures with alkali-silica reactions." *Proc., 11th Intern. Conf. on Alkali Aggregate Reaction*: pp. 1029-1038.
- [50] Steffens A, Li K, Coussy O. Aging approach to water effect on alkalisilica reaction degradation of structures. *J Eng Mech Mater* 2003;129:509.
- [51] Suwito A, Jin W, Xi Y, Meyer C. A mathematical model for the pessimum size effect of ASR in concrete. *Concr Sci Eng* 2002;4(13):2334.
- [52] Swamy RN, Al-Asali MM. Effect of alkalisilica reaction on the structural behavior of reinforced concrete beams. *ACI Mater J* 1989;86:4519.
- [53] Swamy R.N (1992). "Testing for alkali-silica reaction in concrete." *The alkali silica reaction in concrete*, ed. R N Swamy, Blackie, Van Nostrand Reinhold: pp 54-95.
- [54] Swamy R.N, and A.-A. M. M. (1986). "Influence of alkali silica reaction on the engineering properties of concrete." *Alkalis in concrete*, ASTM STP-930; ed., V.H. Dodson, American Society for Testing and Materials Journal, Philadelphia: pp. 69-86.
- [55] Toutlemonde F. Structural behavior of concrete beams affected by alkalisilica reaction. *ACI Mater J* 2005; 102(2): 6776.
- [56] Ulm F, Coussy O, Kefei L, Larive C. Thermo-chemo-mechanics of ASR expansion in concrete structures. *J Eng Mech* 2000;126(3):23342.
- [57] Wendner, R., Hubler, M.H., and Bažant, Z.P. (2015). "Statistical justification of model B4 for multi-decade concrete creep using laboratory and bridge databases and comparisons to other models. *Materials and Structures* 48 (4), 815-833.
- [58] Xi Y, Suwito A, Wen X, Meyer C, Jin W. Testing and modeling alkalisilica reaction and the associated expansion of concrete. *Mechanics of Quasi-Brittle Materials and Structures*. Proceedings of international workshop in honor of Prof Z.P. Bazant 60th birthday. Hermes Science Publications; Paris 1998.

Appendix I.—Basic Notations

- v = volume fraction of gel-filled concrete, or the volume of the extruded ASR gel in m^3 per m^3 of concrete, i.e., dimensionless;
- $\xi = \rho v$ = mass of extruded ASR gel per unit volume of concrete, i.e., gel mass concentration (kg/m^3);
- $\xi(t)$ = specified evolution of ξ in time;
- ρ = mass density of the ASR gel, which depends on p (as well as temperature) and is considered about the same as the mass density of water (kg/m^3);
- ρ_0 = reference ρ -value at atmospheric pressure and room temperature);
- $M(t)$ = ASR gel mass extruded into pores of matrix per unit surface area of mineral aggregate grain (kg/m^3) (not counting the gel within the aggregate);
- p = average pressure in the ASR gel extruded from the aggregate grains (N/m^2), positive for compression;
- η = effective viscosity of pressure relaxation by diffusion;
- n = gel porosity = area fraction of cross section through concrete that is occupied by gel-filled pores;
- np = resultant of gel pressure in the gel-filled pores (N/m^2);
- σ_V, ϵ_V = volumetric stress and strain in solid, positive for tension (N/m^2 or MPa);
- $(1 - n)\sigma_V$ = resultant of volumetric stress in concrete per unit cross section of concrete;
- S_V = total volumetric stress applied on the element of concrete, positive for tension;
- κ = bulk modulus of ASR gel, which is the inverse of volume compressibility (assumed the same as for water) (N/m^2);
- b = Darcy permeability of pores in concrete (dimension $\text{m}^3\text{s}/\text{kg} = \text{m}^2/\text{N s}$);
- \bar{b} = effective Darcy permeability on the macroscale (dimension $\text{m s}/\text{kg} = 1/\text{N s}$);
- v_0 = volume fraction of empty, readily accessible, pores that get filled at negligible pressure.

List of Figures

- | | | |
|---|--|----|
| 1 | ASR gel formation due to water diffusion into reactive aggregate; (a) Early stage of diffusion, (b) late stage of diffusion, (c) idealization with spherical diffusion | 17 |
| 2 | ASR reaction process and schematic illustration of ASR induced damage; (a) Alkali-silica reaction, (b) formation of swelling and non-swelling ASR gel, and (c) ASR induced damage and cracking | 17 |
| 3 | Simulation of specimens tested by Multon and Toutlemonde [36]; (a) Unconfined case, (b) confined case | 17 |
| 4 | Cracking patterns for different stress states; (a) unconfined, no load, (b) Radial confined, no axial load, (c) unconfined and loaded axially, and (d) laterally confined and axially loaded | 18 |
| 5 | Axial strain versus reaction time for: (a) unconfined specimen under 10 MPa axial load, (b) unconfined, with axial load up to 20 MPa, (c) 3 mm confinement with no axial load, (d) 5 mm confinement with no axial load, (e) 3 mm confinement with 10 MPa axial load, (f) 5 mm confinement with 10 MPa axial load, (g) 3 mm confinement with 20 MPa axial load, (h) 5 mm confinement with 20 MPa axial load | 18 |

6	Radial strain versus reaction time for: (a) unconfined specimen with 10 MPa axial load, (b) unconfined under 20 MPa axial load, (c) 3 mm confinement with no axial load, (d) 5 mm confinement with no axial load, (e) 3 mm confinement with 10 MPa axial load, (f) 5 mm confinement with 10 MPa axial load, (g) 3 mm confinement with 20 MPa axial load, (h) 5 mm confinement with 20 MPa axial load	19
7	Volume change relative to initial volume (or 3-times the volumetric strain), for unconfined and load-free case	19

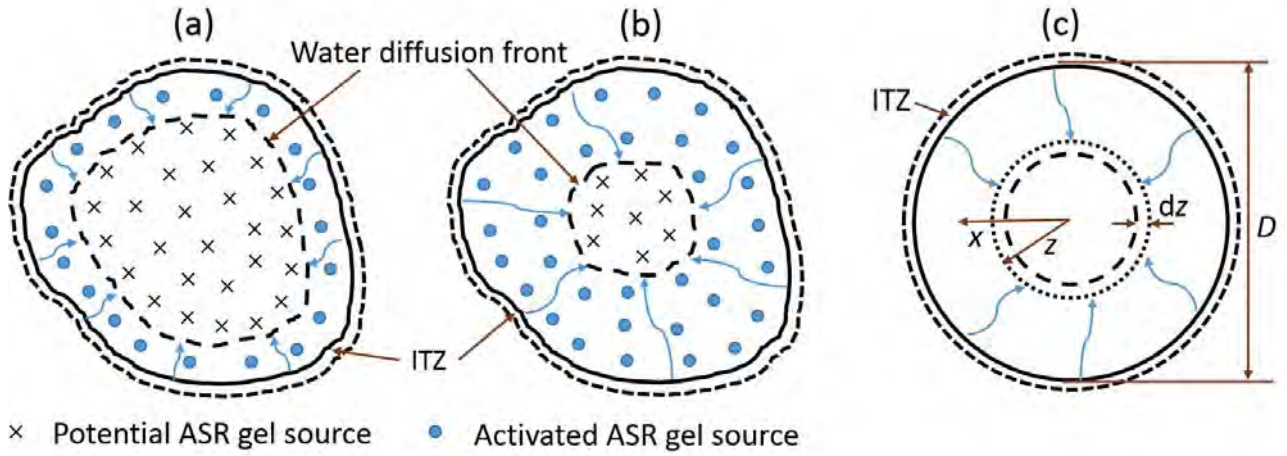


Figure 1: ASR gel formation due to water diffusion into reactive aggregate; (a) Early stage of diffusion, (b) late stage of diffusion, (c) idealization with spherical diffusion

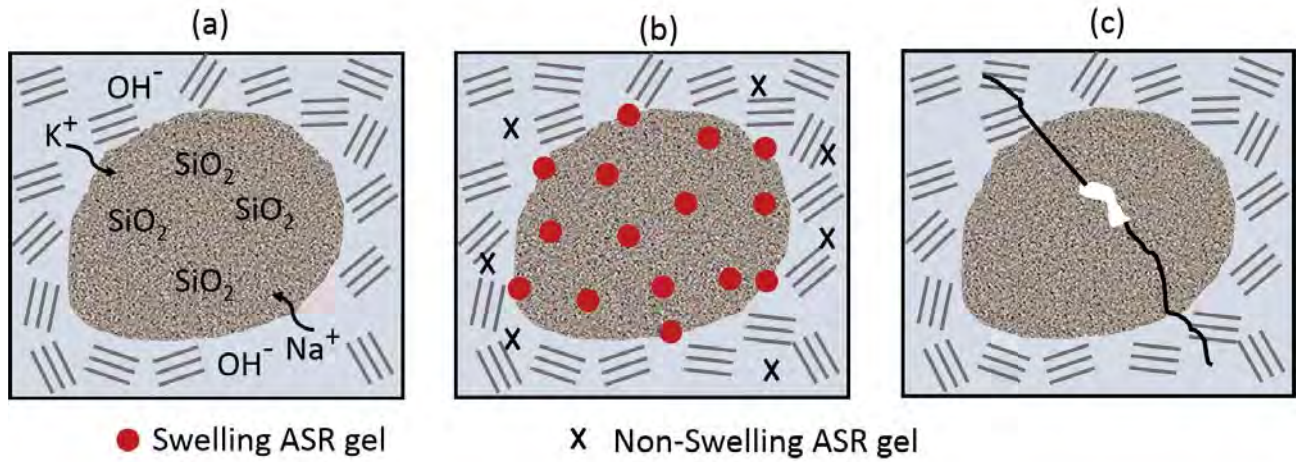


Figure 2: ASR reaction process and schematic illustration of ASR induced damage; (a) Alkali-silica reaction, (b) formation of swelling and non-swelling ASR gel, and (c) ASR induced damage and cracking

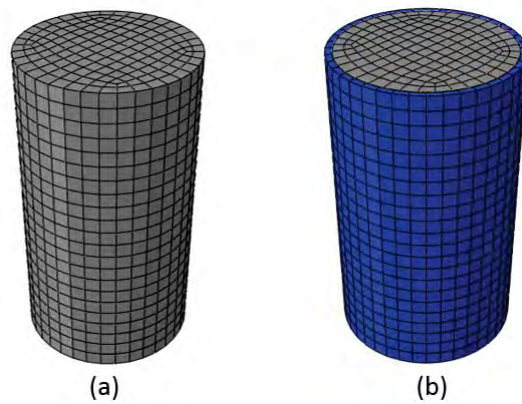


Figure 3: Simulation of specimens tested by Multon and Toutlemonde [36]; (a) Unconfined case, (b) confined case

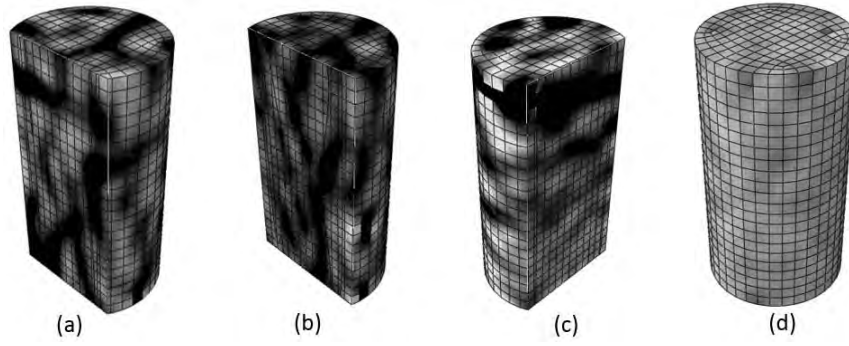


Figure 4: Cracking patterns for different stress states; (a) unconfined, no load, (b) Radial confined, no axial load, (c) unconfined and loaded axially, and (d) laterally confined and axially loaded

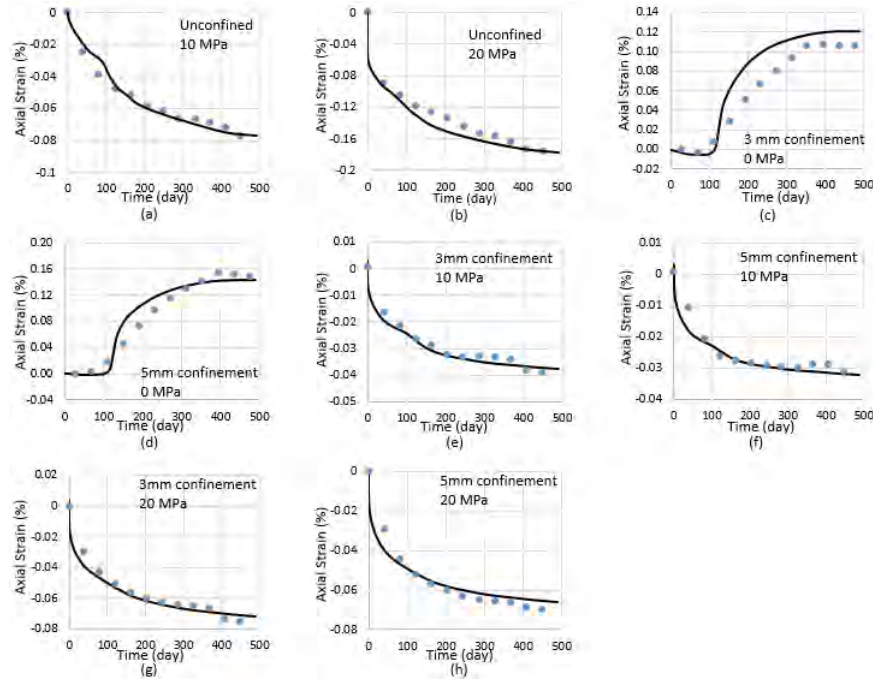


Figure 5: Axial strain versus reaction time for: (a) unconfined specimen under 10 MPa axial load, (b) unconfined, with axial load up to 20 MPa, (c) 3 mm confinement with no axial load, (d) 5 mm confinement with no axial load, (e) 3 mm confinement with 10 MPa axial load, (f) 5 mm confinement with 10 MPa axial load, (g) 3 mm confinement with 20 MPa axial load, (h) 5 mm confinement with 20 MPa axial load

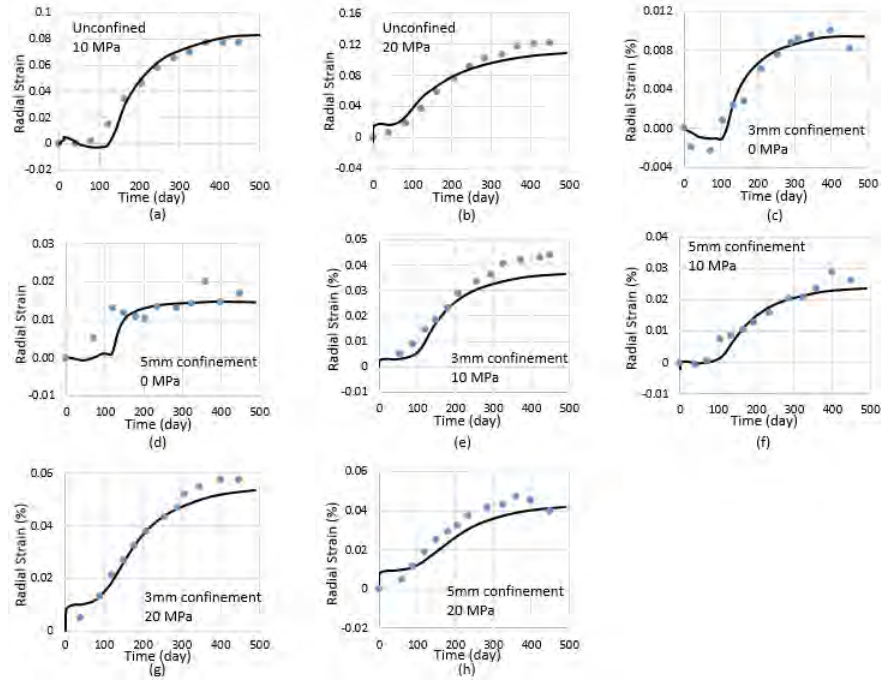


Figure 6: Radial strain versus reaction time for: (a) unconfined specimen with 10 MPa axial load, (b) unconfined under 20 MPa axial load, (c) 3 mm confinement with no axial load, (d) 5 mm confinement with no axial load, (e) 3 mm confinement with 10 MPa axial load, (f) 5 mm confinement with 10 MPa axial load, (g) 3 mm confinement with 20 MPa axial load, (h) 5 mm confinement with 20 MPa axial load

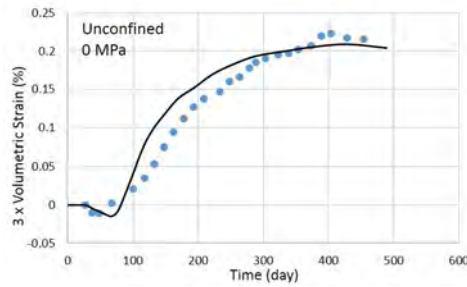


Figure 7: Volume change relative to initial volume (or 3-times the volumetric strain), for unconfined and load-free case